

Mechanical Behavior of Ultrastructural Biocomposites

by

Cathal Kearney

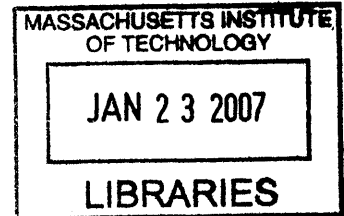
B.A., B.A.I. in Mechanical Engineering
Trinity College, Dublin, Ireland, 2004

SUBMITTED TO THE DEPARTMENT OF MECHANICAL ENGINEERING IN PARTIAL
FULFILLMENT OF THE REQUIREMENTS FOR THE DEGREE OF

MASTER OF SCIENCE IN MECHANICAL ENGINEERING
AT THE
MASSACHUSETTS INSTITUTE OF TECHNOLOGY

June 2006

© 2006 Massachusetts Institute of Technology
All rights reserved.



Signature of Author: _____

Department of Mechanical Engineering
May 19, 2006

Certified by: _____

Professor Mary C. Boyce
Gail E. Kendall Professor of Mechanical Engineering

Certified by: _____

Professor Christine Ortiz
Associate Professor of Materials Science and Engineering

Accepted by: _____

Professor Lallit Anand, Chairman
Department Committee on Graduate Students

BARKER

Mechanical Behavior of Ultrastructural Biocomposite Materials

by

Cathal Kearney

Submitted to the Department of Mechanical Engineering
on May 19, 2006, in partial fulfillment of the
requirements for the degree of
Master of Science in Mechanical Engineering

ABSTRACT

For numerous centuries nature has successfully developed biocomposite materials with detailed multiscale architectures to provide a material stiffness, strength and toughness. One such example is nacre, which is found in the shells of many mollusks, and consists of an inorganic phase of aragonite tablets 5-8 μm in planar dimension and 0.5-1 μm in thickness direction and an organic phase of biomacromolecules. High resolution microscopy imaging was employed to investigate the microscale features of seashell nacre to reveal the nucleation points within tablets, the sector boundaries and an overlap between tablets of neighboring layers of $\sim 20\%$.

Aragonite, the mineral constituting the inorganic phase of nacre, is a calcium carbonate mineral that is ubiquitous in many natural systems, including both living organisms and geological structures. Resistance to yield is an important factor in the ability of aragonite to provide both strength and toughness to numerous biological materials. Conversely, plastic deformation of aragonite is a governing factor in the formation and flow of large scale geological structures. The technique of nanoindentation combined with in-situ tapping mode atomic force microscopy imaging was used to show the anisotropic nanoscale plastic behavior of single crystal aragonite for indentations into three mutually orthogonal planes. Force vs. indentation depth curves for nanoindentation coaxial to the orthorhombic crystal c-axis exhibited distinct load plateaus, ranging between 275-375 μN for the Berkovich indenter and 400-500 μN for the cono-spherical indenter, indicative of dislocation nucleation events. Atomic force microscopy imaging of residual impressions made by a cono-spherical indenter showed four pileup lobes; residual impressions made by the Berkovich indenter showed protruding slip bands in pileups occurring adjacent to only one or two of the Berkovich indenter planes.

Anisotropic elastic simulations were used to capture the low load response of single crystal aragonite, with the elastic simulations for the (001) plane matching the experimental data up until the onset of plasticity. Numerical simulations based on a crystal plasticity model were used to interrogate and identify the kinematic mechanisms of plastic slip leading to the experimentally observed plastic anisotropy. In particular, in addition to the previously reported slip systems of the $\{100\}\langle 001\rangle$ family, the family of $\{110\}\langle 001\rangle$ slip systems is found to play a key role in the plastic response of aragonite.

Thesis Supervisors:
Professor Mary C. Boyce
Gail E. Kendall Professor of
Mechanical Engineering

Professor Christine Ortiz
Associate Professor of Materials
Science and Engineering

Acknowledgements

First and foremost, I would like to thank both Professor Mary Boyce and Professor Christine Ortiz for their dedication, encouragement and guidance in this Thesis work. Their commitment to excellence and energy was an inspiration to me and I would not have achieved my goals over the past two years without their support and encouragement, for which I'm eternally grateful.

My colleagues on the project: Benjamin Bruet, Terianne Hall, Jeff Palmer and Julian Villareal, were not only good work partners but became great friends and I would like to thank them for their input and assistance during my Masters work.

For assistance and training during my nanoindentation experiments, I would like to thank Alan Schwartzmann in the nanolab at MIT. For the modeling work on single crystal aragonite, I would like to thank Prof Radovitsky and Dr. Zisu Zhao of the Aero-astro department at MIT.

A special thanks to all the administrative staff at MIT, in particular Ms. Leslie Regan, Ms. Joan Kravit, Mr. Daniel O' Shea in the Graduate office and Ms. Una Sheehan, for helping to provide the right environment for me at MIT to pursue my studies.

I would like to thank Fulbright & the Institute of International Education and the Institute for Soldier nanotechnologies at MIT for providing me with funding and sponsorship during my Masters program.

To the many friends I have at MIT for being there during the highs and the lows, for introducing me to numerous cultures, for broadening my horizons and for keeping me balanced .at least balanced for an MIT kid!

Finally, I am forever indebted to my family: my Mam & Dad, Bernie & Pat and my three brothers, Seaghan, Lorcan & Paraic. They are the mainstay that keeps me, me.

for Granda John

Table of Contents

| | |
|--|-----------|
| <u>Abstract</u> | 2 |
| <u>Acknowledgements</u> | 4 |
| <u>Contents List</u> | 6 |
| <u>List of figures</u> | 8 |
| Chapter 1 <i>Introduction to biocomposite materials and seashell nacre</i> | |
| Background | 14 |
| <u>1.1</u> Mechanical properties | 15 |
| <u>1.2</u> Biocomposite materials | 16 |
| <u>1.3</u> Microstructural features in mollusc shells and the shell of <i>Trochus niloticus</i> | 24 |
| <u>1.3.1</u> Layer types found in mollusc shells and their microstructures | 25 |
| <u>1.3.2</u> <i>Trochus niloticus</i> shells and the layers found through the thickness | 27 |
| <u>1.4</u> Seashell nacre | 28 |
| <u>1.4.1</u> Ultrastructure of seashell nacre | 29 |
| <u>1.4.2</u> Columnar nacre, sheet nacre and the Nacreous layer in <i>Trochus niloticus</i> | 30 |
| <u>1.4.3</u> Mechanical properties of seashell nacre | 31 |
| <u>1.5</u> Outline of Thesis | 41 |
| Chapter 2 <i>Microscale geometrical study of the nacre from the species Trochus niloticus</i> | |
| Introduction | 42 |
| <u>2.1</u> Geometrical features of Seashell nacre | 42 |
| <u>2.1.1</u> Sample preparation for imaging | 43 |
| <u>2.1.2</u> Geometrical features and statistical analysis of cross-sectional images | 44 |
| <u>2.1.3</u> Geometrical features of <i>c</i> -plane images | 49 |
| <u>2.1.4</u> Creation of <i>SolidWorks</i> model of nacre from micrographs and geometrical analysis | 55 |
| <u>2.1.5</u> Solid modelling of idealized hexagonal tablets | 59 |
| <u>2.1.6</u> Idealized Voronoi layer | 61 |
| <u>2.1.7</u> Biological & mechanical significance of results | 63 |
| <u>2.2</u> Summary | 64 |
| Chapter 3 <i>Nanoindentation study of single crystal aragonite</i> | |
| Introduction | 65 |
| <u>3.1</u> Aragonite: biologically, geologically and technologically | 66 |

| | | |
|--|--|------------|
| <u>3.2</u> | Previous Investigations on aragonite | 67 |
| <u>3.3</u> | Nanoindentation study on <i>c</i> -plane of nacre aragonite tablets | 71 |
| <u>3.4</u> | Nanoindentation in crystalline materials | 74 |
| <u>3.5</u> | Investigation of plasticity in similar materials | 77 |
| <u>3.6</u> | Nanoindentation investigation of single crystal aragonite | 79 |
| <u>3.6.1</u> | Experimental setup | 79 |
| <u>3.6.2</u> | Nanoindentation results for Berkovich indenter: Force vs. penetration depth curves | 81 |
| <u>3.6.3</u> | Nanoindentation results for Berkovich indenter: Tapping mode atomic force microscopy of residual indents on the (001) plane | 84 |
| <u>3.6.4</u> | Nanoindentation results for cono-spherical indenter: Force vs. penetration depth curves | 90 |
| <u>3.6.5</u> | Nanoindentation results for cono-spherical indenter: Tapping mode atomic force microscopy of residual indents on the (001) plane | 92 |
| <u>3.7</u> | Comparison of micro- vs. nano-indentation using a Knoop tip on the (001) plane of single crystal aragonite | 94 |
| <u>3.8</u> | Nanoindentation on <i>c</i> -plane of aragonite vs. nanoindentation on <i>c</i> -plane of nacre tablets | 96 |
| <u>3.9</u> | Summary | 98 |
| | | |
| <u>Chapter 4</u> <i>Finite element simulation of the elastic and the elastic-plastic indentation of single crystal aragonite</i> | | |
| Introduction | | 101 |
| <u>4.1</u> | Details of model | 102 |
| <u>4.1.1</u> | Geometric description of finite element model and nanoindentation tips | 102 |
| <u>4.1.2</u> | Material models | 106 |
| <u>4.2</u> | Results | 112 |
| <u>4.2.1</u> | Results for elastic finite element model | 112 |
| <u>4.2.2</u> | Results for elastic-plastic finite element model | 120 |
| <u>4.4</u> | Summary | 127 |
| | | |
| <u>Chapter 5</u> <i>Conclusions and Future Work</i> | | 129 |
| | | |
| <u>Appendix A</u> <i>Nanoindentation study on the three cleavage planes of calcite</i> | | 133 |
| | | |
| <u>Appendix B</u> <i>Individual load-unload curves from nanoindentation study</i> | | 138 |
| | | |
| <u>Appendix C</u> <i>Oliver-Pharr analysis method</i> | | 152 |
| | | |
| <u>References</u> | | 154 |

List of Figures

| | |
|--|----|
| <u>1.1.1</u> Stress-strain curves under uniaxial tensile loading for ductile and brittle materials [Ashby et al] | 15 |
| <u>1.2.1</u> Storage of iron clusters in organisms [Mann] | 17 |
| <u>1.2.2</u> Electron micrograph of magnetotactic bacteria [Mann et al] | 18 |
| <u>1.2.3</u> Electron micrograph of the spine of a sea urchin [Sarikaya et al] | 18 |
| <u>1.2.4</u> Electron micrographs of sea urchin tooth [Wang et al] | 19 |
| <u>1.2.5</u> Longitudinal section of sea urchin tooth [Wang et al] | 19 |
| <u>1.2.6</u> Organic/organic biocomposites [Sarikaya et al; Chen et al] | 20 |
| <u>1.2.7</u> Multiscale architectural features of cancellous bone [Lakes] | 21 |
| <u>1.2.8</u> Scleratinian stony corals [Hartman et al; Lowenstam et al] | 22 |
| <u>1.2.9</u> Electron micrographs of rat tooth enamel [Mann; Lowenstam et al] | 23 |
| <u>1.2.10</u> Electron micrograph nacre of <i>Trochus niloticus</i> | 23 |
| <u>1.3.1</u> Layers found in the seashell of <i>Trochus niloticus</i> | 24 |
| <u>1.3.2</u> SEM image of periostracum from <i>Potomida littoralis</i> [Checa, 2000] | 25 |
| <u>1.3.3</u> Electron Micrograph images of prismatic layer [Feng et al; Tong et al] | 26 |
| <u>1.3.4</u> Cross-lamellar layers in the shell from the species <i>Strombus decorus persicus</i> [Pokroy et al] | 26 |
| <u>1.3.5</u> Photographs of <i>Trochus niloticus</i> seashell | 27 |
| <u>1.3.6</u> Electron micrograph of outer and inner prismatic layers of <i>Trochus niloticus</i> | 28 |
| <u>1.4.1</u> Electron micrograph of top and side view of <i>Trochus niloticus</i> nacre | 28 |
| <u>1.4.2</u> Illustration of the hierarchical ultrastructure of nacre [Bruet et al] | 29 |
| <u>1.4.3</u> Illustration of columnar nacre and sheet nacre [Wang et al] | 30 |
| <u>1.4.4</u> Electron micrographs of cleaved <i>Trochus niloticus</i> nacre | 31 |
| <u>1.4.5</u> Definition of orientations used to define mechanical properties [Currey] | 32 |
| <u>1.4.6</u> Curve of tensile testing of nacre [Currey] | 33 |
| <u>1.4.7</u> Dilation bands in nacre after loading in three-point bending [Wang et al] | 34 |
| <u>1.4.8</u> Shear stress vs. shear strain data for nacre [Menig et al] | 34 |
| <u>1.4.9</u> Load deflection data from three point bend testing of nacre [Wang et al] | 35 |
| <u>1.4.10</u> Oscilloscope trace of a tension test on nacre with three load-unload cycles [Currey] | 35 |
| <u>1.4.11</u> Crack propagation in nacre [Jackson et al] | 38 |
| <u>1.4.12</u> Intertablet organic matrix [Jackson et al; Smith et al.; Qi et al] | 39 |
| <u>1.4.13</u> Nanoasperities in on the top face of nacre tablets [Wang et al] | 39 |
| <u>2.1.1</u> Schematic of where samples were cut from for imaging | 44 |
| <u>2.1.2</u> Electron micrographs of nacre cross-sections revealing ‘brick and mortar’ structure | 45 |
| <u>2.1.3</u> Electron Micrograph of cross sectional image used to perform statistical analysis | 48 |
| <u>2.1.4</u> Histogram distributions of tablet length and percent offset for the statistical analysis performed on figure 2.1.3 | 48 |

| | |
|---|----|
| <u>2.1.5</u> Images of <i>c</i> -plane of nacre | 50 |
| <u>2.1.6</u> Tapping Mode Atomic Force Microscopy amplitude image of nacre tablets | 51 |
| <u>2.1.7</u> Image of two planes of nacre tablets with top layer transparent | 52 |
| <u>2.1.8</u> <i>SolidWorks</i> model of two nacre layers | 55 |
| <u>2.1.9</u> Example of cross-sectional cut taken and analyzed from the model illustrated in figure 2.1.8. | 56 |
| <u>2.1.10</u> Histograms of percent offset and tablet area based on model illustrated in figure 2.1.8 | 56 |
| <u>2.1.11</u> <i>SolidWorks</i> hexagonal model | 59 |
| <u>2.1.12</u> <i>SolidWorks</i> hexagonal model defining the angle of cut | 60 |
| <u>2.1.13</u> Histograms of percent offset and tablet area based on <i>SolidWorks</i> hexagonal model | 60 |
| <u>2.1.14</u> Schematic of Voronoi tessellation process | 61 |
| <u>2.1.15</u> Top view of Voronoi Tessellation layer created in <i>SolidWorks</i> | 62 |
| <u>2.1.16</u> Voronoi Tessellation layer overlaid on upper and lower layer of <i>SolidWorks</i> model | 63 |
| <u>3.1.1</u> Aragonite in living organisms [Hartman et al;Lowenstam et al] | 66 |
| <u>3.1.2</u> Geological example of aragonite [Kelley et al] | 67 |
| <u>3.2.1</u> Aragonite crystal structure | 68 |
| <u>3.2.2</u> Experimental data of microknoop indents in single crystal aragonite [Han et al] | 71 |
| <u>3.3.1</u> Schematic of nanoindentation on <i>c</i> -plane of nacre aragonite tablets [Bruet et al] | 72 |
| <u>3.3.2</u> Force vs. penetration data for the <i>c</i> -plane of nacre tablets using Berkovich indenter (maximum loads of 500 μ N, 750 μ N and 1000 μ N) [Bruet et al] | 72 |
| <u>3.3.3</u> Tapping mode atomic force microscopy amplitude image after nanoindentation in freshly cleaved nacre (maximum load 5000 μ N and 10000 μ N) | 73 |
| <u>3.4.1</u> Load-unload data for load controlled nanoindentation on the (100) plane of a Fe-3wt%Si surface [Gerberich et al] | 74 |
| <u>3.4.2</u> AFM imaging of residual indent in Fe-3wt%Si [Gerberich et al] | 75 |
| <u>3.4.3</u> Force vs. depth curves for nanoindentation (load controlled) of (110) Al [Van Vliet et al] | 76 |
| <u>3.4.4</u> Load v's displacement response for indentation in Sapphire using a Berkovich indenter [Page et al] | 76 |
| <u>3.5.1</u> The calcite unit cell [home.hetnet.nl/~turing/preparation_3dim_4.html] | 78 |
| <u>3.5.2.</u> The olive unit cell [http://www.doitpoms.ac.uk/tlplib/anisotropy/diffusion.php] | 78 |
| <u>3.6.1</u> Indenter tip geometries for the berkovich, cono-spherical and Knoop indenters | 80 |
| <u>3.6.2</u> Nanoindentation data for single crystal aragonite using a Berkovich probe tip with loading direction perpendicular to the (001), ($\bar{1}10$) and the ($\bar{1}\bar{3}0$) planes (maximum loads of 500 μ N and 1000 μ N) | 82 |
| <u>3.6.3</u> Early portion of loading curve for 500 μ N Berkovich indents shown in figure 3.6.1 | 82 |
| <u>3.6.4</u> Three-individual loading-unloading curves from the (001) plane data shown in | |

| | |
|--|-----|
| figure 3.6.1 | 84 |
| 3.6.5 Higher load nanoindentation using a Berkovich tip on (001) plane of single crystal aragonite (maximum loads 5000 μN and 10000 μN) and image of residual 5000 μN indent | 85 |
| 3.6.6 Tapping mode atomic force microscopy image of residual indents after nanoindentation on the (001) plane of single crystal aragonite (maximum load 10000 μN) and corresponding line profiles of single crystal aragonite | 86 |
| 3.6.7 Tapping Mode Atomic Force Microscopy images of residual Berkovich indents (maximum load 10000 μN) for different orientations of the crystal relative to the indenter | 87 |
| 3.6.8 Nanoindentation data for single crystal aragonite using an (ideally) 1 μm radius, 60° conical tip with loading direction perpendicular to the (001), ($\bar{1}10$) and the ($\bar{1}\bar{3}0$) planes (maximum loads of 500 μN and 1000 μN) | 90 |
| 3.6.9 Initial portion of loading curve for 500 μN 1 μm 60° cono-spherical indents shown in figure 3.6.7 | 91 |
| 3.6.10 Three-individual loading-unloading curves from the (001) plane data shown in figure 3.6.7 | 92 |
| 3.6.11 Higher load nanoindentation using a 1 μm 60° cono-spherical tip on (001) plane of single crystal aragonite (maximum loads 5000 μN and 10000 μN) | 92 |
| 3.6.12 Tapping mode atomic force microscopy image of residual cono-spherical indents after nanoindentation on the (001) plane of single crystal aragonite and corresponding line profiles (maximum load 5000 μN) | 93 |
| 3.6.13 Tapping mode atomic force microscopy image of residual cono-spherical indents after nanoindentation on the (001) plane of single crystal aragonite to a maximum load of 10000 μN | 93 |
| 3.7.1 Load vs. penetration depth curves for nano-Knoop indentation on the (001) plane of single crystal aragonite up to maximum loads of 500 μN and 1000 μN | 94 |
| 3.7.2. Microscopy images of residual Knoop indents on the <i>c</i> -plane of single crystal aragonite. | 95 |
| 3.8.1 Comparison of nanoindentation data for single crystal aragonite with dry and wet nacre [Bruet et al] | 96 |
| 3.8.2 TMAFM images of Berkovich indents on <i>c</i> -plane of aragonite and nacre (maximum load 5 mN, 10 mN) [Bruet et al] | 98 |
| 4.1.1 Berkovich tip geometry | 102 |
| 4.1.2 Berkovich tip used in elastic finite element simulations | 103 |
| 4.1.3 Ideally sharp Berkovich tip used for the elastic-plastic finite element simulations | 104 |
| 4.1.4 Sample used for elastic finite element simulations | 105 |
| 4.1.5 Meshed Sample for elastic-plastic finite element simulations | 106 |
| 4.1.6 Orientation for (001) indents | 107 |
| 4.1.7 Schematic of orientations of indents for the ($\bar{1}10$) and ($\bar{1}\bar{3}0$) planes. | 107 |
| 4.1.8 Schematic of different configurations used to describe crystal plasticity model [Anand] | 109 |

| | |
|--|-----|
| <u>4.2.1</u> Overlay of isotropic finite element simulation result with the averaged experimental load-unload curves for single crystal aragonite on the (001), $(\bar{1}10)$ and $(\bar{1}\bar{3}0)$ planes. | 112 |
| <u>4.2.2</u> Low load/depth portion of curve shown in figure 4.2.1 | 112 |
| <u>4.2.3</u> Overlay of anisotropic elastic finite element analysis simulation result for indentation on the (001) plane with experimental data for the (001) plane | 113 |
| <u>4.2.4</u> Low load/depth portion of curve shown in figure 4.2.3 | 114 |
| <u>4.2.5</u> Stress contours from <i>Abaqus</i> finite element simulations of Berkovich indentation | 115 |
| <u>4.2.6</u> Comparison of anisotropic elastic finite element analysis simulations for the (001), $(\bar{1}10)$ and $(\bar{1}\bar{3}0)$ planes with the experimental data. | 119 |
| <u>4.2.7</u> Low load/depth portion of curve shown in figure 4.2.6. | 120 |
| <u>4.2.8</u> Initially postulated slip systems based on investigations by previous authors | 121 |
| <u>4.2.9</u> Results of the <i>Abaqus</i> single crystal plasticity model using the cubic family of slip systems | 122 |
| <u>4.2.10</u> Schematic showing the ratio of the pile-up angles is closely related to the length of the unit crystal sides | 122 |
| <u>4.2.11</u> Schematic of newly posulated slip systems | 123 |
| <u>4.2.12</u> Results of cono-spherical simulations | 124 |
| <u>4.2.13</u> Pile-up mechanism of single crystal aragonite under nanoindentation with cono-spherical | 125 |
| <u>4.2.14</u> Pile-up mechanism of single crystal aragonite under nanoindentation with Berkovich indenter | 126 |
| <u>4.2.15</u> Image of the <i>a-b</i> plane of CaCO ₃ aragonite structure | 127 |

List of Tables

| | |
|--|-----|
| <u>1.4.1</u> Summary of mechanical properties for nacre, aragonite and calcite | 40 |
| <u>3.2.1</u> Experimental reports of the elastic constants of aragonite [Voigt et al; Liu et al] | 69 |
| <u>4.1.1</u> Elastic constants of aragonite used in anisotropic elastic finite element simulations | 107 |
| <u>4.1.2</u> Transformed elastic constants of aragonite to line up perpendicular to indented planes | 108 |

Chapter 1: *Introduction to biocomposite materials and seashell nacre*

Background

For many centuries, materials in nature have evolved to achieve hierarchically structured biocomposites that exhibit a variety of material behaviors and functions. One such desirable function is to provide a material with a combination of excellent stiffness, strength and toughness. This Thesis research forms part of a greater study to investigate the multiscale structure and deformation mechanisms of biocomposites and to advance this knowledge to the design and synthesis of new materials.

The key to these biocomposite materials lies in the fact that they consist of a well defined ultrastructure, spanning the nano-, micro-, meso- & macro-scales. These biocomposite materials have intrigued many researchers for their capabilities to provide stiffness, strength and toughness by integrating organic material with inorganic compounds to achieve dramatic improvements in material properties.

This Thesis will introduce aspects of the overall structure and properties of the nacre of *Trochus niloticus* and will then focus on the inorganic component of seashell nacre, namely aragonite, an orthorhombic form of CaCO_3 . A nanoindentation study was performed to investigate the nanoscale elastic-plastic mechanical response of single crystal aragonite. This experimental investigation was complimented with a modeling investigation into the single crystal behavior of aragonite.

This Chapter begins by defining mechanical properties frequently used throughout the Thesis. Several biocomposite materials and key aspects of these materials are then introduced. The final sections focus on seashell nacre, its structure and mechanical properties.

1.1 Mechanical Properties

Several important mechanical properties are referred to repeatedly in this Thesis and a brief explanation of each is given below.

Stiffness: Stiffness is defined as the resistance to elastic deformation and for isotropic materials is typically characterized by the Young's modulus, E , and the Poisson's ratio, ν ; or, alternatively, by the shear modulus, G , and the bulk modulus, K_b . For an anisotropic material, the stiffness is direction-dependent and the elastic stiffness must be defined in multiple directions. In general, whether isotropic or anisotropic, the elastic stress vs. strain is described by a fourth order tensor. Stiffness is generally governed by the interatomic forces of the material.

Strength: When a material reaches the limit of the elastic regime, it either flows plastically or sudden failure can occur before plastic flow. For a material that deforms plastically, the end of the elastic regime is characterized by the yield strength, σ_y , of the material. Materials that flow plastically for appreciable levels of strain beyond this elastic limit are considered "ductile" materials (in tension); a representative curve for a ductile metal material is shown in figure 1.1.1 (a). In a ductile metal, local plastic instabilities typically occur as the plastic strain is increased and the deformation becomes localized

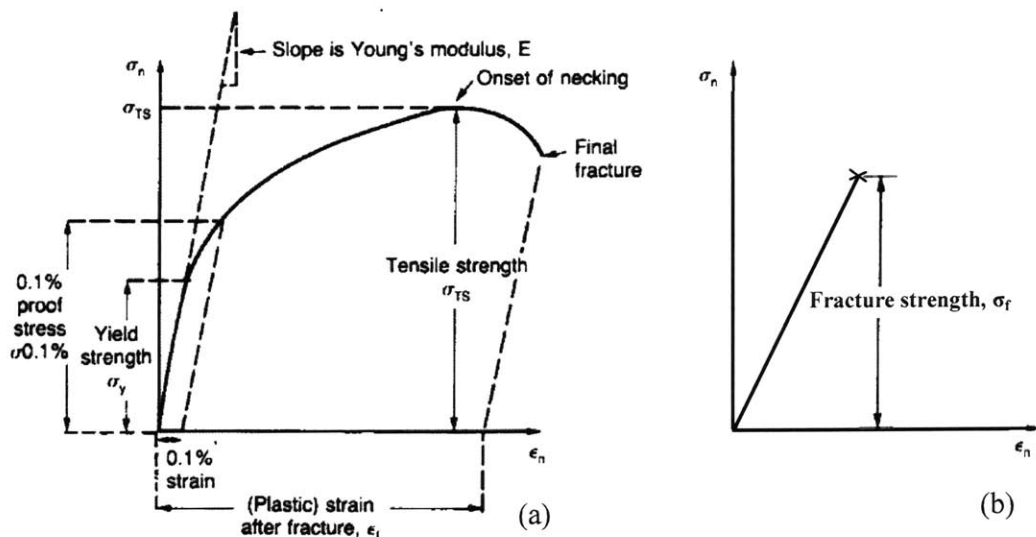


Figure 1.1.1 Examples of stress-strain curves under uniaxial tensile loading for (a) ductile materials and (b) brittle materials [Ashby et al, 1996]

in the form of a neck in the uniaxial tensile specimen, eventually leading to failure. The stress at which the deformation becomes localized is defined as the ultimate tensile strength. Some materials, ceramics for example, may fail in uniaxial tension by crack propagation (related to toughness, see below) before the yield strength is reached. For these materials, the yield stress (stress for the onset of plastic flow) is measured by compression tests. Materials that exhibit this behavior are considered “brittle” and a typical tensile stress vs. strain curve is shown in figure 1.1.1 (b). The stress at which failure occurs in uniaxial tension for brittle materials is known as the fracture strength. The yield strength of a material is dependent on the material bond strength, microstructure, dislocation density and its resistance to dislocation motion; the fracture strength is dependent on its bond strength and its microflaws/microcracks.

Fracture toughness: Fracture toughness is the ability of a material to resist crack propagation, or the energy required to propagate cracks in a material. Ductile materials require more energy for crack propagation due to plastic dissipation at the crack tip. Within a particular class of materials (for example, the steel family), there will be an inverse relationship between the yield strength and toughness. For example, heat treating a steel to increase the yield strength will decrease toughness.

Hardness: Hardness quantifies the resistance to permanent deformation via indentation. It is defined as the load divided by the projected area of the permanent indent. For homogeneous materials it is related to the yield strength of the material through $H = 3\sigma_y$ (with a correlation factor for work hardening). The wear resistance of a surface is strongly dependent on the hardness of the material.

1.2 Biocomposite Materials

Examples of Biocomposite materials are abundant in nature. Organisms create composites with unique material properties (e.g. stiffness and strength to weight ratios, toughness, magnetic, electrical) utilizing a combination of soft and hard materials with specific ultrastructures [see, for example, Wainwright, 1976; Lowenstam et al, 1989;

Sarikaya, 1994]. A variety of biocomposites are discussed below under the classifications used by Sarikaya [Sarikaya, 1994]: Biogenic small inorganic particles, Ceramic/Ceramic Biological composites, Organic/Organic Biological composites and Ceramic/Organic composites. It should be noted that this list is by no means comprehensive and examples here are used to give a general introduction to the field and to highlight some key features.

Biogenic small inorganic particles

Biogenic inorganic particles are analogous with synthetic nanoparticles used in technological systems today to improve material performance [Sarikaya, 1994; Kotov, 2006]. A variety of organisms produce ultrafine inorganic particles to enhance a material property: stiffness, strength, toughness, magnetic or optical, or to perform a particular function [see, for example, Mann et al, 1989; Frankel et al, 1991; Sarikaya, 1994].

An illustration of one such function is iron clusters (see figure 1.2.1(a)) that form at the center of ferritin molecular cages (or vesicles) in organisms (see figure 1.2.1(b)). The small inorganic iron

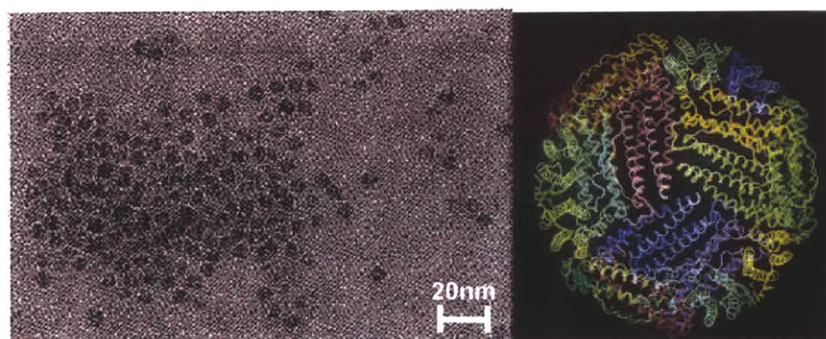


Figure 1.2.1 Storage of iron clusters in organisms (a) Transmission electron microscopy image of discrete nanoparticles of ferritin clusters [Mann, 2001] (b) computer graphics drawing of a ferritin molecular cage (main chain ribbons), which is used to store the iron particles [Mann et al, 1989]

particles are stored and released by the molecule when required by the organism, for example, in the production of new red blood cells in humans [Mann et al., 1989].

A second, very functional application is magnetosomes in magnetotactic bacteria found in freshwater and seawater [Lowenstam et al, 1989; Mann et al, 1989]. Magnetotactic bacteria use the magnetic properties of biogenic nanoparticles (magnetosomes, which are single crystal particles of iron oxide, magnetite, Fe_3O_4 , see figure 1.2.2) to establish orientation and direct the bacteria along geomagnetic field lines [Lowenstam et al, 1989;

Mann et al, 1989]. The vertical components of these geomagnetic lines direct the bacteria vertically downwards, away from the toxic effects of the oxygen rich surface water and towards the sediments [Lowenstam et al, 1989; Mann et al, 1989].

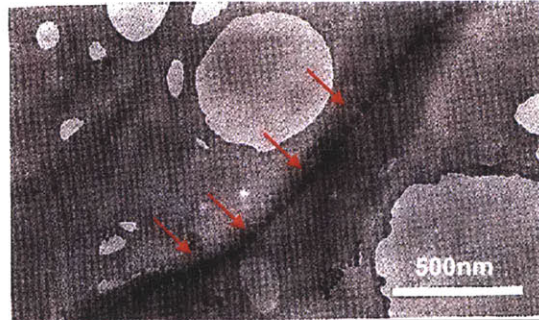


Figure 1.2.2 Electron micrograph of magnetotactic bacteria, which has a chain of magnetosomes (particles of Fe_3O_4), the electron opaque particles highlighted by arrows, which the bacteria uses to orient itself [Mann et al, 1989]

Ceramic/Ceramic Biological Composites

Typically, ceramic phases are coupled with organic molecules although there are some instances where this is not the case [Sarikaya, 1994]. The body and spine of a sea-urchin for instance is a single porous calcitic crystal 600-800 μ m in diameter and several centimeters long, with the crystallographic *c*-axis aligned longitudinally with the spine (see figure 1.2.3) [Lowenstam et al, 1989; Sarikaya, 1994, Sarikaya et al 1995; Politi, 2005].

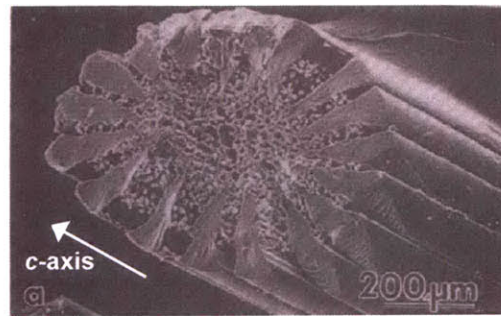


Figure 1.2.3 Electron micrograph of the spine of a sea urchin, showing the calcite structure [Sarikaya et al, 1995]

The teeth of sea urchins also possess a very interesting microarchitecture, which has been described as a fiber reinforced ceramic matrix composite, even though there is a small amount of organic macromolecules present (0.2-0.25 wt %) [Lowenstam et al, 1989; Sarikaya, 1994; Wang et al, 1997]. Sea urchin teeth are composed of three main regions: the primary plate zone, the stone part and the keel (see figure 1.2.4(a)) [Wang et al, 1997]. The stone and keel part of the tooth consists of amorphous $CaCO_3$, which is referred to as the ‘matrix’, with crystalline calcitic fibers, known as ‘needles’, embedded in this matrix (see figure 1.2.4(b)) [Wang et al, 1997]. The matrix consists of ‘discs’, which are of the order of microns. These discs are composed of $CaCO_3$ crystals with dimensions of 50-80nm [Wang et al, 1997]. The embedded fibers vary in diameter from 1 μ m at the stone part of the tooth to 20 μ m in the keel and the magnesium concentration,

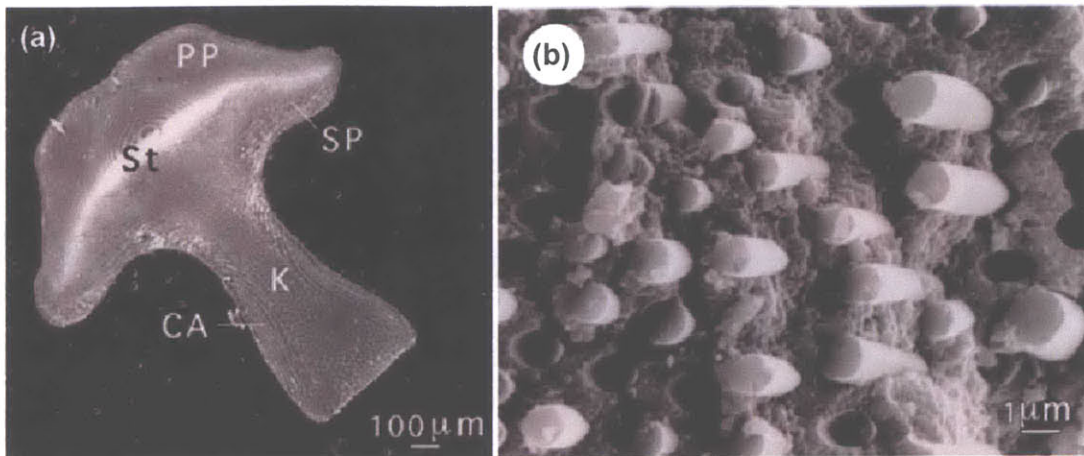


Figure 1.2.4 Scanning electron microscopy images of sea-urchin tooth (a) Cross-sectional cut of the tooth showing its three main regions: the primary plate zone (labeled 'PP'), the stone part (labeled 'St') and the keel (labeled "K") (b) image of stone part of the tooth comprised of calcite fibres embedded in an amorphous CaCO_3 matrix [Wang et al, 1997].

and hence hardness, increases from the keel to the stone part of the tooth [Wang et al, 1997]. The variation in diameter of the fibers results in a variation in microstructure through the tooth cross-section and the volume fraction of fibres:discs changes continuously from 50:50 in the stone part of the tooth to 90:10 in the keel part of the tooth [Wang et al, 1997]. As a result of the changes in microarchitecture and composition, the stone part of the tooth is the hardest of the three defined areas (as measured by Vicker's hardness). Consequently its wear rate is less than the surrounding keel and primary plate zone [Wang et al, 1997].

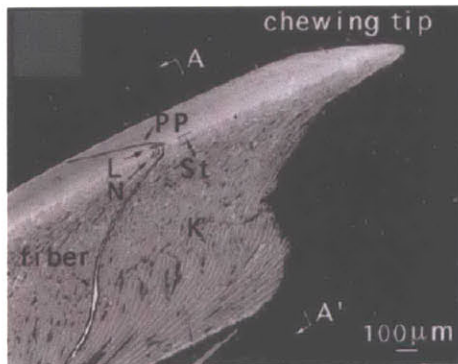


Figure 1.2.5 Longitudinal section of sea urchin tooth, showing the narrow Stone zone (labeled 'St') protruding the most at the tooth tip as it has a higher hardness than the surrounding Primary Plate zone (labeled 'PP') and keel (labeled 'K') [Wang et al, 1997]

This results in the narrow stone part protruding the most at the tooth tip (see figure 1.2.5) and the tooth is said to 'self-sharpen' [Wang et al, 1997].

Organic/Organic Biological Composites

Stiff biological tissues, analogous to particle or fibre reinforced polymeric composites, are formed using composites of fibrous organic components implanted in a softer organic

matrix. A classical example is tendon in humans, which connects muscle tissue to bone tissue (see figure 1.2.6 (a)) [Sarikaya, 1994; Wainwright et al, 1994]. Another example is silk, which is found in the cocoons of silk moths and webs of spiders. Silk is a unique structure consisting of silk fibroin proteins in an amorphous protein matrix and has a specific strength (strength/density) of ~ 770 kNm/kg exceeding high specific tensile strength metallic fibers (for example, alloy steel ~ 100 kNm/kg) or high specific strength polymeric fibers ~ 50 - 100 kNm/kg (see figure 1.2.6 (b)) [Wainwright et al, 1976; Sarikaya, 1994; Sarikaya et al, 1995; Ashby, 2005].

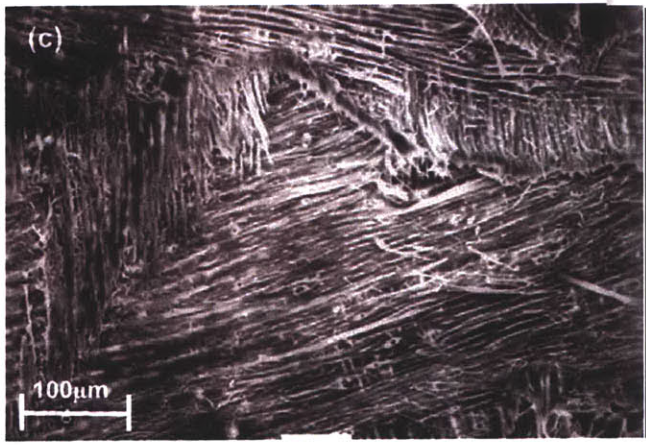
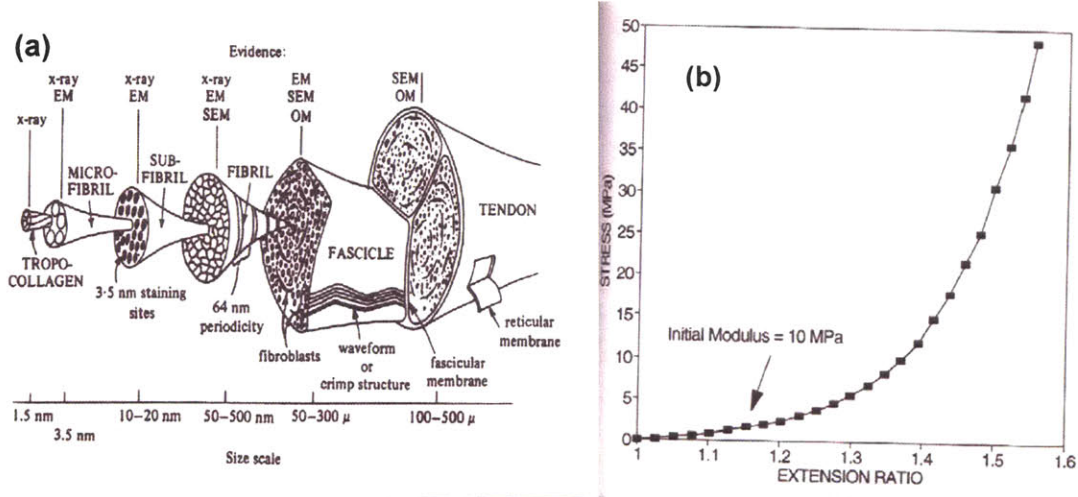


Figure 1.2.6
 Organic/organic biocomposites (a) hierarchical structure of tendon at different lengthscales [Sarikaya et al, 1995] (b) Stress v's extension ratio data for hydrated contracted dragline silk [Sarikaya et al, 1995]. (c) Cross section of the cuticle of the *Hydrophilidae* beetle, showing the laminated collagen layers [Chen et al, 2002]

A major class of organic/organic biocomposites are cuticles, which are the exoskeletons of insects that covers their entire body and provide protection via a light and versatile armor [Wainwright et al, 1979; Sarikaya et al, 1994; Sarikaya et al, 1995]. The structure is similar to a fiber reinforced polymer matrix, where the fibers are collagen and the matrix primarily consists of proteins (see figure 1.2.6(c)) [Wainwright et al, 1979;

Sarikaya et al, 1994; Sarikaya et al, 1995]. The composite is a sheet like structure, with layers (thickness on the order of 10nm) of parallel collagen fibers and with each consecutive layer oriented differently to the last [Wainwright et al, 1979; Sarikaya et al, 1994; Sarikaya et al, 1995].

Ceramic/Organic Composites

Biological composites containing both ceramic and organic phases take on numerous forms and are typically found as structural materials or protective covers [see for example, Waingwright et al, 1976; Lowenstam et al, 1989; Mann et al, 1989; Sarikaya et al, 1994; Sarikaya et al, 1995]. The bones of numerous mammals, including humans, consist of multiscale architected ceramic/organic composites, which provide stiffness, strength and toughness while remaining light [Wainwright et al, 1976; Lowenstam et al, 1989; Sarikaya et al, 1995]. For example, cortical bone in humans consists of collagen fibrils with mineralized calcium phosphate and calcium carbonate and a detailed multiscale architecture (see figure 1.2.7) [see, for example, Lowenstam et al, 1989; Lakes, 1993, Bilezikian et al, 2002].

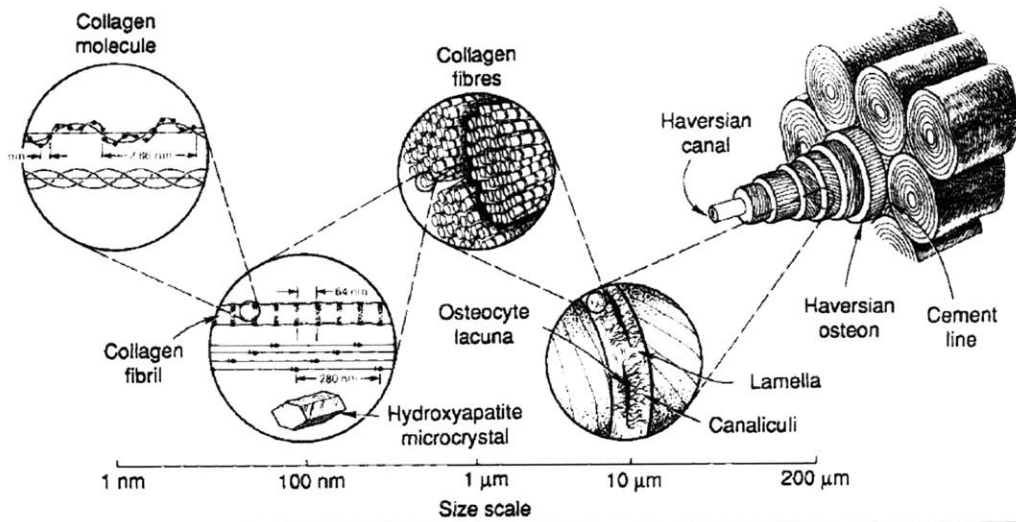


Figure 1.2.7 Schematic of multiscale architectural features of cancellous bone, which consists of organic collagen fibrils and inorganic calcium phosphate and carbonate crystals [Lakes, 1993]

The structural support for stony coralline sponges also consists of a ceramic/organic composite of calcium carbonate and proteins, which combines stiffness and strength [Hartman et al, 1970; Wainwright et al, 1976; Lowenstam et al, 1989].

The basic ultrastructural units of the majority of scleratinian stony corals are spherulitic arrays or bunches of needlelike crystals of aragonite, with the crystallographic *c*-axis aligned with the longitudinal axis of the crystals (see figure 1.2.8) [Lowenstam et al, 1989]. These spherulitic arrays grow from ‘centers of calcification’ (see figure 1.2.8 (b)) and in the *Mussa angulosa* species (where the centers of calcification are large enough for study) these centers of calcification were found to be composed of calcite crystals that are frequently twinned [Lowenstam et al, 1989].

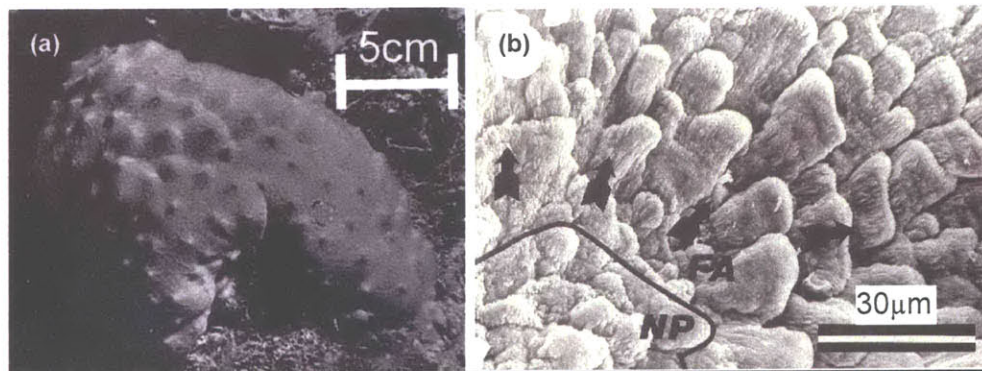


Figure 1.2.8 Scleratinian stony corals (a) Underwater photograph of *Ceratoporella nicholsoni* [Hartman et al, 1970] and (b) SEM micrograph of *Acropora palmate* showing the fiber bundles. The center of calcification is the region labeled ‘NP’ and the arrows point in the direction of needle growth, which is parallel to the crystallographic *c*-axis [Lowenstam et al, 1989]

Strength, hardness and toughness are also provided by ceramic/organic composites in the teeth of most fish and mammals [see, for example, Lowenstam et al, 1989; Mann et al, 1989; Sarikaya et al, 1994]. For example, the outer portion of most mammalian teeth, enamel (see figure 1.2.9), is a highly mineralized tissue and is the hardest tissue found in the human body [Habelitz et al, 2002; Beniash et al, 2005]. It consists of keyhole shaped interwoven enamel rods, 4-5µm in diameter, which are parallel arrays of protein covered carbonated hydroxyapatite fibers elongated in the crystallographic *c*-axis direction [Lowenstam et al, 1989; Habelitz et al, 2002; Beniash et al, 2005].

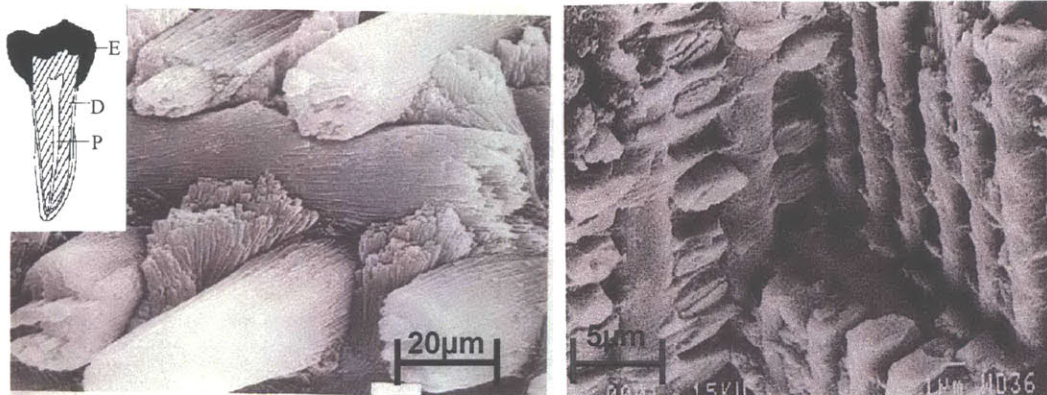


Figure 1.2.9 SEM micrographs of rat tooth enamel. (a) Hydroxyapatite fibers and enamel rods *inset*: schematic showing location of enamel (labeled 'E') in teeth. [Mann, 2001]. (b) Interwoven enamel rods [Lowenstam et al, 1989]

Finally, the subject of this Thesis, the nacre component of mollusk shells (see figure 1.2.10), also falls into this category. It is a hierarchical inorganic/organic material that provides a lightweight, stiff, strong and tough armor [Sarikaya et al, 1995, Lowenstam et al, 1989, Wainwright et al, 1976] and is described in detail in section 1.4.

In many of the inorganic/inorganic and inorganic/organic biocomposite materials, the inorganic phase takes on a specific crystal orientation [see for example Lowenstam et al, 1989; Weiner et al, 2005]. This is true of seashell nacre, in which the crystallographic *c*-axis is oriented perpendicular to the plane of the nacre layers (see figure 1.2.10) [see, for example, Lowenstam et al, 1989]. In teeth, the enamel is composed of intersecting rods and these rods grow in the crystallographic *c*-axis

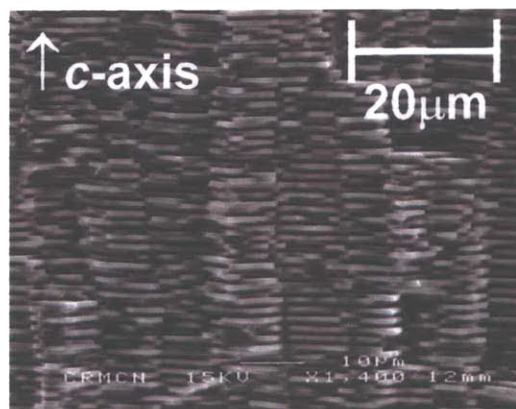


Figure 1.2.10 SEM micrograph of the columnar nacre of *Trochus niloticus*, with the crystallographic *c*-axis aligned in the longitudinal direction of the columns as shown [courtesy of B. Bruet]

direction (see figure 1.2.9) [Lowenstam et al, 1989; Beniash et al, 2005]. The body and spine of sea-urchins is a single calcitic crystal with the crystallographic *c*-axis parallel with the longitudinal axis of the spine see figure 1.2.3) and the spherulitic arrays in

coralline sponges consist of aragonite needles, with the crystallographic *c*-axis aligned with the axis of the needles (1.2.10) [Lowenstam et al, 1989; Politi, 2005]. Although it is recognized that the inorganic crystals take on specific orientations in biocomposite materials, the relationship between crystal orientation and property/function is still under investigation [see for example Lowenstam et al, 1989; Weiner et al, 2005].

1.3 Microstructural features in mollusc shells and the shell of *Trochus niloticus*

Mollusc shells consist of several layers through their thickness. The thickness and microstructure of these layers is dependent on the specific species [see, for example, Lowenstam et al, 1989]. The order of these layers is typically: the outermost periostracum, an outer prismatic layer, an inner nacre layer and an innermost irregular crossed lamellar layer (see schematic, figure 1.3.1). For example, *Haliotis rufescens* (Red Abalone) can grow up to a thickness of ~15mm, consisting of (from outermost part of the shell to innermost): periostracum (100-200nm), prismatic calcite layer (0.5-3mm) and an inner nacreous layer that thickens throughout the shells life (0-12mm) [Zaremba et al, 1996]. The shell of *Mytilus edulis* has a total thickness of ~ 800µm consisting of (from outermost part of shell to innermost): a periostracum (~35µm), an oblique prismatic layer (~640µm), a normal prismatic layer (~4µm) and a nacreous layer (~120µm) [Feng et al, 2000]. Typically, nacre is the central layer and the structure of the inner and outer layers varies [see, for example, Lowenstam et al, 1989].

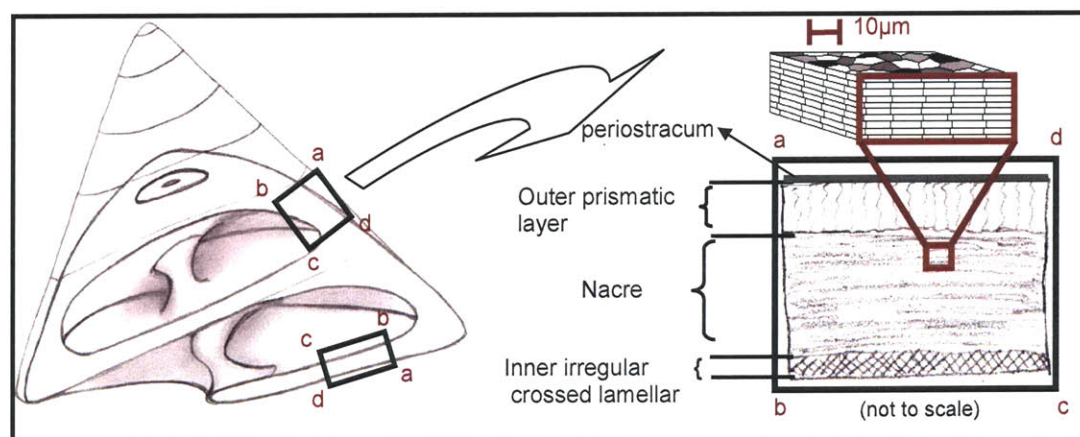


Figure 1.3.1 Schematic showing the layers found in the seashell of *Trochus niloticus* (not to scale).

Section 1.3.1 introduces the main layer structures commonly found in mollusc shells and section 1.3.2 describes mollusc specimens used for this study, from the species *Trochus niloticus*, and the layers found. The middle layer of seashell, nacre, has received considerably more attention than the other layers and is described separately in section 1.4.

1.3.1 Layer types found in mollusc shells and their microstructures

Periostracum: The outermost layer is called the periostracum, which is a very thin organic layer of sclerotized protein that protects the shell from the erosive action of its environment (see figure 1.3.2) [Hunt et al, 1978; Checa, 2000]. It is also understood that the periostracum plays a role in the biomineralization process of the calcified layers of the shell [Hunt et al, 1978; Checa, 2000]. The thickness of the periostracum has been reported as 2-3 μ m for the *Unio elongatulus* and *Potomida littoralis* species (see figure 1.3.2) and 25 μ m for the *Amblema* species [Checa, 2000].

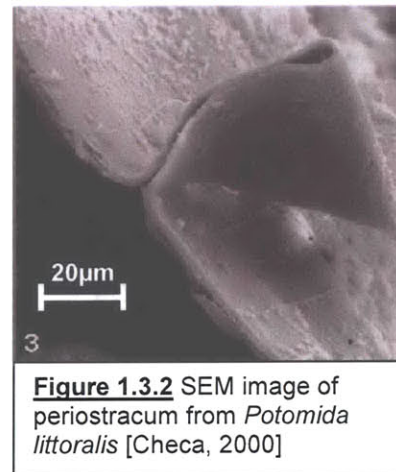


Figure 1.3.2 SEM image of periostracum from *Potomida littoralis* [Checa, 2000]

Outer Prismatic Layer: The outer prismatic layer is the first line of defense against penetrating attacks by predators. Relative to the inner nacreous layer of seashells, little information exists for this calcite-rich layer. It consists of layers of mutually parallel, adjacent structural units of crystallographic calcite and an interconnected organic network that traverses between and within the prisms (see figure 1.3.3) [Chateigner et al, 2000; Tong et al, 2002]. In some shells this layer constitutes the majority of the shell, e.g. *Mytilus edulis*, where it is ~ 650 μ m thick and makes up 80% of the total shell thickness [Feng et al, 2000].

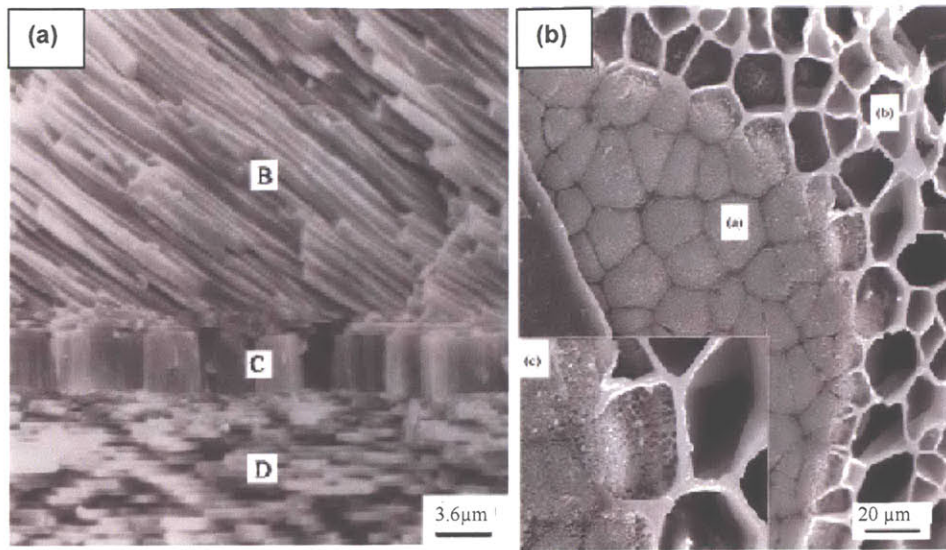


Figure 1.3.3 Scanning Electron Micrograph images of prismatic layer (a) in the species *Mytilus edulis*. There are two prismatic layers: an 'oblique layer' labeled 'B' and a 'normal layer' labeled 'C'. The nacre layer is labeled 'D' [Feng et al,2000] (b) Prismatic layer of partially decalcified *Cristaris plicata* mollusc shell, showing organic network between calcite prisms [Tong et al, 2002]

Crossed lamellar layer: The innermost layer consists of irregular crossed lamellar calcite. As with the outer prismatic layer, it has not been studied as intensely as the nacreous layer. The crossed-lamellar layer consists of lamellae of thin mutually parallel laths or rods with neighboring lamellae rotated relative to each other (see figure 1.3.4) [Chateigner et al, 2000]. Although this layer typically only constitutes a small percentage of the shells thickness, some shells, for example *Strombus decorus persicus*, have several crossed lamellar layers through 99% of the shells thickness and no nacreous layer (see figure 1.3.4) [Pokroy et al, 2003].

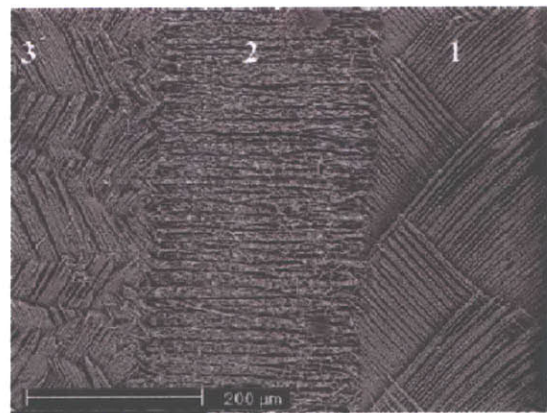


Figure 1.3.4 Cross-lamellar layers in the shell from the species *Strombus decorus persicus*, which has cross-lamellar layers through 99% of its thickness [Pokroy et al, 2003]

1.3.2 *Trochus Niloticus* shells and the layers found through the thickness

The gastropod mollusk shells used in this study come from *Trochus Niloticus*. This gastropod is commonly found near the coasts of the Indian Ocean.

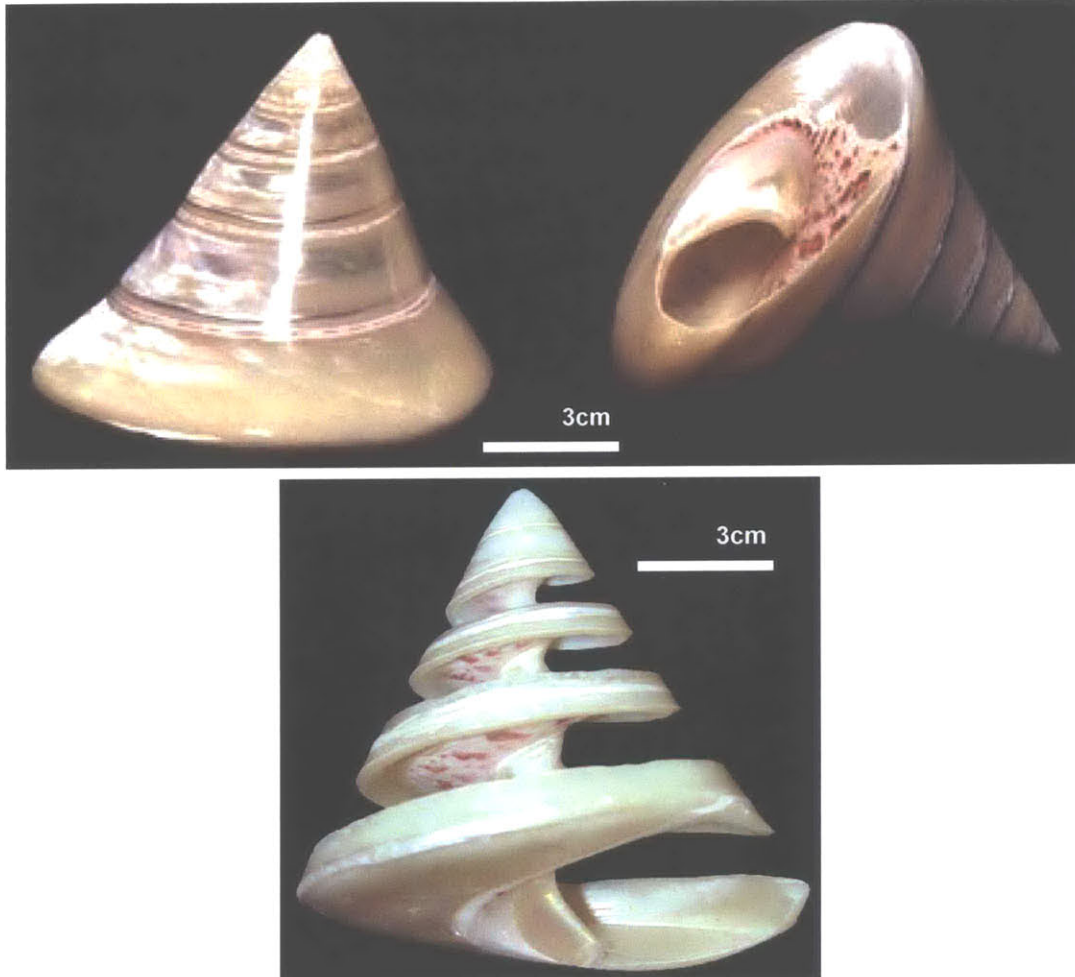
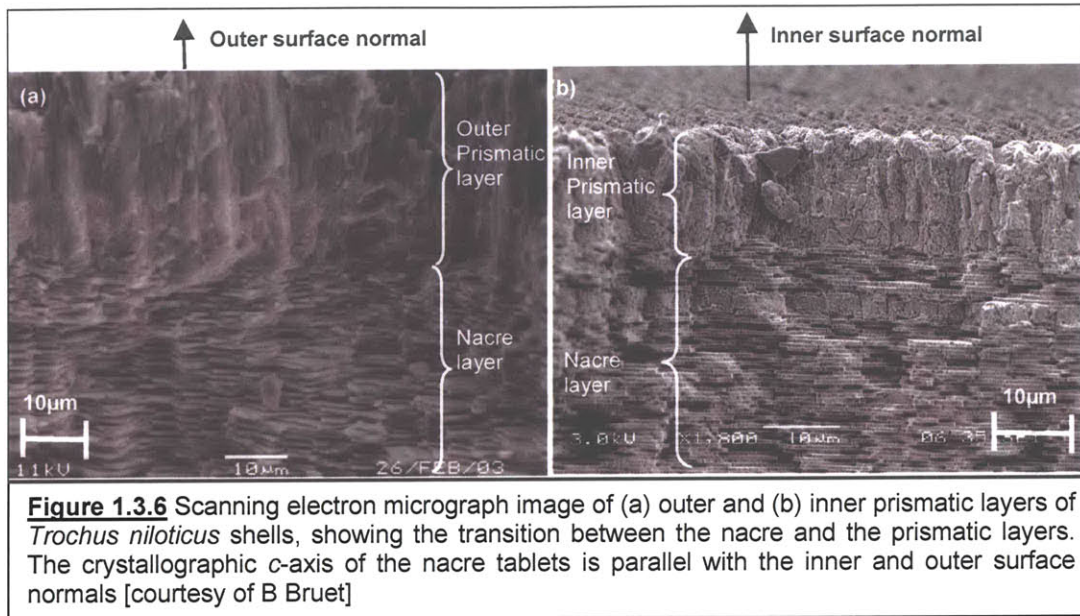


Figure 1.3.5 Selection of images of *Trochus niloticus* seashell, including a spirally cut shell which shows the seashells inner structure.

The images in figure 1.3.5 show the overall shape of *Trochus niloticus* seashells. Their base diameter is approximately 10cm and they are approximately 10-12cm tall. Shell thickness varies between 3-6mm. The dimensions given here and henceforth for the *Trochus niloticus* are based on measurements taken in the as-received state. The shells had been polished prior to our receipt of them and thus the shell thickness is inaccurate. SEM micrographs taken through the shells thickness showed the outermost layer had

been removed by polishing, leaving the nacre layer exposed in the as-received state. There was evidence of an outer layer on one shell, which appeared to be a prismatic layer (see figure 1.3.6(a)). The innermost layer also looks prismatic in form (see figure 1.3.6(b)) and is very thin ($\sim 10\mu\text{m}$).



1.4 Seashell nacre

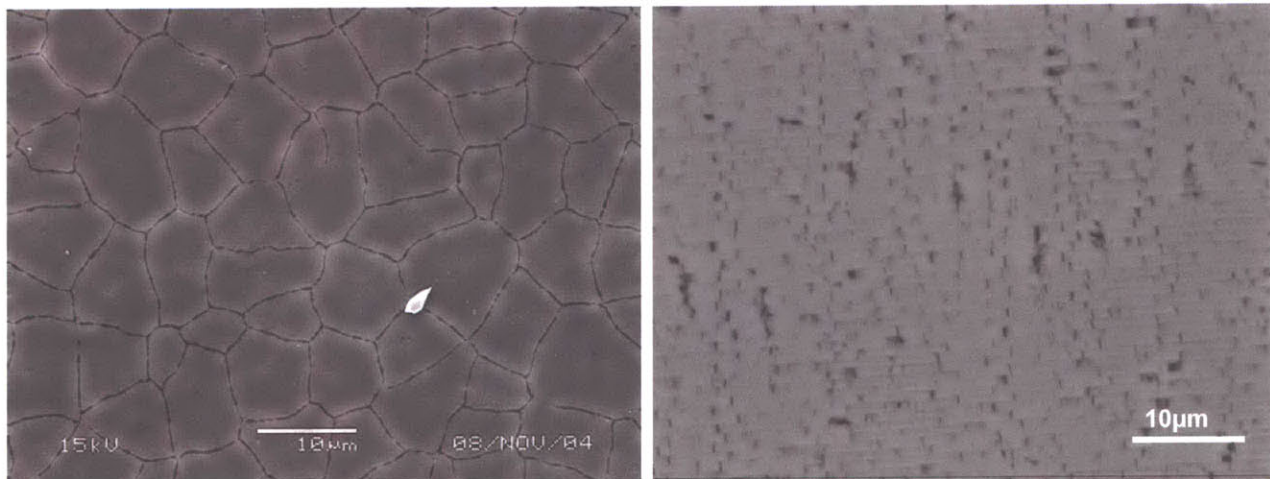


Figure 1.4.1 SEM images of seashell nacre from the species *Trochus niloticus* (a) Top-view image of nacre tablets, showing the polygonal shape (b) side view of nacre, showing the 'brick and mortar' structure

Nacre is an example of an organic/inorganic biocomposite that has exceptional material properties in terms of stiffness to weight ratio, strength to weight ratio, toughness and

impact resistance (see section 1.4.3) [see, for example, Wainwright et al, 1976; Jackson et al, 1988; Lowenstam et al, 1989; Sarikaya et al, 1995; Wang et al, 2001; Bruet et al, 2005]. Although the primary constituent material, aragonite, exhibits low toughness and strength, the highly organized structural features at both the nano and micro scale and a small fraction of organic matrix combine to give the material its exceptional properties (see section 1.4.1) [see, for example, Wainwright et al, 1976; Taylor et al, 1988; Lowenstam et al, 1989; Sarikaya et al, 1995; Wang et al, 2001; Bruet et al, 2005]. It is composed of more than 95% inorganic phase, which is aragonite (the orthorhombic form of CaCO_3) and ~5% inorganic phase, consisting of biomacromolecules and proteins [Jackson et al, 1988; Wang et al, 2001].

1.4.1 Ultrastructure of Seashell Nacre

Nacre is a hierarchical biological nanocomposite with a “brick and mortar” type structure on the microscale, consisting of alternating layers of mineral tablets and a thin layer (~40nm) of biomacromolecular “glue” [Mutvei et al, 1978; Jackson et al, 1988; Sarikaya et al, 1995; Bruet et al, 2005] (see figure 1.4.2(a)). The mineral tablets, typically polygonal in shape, are aragonitic CaCO_3 tablets, 5~20 μm in planar dimension and ~0.3-1.5 μm thick, where the crystallographic c-axis is the through-thickness direction [Taylor

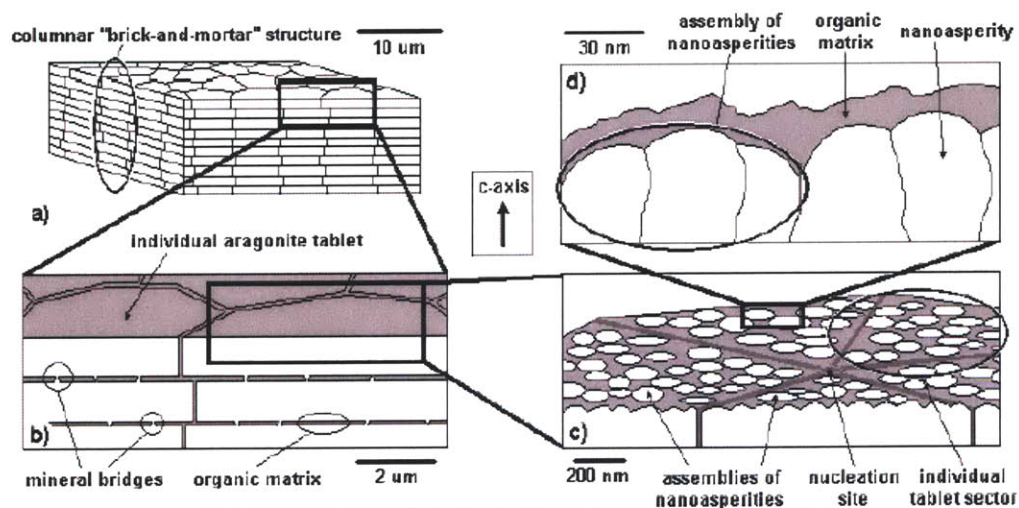


Figure 1.4.2 Illustration of the hierarchical ultrastructure of nacre: (a) at the micron length scale, the so-called “brick and mortar” structure of columnar nacre is evident, with the tablets stacked vertically in the direction of the c-axis., (b) 2 μm length scale, illustrating some individual tablet features, (c) individual tablet features at 200nm lengthscale, (d) 30nm lengthscale, showing the assembly of nanoasperities constructed from single crystal aragonite. [Bruet et al, 2005].

et al, 1969; Erban, 1972; Bruet et al, 2005]. It is further suggested that there exists a hierarchical structure within the tablets [Mutvei, 1978]. Scanning electron microscopy performed on demineralized gastropod nacre suggests that each tablet is subdivided into sectors separated by vertical organic membranes [Mutvei, 1978; Bruet et al, 2005] (see figure 1.4.2(c)). Nanoasperities have been identified by atomic force microscopy on the surface of the tablets of California red abalone ($\sim 30\text{-}100\text{nm}$ diameter and $\sim 10\text{nm}$ in height) [Li et al, 2001; Wang et al, 2001] and *Trochus niloticus* nacre ($\sim 109.9 \pm 37.4$ nm maximum lateral dimension and $\sim 7.4 \pm 3.4$ nm in height) [Bruet et al, 2005], as well as mineral "bridges" between sheets and through the organic intertablet layers ($\sim 25\text{-}34$ nm in size, $\sim 91\text{-}116$ mm² surface density) identified by scanning electron microscopy [Bevelander et al, 1969] (see figure 1.4.2(b)). Mutvei [Mutvei et al, 1978] also describes vertical crystalline elements within each sector of nacre tablets (see figure 1.4.2(d)), completing the multiscale architecture.

1.4.2 Columnar Nacre, Sheet Nacre and the Nacreous layer in *Trochus Niloticus*

Seashell nacre occurs in two forms; columnar nacre exhibits nearly columnar stacks of aragonite tablets where tablet-nucleation points from layer to layer are vertically aligned, whereas sheet nacre has no correlation between layers for the nucleation points (see figure 1.4.3).

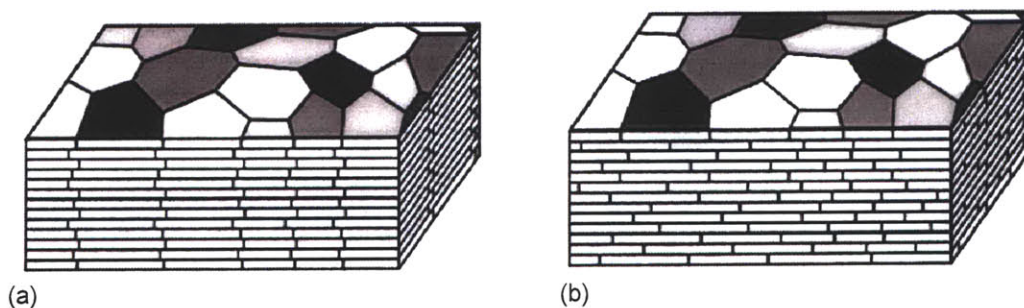


Figure 1.4.3 Schematic illustration of (a) columnar nacre and (b) sheet nacre [Wang et al, 2001].

In *Trochus niloticus*, the inner layer is 3-5mm thick and consists of columnar nacre, with the aragonite tablets arranged in a near columnar structure, in the direction of the crystallographic *c*-axis (see figure 1.4.4 and earlier images 1.2.10, 1.4.2). For *Trochus niloticus* nacre, the tablets are 8.0 μm wide, 0.9 μm thick with an organic layer of 40 nm [Bruet et al, 2005].

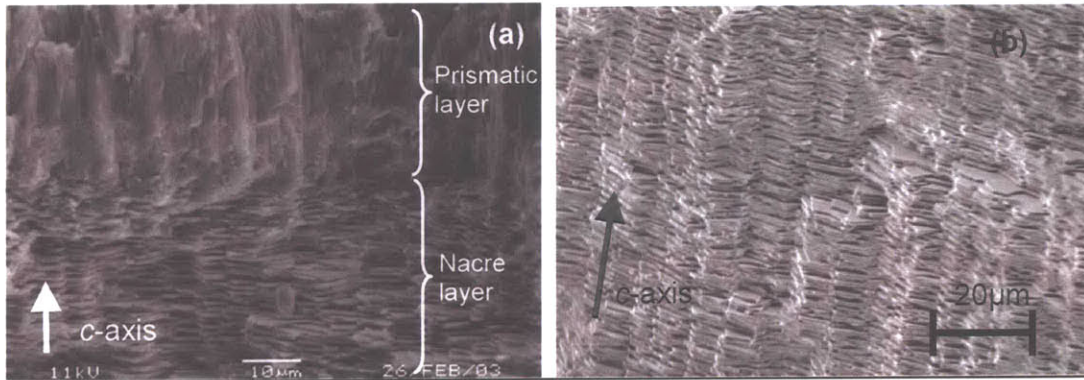


Figure 1.4.4 *Trochus niloticus* nacre (a) Cleaved specimen imaged in a Scanning Electron Microscope (SEM) showing the outer prismatic layer and the inner nacre layer. The crystallographic *c*-axis of the nacre tablets is oriented as shown and is parallel to the outer surface normal (b) Cleaved specimen imaged in SEM showing the columnar stacking in the crystallographic *c*-direction.

1.4.3 Mechanical Properties of Seashell Nacre

A variety of investigations have been conducted on nacre to measure its outstanding mechanical properties. The mechanical measurements reported by various authors will be reported first, followed by a tabulated summary of these results along with the reported values for aragonite and calcite.

Micro and macroscopic tests have been performed on nacre from various species in tension [Currey, 1977; Jackson et al, 1988], three-point bend [Currey, 1977; Jackson et al, 1988; Wang et al, 2001], four-point bend [Wang et al, 2001], and indentation [Wang et al, 1995; Li et al, 2004; Bruet et al, 2005]. In defining properties, the orientations defined by Currey [Currey, 1977] for the direction of cross-head travel shall be used (see figure 1.4.5 below). The crystallographic *c*-axis of the aragonite tablets is aligned with

the y-axis in figure 1.4.5 below. The density of nacre is $2.7\text{-}3\text{ g/cm}^3$ [Ashby et al, 1995], which can be used to evaluate strength to weight ratio and stiffness to weight ratio.

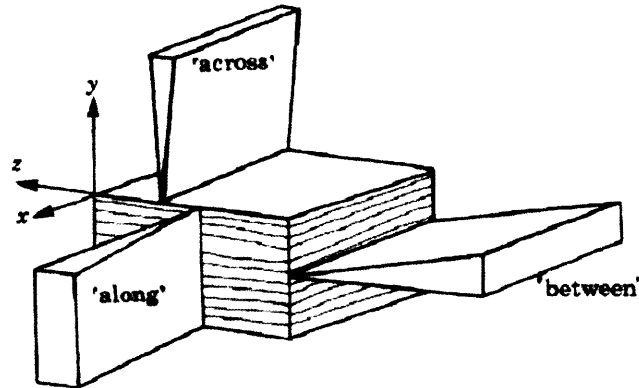


Figure 1.4.5 Definition of orientations used to define mechanical properties below as described by Currey. [Currey, 1997].

Stiffness; The elastic moduli of *Pinctada* nacre, measured from three-point bend tests have found to be 73 ± 9 GPa for dry specimens in the ‘across’ direction, 64 ± 8 GPa for wet specimens in the ‘across’ direction, 70 ± 11 GPa for dry specimens in the ‘along’ direction and 60 ± 10 GPa for wet specimens in the ‘along’ direction [Jackson et al, 1988]. Wang obtained Young’s moduli of 77 ± 12 GPa for wet specimens in the ‘across’ direction and 81 ± 4 GPa for wet specimens in the ‘along’ direction for *Pinctada maxima* and 69 ± 7 GPa for wet specimens in the ‘across’ direction and 66 ± 2 for wet specimens in the ‘along’ direction for *Haliotis rufescens* (Abalone) [Wang et al, 2001]. Shear tests performed on *Haliotis rufescens*, which sheared the layers over each other (G_{yx} and G_{yz} in the above diagram) gave a shear modulus value of 300MPa [Menig et al, 2000]. If we take an average Young’s modulus of 70 GPa for nacre and use a density of 2.85 g/cm^3 [Ashby et al, 1995], the nacre’s stiffness to density ratio is $24.6\text{ MNm}/(\text{kg})$.

The stiffness of individual tablets was measured using the technique of nanoindentation. The top face of the tablets (in the y direction of figure 1.4.5) of *Trochus niloticus* nacre were indented using a Berkovich tip yielding a Young’s Modulus of 92 ± 13 GPa for dry nacre and 79 ± 15 GPa for wet nacre from curve fits using Finite Element Analysis and assuming isotropic elasticity [Bruet et al, 2005].

Strength; In the tension tests reported by Currey [Currey, 1977] and Jackson [Jackson et al, 1988] the specimens failed at the maximum applied stress, which is the reported tensile strength. Tensile tests performed on *Pinctada* nacre in the x- (or, equivalently, z-) direction of figure 1.4.5 gave tensile strengths (maximum stress recorded, equivalent to the stress at failure for these tensile tests) of 167 ± 22 MPa for dry nacre [Jackson et al, 1988], 130 ± 24 for wet nacre [Jackson et al, 1988] and 35-116 MPa for nacre from a variety of species measured in tension in the x- (or, equivalently, z-) direction by Currey [Currey, 1977]. In the tension tests performed by Currey [Currey, 1977], 23 individual tests were performed on nacre from *Pinctada margaritifera*. A variety of load deformation curves were observed: 8 specimens showed a clear yield point and the load remained relatively constant as the specimen deformed plastically until failure (see figure 1.4.6), 4 specimens showed initial linear elastic portion followed by two plastic regions (each having a different slope), 3 specimens were entirely brittle, 2 had an initial linear region with a tiny plastic region at the end and 6 showed a curved load-deformation trace, with no clear yield point. The elastic strain limit is reported as 0.002 but no value for yield stress is reported [Currey, 1977]. The mean strain at failure is reported as 0.005, with the maximum recorded value being 0.018 [Currey, 1977]. No load-displacement curves are graphed in the Jackson paper [Jackson et al, 1988] for the tension tests. For both the Currey [Currey, 1977] and Jackson [Jackson et al, 1988] papers, the plastic deformation is reported to occur by localized tablet separation in regions of the specimen and was observed as ‘white tension lines’ in the optical microscope. This was later confirmed by Wang [Wang et al, 2001] in three-point bending tests, who observed this tablet separation using scanning electron microscopy and described them as ‘dilatation bands’ (see figure 1.4.7).

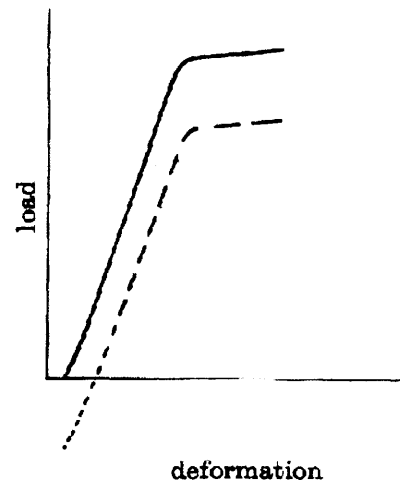


Figure 1.4.6 Sketch of curve observed during tensile testing of the nacre from the *Pinctada marteferita* species. This is the only sample curve presented by Currey and has no values along the axes [Currey, 1977].

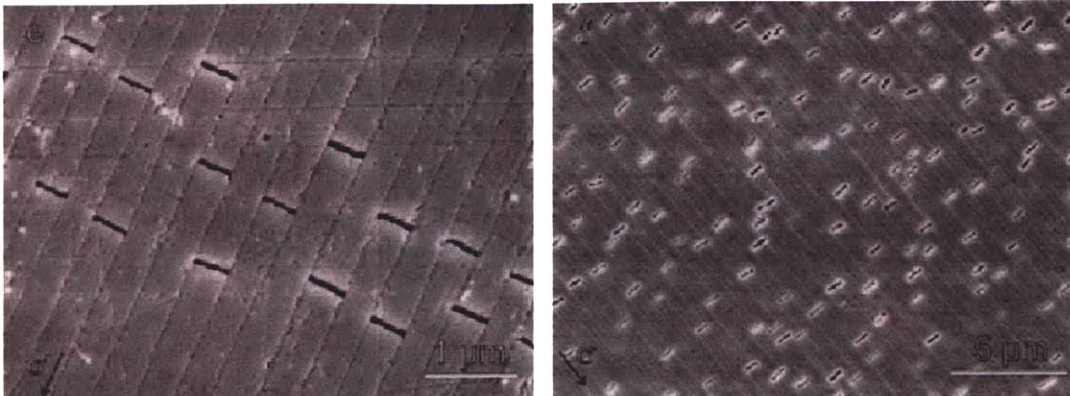


Figure 1.4.7 SEM images of dilation bands in nacre from *Haliotis rufescens* (red abalone), which show tablet separation after loading in three-point bending [Wang et al, 2001].

Compressive strength (maximum stress recorded) of *Haliotis rufescens*, for loading in the x- (or equivalently, z-) direction of figure 1.4.5, were recorded between 200-540 MPa [Menig et al, 2000] and for compressive loading in the y-direction, 440-720 MPa [Menig et al, 2000].

Shear strength tests performed on *Haliotis rufescens* (see figure 1.4.8), which cause shearing of layers over each other (τ_{yx} and τ_{yz} in the figure 1.4.5) gave shear strength (maximum shear stress, equivalent to stress at failure) values of 29.0 ± 7.1 MPa, shear yield strength of 12MPa and a maximum shear strain of 0.45 [Menig et al, 2000]. For the shear strain tests the plastic region is much larger, as the organic matrix can reach large strains before failure.

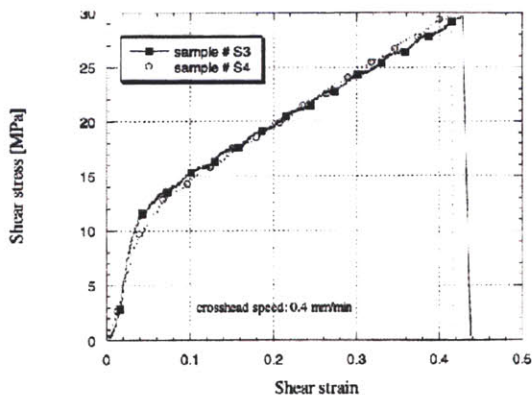


Figure 1.4.8 Shear stress vs. shear strain data for *Haliotis rufescens* (Abalone) nacre [Menig et al, 2000]

Three-point bend strengths (maximum stress value recorded) have been recorded as 223 ± 7 MPa for wet abalone in the ‘across’ direction, 194 ± 8 MPa for wet abalone in the ‘along’ direction, 227 ± 13 MPa for wet *Pinctada maxima* in the ‘across’ direction and

248±14 MPa for wet *Pinctada maxima* in the ‘along’ direction [Wang et al, 2001]. The curves (see figure 1.4.9) show extensive plastic deformation before failure when loaded in three-point bending, which is understood to result from the large amount of shearing that takes place in three-point bending that is accommodated by the organic matrix (see results from shear tests above) and by tablet separation, as previously discussed (see figure 1.4.9).

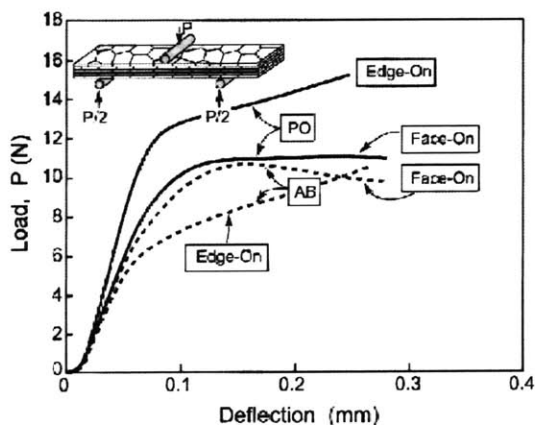


Figure 1.4.9 Load deflection data from three point bend testing of the nacre from *Haliotis rufescens* (Abalone), labeled ‘AB’ and *Pinctada maxima* (Pearl Oyster), labeled ‘PO’. ‘Edge-On’ loading is equivalent to ‘along’ loading as defined in this text; ‘Face-On’ loading is equivalent to ‘across’ loading as defined in this text [Wang et al, 2001]

Finite Element Analysis fitting of the curves from nanoindentation tests performed on the top face of nacre tablets in *Trochus niloticus* (in the y direction of figure 1.4.5) gave values for yield strength of 11.1±3.0 GPa and 9.0±3.2 GPa [Bruet et al, 2005].

Nacre exhibits hysteresis on unloading after tensile deformation, which is understood to result from the polymeric nature of the organic matrix and its contribution to the mechanical response [Currey, 1977]. The time dependent nature of the response is further evident when the load is fixed after unloading and some strain relaxation is observed (see figure 1.4.10) [Currey, 1977]. This graph (figure 1.4.10) is only discussed qualitatively by Currey in the text and no x- or y- scale is given.

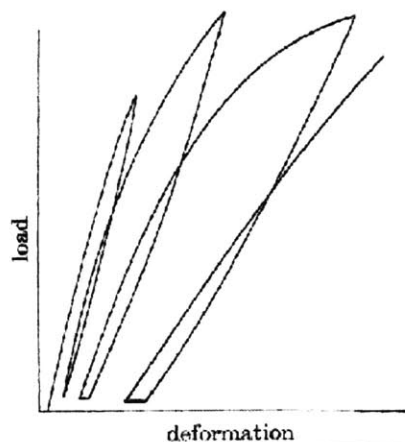


Figure 1.4.10 Copy of oscilloscope trace of a tension test on nacre from the *Pinctada margaritifera* species, with three load-unload cycles and one minute relaxation times between cycles [Currey, 1977]

Using 200 MPa as an order of magnitude estimate of the strength of nacre, and again using a density of 2.85 g/cm^3 [Ashby et al, 1995], the strength to density ratio of nacre is approximated as 70.1 kNm/(kg) .

Toughness; One of the most remarkable achievements of nacre is that the toughness of dry nacre has been found to be 30 times greater than that of pure aragonite (values tabulated at end of this section) [Jackson et al, 1988]. Jackson et al, performed three different fracture toughness tests on *Pinctada* nacre; single edge notch three point bending with unstable fracture, single edge notch three point bending with stable fracture and single edge notch tensile test with unstable fracture [Jackson et al, 1988]. The single edge notch three-point bending with unstable fracture curves are described as being typically linear for ‘dry’ nacre, although some of the samples had a small plastic region in the load displacement curve, and in the ‘wet’ state a more extensive plastic region is observed [Jackson et al, 1988]. No curves are plotted for these tests. In single edge notch three point bending with stable fracture, the crack propagation is controlled until the specimen carries zero load and the crack has propagated through the entire specimen, with the load displacement curve being triangular in form [Jackson et al, 1988]. The curves for single edge notch tensile test with unstable fracture are not illustrated or discussed in the paper [Jackson et al, 1988]. Jackson’s experiments yielded a fracture toughness of $2.9 - 5.0 \text{ MNm}^{-3/2}$ and work of fracture values of $260-1240 \text{ Jm}^{-2}$ [Jackson et al, 1988]. Work of fracture was measured in *Pinctada margaritifera* using notched three point bend specimens loaded in the three orientations given in figure 1.4.5 to give work of fracture values of $1650 \pm 0.04 \text{ Jm}^{-2}$ for ‘across’ loading, $800 \pm 0.08 \text{ Jm}^{-2}$ for ‘along’ loading and $150 \pm 0.01 \text{ Jm}^{-2}$ for ‘between’ loading [Currey, 1977].

It is strongly believed the superior mechanical properties of nacre over its constituents is attributable to its multiscale architecture and the resulting deformation mechanisms [see, for example, Wainwright et al, 1976; Lowenstam et al, 1989; Sarikaya et al, 1995]. A common design principle found in biocomposites is the small lengthscales of the various ‘building blocks’, which avert brittle fracture at the micro- and nano-scale [see, for example, Wainwright et al, 1976; Lowenstam et al, 1989; Sarikaya et al, 1995].

The lengthscale effect can be verified using the Griffith flaw criterion, which is used to evaluate the critical crack length for brittle failure in structures. If the dimensions of the ‘building blocks’ are less than the evaluated critical crack length, then materials that typically fail by brittle behavior on the macro-scale (e.g. calcium carbonate) can avert brittle failure. The analysis performed by Wainwright [Wainwright et al, 1976] is followed here. Wainwright performed the analysis for calcite, as the material properties required in the calculation are not available for aragonite. The Griffith flaw criterion is given as:

$$\sigma = (2ES/\pi)^{1/2} a^{-1/2}$$

The values and property of the components of the criterion are given as;

| |
|---|
| <p><u>Calcite</u> E = 137 [GPa] = Young’s modulus S = 0.23 [Jm⁻²] = Surface energy σ = 50 – 100 [MPa] = Tensile strength a = critical crack length</p> |
|---|

Substituting these values into the Griffith criterion gives a critical crack length, a, of 2-5µm. This analysis is approximate but shows that if the ‘building blocks’ used by biocomposite materials are less than these critical values, brittle failure can be averted in these structures. Typical tablet dimensions are 0.5-1 µm thickness and 2-8 µm in planar dimensions, where the planar dimension is further broken down into sectors. These dimensions and the Griffith argument suggest that the tablets are sized to avert brittle failure. This analysis has recently been redone in a slightly more sophisticated manner by Gao et al [see, for example, Gao et al, 2003] yielding the same basic result.

One deformation mechanism that has been widely observed for nacre is tablet pull-out due to debonding or failure of the organic matrix, creating ‘dilatation bands’ as previously discussed (see figure 1.4.7) [see, for example, Currey, 1977; Jackson et al, 1988; Wang et al, 2001].

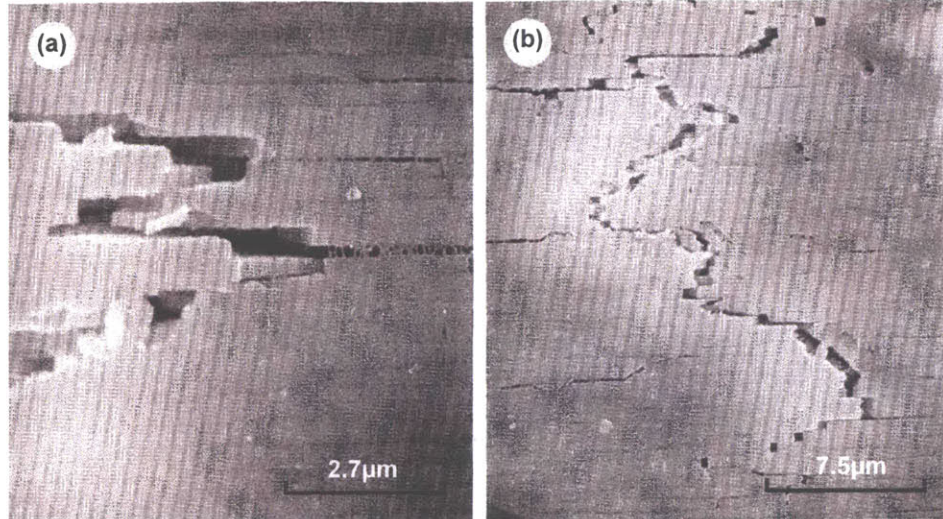


Figure 1.4.11 Image of crack in nacre from *Pinctada*. Both images show the crack traveling around the tablets and tablet pull-out occurring, as well as, (a) organic matrix bridging crack (b) minor cracks at right angles to the main crack [Jackson et al, 1988].

Examination of crack propagation in nacre (for single edge notch samples tested in three-point bending with unstable fracture) shows multiple cracks initiating ahead of the crack tip, increasing the energy required for crack propagation (see figure 1.4.11) [Jackson et al, 1988]. Further, the compliant organic matrix can undergo large stretches to bridge the crack and prevent catastrophic failure (see figure 1.4.11, figure 1.4.12) [Jackson et al, 1988; Smith et al, 1999]. In undergoing these large stretches, the biomacromolecules exhibit a “saw-tooth” pattern: a repeating pattern of a nonlinear rise in force for increasing displacement up to a peak, followed by a significant force drop (see figure 1.4.12) [Smith et al, 1999; Qi et al, 2006]. It is believed that this characteristic pattern results from stretch-induced unfolding of modules along the molecular chain and this increases the molecules energy dissipation during stretching [Smith et al, 1999; Qi et al, 2006].

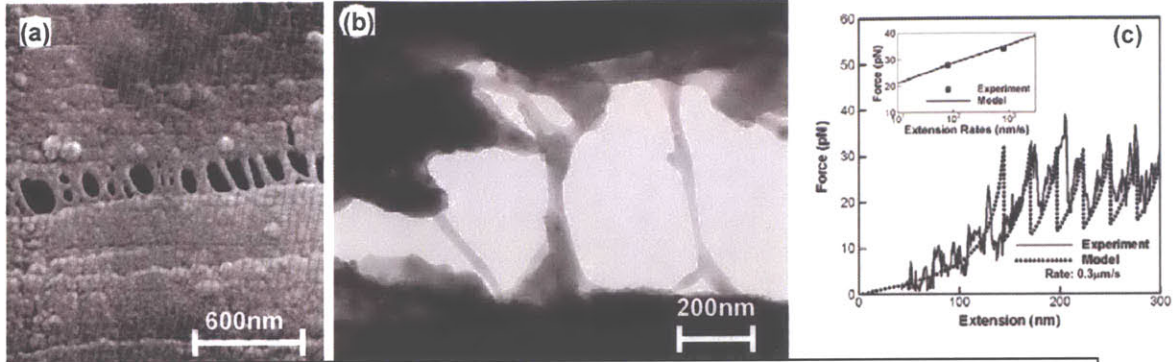


Figure 1.4.12 Intertablet organic matrix (a) SEM image of organic matrix undergoing large stretch between the nacre tablets of *Pinctada* [Jackson et al, 1988] (b) TEM image of organic matrix between two tablets of abalone [Smith et al, 1999]. (c) ‘Saw tooth’ pattern resulting from unfolding of modules in spectrin biomacromolecules. *Inset*: dependence of unfolding force on extension rate [Qi et al, 2006].

Interactions between interdigitated nanoasperities and elastic/plastic deformation of the mineral bridges between tablets are also believed to increase the strength and toughness of nacre (see figure 1.4.13) [Evans et al, 2001; Wang et al, 2001; Song et al, 2003].

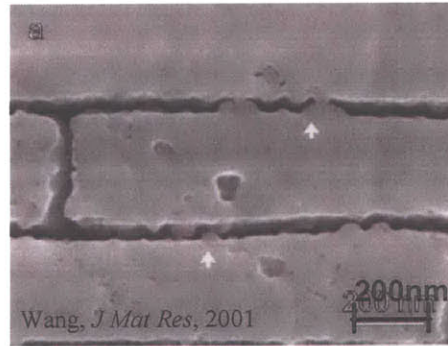


Figure 1.4.13 Cross-section of *Haliotis rufescens* (Abalone), showing interacting nanoasperities [Wang et al, 2001].

A summary of the above mentioned properties for nacre and the corresponding properties for aragonite and calcite, where available, are tabulated overleaf.

| | Elastic Modulus (GPa) | Tensile Strength (MPa) | Compressive Strength (MPa) | 3-point Bending Strength (MPa) | Fracture Toughness (MPa·√m) | Work of Fracture (Jm ⁻²) |
|------------------|-------------------------|---------------------------|----------------------------|--------------------------------|-----------------------------|--------------------------------------|
| Nacre | 60 - 80 ^{1, 2} | 130 - 168 ^{1, 3} | 235 - 540 ⁴ | 194 – 248 ² | 2.9 - 5.7 ¹ | 150-1650 ³ |
| Aragonite | 98 – 171 ⁵ | - | ~ 30 ⁶ | - | 0.1 - 0.2 ⁶ | - |
| Calcite | 85-149 ⁷ | 50-100 ⁸ | ~150 ⁹ | - | - | 1-3 ⁸ |

1. [Jackson et al, 1988], 2. [Wang et al,2001], 3. [Currey, 1977], 4. [Menig et al, 2000], 5. [Liu et al., 2005], 6. [Sarikaya et al, (1995)], 7. [Chen et al, 2001], 8. [Wainwright et al, 1976], 9. [Ashby et al, 1995]

Table 1.4.1 Summary of mechanical properties (where available) for nacre, aragonite and calcite

1.5 Outline of Thesis

Chapter 1 has introduced some of the key aspects of biocomposite materials and specifically the nacre in the seashell of *Trochus niloticus*.

In chapter 2, results from a geometric study on the microscale geometric features of aragonite are presented. Specifically, the tablet area, overlap between tablets on neighboring layers and tablet dimensions are reported.

Chapters 3 and 4 focus on the inorganic component of seashell nacre, namely aragonite, an orthorhombic form of CaCO_3 . The details and results of a nanoindentation study performed on single crystal aragonite are presented in Chapter 3. This study was performed at several loads (500 μN , 1000 μN , 5000 μN and 10000 μN), using a cono-spherical tip, Berkovich tip and Knoop tip. The high load indents (5000 μN and 10000 μN) were imaged using tapping mode atomic force microscopy (TMAFM) to examine the residual indents and pile-up patterns.

A classic single crystal plasticity model was used together with the nonlinear finite element method to model the residual nanoindentation patterns and to investigate and interrogate the activated slip systems. This work is presented in chapter 4.

A study similar to the one conducted for aragonite has been initiated for single crystal calcite and the early results of this study are presented in Appendix A.

Chapter 2: *Geometric study of the nacre from the species Trochus niloticus*

Introduction

Chapter 1 discussed the excellent combination of mechanical properties achieved by seashell nacre, including stiffness, fracture toughness and strength. The multiscale geometrical features strongly contribute to these properties and understanding them will help enable future investigators to mimic the materials found in nature. It is also necessary to understand the interdependencies of these geometrical features at different lengthscales so that we can model their deformation behavior and interpret the mechanisms used by nature to attain the high stiffness, strength and toughness.

This chapter focuses on an investigation into the microscale geometrical features of seashell nacre from *Trochus niloticus*, the seashell chosen for this study. Here a detailed investigation into the microscale structure, tablet size, growth bias and overlap was conducted.

2.1 Geometrical features of Seashell nacre

As part of this study, in collaboration with MIT undergraduate student researcher T. Hall, a detailed investigation of the microstructural geometrical features of *Trochus niloticus* nacre was conducted. As previously discussed, the possibility of successfully biomimicking nacre or other biocomposites lies in our ability to capture nacre's geometrical features and their interplay. In order to successfully model and understand key structural features at the micron scale, it is necessary to quantify tablet size, the relative arrangement of the aragonite tablets and recognize any growth patterns.

An experimental investigation utilizing scanning electron microscopy (SEM) imaging techniques was employed to obtain precise micrographs of the seashell structure from viewpoints parallel and perpendicular to the *c*-axis, where the aragonite *c*-axis is coaxial to the through thickness direction of nacre (see section 1.4.1). These micrographs were

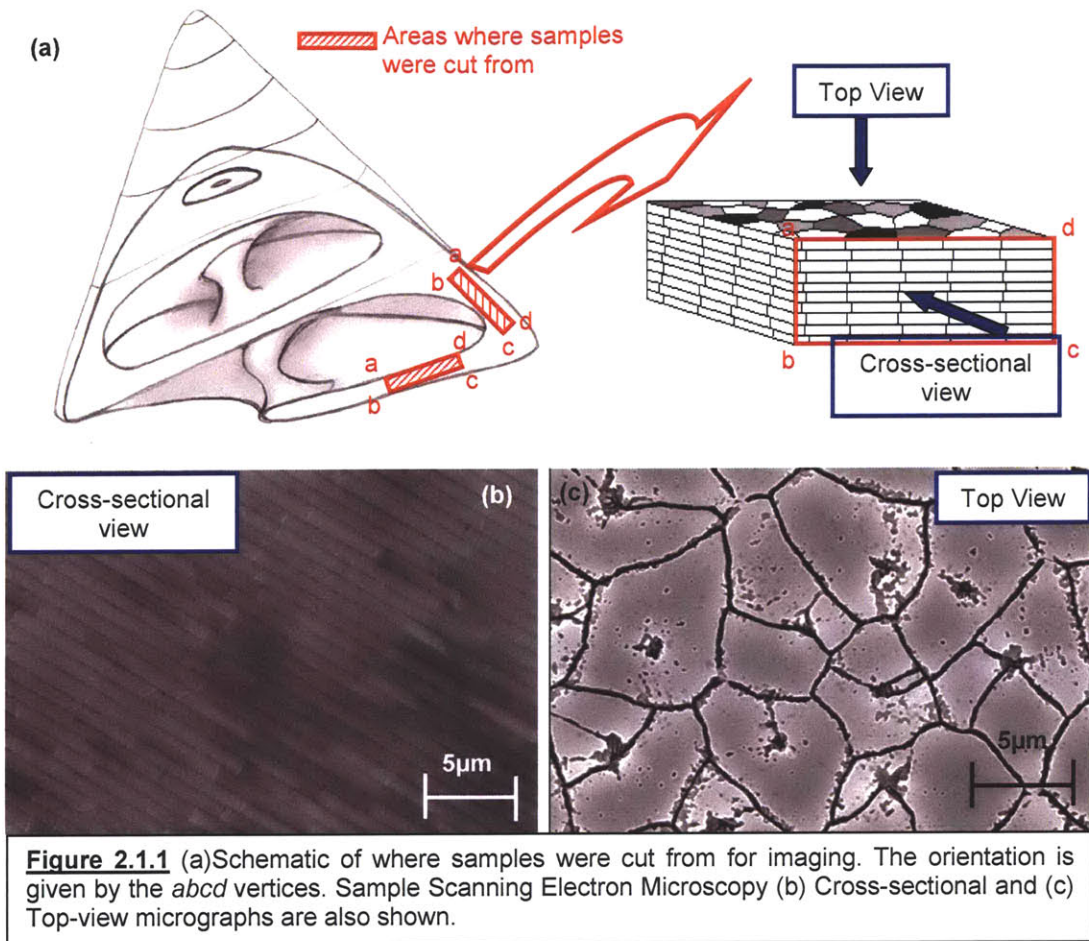
then used to create a 3-dimensional *SolidWorks* model of the nacre, which facilitated our geometrical investigation.

Firstly, the sample preparation used to obtain the micrographs with viewpoints parallel and perpendicular to the crystallographic *c*-axis of the aragonite tablets are described. The geometric analysis of the micrographs with viewpoints perpendicular to the *c*-axis are then presented, followed by the analysis of the micrographs with viewpoints parallel to the crystallographic *c*-axis. This is followed by a description and analysis of the *SolidWorks* models: a model developed from micrograph images, a model developed assuming perfect hexagonal tablets and a model of an idealized Voronoi tessellation layer.

2.1.1 Sample preparation for imaging

All samples of nacre were extracted from the shell of *Trochus niloticus* using a diamond saw (Buehler, Isomet 1000) operating at 900 rpm. The outer prismatic layer and the inner cross-lamellar layer were both removed by cutting (or polishing). Knowledge of the seashell growth patterns allowed us to selectively cut the orientation of the samples (see figure 2.1.1). Sample preparation for images taken from the ‘Top view’ of a plane of tablets (called the *c*-plane henceforth) and from the ‘cross-sectional’ view as labeled in figure 2.1.1, were different and both are discussed below.

Sample preparation for cross-sectional images: Once the sample is cut to appropriate dimensions, a polishing wheel (*South Bay Technology Inc., Model 920, Lapping & Polishing wheel*) is used to yield a suitable surface for imaging. A diamond grinding disk (*Buehler, Apex diamond grinding disk*) is used to remove the coarse surface roughness (60 s, 10-15 rpm). This step was followed by successive diamond suspensions (*Buehler, Metadi Diamond suspensions 15 μm, 6 μm and 1 μm*) on a suspension pad (*Buehler, Ultrapad*) for periods of 300 s at 10-15rpm. Finally, a colloidal silica suspension (*Buehler, microcloth and colloidal silica suspension*) was used to complete the polishing. The sample was sonicated for 120 seconds before imaging.



Sample preparation for c-plane images: Once the sample is cut from the shell, it is cleaved perpendicular to the *c*-axis. Based on our knowledge and experience in preparing the samples, we are confident that the tablets cleave cleanly between two layers of tablets (as the organic matrix is weaker than the aragonite tablets), exposing the top surface of the tablet. The cleaved samples were then air dried for 120 days, which dries out the organic matrix on the top layer.

2.1.2 Geometrical features and statistical analysis of cross sectional images

The micrographs of cross-sections (see for example figure 2.1.2) clearly reveal the tablets to be arranged in well-defined layers and the “brick and mortar” structure which is often attributed to nacre is apparent. The crystallographic *c*-axis is coaxial to the tablet through

thickness direction as indicated. The tablet length is approximately $8\mu\text{m}$ and the thickness is approximately 870 nm , with an organic layer of $\sim 40\text{ nm}$ surrounding the tablets [Bruet et al, 2005]. The near columnar structure and the overlap between alternating layers is evident.

Figure 2.1.2 SEM cross-sectional images at different lengthscales of nacre illustrating the 'brick and mortar' structure commonly used to describe nacre

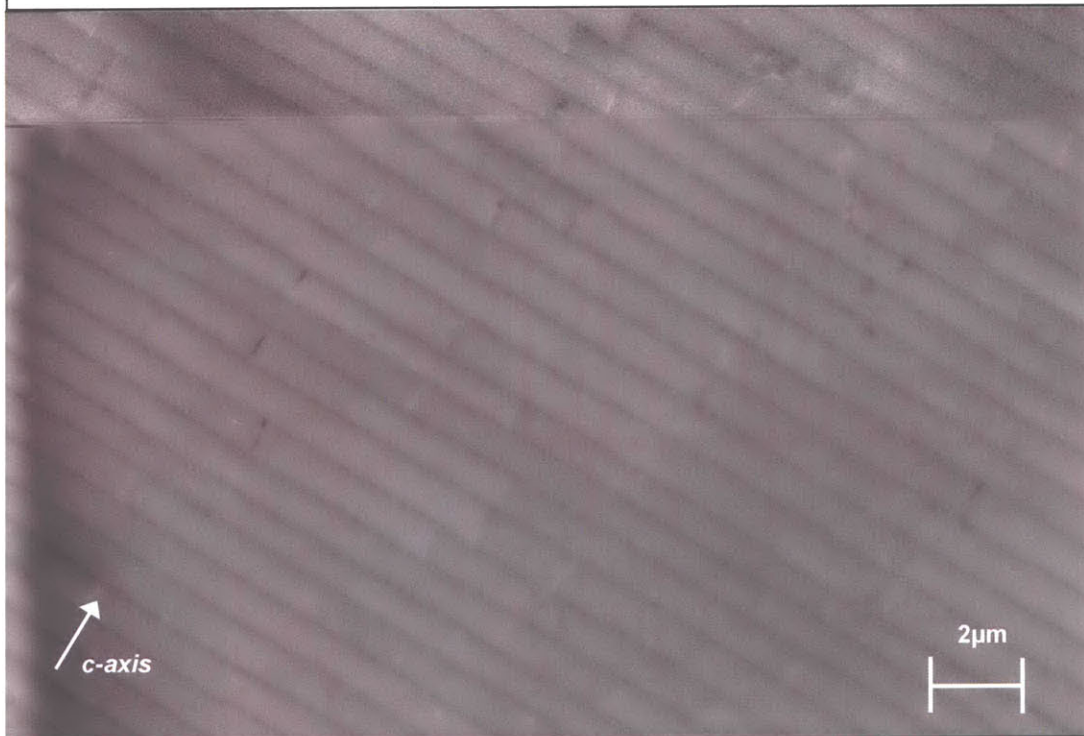
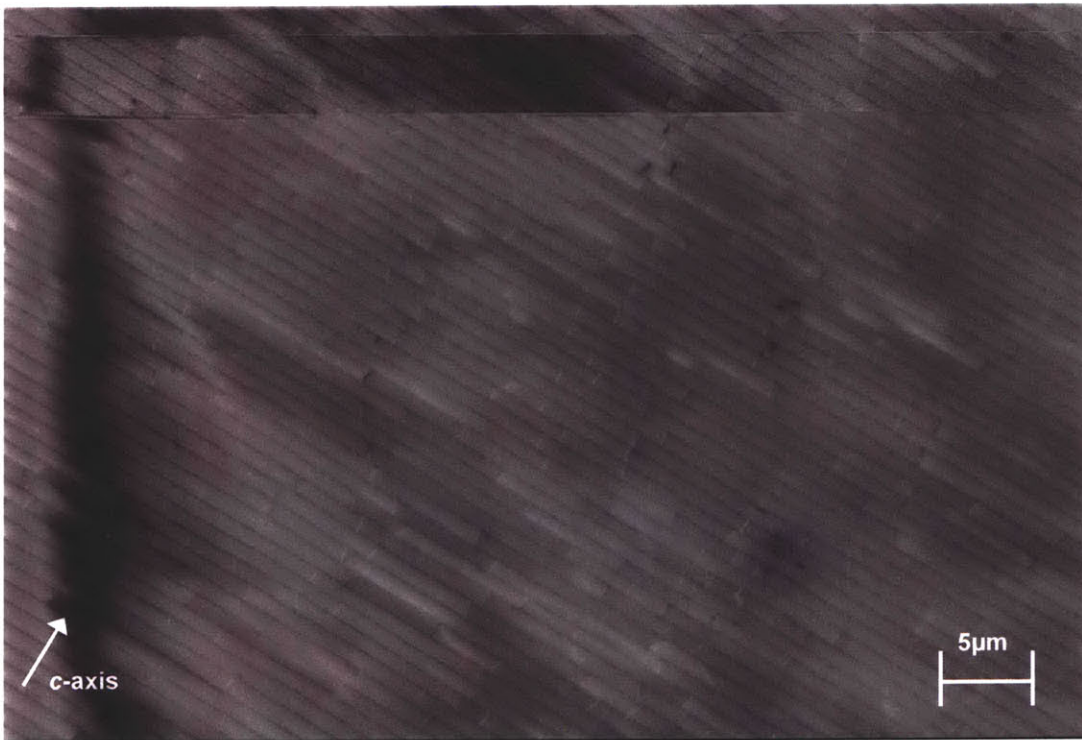
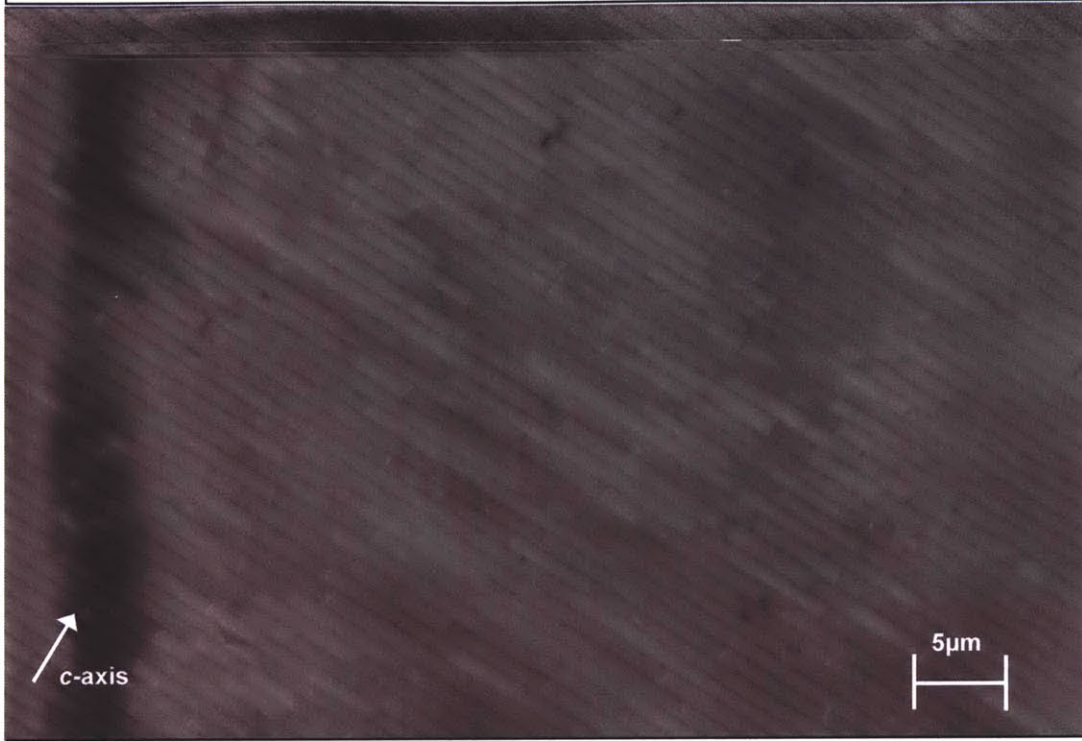


Figure 2.1.2 (continued) SEM cross-sectional images at different lengthscales of nacre illustrating the 'brick and mortar' structure commonly used to describe nacre



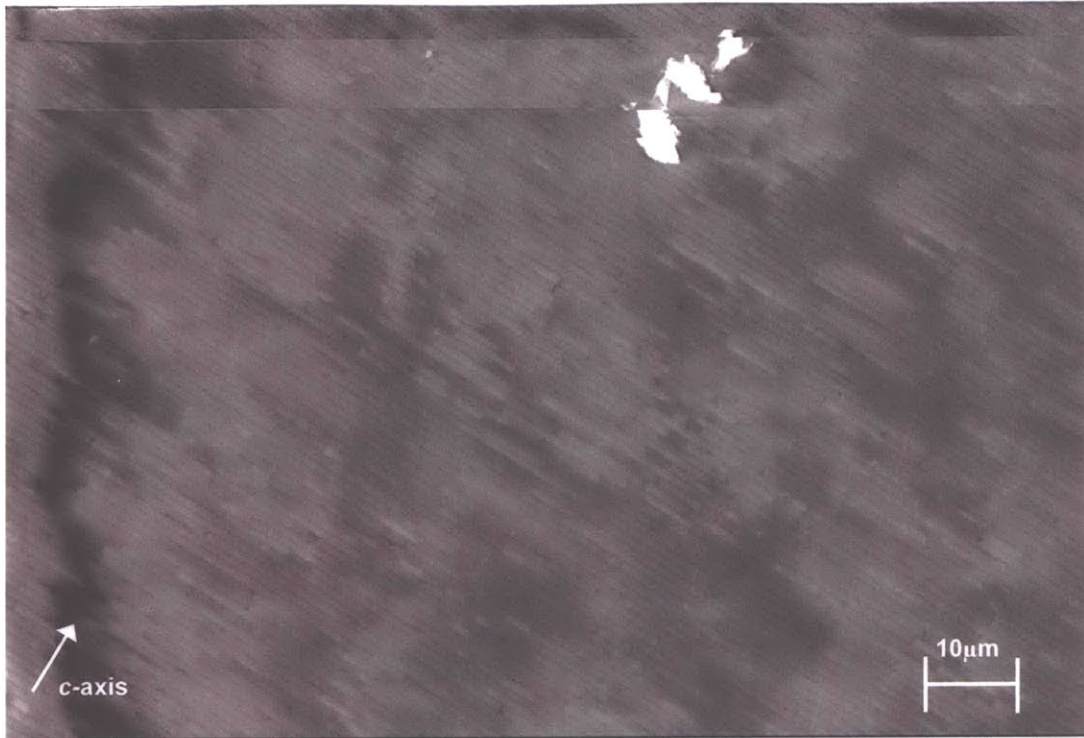


Figure 2.1.2 (continued) SEM cross-sectional images at different lengthscales of nacre illustrating the 'brick and mortar' structure commonly used to describe nacre

A statistical geometric analysis was performed on figure 2.1.3 aimed at quantitatively evaluating the tablet offset of neighboring aragonite layers. Tablet length was measured as $7.8 \pm 2.7 \mu\text{m}$; the relatively high standard deviation is understandable given the irregular polygonal shape of the tablets. The tablet percent offset for this analysis is defined by the distance between tablet boundaries in adjacent layers divided by the length of the upper tablet. The average percent offset was $22.2 \pm 9.0 \%$ (where \pm implies standard deviation, here and henceforth). The sample size, n , was 40. Relative to a full shell, only a small area was examined ($\sim 60 \mu\text{m} \times 40 \mu\text{m}$) and considering this along with the substantial deviation measured, this result can only be considered a good first approximation.

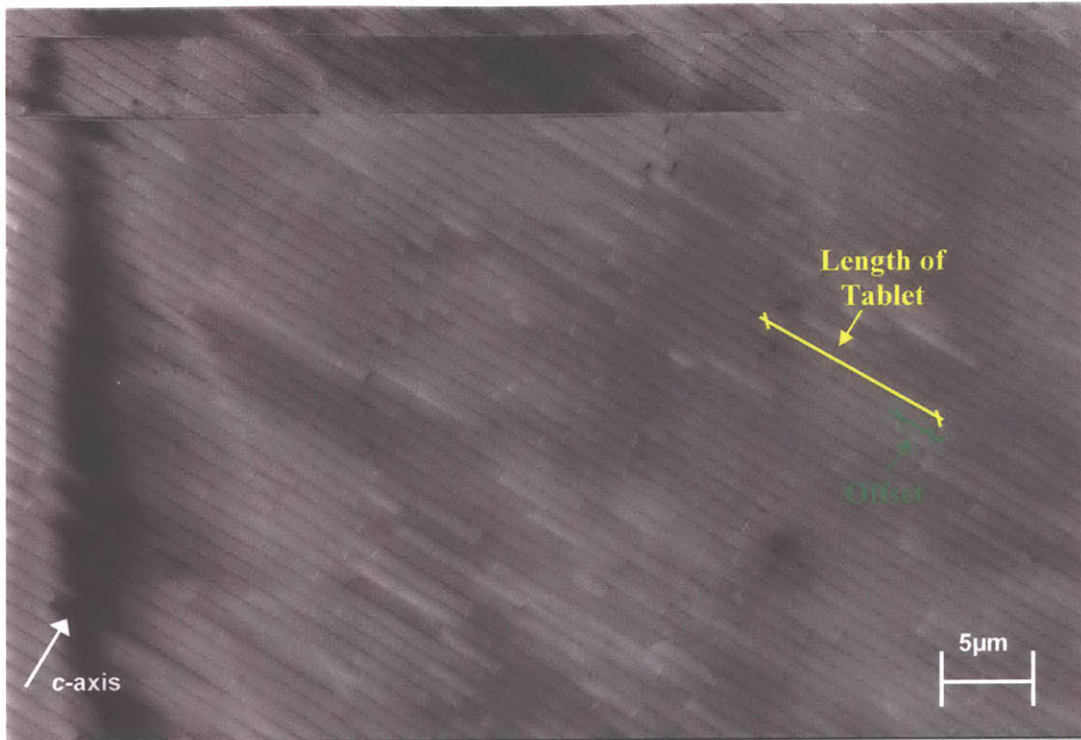


Figure 2.1.3 SEM cross-sectional image used to perform statistical analysis

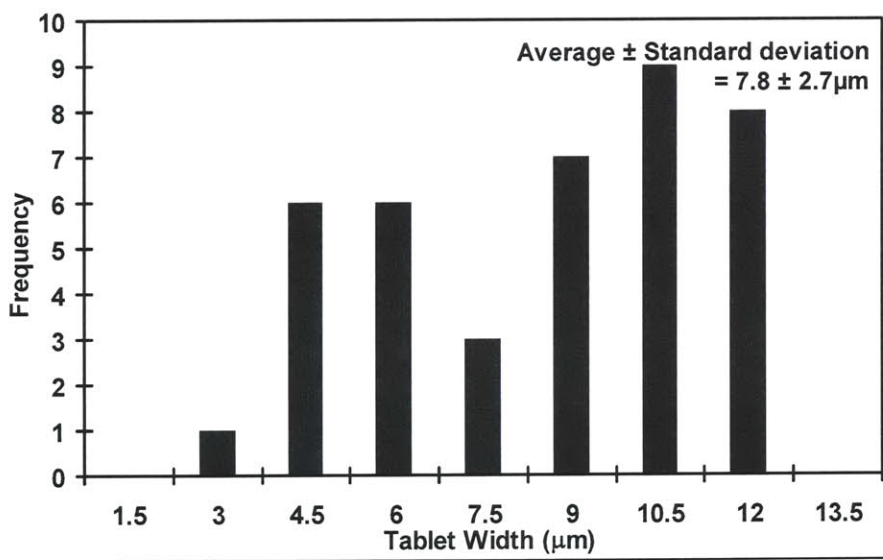


Figure 2.1.4 Histogram distributions of (a) Tablet length and (b) Percent offset for the statistical analysis performed on figure 2.1.3. Bin sizes were chosen based on Sturge's Rule [courtesy of T. Hall].

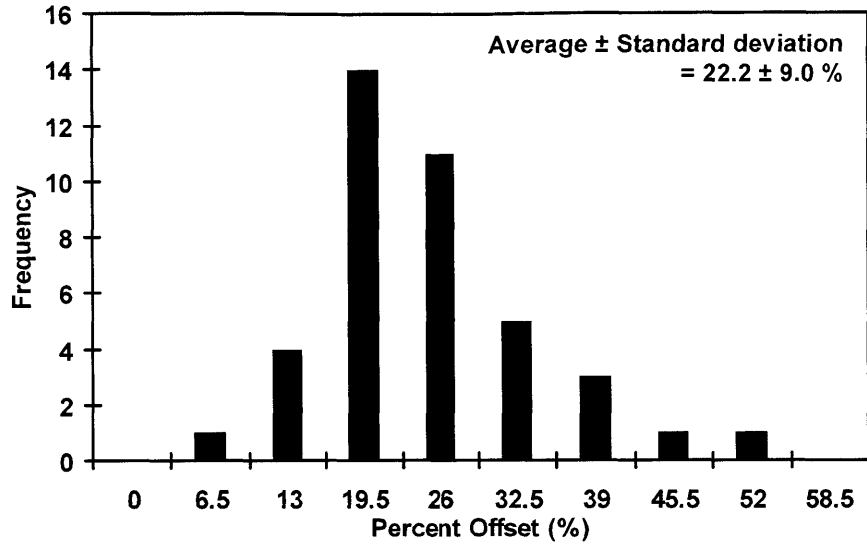

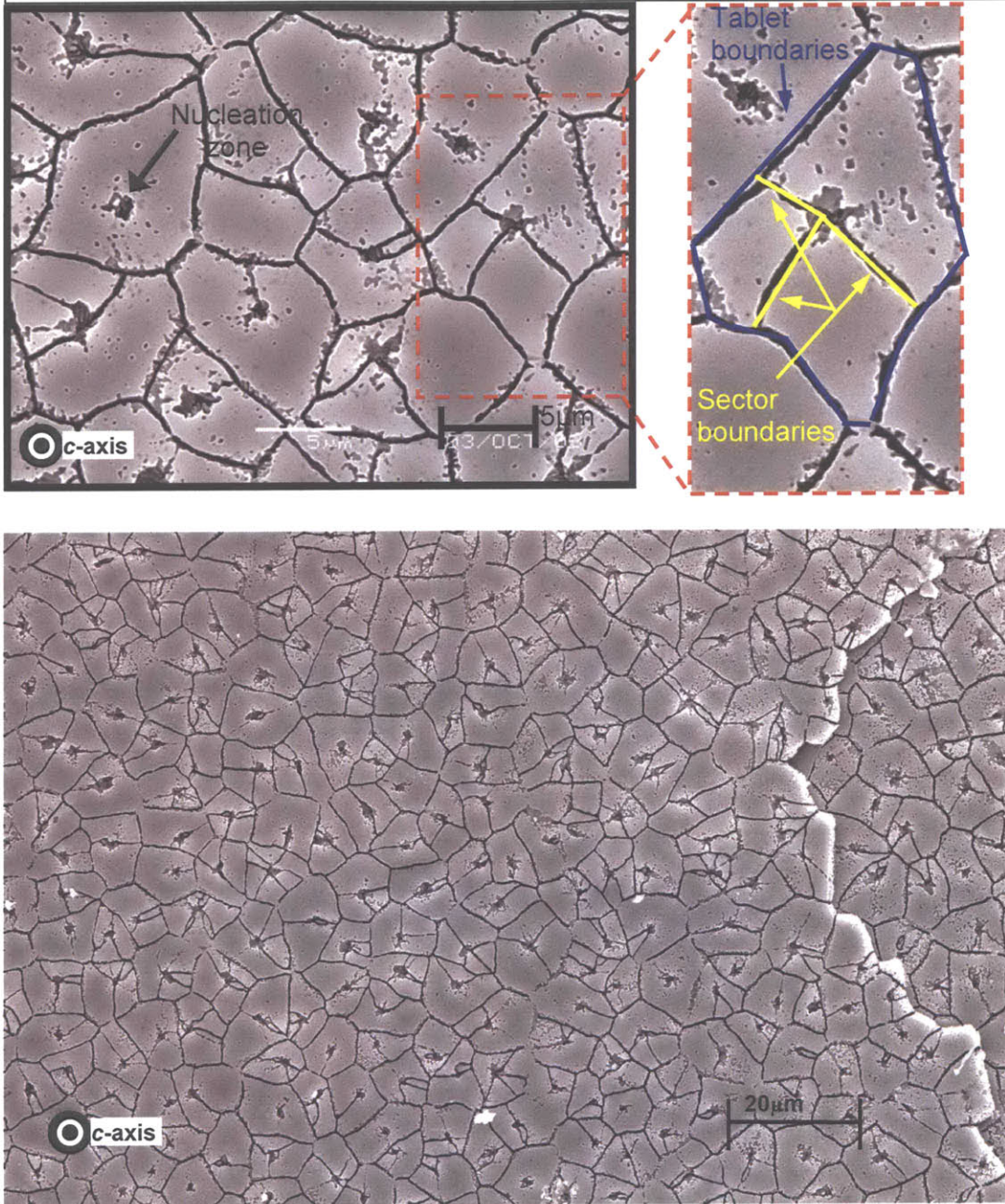


Figure 2.1.4 (continued) Histogram distributions of (a) Tablet length and (b) Percent offset for the statistical analysis performed on figure 2.1.3. Bin sizes were chosen based on Sturge's Rule [courtesy of T. Hall].

2.1.3 Geometrical features of *c*-plane images

Figure 2.1.5 shows exemplar SEM *c*-plane micrographs of nacre, with the samples prepared as described in section 2.1.1. Most tablets are approximately polygonal in shape and range in planar dimension between 5 μm and 10 μm . The nucleation zones are typically centrally located within each of the irregularly shaped tablets. The sector boundary lines emanate from the nucleation zone to the tablet edge, sectioning each tablet creating 'sectors' within each tablet. The distinct dark lines result from areas where the organic matrix has been removed and thus we conclude that the organic matrix covers the nucleation zone and lines the sector boundaries, as well as surrounding the tablets. Figure 2.1.6 shows a tapping mode atomic force microscopy image of the tablets, which also highlights the tablet boundaries, sector boundaries and nucleation points.

Figure 2.1.5 Images of *c*-plane of nacre after sample preparation as described in section 2.1.2.  indicates that the aragonite crystallographic *c*-axis is directed out of the page [courtesy of B. Bruet].



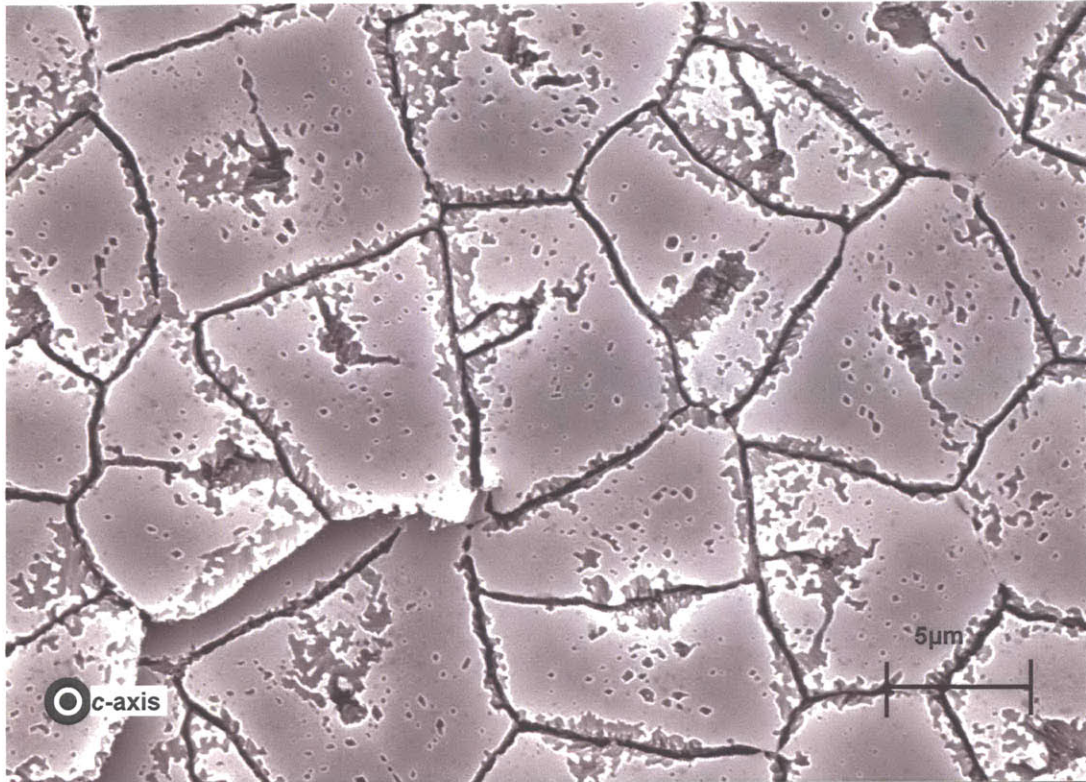



Figure 2.1.5 (continued) Images of *c*-plane of nacre after sample preparation as described in section 2.1.2.  indicates that the aragonite crystallographic *c*-axis is directed out of the page [courtesy of B. Bruet]

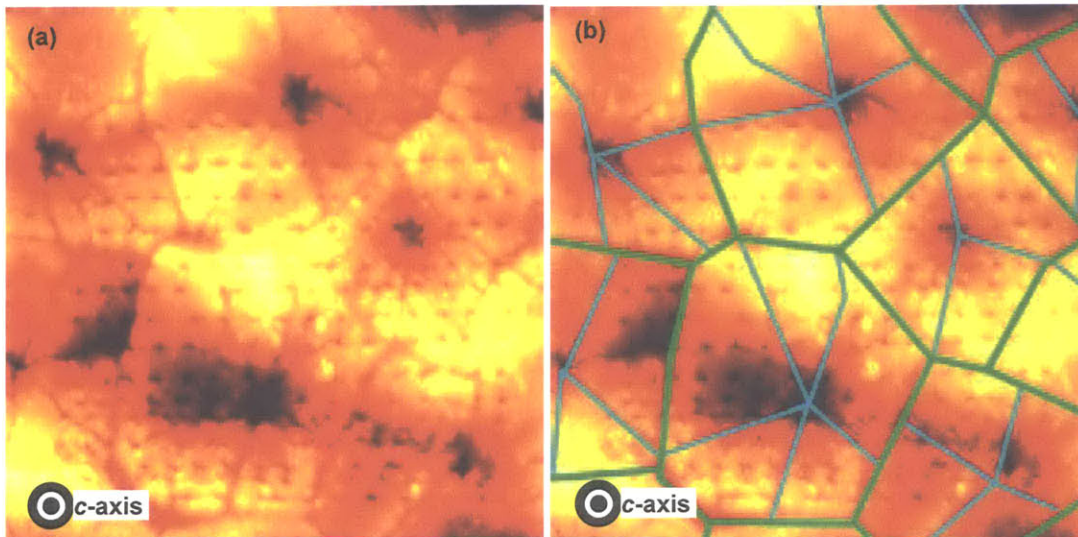


Figure 2.1.6 Tapping Mode Atomic Force Microscopy amplitude image of nacre tablets after the organic matrix has been removed by dissolving it in EDTA. The minor regular impressions on the surface result from nanoindentation performed on the tablets. The nucleation points are visible at the center of the tablets, as are the tablet and sector boundaries. (a) Shows the raw image and (b) is a repeat of the image with the tablet boundaries marked in green and the sector boundaries marked in blue. The nucleation points are positioned at tablet centers where the blue lines converge in (b) [courtesy of J. Villareal].

If the sample is exposed to ethylenediaminetetraacetic acid (EDTA) for ~25 mins the top layer becomes 'transparent' in the SEM and the layer below is exposed (see figure 2.1.7). It is evident that the nucleation zones consistently overlap between planes and we can visualize the shape and overlap of tablets relative to their neighbors in the plane below.

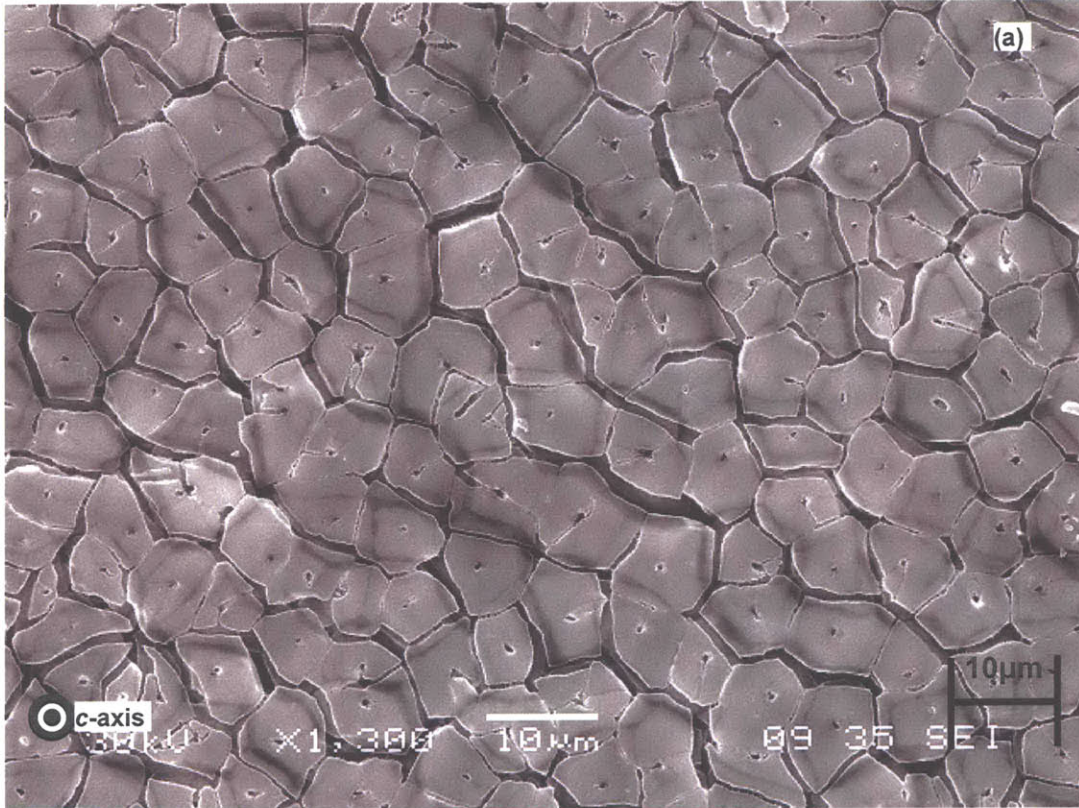
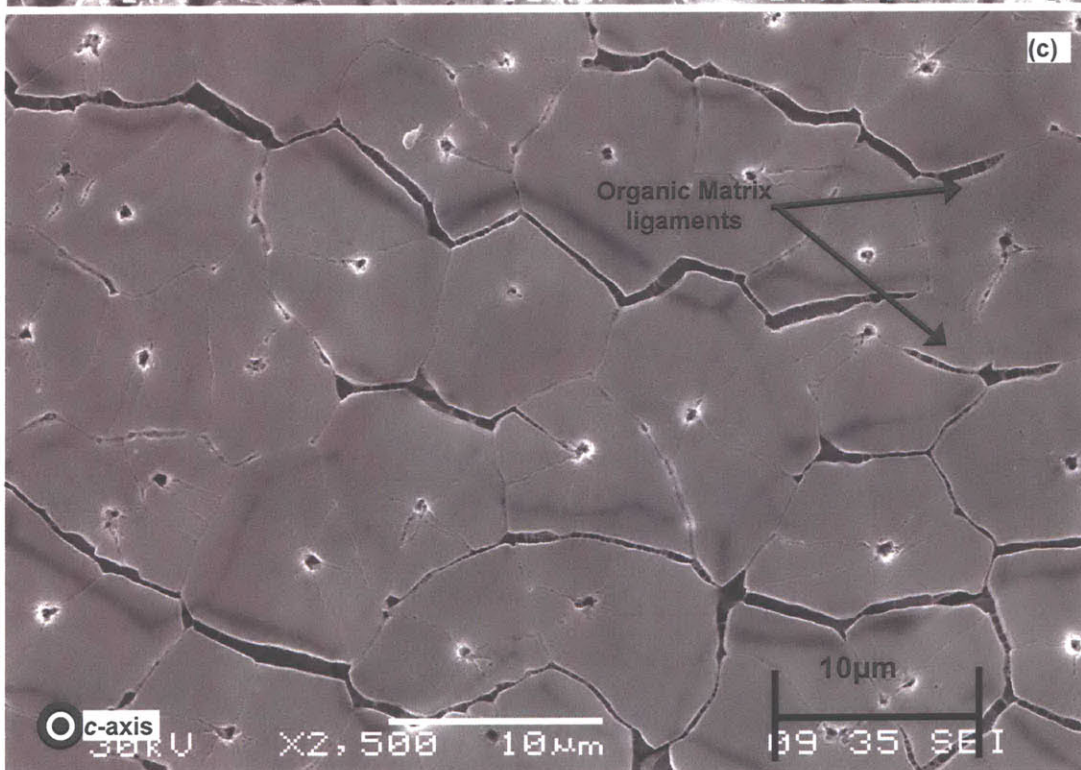
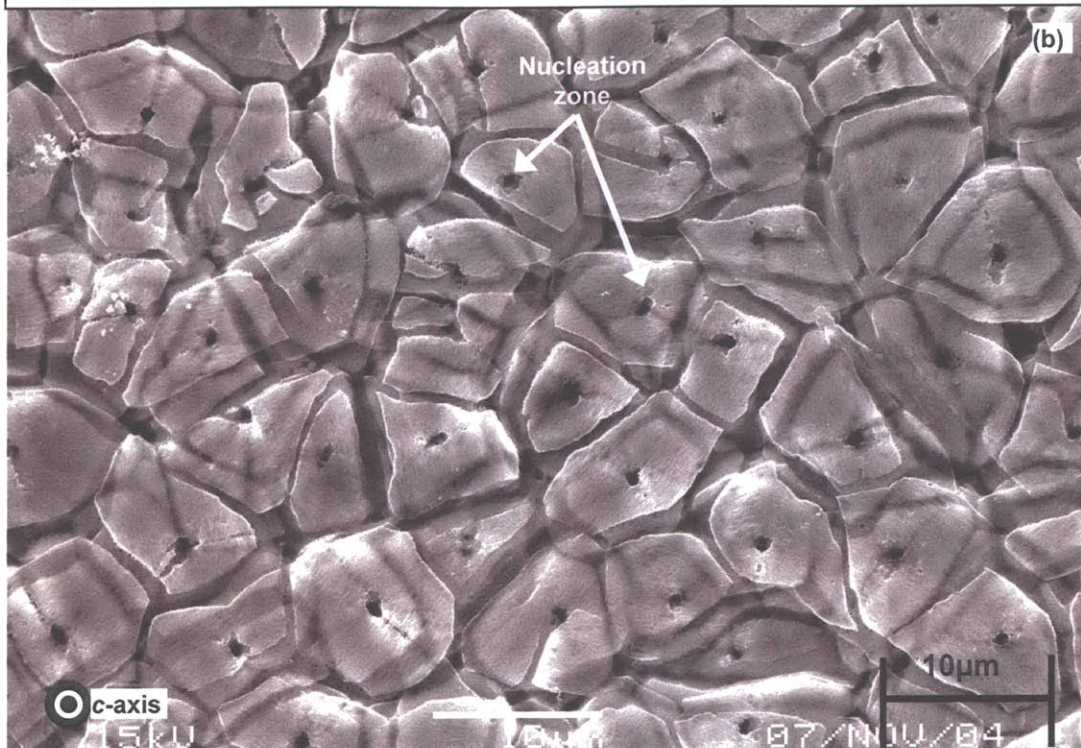


Figure 2.1.7 Two layers of nacre tablets, with the top layer transparent in the SEM, where we can visualize the overlap between overlying tablets. \odot indicates that the aragonite crystallographic *c*-axis is directed out of the page. *Overleaf*: Images of nacre tablets with transparent upper layers: the nucleation zone and ligaments of organic matrix are highlighted [courtesy of B. Bruet].

Figure 2.1.7 (continued) Two layers of nacre tablets, with the top layer transparent in the SEM, where we can visualize the overlap between overlying tablets. \odot indicates that the aragonite crystallographic *c*-axis is directed out of the page. [courtesy of B. Bruet]



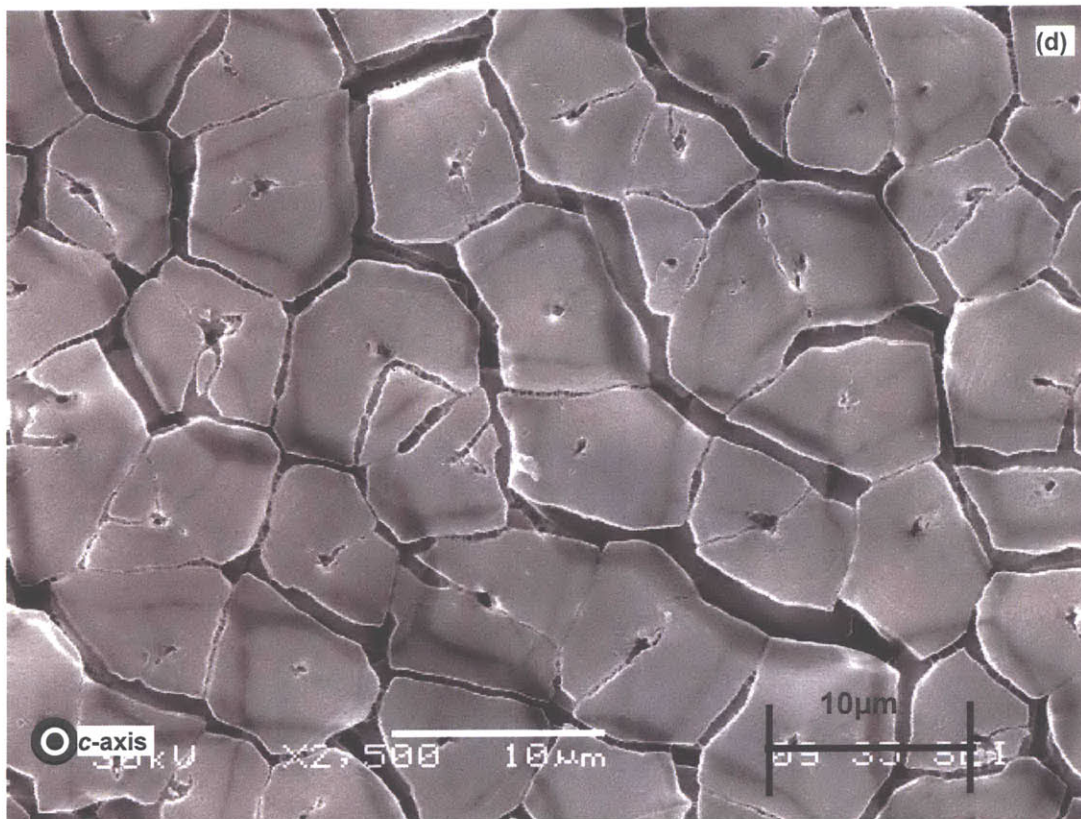


Figure 2.1.7 (continued) Two layers of nacre tablets, with the top layer transparent in the SEM, where we can visualize the overlap between overlying tablets. ● indicates that the aragonite crystallographic *c*-axis is directed out of the page [courtesy of B. Bruet].

The images in figure 2.1.7, as well as revealing the common nucleation zones, the tablet boundaries and the overlap between the layers, highlight some other important features. Inter- and intra-tablet organic ligaments are visible in regions of the images. Figure 2.1.7(b) has been etched more noticeably than the other three images. This likely results in discrepancies between the samples examined or a small inconsistency in the period of exposure to EDTA. In figure 2.1.7(b), there is no evidence of organic ligaments in the upper layer and it appears the second layer from the top has also been etched. There is also a very faint outline in parts of the image of the third layer down from the top.

2.1.4 Creation of SolidWorks model of nacre from micrographs and geometrical analysis

A SolidWorks model, based on the *c*-plane micrograph with the transparent upper layer in figure 2.1.7 (b), was created to enable a detailed quantitative analysis of the nacre structure. Two layers were modeled, to represent the upper and lower layer in the image and these were aligned using the positions of the nucleation zones. It is assumed that layers beneath the top two layers (created from the SEM micrograph) are a repeat of these layers. The various layers and 3-D model are illustrated in figure 2.1.8. This model enables a 3-dimensional analysis of the microstructure and arbitrary cuts can be taken to reveal the cross section.

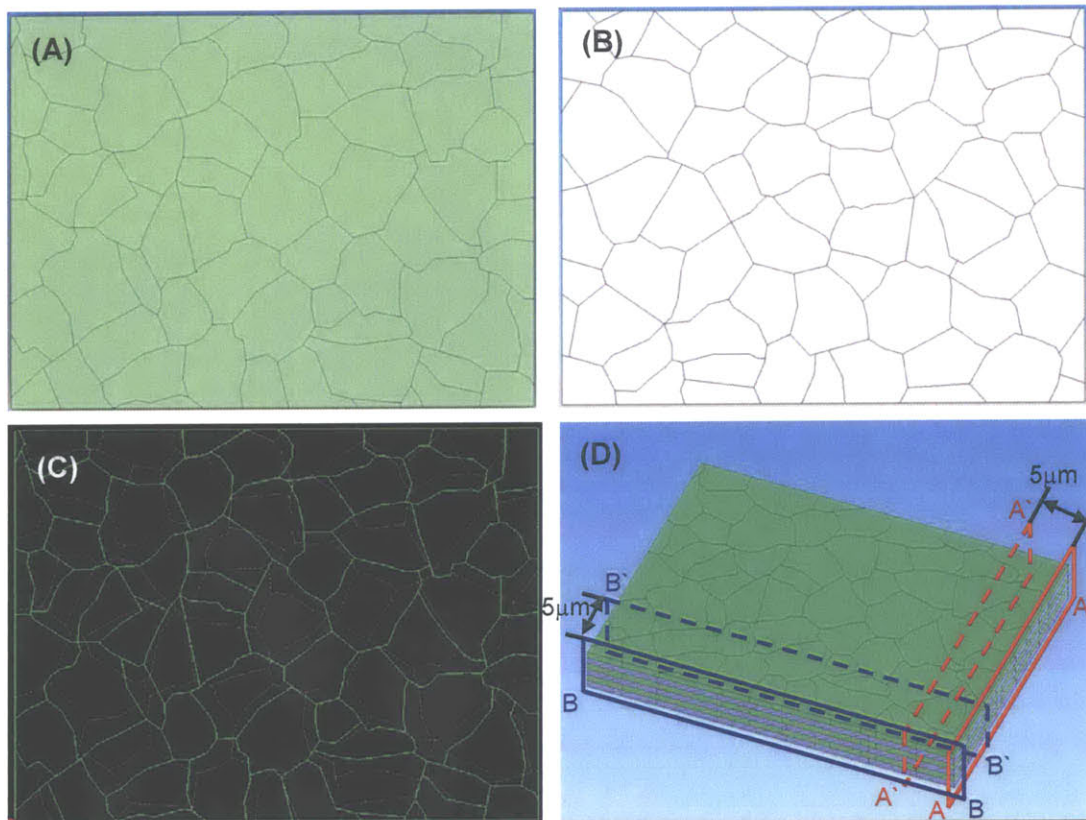


Figure 2.1.8 SolidWorks model two real nacre layers, as micrographed in figure 2.1.7 (b): (a) Top view of upper layer from micrograph, (b) Top view of second layer from micrograph, (c) overlay of these two layers and (d) 3-D representation of these layers, with the two layers in (c) repeated periodically, with each layer 870nm thick. The model is cut in 5 μ m increments in the A-A and B-B directions (the first two cuts in both directions are shown) [courtesy of B. Bruet].

A statistical analysis taken from cross-sectional cuts of the model in both directions (which are labeled A-A and B-B) was performed. The total model size is $65\ \mu\text{m} \times 50\ \mu\text{m}$ and cuts are taken every $5\ \mu\text{m}$ to give 12 x A-A sections and 9 x B-B sections (see figure 2.1.8 (d)). The cross sections were typically irregular and had a range of offsets in one section view, highlighting the randomness of the data set (see figure 2.1.9).

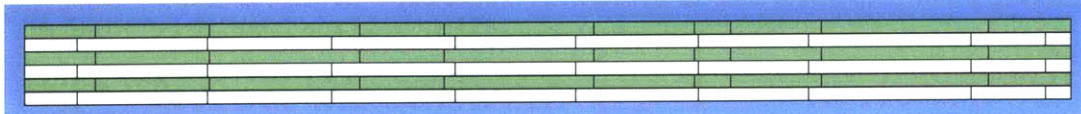


Figure 2.1.9 Example of cross-sectional cut taken and analyzed from the model illustrated in figure 2.1.8 [courtesy of T. Hall].

The percentage offset for all the data taken from A-A cuts was $24.9 \pm 16.9\%$ and the percentage offset for all the B-B cuts was $23.7 \pm 12\%$. The outliers ($> \pm 2$ standard deviations) were removed and this data is graphed (see figure 2.1.10) with this data having an average percent offset of $21.8 \pm 12.3\%$ and $23.0 \pm 11\%$ for the A-A and B-B cuts respectively. The tablet lengths recorded for the A-A cuts were $6.8 \pm 2.6\ \mu\text{m}$ and the lengths for the B-B cuts were $6.6 \pm 2.5\ \mu\text{m}$ (see figure 2.1.10). The data is approximately normally distributed, supporting our chosen method for statistical analysis. For the A-A direction, $n=348$ and for the B-B direction, $n=291$.

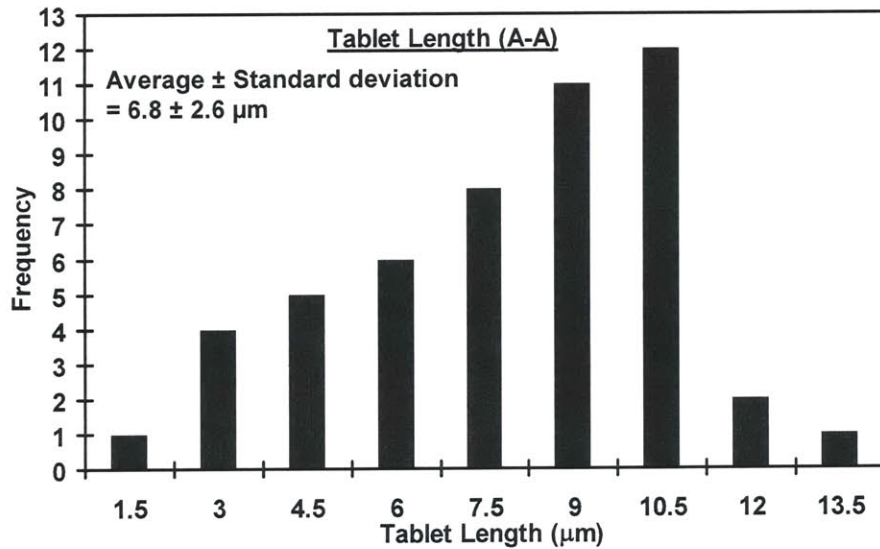


Figure 2.1.10 Histograms of percent offset and tablet area based on model illustrated in figure 2.1.8. Bin sizes were chosen based on Sturge's Rule [courtesy of T. Hall].

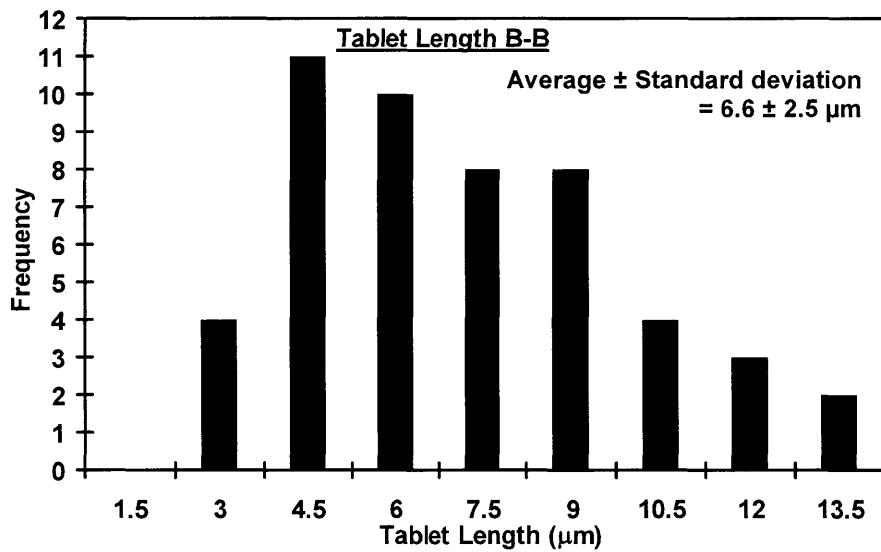
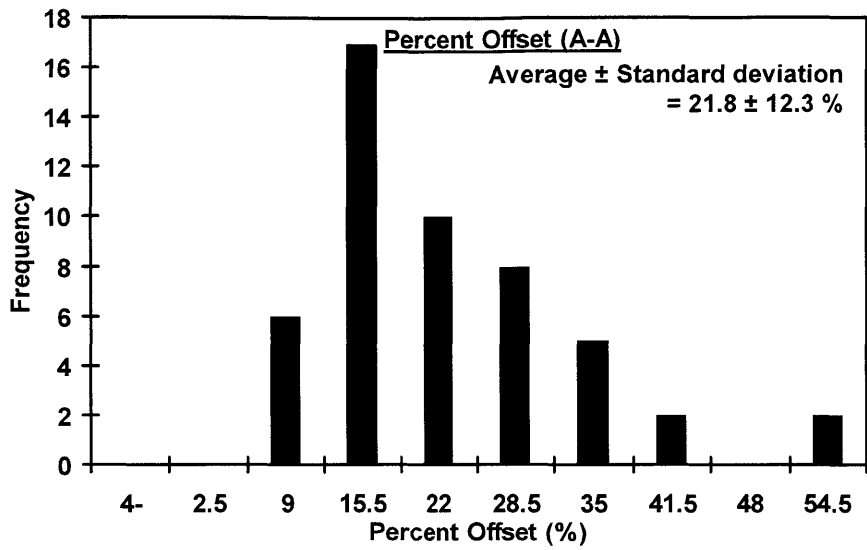


Figure 2.1.10 (continued) Histograms of percent offset and tablet area based on model illustrated in figure 2.1.8. Bin sizes were chosen based on Sturge's Rule [courtesy of T. Hall].

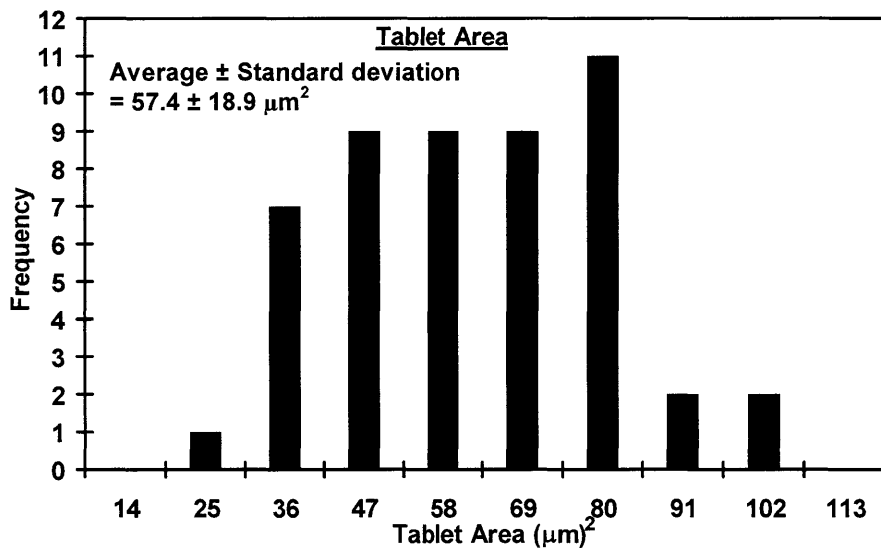
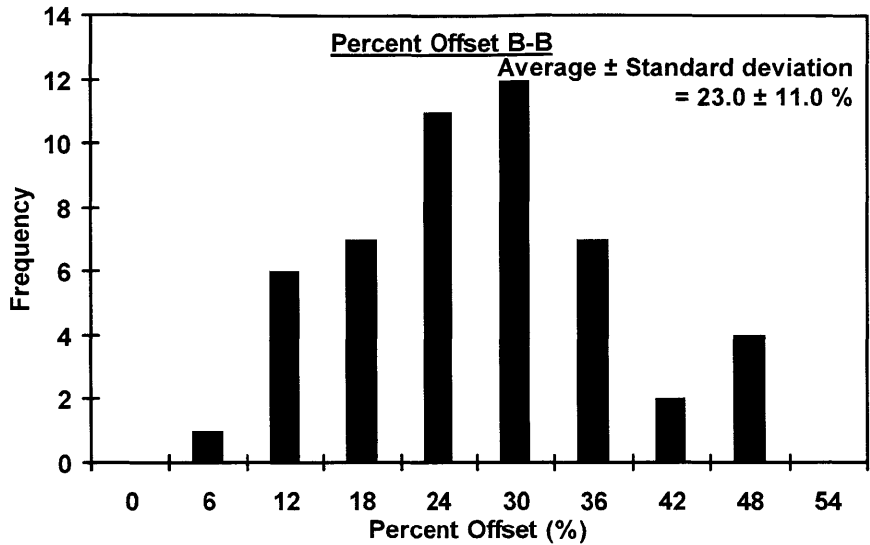


Figure 2.1.10 (continued) Histograms of percent offset and tablet area based on model illustrated in figure 2.1.8. Bin sizes were chosen based on Sturge's Rule [courtesy of T. Hall].

Tablet area was then quantified for each full tablet and the average area was found to be $57.4 \pm 18.9 \mu\text{m}^2$. These values were based on the areas of the tablets that were completely visible, i.e. the tablets on the boundary of the model were excluded ($n=77$). An equivalent diameter of $8.5 \mu\text{m}$ was evaluated. When the upper and lower layer results are evaluated separately, the values are $56.48 \pm 21.02 \mu\text{m}^2$ and $58.43 \pm 16.72 \mu\text{m}^2$ for the upper and lower layers respectively.

2.1.5 Solid modelling of idealized hexagonal tablets

A *SolidWorks* model was created based on a planar array of perfectly uniformly sized hexagonal tablets of $8\ \mu\text{m}$ in length from vertex to vertex, which gives a tablet area of $55.4\ \mu\text{m}^2$ (see figure 2.1.11). This is close to the average area evaluated in section 2.1.4 for the *SolidWorks* model of the two nacre layers (see figure 2.1.8), $57.4\ \mu\text{m}^2$. Given the regularity of the hexagonal structure, the offset between layers becomes the dominant factor for geometric analysis. Preliminary data was collected for a range of regular offsets and cuts at different angles. The final analysis presented is for a 20% offset in two directions ($1.6\ \mu\text{m}$ along one vertex, followed by $1.6\ \mu\text{m}$ perpendicular to the first offset-see figure 2.1.11)).

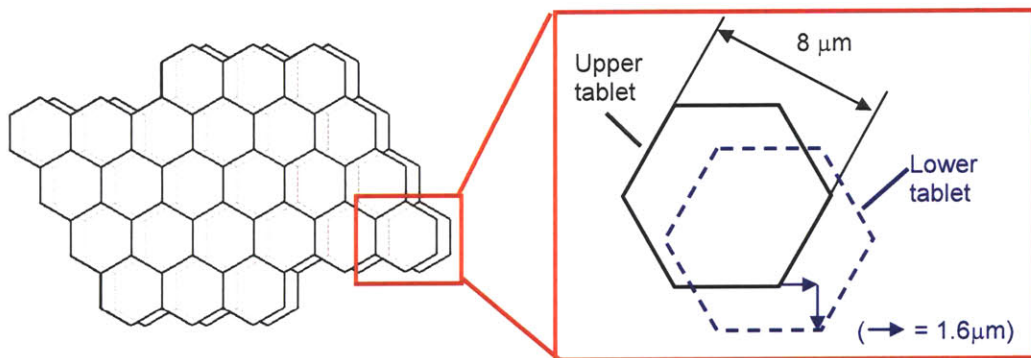


Figure 2.1.11 SolidWorks hexagonal model, with details of the tablet offset.

The model was cut at two different angles, 30° and 45° (see figure 2.1.12). At each angle, the model was cut in $5\ \mu\text{m}$ increments, to give cross-sectional images (see figure 2.1.12). The 30° angle gives very regular cross-sections as it cuts the tablets parallel to one edge and perpendicular to another whereas the 45° angle gives no regularity between the section cuts.

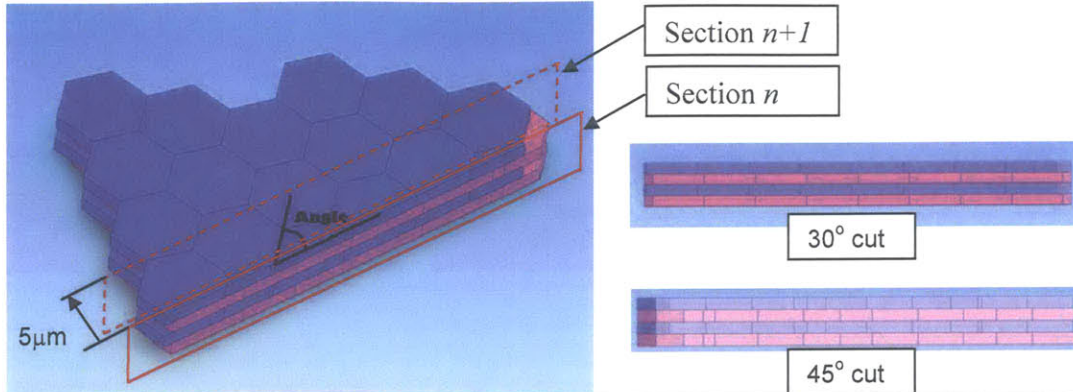


Figure 2.1.12 SolidWorks hexagonal model defining the angle of cut, the offset of different cuts and two sample cross sectional cuts from the 30° and 45° cross-sections [courtesy of T. Hall].

The 30° slices yielded a percent offset of $16.0 \pm 4.1\%$ and tablet length of $8.0 \pm 0.6 \mu\text{m}$. The 45° slices yielded a percent offset of $24.3 \pm 14.2\%$ and tablet length of 6.1 ± 1.7 . The combined results for both angles, gave an average offset of $21.7 \pm 12.6\%$ and tablet length of 6.7 ± 1.7 (see figure 2.1.13) (total sample size, $n = 229$). If the outliers (results that are outside ± 2 standard deviations) are removed the average percent offset is $20.1 \pm 10.1\%$ (see figure 2.1.13(b)). Although the hexagonal model is a good first approximation for the nacre structure, its regularity limits its ability to capture the randomness seen in the micrographs.

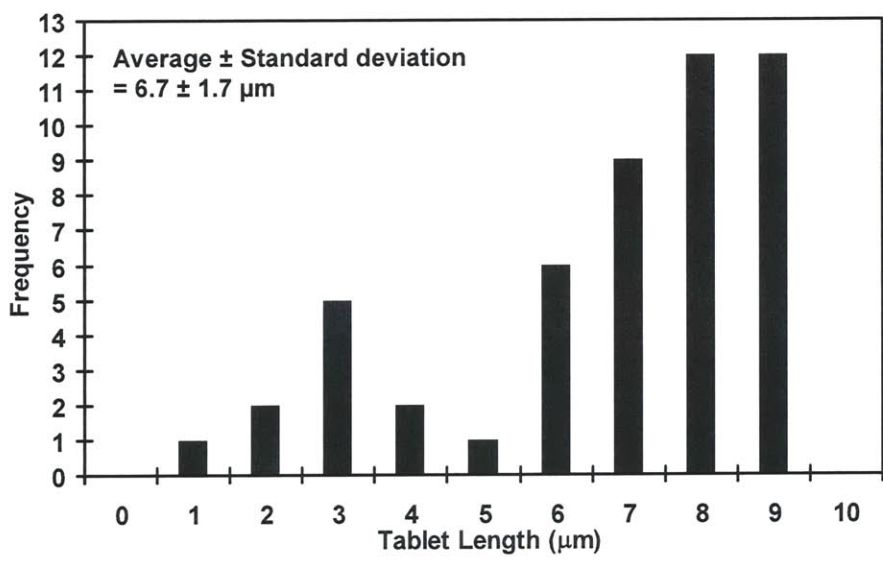


Figure 2.1.13 Histograms of percent offset and tablet area based on *SolidWorks* hexagonal model (a) Tablet Length (full dataset), (b) percent offset (outliers removed). Bin sizes were chosen based on Sturge's Rule [courtesy of T. Hall]

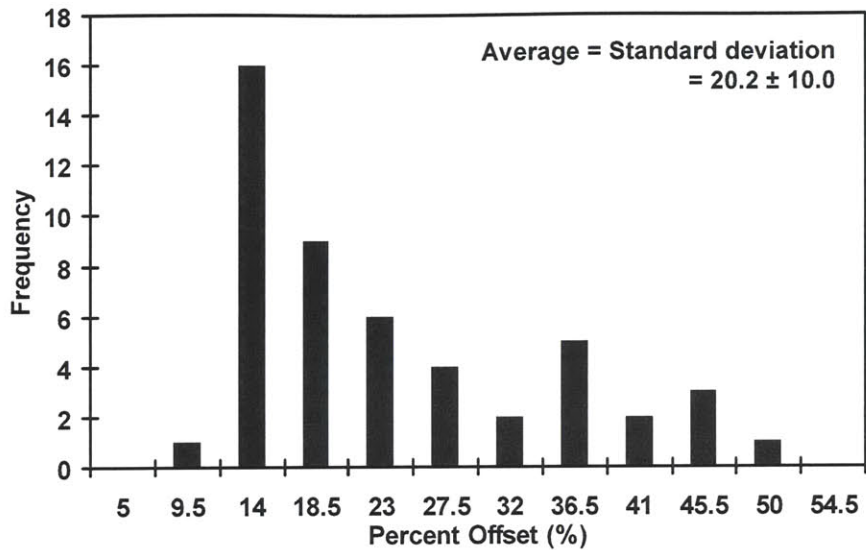


Figure 2.1.13 (continued) Histograms of percent offset and tablet area based on *SolidWorks* hexagonal model (a) Tablet Length (full dataset), (b) percent offset (outliers removed). Bin sizes were chosen based on Sturge's Rule [courtesy of T. Hall]

2.1.6 Idealized Voronoi layer

A Voronoi Tessellation (with the centers of the nucleation zones chosen as the scattered points), was used to evaluate the ideal pattern for homogeneous growth in all directions. In a Voronoi tessellation, we assume equal growth from the nucleation points. A line is drawn joining the nucleation points and the bisector of this line is constructed. This line creates the boundary of two neighboring tablets. This is repeated for all the nucleation points, until the full outline of the tablet is found (see figure 2.1.14).

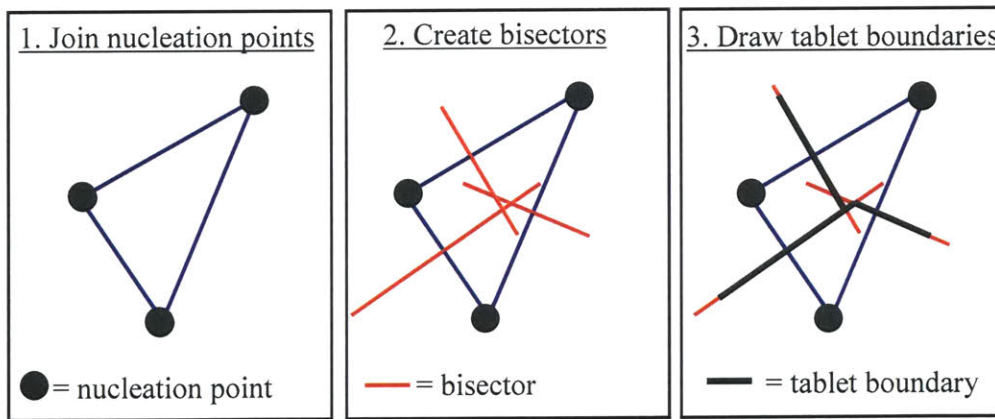


Figure 2.1.14 Schematic of Voronoi tessellation process. The illustration is shown for three nucleation points; the analysis is repeated for all nucleation points.

This Voronoi layer (shown in figure 2.1.15) is an idealized layer that can be used as a control when comparing the upper and lower layer of the *SolidWorks* model. The averaged tablet area for the Voronoi layer was $60.8 \pm 11.88 \mu\text{m}^2$ (normally distributed) and $n = 28$.

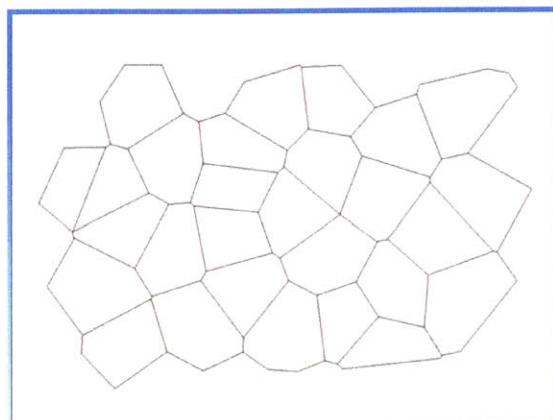


Figure 2.1.15 Top view of Voronoi Tessellation layer created in *SolidWorks* [courtesy of T. Hall]

In comparing the Voronoi Layer to the layers described in figure 2.1.8, it should be noted that there are less tablets in the Voronoi layer, since some of the nucleation zones fall outside the micrograph and thus, only relevant tablets are considered when comparing the models. The relevant tablets are those which have a common nucleation point with a complete Voronoi tablet (see schematic in figure 2.1.16). The Voronoi layer approximates both the nacre layers quite well (see figure 2.1.16), which suggests that there is not an in-plane directional bias for the rate of crystal growth.

The tablets appear to have no fixed orientation or shape in the plane but there is an almost constant offset (~20%), independent of direction in the plane, between corresponding layers. The Voronoi layer is an ideal layer that is used to check if there is a growth differential from layer to layer. This is examined by checking if a discrepancy exists between the tablet area of the Voronoi layer and the average tablet area of the upper and lower layers. The average tablet areas for both the upper and lower layers are

approximately equal to the average tablet area of the Voronoi layer and thus the data suggests that there is no growth bias.

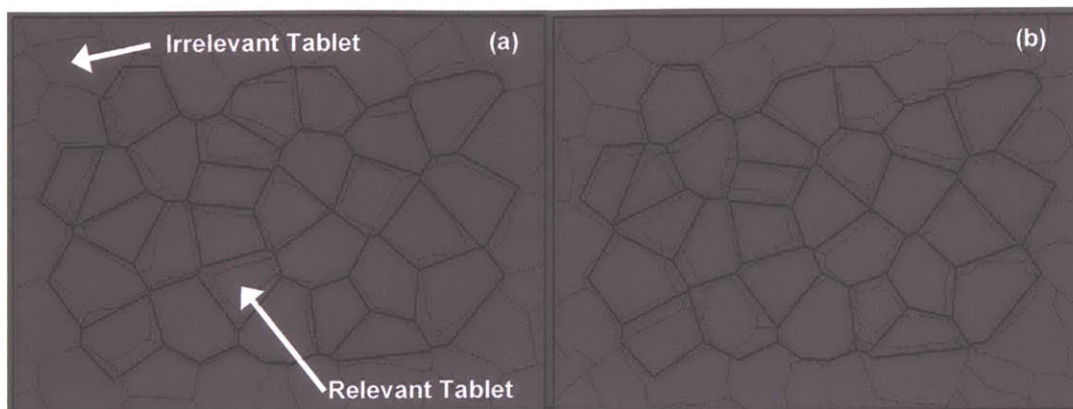


Figure 2.1.16 Top view of Voronoi Tesselation layer created in *SolidWorks* overlaid on (a) lower layer of ghost image tablets and (b) upper layer of ghost image tablets [courtesy of T. Hall]

2.1.7 Biological & mechanical significance of results

The tablet length was consistently found to be $\sim 6\text{-}9\mu\text{m}$ for the analysis performed. The lengthscale chosen by nature for these tablets results from a common design principle in biocomposite materials where the small lengthscales of the various ‘building blocks’ are employed to avert brittle behavior [see, for example, Wainwright et al, 1976; Lowenstam et al, 1989; Sarikaya et al, 1995]. This has previously been discussed in section 1.4.3.

Figure 2.1.7 reveals inter- and intra-tablet organic ligaments. It is already well documented that the inter-tablet organic ligaments play a significant role in the mechanical response of seashell nacre [see, for example, Jackson et al, 1988; Smith et al, 1999; Qi et al, 2006]. These SEM images confirm intra-tablet organic matrix, which likely plays a key mechanical role also.

In columnar nacre, the nacre tablets grow in vertical stacks with common nucleation zones between layers [see, for example, Wainwright et al, 1976; Lowenstam et al, 1989]. From the mechanical point of view of fracture, the ideal percent offset of tablets in neighboring layers would be 50%, as this would necessitate the largest tortuous path for

fracture. However, a 50% offset is not possible in columnar nacre, since tablets share nucleation sites as is evident in figure 2.1.7. Further, the ~20% offset may have a mechanical significance in terms of load transfer. A better understanding of inter-tablet behavior and the organic matrix will allow interpretation of the offset more fully.

2.2 Summary

This chapter reports the results and details of a study of the microscale geometric features of nacre from the species *Trochus Niloticus*. The key findings were as follows:

- Following sample preparation protocols developed in our group, several features of nacre were revealed: the ‘brick and mortar’ structure, the nucleation zones, the tablet boundaries and the sector boundaries.
- Tablet length is reported as $7.8 \pm 2.7 \mu\text{m}$ from measurements taken from the cross-sectional images. The *SolidWorks* model based on a *c*-plane image with a transparent top layer yielded a tablet area distribution with mean and standard deviation of $57.4 \pm 19.0 \mu\text{m}^2$ (with an equivalent average diameter of $8.5 \mu\text{m}$) and tablet lengths of $6.84 \pm 2.6 \mu\text{m}$ and $6.64 \pm 2.5 \mu\text{m}$ (one value each for horizontal and vertical cuts). This data correlates quite well with previously published data on *Trochus niloticus* by Bruet [Bruet et al, 2005], which reported tablet length as $\sim 8 \mu\text{m}$.
- The overlap was measured from a cross-sectional image and a *SolidWorks* model of two nacre layers to yield average values that were consistently between 20-22%. This value may have a mechanical significance, which will be investigated in future work.
- A Voronoi tessellation was performed based on the *c*-plane image with a transparent top layer used to create the *SolidWorks* model, using the nucleation points as the centers of tessellation. This layer was overlaid on the upper and lower layers from the *SolidWorks* model and matched both layers reasonably accurately, suggesting that there was no directional bias for the growth in-plane.

Chapter 3: *Nanoindentation study of single crystal aragonite*

Introduction

Aragonite, the orthorhombic form of CaCO_3 , is ubiquitous in nature both geologically and in biocomposites. A variety of investigations have been performed on aragonite and an overview is given here. However, there is a dearth of data on the mechanical behavior of aragonite, specifically, the plastic behavior of single crystal aragonite.

To this end, the nanoscale plastic behavior of single crystal aragonite was investigated using the technique of nanoindentation accompanied with Tapping Mode Atomic Force Microscopy (TMAFM) imaging. The investigation was performed using three indenter tips, Berkovich, cono-spherical and Knoop. The force vs. penetration depth response was recorded and the surfaces imaged after indentation using in-situ TMAFM. Three different faces of aragonite were indented to investigate any anisotropy in the mechanical behavior of the material as evidenced by different force-depth curves for different directions. The micrographs of the residual impressions were examined for any non-symmetric pile-up around the indenter attributable to the crystallographic structure of aragonite.

This chapter begins by discussing the role of aragonite in biological, geological and technological systems. An overview of previous investigations on aragonite is then given. A nanoindentation study, similar to the one performed on single crystal aragonite here, was performed on the *c*-plane of nacre aragonite tablets by our group [Brueet et al, 2005] and the key findings are summarized here. This is followed by a discussion of nanoindentation studies on crystalline materials. The results from each of the indenter tips: Berkovich, cono-spherical and Knoop are then presented. Finally, the Berkovich study is compared with the previous nanoindentation study on the *c*-plane of nacre tablets.

3.1 Aragonite: biologically, geologically and technologically

Aragonite (an orthorhombic form of calcium carbonate, CaCO_3) is commonly found in natural systems including both living organisms [see, for example, Lowenstam et al, 1989; Wainwright et al, 1976] and geological structures [Reeder et al, 1983].

Examples of the former include the nacre under investigation in this study, which is comprised of more than 95% aragonite [Wainwright et al, 1976; Lowenstam et al, 1989; Sarikaya et al, 1995]. Aragonite is also found in large dome shaped porous skeletal masses of certain coralline sponges, such as the *ceratoporella nichilsoni*, imaged in figure 3.1.1(a) [Hartman et al, 1970; Wainwright et al, 1976]. Nanometer to micrometer sized polycrystalline fibers of aragonite form the basic structural units of Scleratinian stony coral skeletons (see fig. 3.1.1. (b)) [Bryan et al, 1941; Lowenstam et al, 1989].

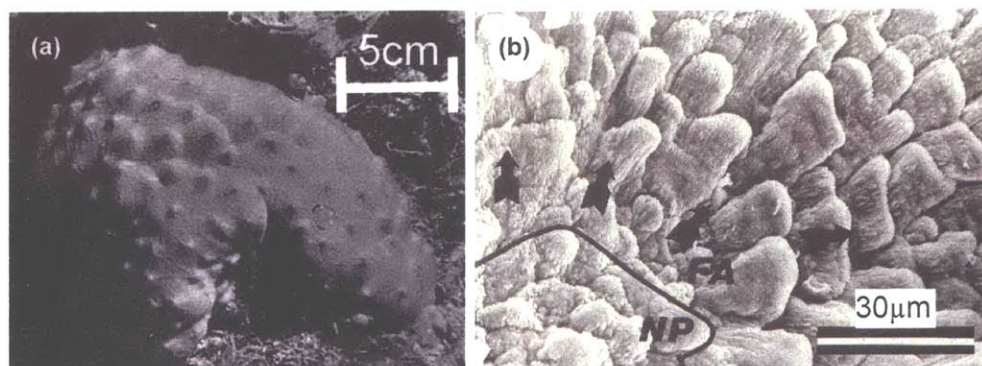


Figure 3.1.1 Examples of aragonite found in living organisms; (a) Underwater photograph of *Ceratoporella nichilsoni* [Hartman et al, 1970] and (b) SEM micrograph of *Acropora palmate* showing the aragonite fiber bundles [Lowenstam et al, 1989]

Geologically, aragonite is found in the uppermost part of the upper mantle [Ono et al, 2005] and recently, a hydrothermal vent field has been discovered consisting of large aragonite chimneys [Kelley et al, 2001].

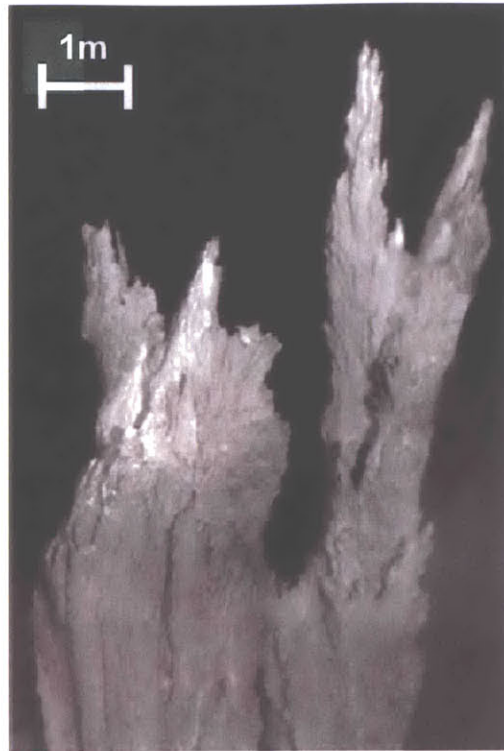


Figure 3.1.2 Geological example of aragonite; aragonite chimney from a recently discovered hydrothermal vent field [Kelley et al, 2001]

Aragonite is also providing opportunities in technological applications, including forms for bone grafting [Guillemin et al, 1987; Lucas et al, 2001; Yoshio et al, 2002]. Aragonite and aragonite based materials are an attractive material for bone grafting, given their biocompatibility and biodegradable capabilities [Guillemin et al, 1987; Lucas et al, 2001; Yoshio et al, 2002]. In vivo bone graft trials in dogs [Guillemin et al, 1987], sheep [Lucas et al, 2001] and rats [Yoshio et al, 2002] have been successfully conducted using corals (99% aragonite) [Guillemin et al, 1987], synthetic macroporous aragonite cylinders [Lucas et al, 2001] and a needle shaped aragonite powder [Yoshio et al, 2002].

3.2 Previous Investigations on aragonite

Since the identification of the orthorhombic crystal structure of aragonite (see figure 3.2.1) by Bragg in 1924 [Bragg, 1924] ongoing research has been performed on a range of aspects of this mineral.

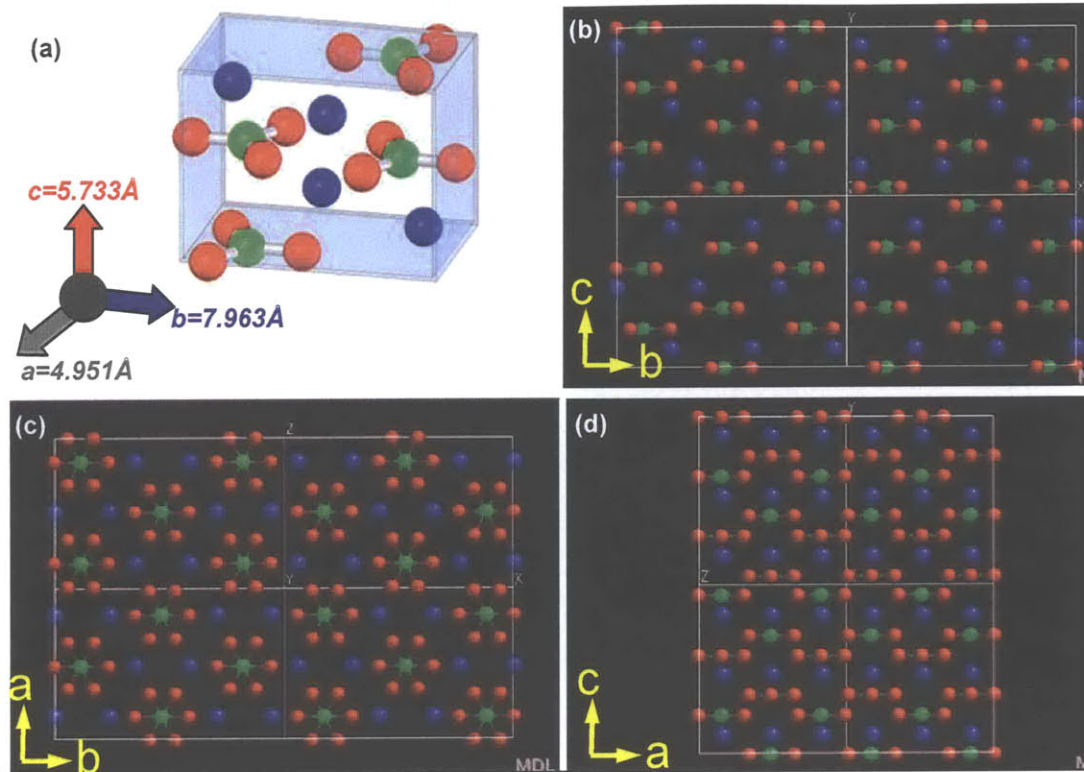


Figure 3.2.1 Aragonite crystal structure (a) orthorhombic unit cell with axes and their magnitudes as shown (b) crystal structure as viewed on the a -plane or (100) plane (c) crystal structure as viewed on the c -plane or (001) plane and (d) crystal structure as viewed on the b -plane or (010) plane. The red spheres represent oxygen (O) atoms, the green spheres represent the carbon atoms (C) and the blue atoms represent the calcium (Ca).

Bridgman [Bridgman, 1939] initiated the investigation of high pressure experiments which eventually identified the pressure and/or temperature induced calcite-to-aragonite transition and the development of the CaCO_3 phase diagram [Suito et al, 2001; Ivanov, 2002]. While this has implications for the formation of the earth's mantle, this phase change also occurs in biogenic crystals, induced by biomacromolecules [see, for example, Belcher et al, 1996; Falini et al, 1996; Thompson et al, 2000]. During biomineralization, crystals grow on nucleating protein sheets [see, for example, Lowenstam et al, 1989] and the switch between calcite and aragonite has been found to result from polyanionic proteins that control the crystal phase and morphology [see, for example, Belcher et al, 1996]. The charge distribution in aragonite was determined by minimizing the lattice energy by Yuen et. al [1978]. Optical and magnetic properties have been investigated by Hintze [see, Reeder et al, 1983]. Carbonate mineral dissolution and precipitation reactions have also been intensely investigated (for a review, see Reeder et. al, 1983).

Although the mechanical behavior of aragonite is a critical determinant of its many biological and geological functions, only a few reports exist in this area and a fundamental mechanistic understanding is lacking. The elastic constants have been relatively unexplored: the anisotropic elastic constants of aragonite were originally experimentally determined in 1910 [Voigt et al, 1910], using static bending and torsion experiments, and again only recently using Brillouin spectroscopy [Liu et al, 2005]. Given the orthorhombic structure of aragonite, 9 elastic constants are needed to describe the elastic behavior and these are reported in Table 3.2.1. The linear compressibilities (β_x) for the three crystallographic axes ($x = a, b, c$) were derived from the measured data. The aggregate Bulk modulus (K) and aggregate shear modulus (G) were calculated from the appropriate averaging of the anisotropic properties [Voigt, 1910; Liu et al, 2005].

| | Voigt [Gpa] | Liu et al [GPa] | | Voigt [Gpa] | Liu et al [GPa] |
|----------|----------------|--------------------|-----------|-------------------------------|-------------------------------|
| C_{11} | 159.6 | 171.1 | K | 46.9 | 68.9 |
| C_{22} | 87.0 | 110.1 | G | 38.5 | 35.8 |
| C_{33} | 85.0 | 98.4 | | | |
| C_{44} | 41.3 | 39.3 | | Voigt | Liu et al |
| C_{55} | 25.6 | 24.2 | | $[x10^{-3} \text{ GPa}^{-1}]$ | $[x10^{-3} \text{ GPa}^{-1}]$ |
| C_{66} | 42.7 | 40.2 | β_a | 4.3 | 3.0 |
| C_{12} | 36.6 | 60.3 | β_b | 7.8 | 4.6 |
| C_{13} | 2.0 | 27.8 | β_c | 10.2 | 7.3 |
| C_{23} | 15.9 | 41.9 | | | |

Table 3.2.1 Experimental reports of the elastic constants of aragonite, including the 9 stiffness matrix constants, the aggregate shear and bulk moduli and the linear compressibilities along each of the orthorhombic axes as reported by Voigt et al. [1910] and Liu et al. [2005]

Little is known about the plastic deformation of aragonite. The plastic deformation plays a governing role in the flow and formation of rocks and has been investigated in other geological minerals, including calcite [Schmid et al, 19; Wenk et al, 1986; Carter et al, 1976] (the rhombohedral form of CaCO_3) and olivine [Carter et al, 1976], which, like aragonite, has an orthorhombic structure. These reports are discussed in further detail in section 3.5. A more limited investigation into the plastic flow of polycrystalline and in some cases, porous, aragonite at high temperatures and pressures, has been conducted [Renner et al, 1996; Rybacki et al, 2003], although, no specific data exists to identify the plasticity of single crystal aragonite. For porous aragonite, it was found that the inelastic response was strongly dependent on confining pressure (tests were conducted up to confining pressures of 195MPa) and porosity (ranging from 5-25%) and that particle size (average grain size 5 to 400 μm) also had a minor effect [Renner et al, 1996]. Further, there was a transition from localized brittle failure to non-localized cataclastic flow with increasing confining pressure, porosity and particle size [Renner et al, 1996]. (010) cleavage fractures were recorded and kink-band orientations (under microscopy) suggested dislocation glide on the (010)[100] (previously reported by [Veit, 1922]) and (001)[010] systems [Renner et al, 1996]. High temperature (ranging from 600-900°C) and pressure (1.6-2.8 GPa) experiments, with superposed compression along one axis, on polycrystalline aragonite identified (001) as the predominant glide plane using microscopy [Rybacki et al, 2003]. The mechanical and microstructural data indicate dislocation creep as the dominant mechanism for this regime, with a power law flow law capturing the experimental data [Rybacki et al, 2003].

A single paper on the Knoop microhardness of aragonite at room temperature, measured by Han, [Han et al, 1991], records the anisotropy between the (100), (010) and (001) planes, the in plane anisotropy of the (100) and (010) plane and the approximately isotropic microhardness in the (001) plane (see figure 3.2.2). The (100) plane is the stiffest plane, suggesting that this might be the hardest crystal plane. However, the Han report shows this is not the case, reporting the *c*-plane (or (001)) as the hardest plane [Han et al, 1991]. As is evident in the graphs in figure 3.2.2, there is an indentation load/size effect, which the author addresses through the application of Meyer's law ($P =$

Ad^n : with P , the indentation test load; d , the indentation size and A and n Meyer's law parameters) [Han et al, 1991]. Application of this law yields load independent hardness values between 130 – 280 kg/mm² [Han et al, 1991].

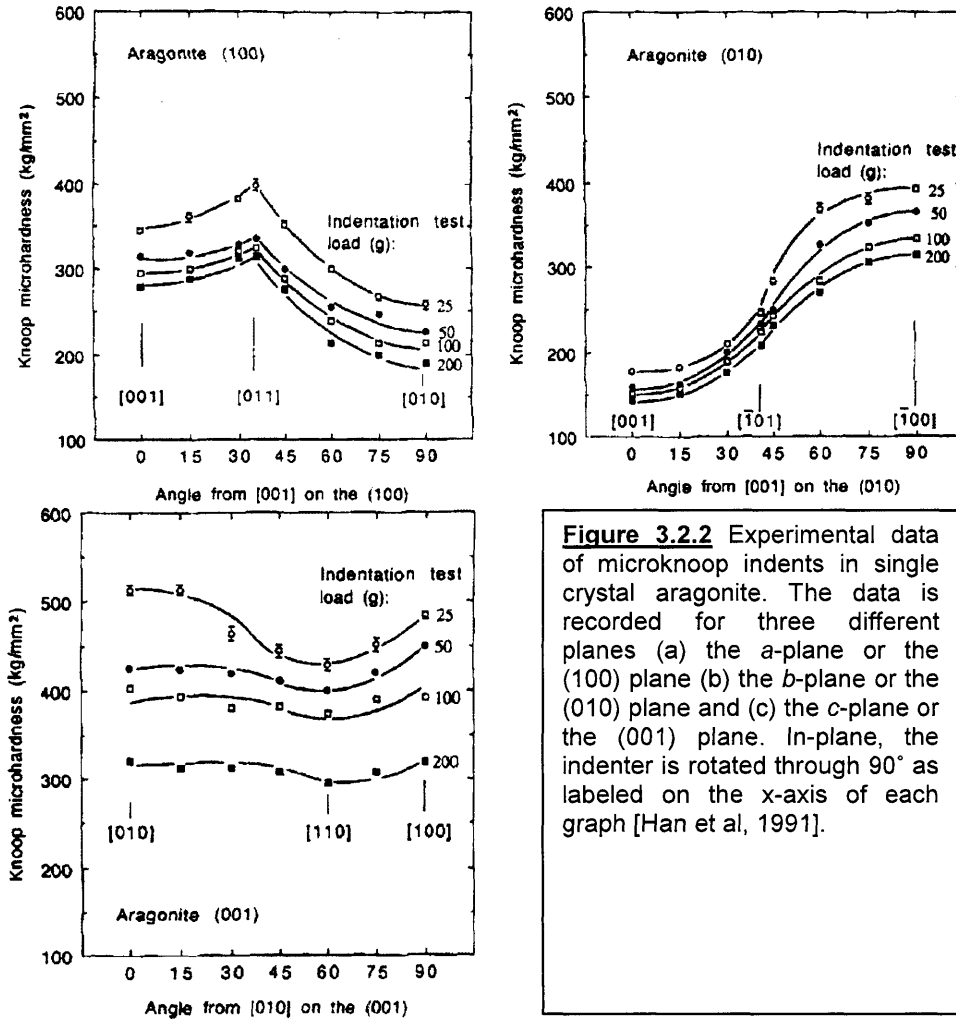


Figure 3.2.2 Experimental data of microknoop indents in single crystal aragonite. The data is recorded for three different planes (a) the a -plane or the (100) plane (b) the b -plane or the (010) plane and (c) the c -plane or the (001) plane. In-plane, the indenter is rotated through 90° as labeled on the x-axis of each graph [Han et al, 1991].

3.3 Nanoindentation study on c -plane of nacre aragonite tablets

A previous study in our group investigated the response of *Trochus niloticus* nacre tablets under nanoindentation on the c -plane [Bruet et al, 2005]. Nacre was cleaved in compression to expose the top face (c -plane) of the nacre tablets and nanoindentation was performed using a Berkovich indenter (see figure 3.3.1). Samples were tested ‘freshly

cleaved' (tested within 1 hr of cleaving) and 'wet' (soaked in artificial seawater for 10 weeks prior to cleaving and testing) [Bruet et al, 2005].

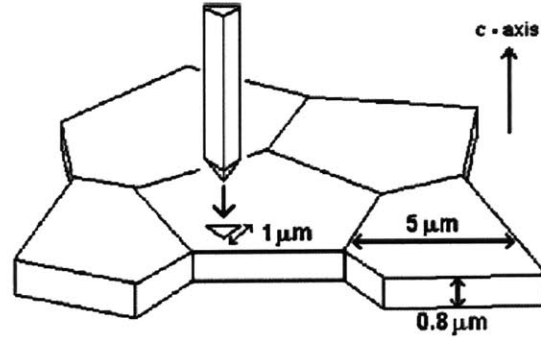


Figure 3.3.1 Schematic of nanoindentation on *c*-plane of nacre aragonite tablets. Indents were performed with a Berkovich indenter parallel to the *c*-axis of the crystal on the top face of the tablets (*c*-plane) [Bruet et al, 2005]

Indentations were performed in both the freshly cleaved and artificial seawater soaked nacre up to maximum loads of 50, 100, 250, 500, 750 and 1000 μN at load-unload rates of 10 $\mu\text{N/s}$ (the curves for maximum loads of 500, 750 and 1000 μN are shown in figure 3.3.2) [Bruet et al, 2005]. An Oliver-Pharr (O-P) [Oliver et al, 2004] reduction of this data gave elastic moduli of 114-143 GPa (depending on maximum load) for freshly cleaved nacre and 101-126 GPa for artificial seawater soaked nacre [Bruet et al, 2005]. Average O-P hardness values of 9.7 – 11.4 GPa for freshly cleaved nacre and 3.6-8.7 GPa for artificial seawater soaked nacre are also reported [Bruet et al, 2005]. Qualitatively, these findings are consistent with other authors who have found 'wet' nacre to have a lower elastic modulus and strength than 'dry' nacre (refer to section 1.4.3) [Jackson et al, 1988].

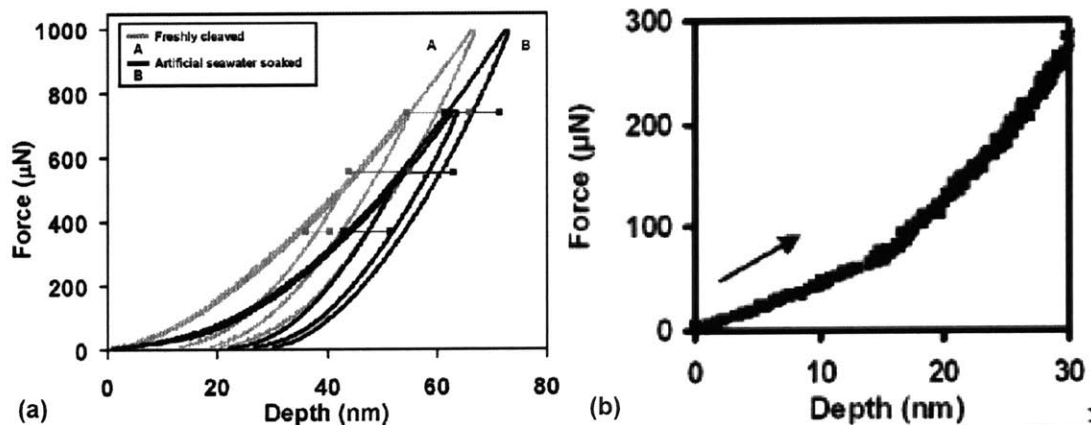


Figure 3.3.2 Force vs. penetration data for the *c*-plane of nacre tablets using Berkovich indenter (a) averaged load-unload nanoindentation data for freshly cleaved and artificially seawater soaked nacre ($n = 15$, maximum loads of 500 μN , 750 μN and 1000 μN , load-unload rate = 10 $\mu\text{N/s}$). Horizontal error bars indicate the standard deviation for that particular dataset. (b) Individual loading curve from 300 μN dataset, showing a distinct change in slope. [Bruet et al, 2005]

Figure 3.3.2 shows an individual curve for freshly cleaved nacre from the 1000 μ N dataset, which shows a marked change in slope [Bruet et al, 2005]. This slope change is reported as consistently lying between 7-15 nm depth [Bruet et al, 2005]. The TMAFM images shown in figure 3.3.3 show nanoasperities on the indented *c*-plane of nacre, which are believed to be responsible for the observed slope change [Bruet et al, 200]. High resolution atomic force microscopy imaging was used in the reported study to measure the peak-to-valley height of these nanoasperities and it is reported as 7.4 ± 3.2 nm, which is consistent with the depth at which the slope change occurs [Bruet et al, 2005].

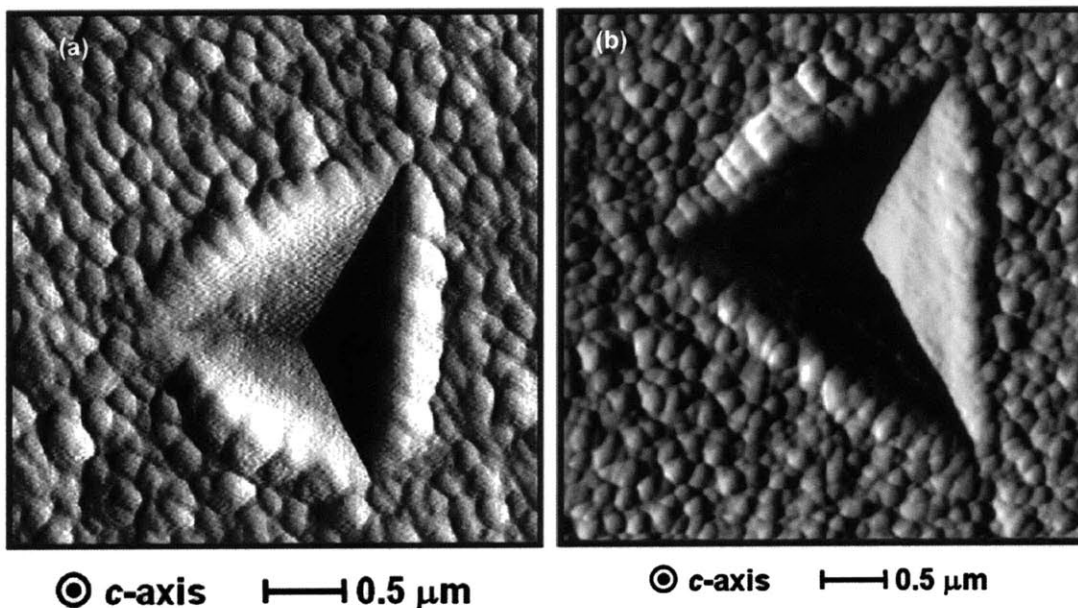


Figure 3.3.3 Tapping mode atomic force microscopy amplitude image after nanoindentation in freshly cleaved nacre (a) maximum load 5000 μ N and (b) maximum load 10000 μ N [Bruet et al, 2005].

TMAFM microscopy imaging of the indents showed a distinct residual indent with pile-up surrounding all three sides of the indenter (see figure 3.3.3) [Bruet et al, 2005]. No microcracks were observed in the indented region or surrounding the indenter [Bruet et al, 2005]. For the 5000 μ N indent the pileup region was stretched \sim 800 nm from the center of the indent and for the 10000 μ N indent the pileup zone stretched \sim 1200 nm away from the center of the indent [Bruet et al, 2005].

Finite Element Simulations were employed in the study to examine elastic-plastic mechanical response of the nacre tablets [Bruet et al, 2006]. An isotropic elastic-plastic

model was used to fit the experimental curves giving a Young's modulus, E , of 92 GPa and a very high yield stress, σ_y , of 11 GPa for freshly cleaved nacre ($E = 79$ GPa and $\sigma_y = 9$ GPa for artificial seawater soaked nacre). No microcracking was observed for residual indents and thus, the tablet is able to withstand very high stresses before deformation/failure [Bruet et al, 2006].

A distinct change in slope is seen in the loading curve (see earlier figure 3.3.2), which results from the heteronanostructured nature of the material. In order to more fully understand the behavior of the aragonite tablets, nacre's ultrastructure and the role of the organic material within the tablet, it is necessary to isolate the inorganic component, aragonite, so that a better understanding of its role in nacre can be interpreted.

3.4 Nanoindentation in crystalline materials

Force vs. penetration curves depicting distinct load plateaus have been observed by numerous authors during nanoindentation of a variety of materials including metals, semiconductors and oxides [see, for example, Gerberich et al, 1996; van Vliet et al, 2003; Zhu et al, 2004]. In crystalline materials, the load plateaus have been identified to correlate with dislocation nucleation at a certain depth beneath the nanoindenter, where various constitutive criteria have been used to quantify this phenomenon [Gerberich et al, 1996; van Vliet et al, 2003].

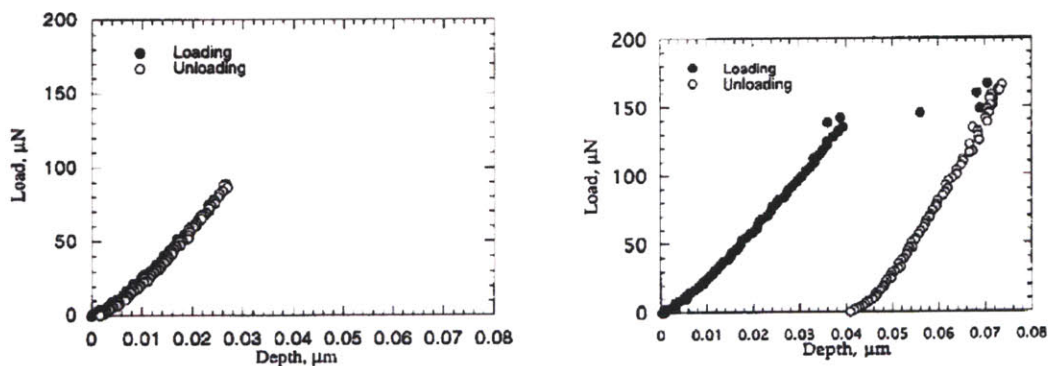


Figure 3.4.1 Load-unload data for load controlled nanoindentation on the (100) plane of a Fe-3wt%Si surface with a diamond tip with radius of curvature 66nm (a) Load vs. depth data for loading in the elastic regime (b) load vs. depth data for loading past the initial yield point, showing a large displacement discontinuity at 150μN [Gerberich et al, 1996]

Gerberich et al [1996] developed a model for the onset of yielding consistent with Rice's unstable stacking energy concept and mean free path considerations, where dislocations are generated due to indentation. Hertzian contact stresses (including a factor for tip geometry) were employed and for nucleation to occur, the resolved shear stress on a slip plane must reach the critical resolved shear stress on that plane [Gerberich et al, 1996]. The reader is referred to Gerberich et al [1996] for the details of the derivation. The calculated values successfully matched experimental data for GaAs and Fe-3wt%Si [Gerberich et al, 1996]. The elastic-plastic transition under nanoindentation was also investigated experimentally: Fe-3wt%Si single crystals were loaded to below the first displacement discontinuity and behaved elastically with no residual indent or pileup visible with AFM imaging (see figure 3.4.1(a), the AFM image is not included here, but it shows no evidence of a residual indent). When Fe-3wt%Si single crystals were loaded just past the first dislocation discontinuity (see figure 3.4.1 (b)), a residual indent with surrounding pileup, confirmed by cross-section profile, was clearly evident (see figure 3.4.2) [Gerberich et al, 1996].

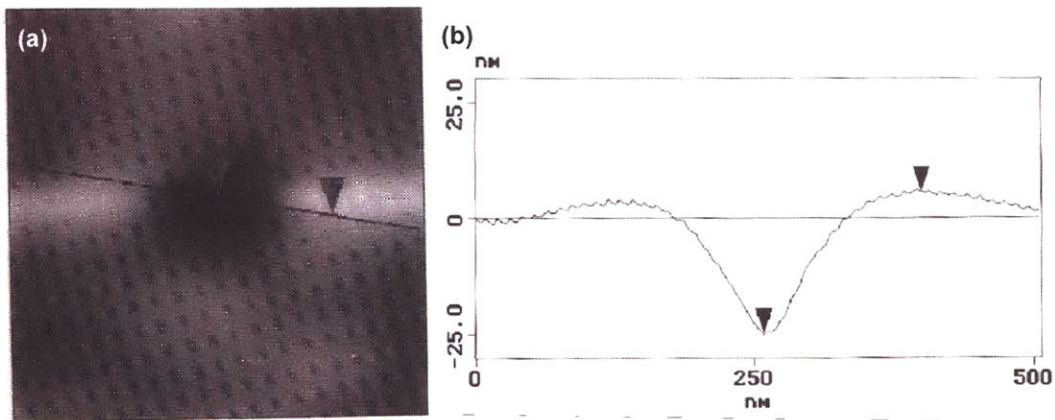


Figure 3.4.2 AFM imaging residual indent in Fe-3wt%Si (a) AFM height image showing residual indent and pile up (b) cross-section line profile, confirming the residual indent and surrounding pileup. No scale bar is given for the AFM image but from the cross-section line profile, the AFM image is inferred to be ~500nm. [Gerberich et al, 1996]

Van Vliet et al, also uses Hertzian contact stresses, to show that the first displacement discontinuity occurs when the Hertzian maximum shear stress is on the order of the theoretical shear strength of the crystal and extends the work of Hill and Rice on

continuum formulations of elastic stability to the atomic scale [Van Vliet et al, 2003]. Their model is implemented in both finite element simulations and molecular dynamic simulations and calibrated against nanoindentation data and a bubble raft model (a two-dimensional experimental analogue to a crystal, which they subject to indentation with a geometrically proportional indenter) to model the onset of dislocation nucleation and the early stages of plasticity [Van Vliet et al, 2003].

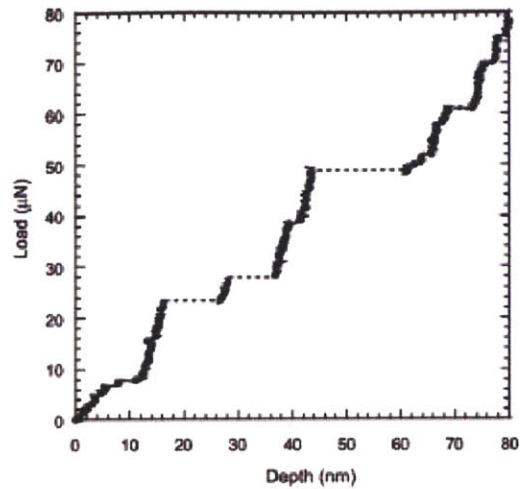


Figure 3.4.3 Force vs. depth curves for nanoindentation (load controlled) of (110) Al with an indenter tip radius 150nm showing distinct force plateaus [Van Vliet et al, 2003]

Page [Page et al, 1992] investigated the nanoindentation response in ceramic single crystals (Al_2O_3 , Si, SiC). In Al_2O_3 (sapphire) distinct load plateaus were seen in curves loaded above ~ 80 nm (see figure 3.4.4(a)) [Page et al, 1992]. SEM imaging of the sapphire indents showed residual impressions for all indents with curves that had a

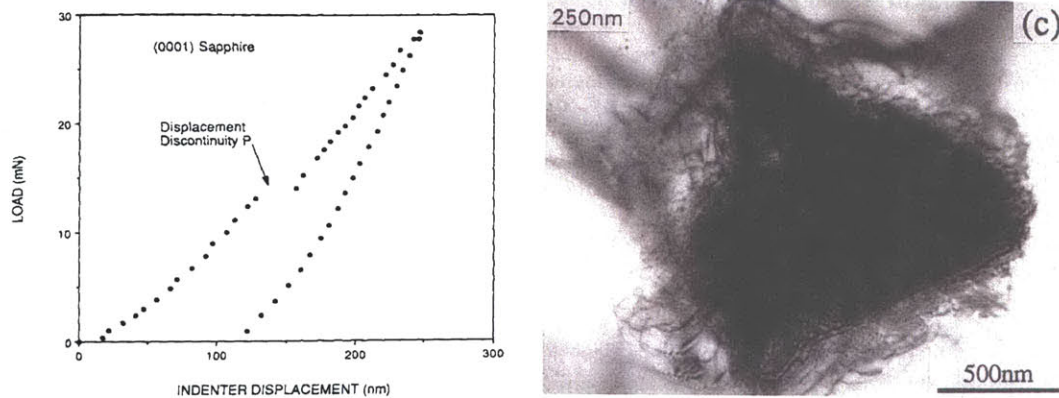


Figure 3.4.4 (a) Load v's displacement response for indentation in Sapphire using a Berkovich indenter. (b) TEM image showing intense dislocation activity around indent, with no evidence of microcracking. 250 nm is the maximum depth upon loading and 500 nm is the scale bar [Page et al, 1992]

displacement discontinuity [Page et al, 1992]. Transmission electron microscopy (TEM) analysis showed extensive dislocation activity surrounding the residual indent for Al_2O_3 (see figure 3.4.4(b)), where load plateaus were seen in the curves at lower indentation depths. When the Al_2O_3 was loaded to values below the first load plateau and the curve was fully elastic, the authors report that no dislocations were seen under extensive microscopy [Page et al, 1992].

For Silicon (Si), the load vs. penetration response showed a load plateau on the unloading portion of the curve and TEM analysis suggested that a densification transformation was occurring underneath the indenter due to the high hydrostatic pressure [Page et al, 1992]. It is presumed that the force plateau in the unload curve is attributable to a relaxation of the densified material [Page et al, 1992]. At higher loads, dislocation activity surrounding the indenter was also seen under TEM [Page et al, 1992].

For SiC, the load vs. displacement curves had the same load-unload response as that for sapphire [Page et al, 1992]. TEM samples were unsuccessful. However, it is believed that the response as with the sapphire is attributable to dislocation nucleation [Page et al, 1992]. The mechanism of densification transformation as being the cause of the displacement discontinuity for SiC was disproved as the loads at which the displacement discontinuities occur correspond to the ideal strength of the material [Page et al, 1992].

3.5 Investigation of plasticity in similar materials

Although there has been a very limited investigation into plasticity in aragonite, similar materials have been intensely investigated, namely calcite, the Hexagonal form of CaCO_3 and olivine, which like aragonite has an orthorhombic structure. For calcite, the most dominant slip mechanism is found to be mechanical twinning and intracrystalline slip [Wenk et al, 1987; Carter, 1976; Schmid et al, 1987]. Twin gliding results from a narrow twin lamella forming (as a result of localized yielding) between two twin lamellae boundaries and this lamella increases in width [Buerger et al, 1945]. A series of these twin lamellae develop, resulting in macroscopic yield [Buerger et al, 1945].

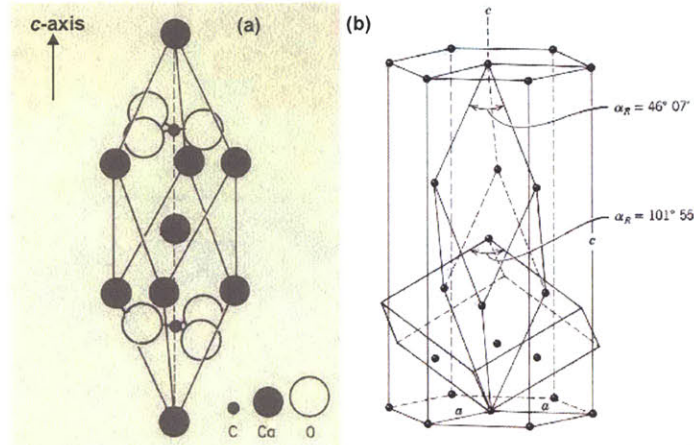


Figure 3.5.1 The calcite unit cell, in its two forms (a) rhombohedral unit cell, with the atoms positioned as labeled (b) hexagonal prism unit cell (only Ca atoms are shown) with the rhombohedral unit cell and the cleavage rhombohedron also drawn. The c-axis and two of the in plane a-axes are shown (with the third a-axes being in plane and at an angle of 120° to the two a-axes shown) [home.hetnet.nl/~turing/preparation_3dim_4.html]

Raleigh [Raleigh; 1968] performed axial compression on olivine under confining pressures of 5 kbar. The deformed specimens and the slip bands, deformation lamellas and kink bands were examined using microscopy. At temperatures below 1000°C the observed slip systems were {110}[001], (100)[001], and (100)[010] [Raleigh, 1968]. At 1000°C slip on, and pencil glide in, the [100] direction dominate in addition to the {110}[001] system and with decreasing strain rate, slip on {0kl}[001] dominates [Raleigh, 1968].

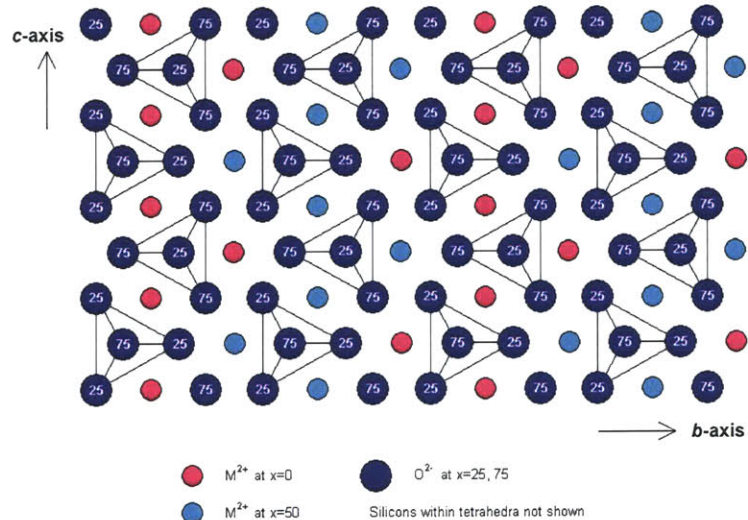


Figure 3.5.2. Illustration of the olivine orthorhombic unit cell. The b-axis and c-axis are as shown and the a-axis is out of the page. The illustration gives x-values for the distance (as a percent of the a-axis) of the atoms along the a-axis of the unit cell [http://www.doitpoms.ac.uk/tlplib/anisotropy/diffusion.php]

3.6 Nanoindentation investigation of single crystal aragonite

3.6.1 Experimental Setup

Sample Preparation: Natural single crystal aragonite was purchased from *Ward's Natural Science (Rochester, NY USA)*. A diamond impregnated annular wafering saw (*Buehler, Isomet 5000*), running at 850-950 rpm, was used to isolate single crystals. From these single crystals, three sliced sections, mutually orthogonal, with one section perpendicular to the *c-axis* were cut. These samples were then polished using a polishing wheel (*South Bay Technology Inc., San Clemente, CA USA, Model 920, Lapping & Polishing wheel*). A *Buehler (Lake Bluff, IL USA) Apex Diamond Grinding disk* was used for a 60 second period (at 10-15 rpm) to remove the coarse surface roughness resulting from the diamond cutting wheel. Following this, a *Buehler Ultrapad* was used with *Metadi Diamond suspensions* of 15 μm , 6 μm and 1 μm (300 s, at 10-15 rpm) in successive steps. The final polishing step was performed using a *Buehler microcloth* and colloidal silica suspension (600 seconds, 10 rpm). After this final step, the sample was sonicated using an *Ultramet ultrasonic cleaner (Pacoima, CA USA, ~ 60 seconds)*. The crystallographic orientation of the sample was determined using *Laue X-ray diffraction* with a *Bruker 2D Single Crystal Diffractometer (Madison, WI USA)*.

Nanoindentation: A *Hysitron Inc. (Minneapolis, MN USA) Triboindenter*, which had a TMAFM attached (*Quesant Q-Scope, Santa Cruz, CA USA*) enabling imaging of residual indents, was used to perform the nanoindentation experiments. Open loop, load controlled experiments were performed using a Berkovich tip and a (ideally) $<1 \mu\text{m}$, 60° cono-spherical tip. The piezoelectric crystal was allowed to settle for 30 seconds prior to indentation, which includes a 10 second period in digital feedback. The software automatically accounts for the drift rate of the transducer before initiation of the indent. The load function consisted of five segments. The first segment at zero force for five seconds allowed for tip sample equilibration. The second segment consisted of a ramp in load, 50 $\mu\text{N/s}$ for the lower loads (500 μN and 1000 μN) and 1000 $\mu\text{N/s}$ for the upper loads (5000 μN and 10000 μN), up to the maximum load. The load was then held at its

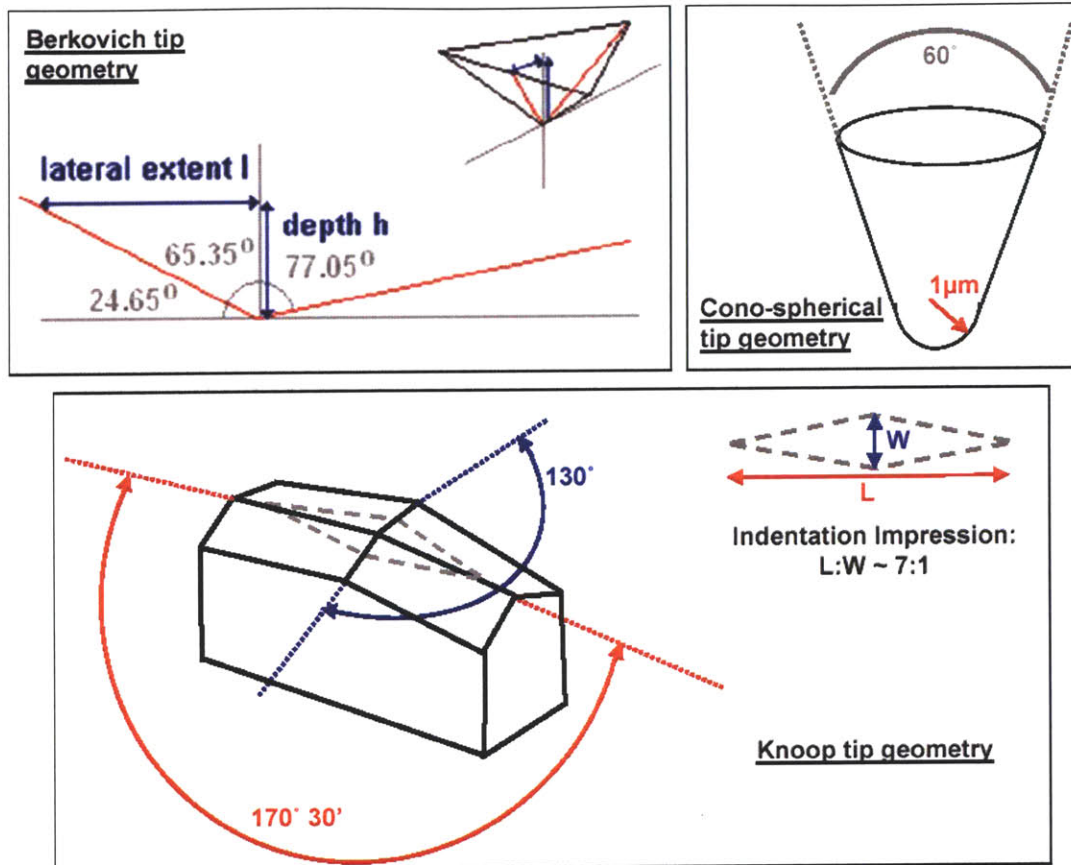


Figure 3.6.1 Indenter tip geometries of three indenters used (a) Berkovich tip (b) 1 μ m, 60° cono-spherical tip and (c) Knoop tip

maximum value for a period of 5 seconds. An equivalent unloading rate to that of segment two was used to reduce the load back to zero. The fifth section of the load function consisted of a further hold at zero load for 10 seconds. Twenty experiments per load-tip combination were performed, with the lower load (500 μ N and 1000 μ N) indents spaced 5 μ m apart and the higher load (5000 μ N and 10000 μ N) indents spaced 15 μ m apart. Load versus penetration depth curves were obtained and each load-tip set combination was averaged and standard deviations calculated and reported. Calibrations were performed prior to each experiment using a fused quartz sample to find the probe tip area function ($A(h_c)$) and frame compliance. $A(h_c)$ is the projected area of the tip under load and is calculated from a 6th order polynomial fit accounting for non-ideal tip geometry as a function of the contact depth, h_c .

Tapping mode atomic force microscopy (TMAFM): TMAFM was employed to obtain in-situ topographical images of the residual indents in ambient conditions. This was performed using a *Quesant Q-Scope 350* (attached to the *Hysitron Inc. Triboindenter, Minneapolis, MN USA*) with a piezoelectric tube scanning element (X-Y scan range ~ 40 μm , vertical Z range ± 4.5 μm) and Si_3N_4 Wavemode NSC16 cantilevers (rectangular shaped with conical probe tip geometry, $l \sim 230$ μm , width ~ 40 μm , cone angle $< 20^\circ$, probe tip height $\sim 15\text{-}20$ μm , resonance frequency ~ 165 Hz, spring constant, $k \sim 40$ N/m, and end radius, $R_{\text{tip}} \sim 10$ nm). A scan rate of 1 Hz was used to raster 4-6 μm scans at a resolution of 512×512 pixels. The drive amplitude and amplitude set-point (~ 0.25 V) as well as the gains (~ 300) were optimized prior to imaging.

Rotation Stage: A *Thorlabs RPO1/M* rotation stage was employed to rotate the sample within the *Hysitron Triboindenter* to enable indentation at various in-plane orientations of the single crystal. The rotation stage is fitted with a dial, which measures the angle in increments of 2° . A magnet was attached to the rotation stage, which is then used to place and hold the stage within the nanoindenter. The sample holder is fixed to the rotation stage using an adhesive.

3.6.2 Nanoindentation Results for Berkovich indenter: Force vs. penetration depth curves

Berkovich indentations were performed on three mutually orthogonal planes of single crystal aragonite, where one plane is perpendicular to the orthorhombic crystal c -axis, (001) and the two other planes are perpendicular to the (001) plane, namely, $(\bar{1}10)$ and $(\bar{1}\bar{3}0)$. The averaged nanoindentation data (force vs. penetration depth for $n = 20$ experiments per set) for the three planes is graphed in figure 3.6.2. Plots containing all individual curves are given in Appendix B. The curves shown are for maximum loads of $500\mu\text{N}$ and $1000\mu\text{N}$ performed at a loading rate of $50\mu\text{N/s}$.

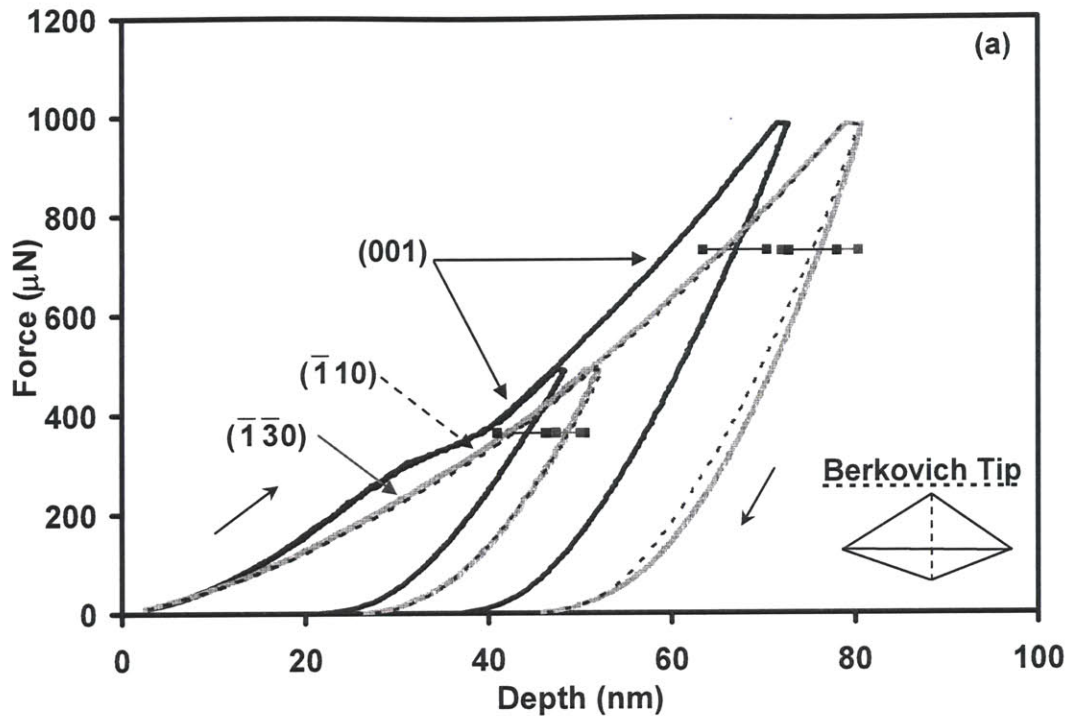


Figure 3.6.2 Nanoindentation data for single crystal aragonite using a Berkovich probe tip. Averaged curves on loading and unloading at maximum loads of 500 μN (number of experiments, $n = 20$, 5 μm spacing in both the X- and Y- direction between each indent) and 1000 μN ($n = 20$, 5 μm spacing in both the X- and Y- direction between each indent) at a loading rate of 50 $\mu\text{N/s}$. The horizontal error bars indicate the maximum standard deviation of the curves for that particular dataset. Data with loading direction perpendicular to the (001), ($\bar{1}10$) and the ($\bar{1}\bar{3}0$) planes are shown. Arrows indicate the direction of loading.

Comparison of the force-depth curves for the three planes reveals an anisotropic nanomechanical response. The very early portion of the curve (0-15nm) suggests a similarity in the elastic response of the three planes (see figure 3.6.3). The depth of the residual impression for planes ($\bar{1}10$)

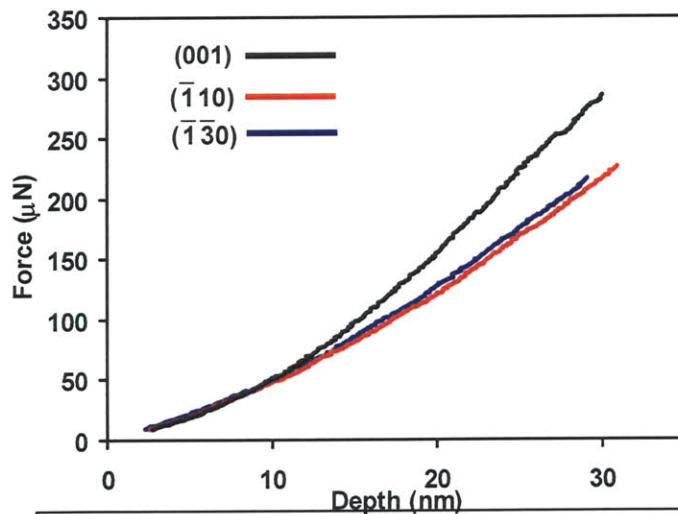


Figure 3.6.3 Early portion of loading curve for 500 μN Berkovich indents shown in figure 3.6.1 (averaged curves from $n=20$ indents, loading rate 50 $\mu\text{N/s}$)

and $(\bar{1}\bar{3}0)$ suggest a lower hardness for these two planes (see figure 3.6.2). An Oliver-Pharr (O-P) [Oliver et al, 2004] reduction of these data¹ for a maximum load of 1000 μN gives (modulus, hardness) pairs of $(102.8 \pm 2.4 \text{ GPa}, 6.2 \pm 0.3 \text{ GPa})$, $(100.1 \pm 3.4 \text{ GPa}, 4.6 \pm 0.3 \text{ GPa})$ and $(108.1 \pm 2.3 \text{ GPa}, 4.36 \pm 0.4 \text{ GPa})$ and for the (001), $(\bar{1}10)$ and $(\bar{1}\bar{3}0)$ planes respectively. Unpaired student t-tests were carried out to evaluate the statistical differences between the datasets, using $p < 0.05$ as the minimum criterion and these confirmed that both the elastic modulus and hardness were statistically different for each plane. Given the close agreement in the moduli values ($<7\%$ variation) the anisotropy of the yield stress is self evident. The anisotropy in the yield stress/hardness indicates that the $(\bar{1}10)$ and $(\bar{1}\bar{3}0)$ planes yield at lower values. Thus, the deviation of the $(\bar{1}10)$ and $(\bar{1}\bar{3}0)$ loading curves from the (001) loading curve at low loads (see figure 3.6.3) may result from yielding occurring at lower values for the $(\bar{1}10)$ and $(\bar{1}\bar{3}0)$ planes (i.e. a plastic response) and is not a result of a higher stiffness of these planes, as confirmed by the O-P analysis. Plastic anisotropy is expected to result from activating slip on specific slip systems which depend on the indentation direction, thus it is believed that the $(\bar{1}10)$ and $(\bar{1}\bar{3}0)$ planes have more favorable orientations for slip activation at lower indentation loads.

The (001) plane indents show a noticeable change in slope in the averaged force-depth curves at forces of ~ 314 and $386 \mu\text{N}$, a phenomenon which is not observed on the orthogonal planes (see figure 3.6.2). The origin of this slope change is seen when examining typical individual load-unload curves which display distinct load plateaus (see figure 3.6.4). The inset histogram quantifies the distribution in observed load plateau ($309.0 \pm 27.6 \mu\text{N}$). Section 3.4 discusses nanoindentation in crystalline materials, including a selection of reports depicting distinct load plateaus suggesting discrete events [Gerberich et al, 1996; Van Vliet et al, 2003; Page et al, 1992]. As with the findings of other authors, who have applied various constitutive stability criteria to quantify this event in crystalline materials [Gerberich et al, 1996; Van Vliet et al, 2003], this behavior

¹The indentation (modulus, hardness) pairs estimated here by the Oliver-Pharr [Oliver et al, 2004] method should be regarded as "apparent" or "effective" since this model is isotropic.

is attributed to the onset of dislocation nucleation. This hypothesis is supported by previous work [Page et al, 1992] which shows extensive dislocation activity in ceramic single crystals (Al_2O_3) after nanoindentation by transmission electron microscopy (see figure 3.4.4).

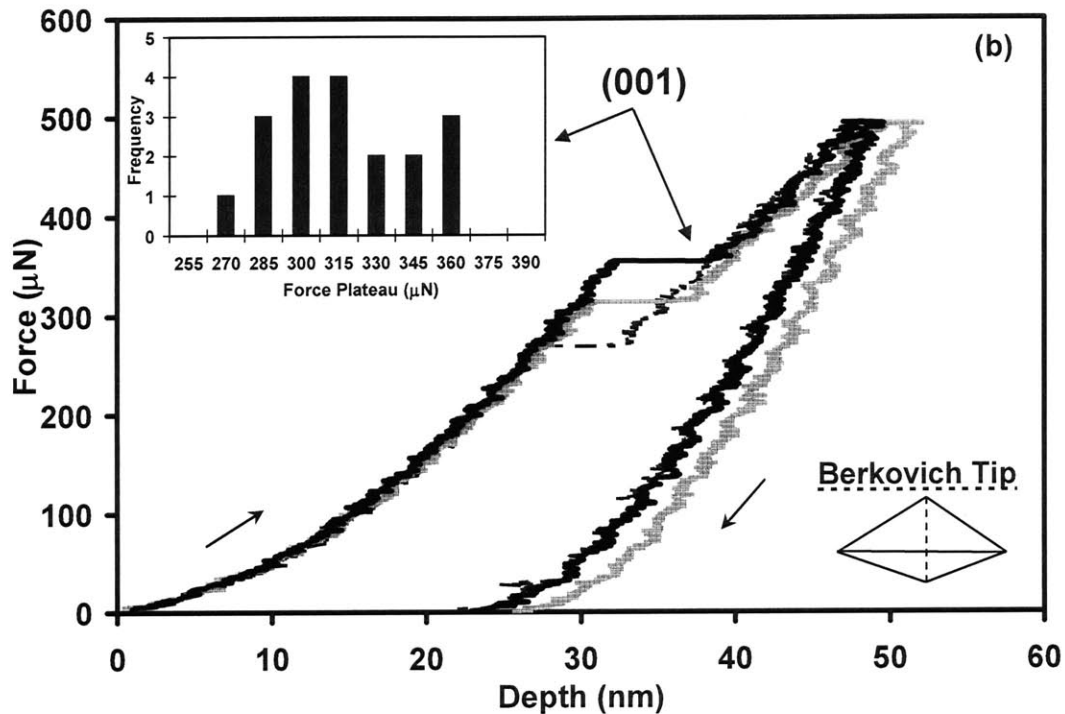


Figure 3.6.4 Three individual loading-unloading curves from the dataset shown in figure 3.6.1 for indents into the (001) plane.

3.6.3 Nanoindentation Results for Berkovich indenter: Tapping mode atomic force microscopy of residual indents on the (001) plane

TMAFM was used to image of residual indents on the (001) plane after unloading from larger maximum indentation loads of 5 mN and 10 mN for the Berkovich tip. Averaged load vs. unload curves for the 5 mN and 10 mN indents ($n=20$ for both datasets, load-unload rate = $1000\mu\text{N/s}$) on the (001) plane are shown in figure 3.6.5 (a).

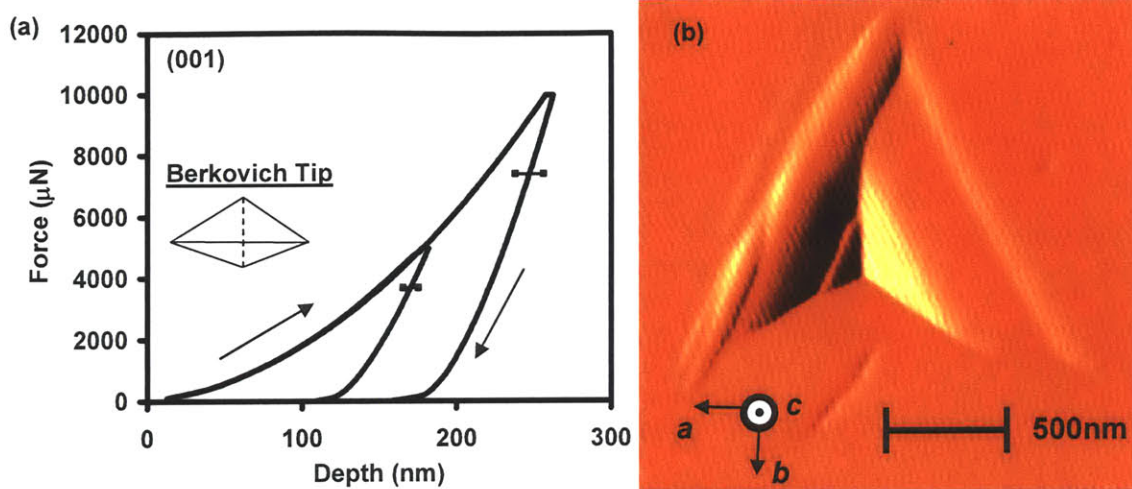


Figure 3.6.5 Higher load nanoindentation on (001) plane of single crystal aragonite (a) Nanoindentation data for single crystal aragonite using a Berkovich probe tip. Averaged curves on loading and unloading at maximum loads of 5000 μN (number of experiments, $n = 20$, 10 μm spacing in both the X- and Y- direction between each indent) and 10000 μN ($n = 20$, 15 μm spacing in both the X- and Y- direction between each indent) at a loading rate of 1000 $\mu\text{N/s}$. The horizontal error bars indicate the maximum standard deviation of the curves for that particular dataset. Arrows indicate the direction of loading. (b) TMAFM amplitude image of residual indent after nanoindentation up to 5000 μN maximum load with Berkovich indenter tip, loading rate 1mN/s. \odot indicates the c-axis direction is out of the page.

For the 5mN maximum loaded indents, the maximum depth recorded is 190nm and the residual depths were $\sim 115\text{nm}$, as measured from the averaged nanoindentation curves. A typical amplitude image of the residual indent using TMAFM is shown in figure 3.6.5 (b). A distinct residual indent is evident and pileup is on two sides of the indenter only.

For the 10 mN maximum loads, maximum depths of $\sim 290\text{ nm}$ and residual depths of $\sim 180\text{ nm}$ were obtained; the corresponding indent and surrounding pile-up are more distinct. A typical result for the 10 mN Berkovich indenter is shown in figure 3.6.6 (a). Residual impressions for the Berkovich indents took the form of a central impression with surrounding pileup occurring on two and sometimes one side of the indenter, for indents on the (001) plane, indicating extensive plastic deformation.

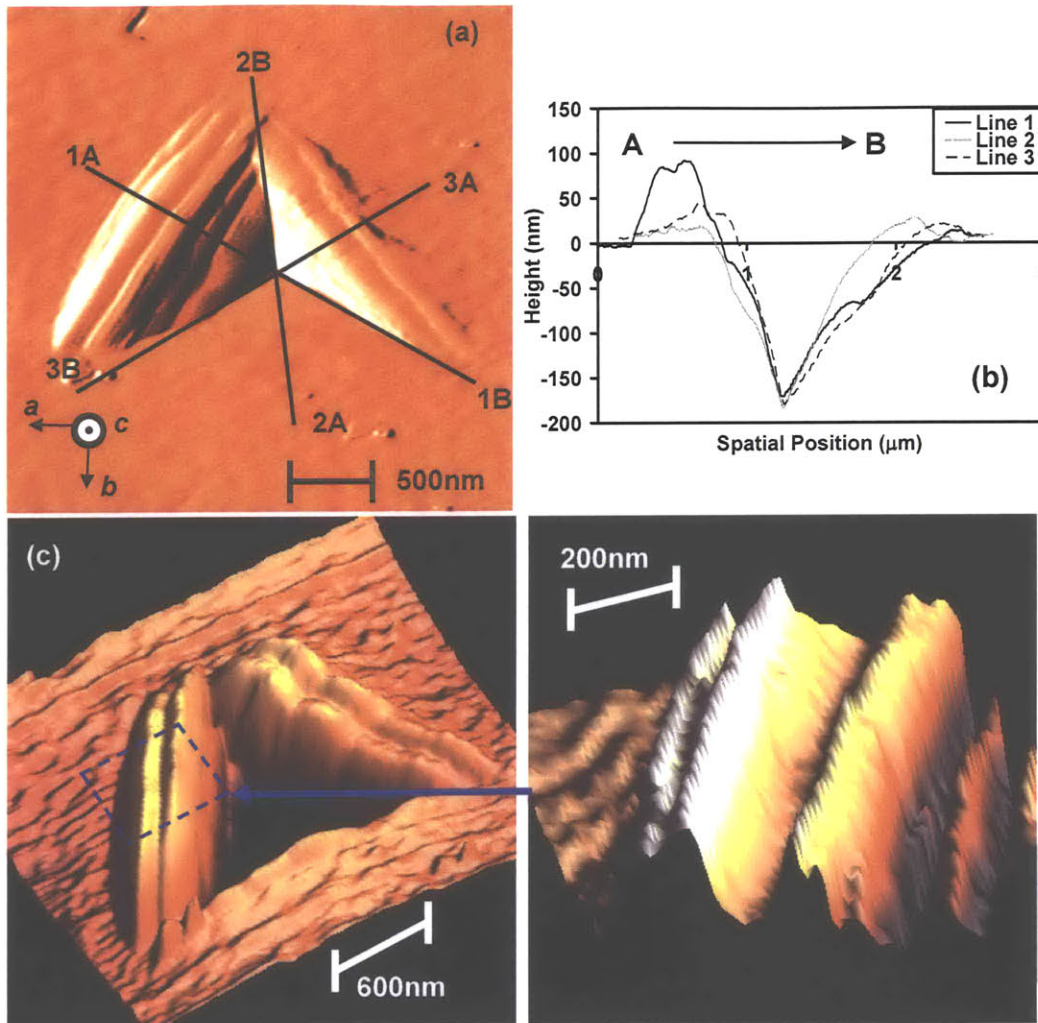


Figure 3.6.6 Tapping mode atomic force microscopy (TMAFM) image of residual indents after nanoindentation parallel to *c*-axis and corresponding line profiles of single crystal aragonite. (a), amplitude image, 10000 μ N maximum load, Berkovich indenter tip, loading rate 1mN/s. \odot indicates the *c*-axis direction is into the page. (b) Line profiles from corresponding height image to indent in (a). (c) (left) 3-D height image of Berkovich indent (*z*-scale exaggerated) and (right) 3-D amplitude image of Berkovich indent (zoom in of the same image shown in a).

The anisotropy in the plasticity is evident from the pileup bias and for the 10mN indent, it is quantified in figure 3.6.6 (b), which is a plot of the line profiles of the three indenter sides. The pile-up is seen to be dramatically less on the side perpendicular to the *b*-axis direction. The same indent is replotted in 3-D in fig. 3.6.6 (c), which again illustrates the anisotropy but also highlights banded striations that appear to be slip bands and the vertical orientation is suggestive of slip in the (001) direction.

The rotation stage was used in the nanoindenter to investigate the in-plane plastic anisotropy for the Berkovich indenter and how the pileup changed with different orientation of the indenter relative to the crystal axes. The TMAFM amplitude micrographs for 10 mN maximum load and 10° rotation between each load are plotted in figure 3.6.7 below.

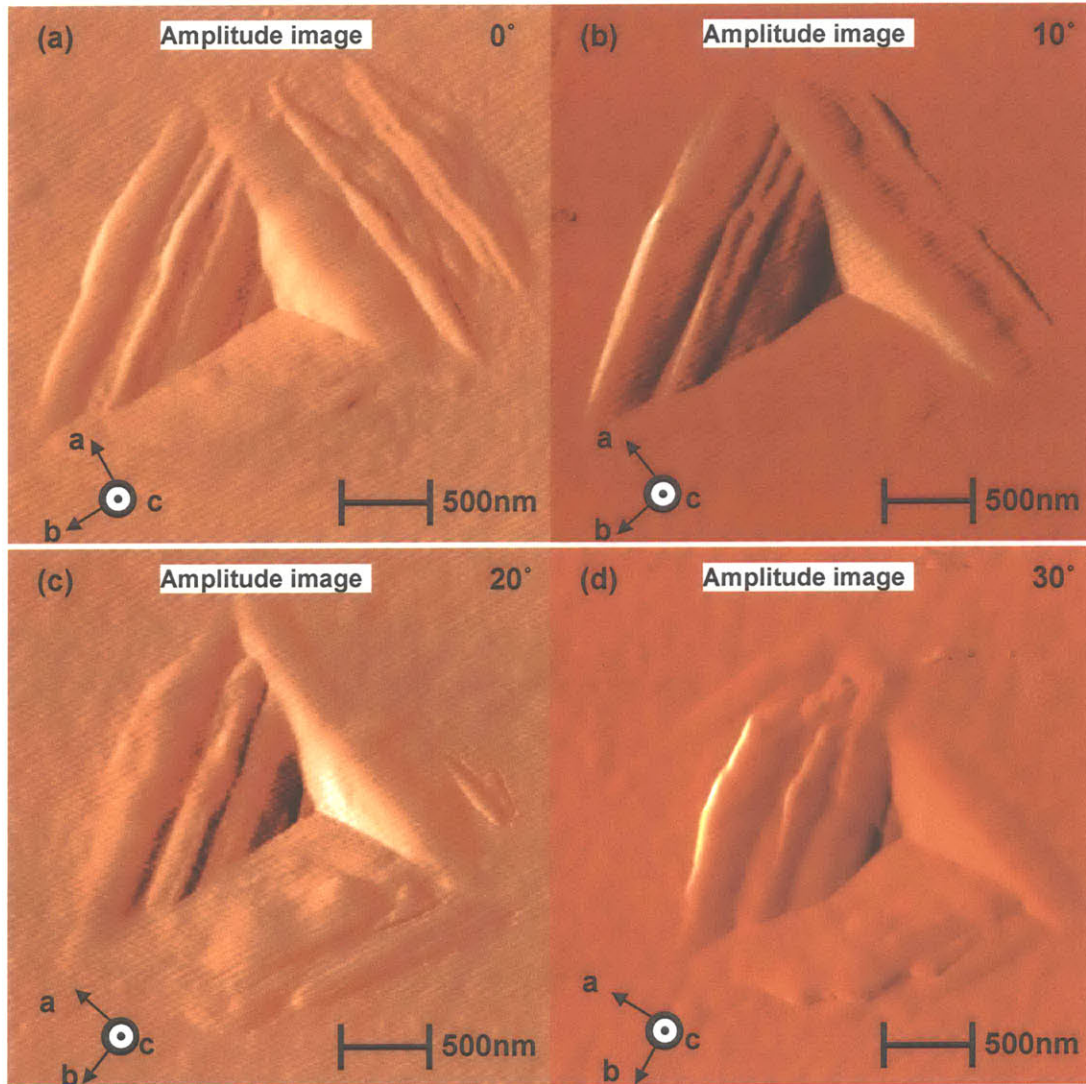
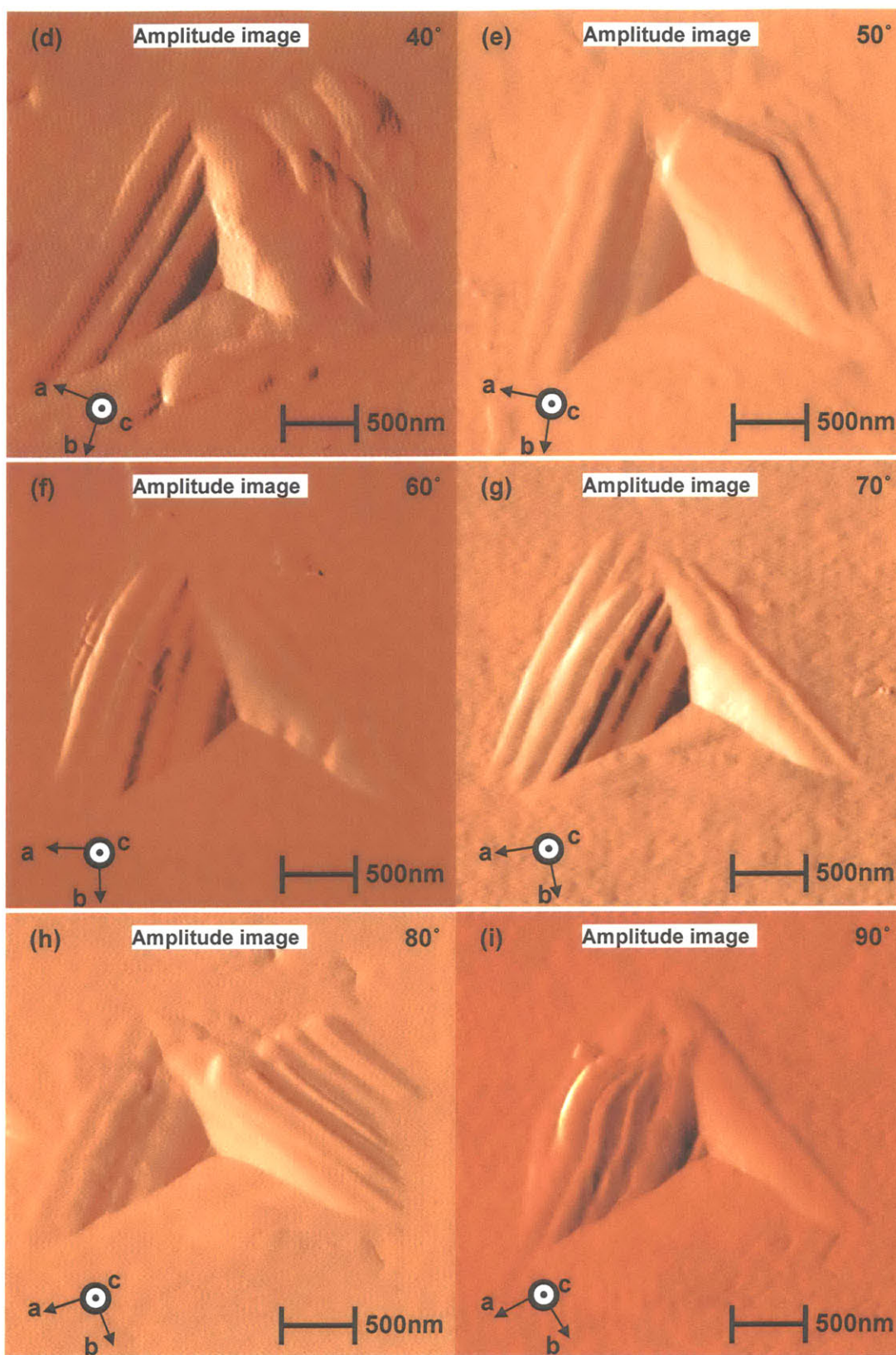
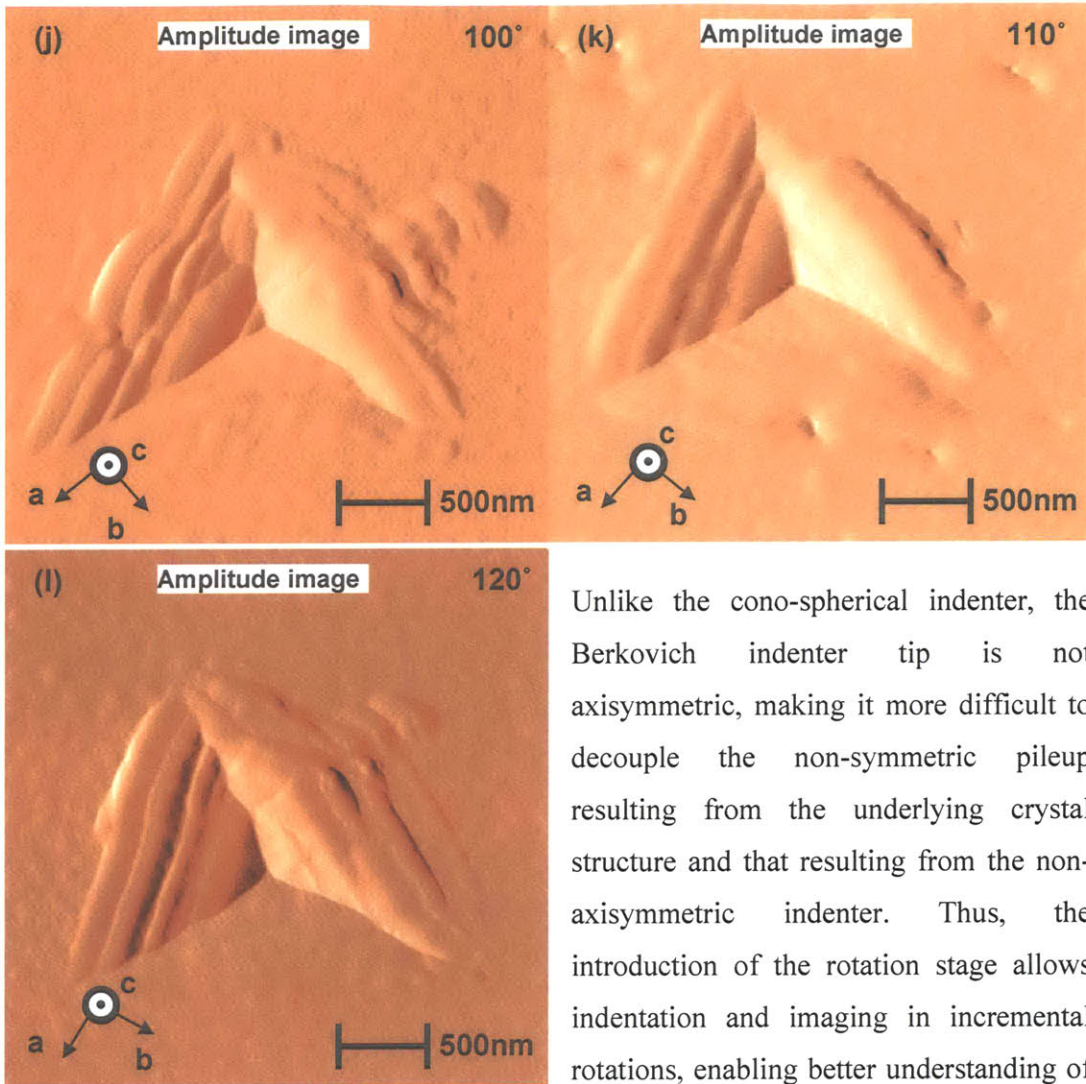


Figure 3.6.7 TMAFM amplitude images of residual Berkovich indents after nanoindentation on the c-plane (maximum load 10000 μ N, load/unload rate 1000 μ N/s). The rotation stage was used to rotate the sample in 10° increments, with the tip remaining stationary. The orientations are as illustrated: (a) 10° rotation (b) 20° rotation (c) 30° rotation (d) 40° rotation (e) 50° rotation (f) 60° rotation (g) 70° rotation (h) 80° rotation (i) 90° rotation (j) 100° rotation (k) 110° rotation (l) 120° rotation. *This figure is continued over the following pages.*





Unlike the cono-spherical indenter, the Berkovich indenter tip is not axisymmetric, making it more difficult to decouple the non-symmetric pileup resulting from the underlying crystal structure and that resulting from the non-axisymmetric indenter. Thus, the introduction of the rotation stage allows indentation and imaging in incremental rotations, enabling better understanding of

the underlying crystal structure response.

All the rotated indents showed clear residual impressions where pileup typically occurred on two sides of the indenter. This trend is reasonably consistent throughout the rotated indents, though there are some incidents where this is not the case. These results suggest highly preferential slip where the slip planes that slip may depend on the particular orientation of the indenter.

3.6.4 Nanoindentation Results for cono-spherical indenter: Force vs. penetration depth curves

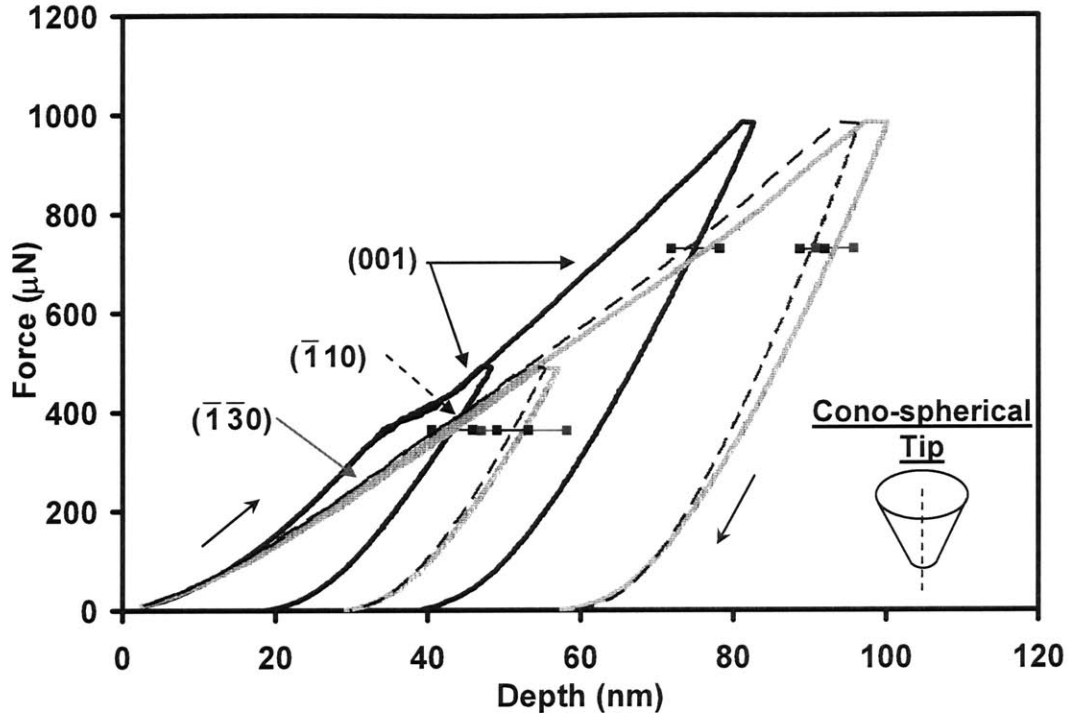


Figure 3.6.8 Nanoindentation data for single crystal aragonite using an (ideally) 1 μm radius, 60° conical tip. Averaged curves on loading and unloading at maximum loads of 500 μN (number of experiments, $n = 20$, 5 μm spacing in both the X- and Y- direction between each indent) and 1000 μN ($n = 20$) at a loading rate of 50 μN/s. The horizontal error bars indicate the maximum standard deviation of the curves for that particular dataset. Data with loading direction perpendicular to the (001), $(\bar{1}10)$ and the $(\bar{1}\bar{3}0)$ planes are shown. Arrows indicate the direction of loading.

Cono-spherical indentations were also performed on the three orthogonal aragonite planes; (001), $(\bar{1}10)$ and $(\bar{1}\bar{3}0)$. This dual indenter approach was employed as, unlike the Berkovich, the cono-spherical indenter is geometrically symmetric and thus any observation of in-plane directional bias in mechanical behavior (e.g. pile-up patterns) is solely attributable to the underlying crystal structure. The averaged nanoindentation data (penetration force versus depth for $n = 20$ experiments per set) for the three planes is graphed in figure 3.6.8. Plots containing all individual curves are given in Appendix B. The results are similar in form to those found for the Berkovich indenter. Once again, the

initial portion of the loading curve (0-15 nm) suggests similar elastic moduli (see figure 3.6.9) and the depth of residual impressions as measured from the unloading curve (see figure 3.6.8), illustrates the higher hardness value of the (001) plane. Again an O-P reduction was performed on this data to give (modulus, hardness) pairs of $(89 \pm 1.8 \text{ GPa}, 8.6 \pm 0.36 \text{ GPa})$, $(95 \pm 2.78 \text{ GPa}, 6.5 \pm 0.13 \text{ GPa})$ and $(85 \pm 2.25 \text{ GPa}, 6.36 \pm 0.19 \text{ GPa})$ ($p < 0.05$, unpaired student t-tests for all comparisons), for the (001), $(\bar{1}10)$ and $(\bar{1}\bar{3}0)$ planes respectively. The data reduction again highlights the anisotropy of the behavior where the properties, as reduced by the O-P method, not only depend on direction but also on indenter geometry. As with the Berkovich indents, the variation in elastic moduli was negligible ($<12\%$) but a more marked change is observed in the hardness of the three planes, with the c -plane being the hardest out of the three planes measured.

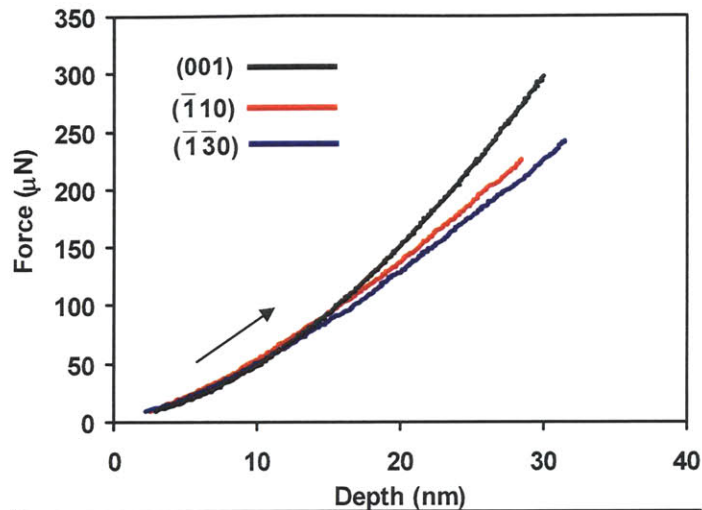


Figure 3.6.9 Initial portion of loading curve for $500\mu\text{N}$ $1\mu\text{m}$ 60° cono-spherical indents shown in figure 3.6.7 (averaged curves from $n=20$ indents, loading rate $50\mu\text{N/s}$)

Similar to the Berkovich indentation, there is a slope change in the averaged curves of the (001) plane indents (see figure 3.6.8) between forces of $\sim 381 \mu\text{N}$ and $\sim 439 \mu\text{N}$. The individual force-depth curves (see figure 3.6.10) again show the distinct load plateaus with the distribution in plateau load shown in the inset ($424.4 \pm 61.0 \mu\text{N}$). Again these distinct load plateaus are consistent with those found by other authors and are suggestive of discrete events occurring, in this instance attributed to the onset of dislocation nucleation.

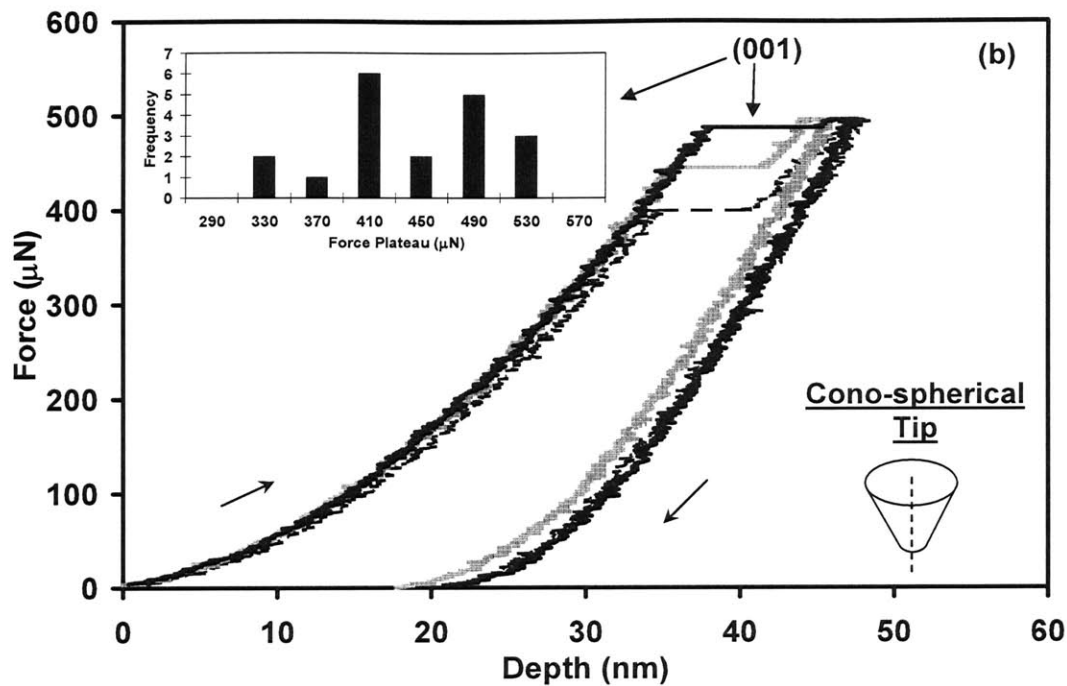


Figure 3.6.10 Three individual loading-unloading curves from the dataset shown in figure 3.6.7 for indents into the (001) plane.

3.6.5 Nanoindentation Results for cono-spherical indenter: Tapping mode atomic force microscopy of residual indents on the (001) plane

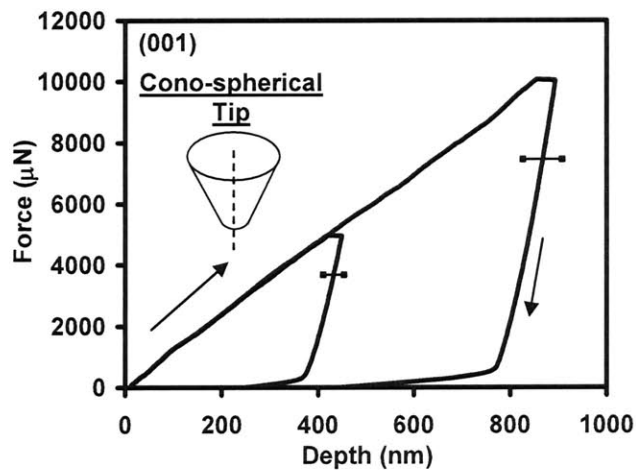


Figure 3.6.11 Nanoindentation data for single crystal aragonite using a $1\mu\text{m}$ radius, 60° conical tip probe tip. Averaged curves on loading and unloading at maximum loads of $5000\mu\text{N}$ (number of experiments, $n = 20$, $10\mu\text{m}$ spacing in both the X- and Y-direction between each indent) and $10000\mu\text{N}$ ($n = 20$, $15\mu\text{m}$ spacing in both the X- and Y- direction between each indent) at a loading rate of $1000\mu\text{N/s}$. The horizontal error bars indicate the maximum standard deviation of the curves for that particular dataset. Arrows indicate the direction of loading.

Higher load cono-spherical indents on the (001) plane up to a maximum load of 5mN (maximum depths $\sim 420\text{nm}$ and residual depths of $\sim 300\text{nm}$, as measured from averaged curves) were imaged using TMAFM. An example is shown in figure 3.6.12 (a). Residual deformations once again took the form of a central impression and a surrounding pileup

zone, with no microcracking observed. Preferential pile-up was observed to be localized predominantly in four lobes around the indenter. Height profiles, shown in Fig. 3.6.12 (b), quantify the pile-up around the indents and show that they extend ~500nm away from the central indent. The observed four pile-up lobes are an important observation in terms of anisotropy in the pile-up in the material. Since the cono-spherical indenter is geometrically symmetric, any observed non-symmetries in the pile-up are directly related to the crystallographic structure and the materials response to deformation.

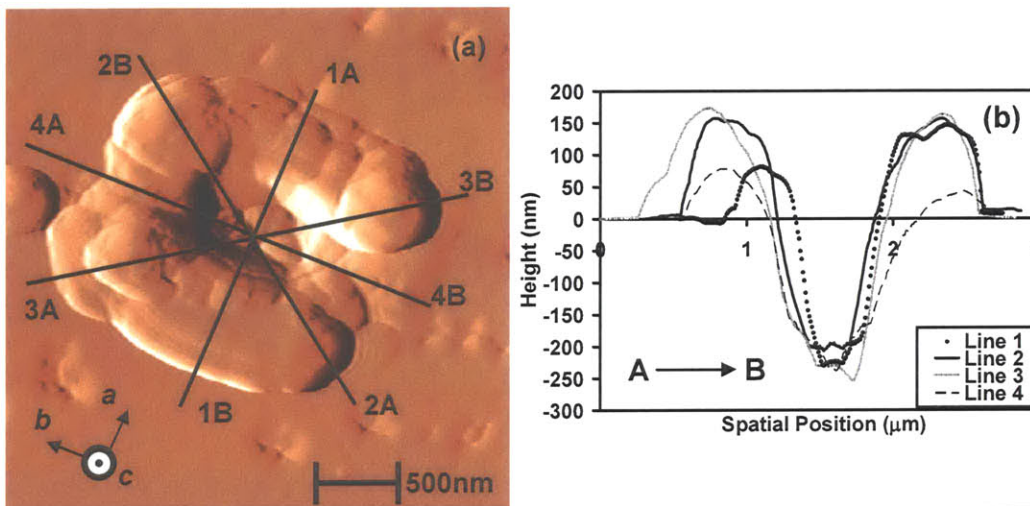


Figure 3.6.12 (a) Amplitude Tapping mode atomic force microscopy (TMAFM) image of residual cono-spherical indents after nanoindentation parallel to *c*-axis up to maximum load of 5000 μ N and (b) corresponding line profiles of single crystal aragonite

When loaded to 10 mN, the maximum indented depth is ~810 nm and the residual impression depth is ~550 nm, as measured from average force vs. displacement curves (see figure 3.6.11). TMAFM imaging of the indent (see figure 3.6.13) shows a distinct residual impression and a significant amount of pileup surrounding the indenter, with the large amount of plastic activity obscuring the distinct pile-up lobes seen in figure 3.6.11.

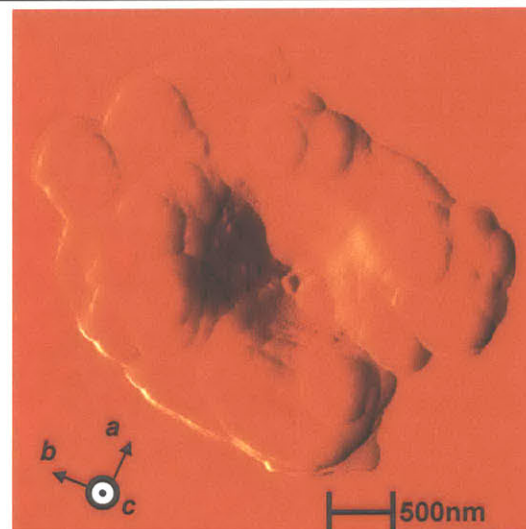


Figure 3.6.13 (a) Amplitude Tapping mode atomic force microscopy (TMAFM) image of residual cono-spherical indents after nanoindentation parallel to *c*-axis up to a maximum load of 10000 μ N

3.7 Comparison of micro- vs. nano-indentation using a Knoop tip on the (001) plane of single crystal aragonite

Micro-Knoop and nano-Knoop indentations were performed on the (001) plane to compare the deformation responses between the micro- and nano-scale. The Knoop hardness measurements for the micro-Knoop indentations were recorded as $343.77 \pm 30.45 H_{kn}$ at 200g force, equivalent to $3.37 \pm 0.3 \text{ GPa}$. The equipment used for micro-Knoop indentations did not output load vs. indentation depth curves. The curves for nano-Knoop indentation at loads of $500 \mu\text{N}$ and $1000 \mu\text{N}$ are shown in figure 3.7.1.

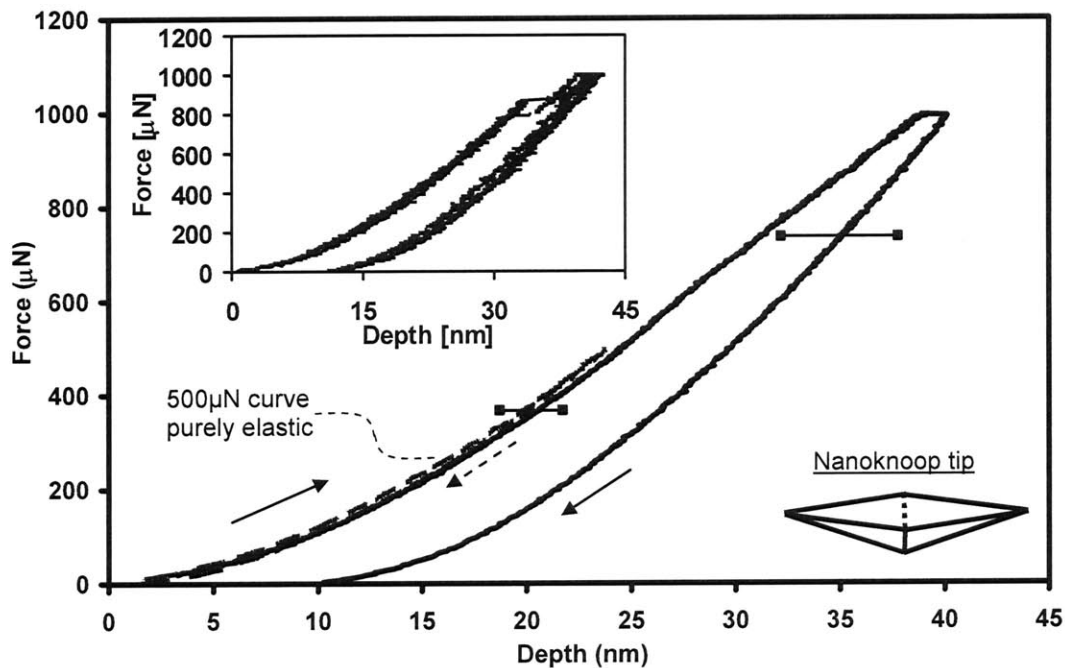


Figure 3.7.1 Load vs. penetration depth curves for nano-Knoop indentation on the (001) plane of single crystal aragonite up to maximum loads of $500 \mu\text{N}$ and $1000 \mu\text{N}$ ($n = 20$, load-unload rate = $50 \mu\text{N/s}$). The horizontal error bars indicate the standard deviation for that particular dataset. *Inset*: two individual load-unload curves showing load plateaus.

The $500 \mu\text{N}$ response is almost entirely elastic, with the unloading curve closely tracking the loading curve. The $1000 \mu\text{N}$ curve has a small residual indent. As discussed previously for the Berkovich and cono-spherical indents, load plateaus were visible in the individual curves (see figure 3.7.1). An O-P reduction of data obtained from the

nanoindentation resulted in measured hardness values of 3.20 ± 0.47 GPa for the $1000\mu\text{N}$ indents. No hardness value is reported for the $500\mu\text{N}$ indents as the load-unload curve is fully elastic.

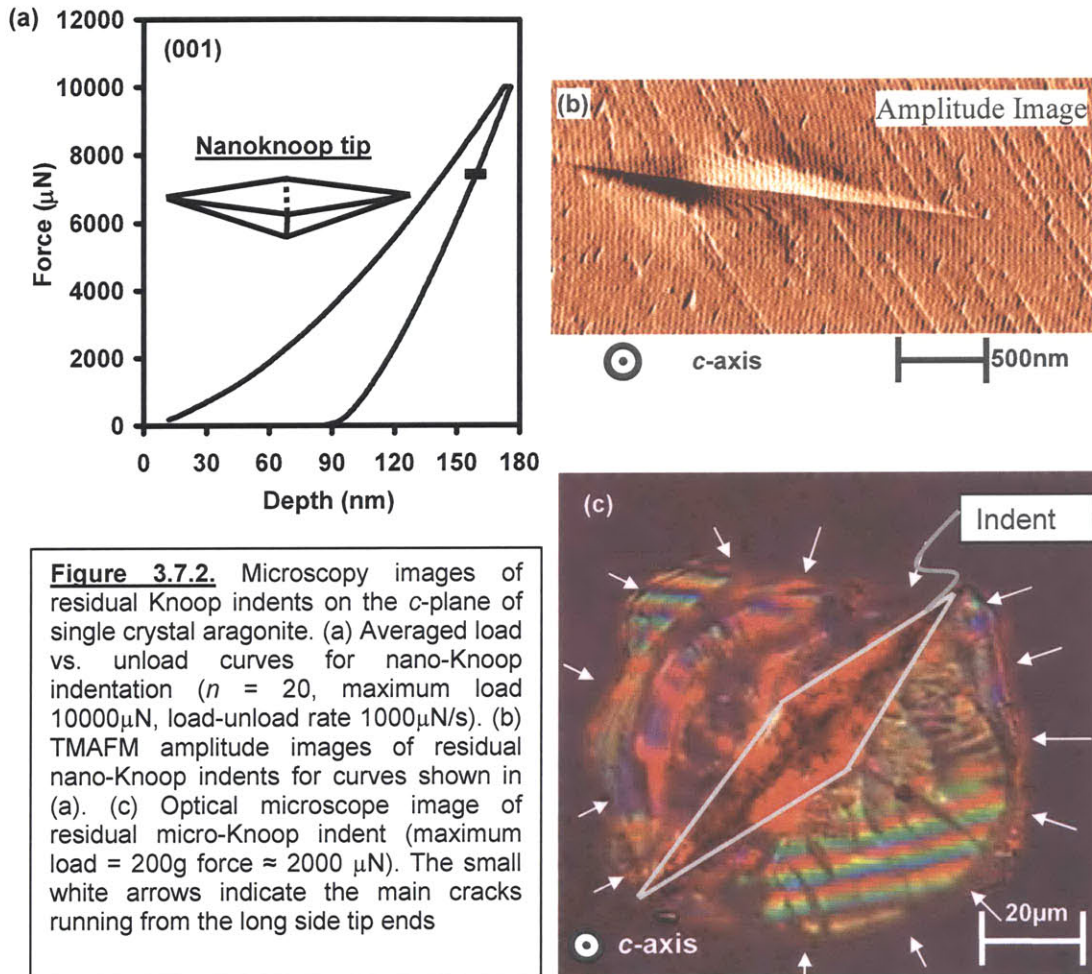


Figure 3.7.2. Microscopy images of residual Knoop indents on the *c*-plane of single crystal aragonite. (a) Averaged load vs. unload curves for nano-Knoop indentation ($n = 20$, maximum load $10000\mu\text{N}$, load-unload rate $1000\mu\text{N/s}$). (b) TMAFM amplitude images of residual nano-Knoop indents for curves shown in (a). (c) Optical microscope image of residual micro-Knoop indent (maximum load = 200g force $\approx 2000\mu\text{N}$). The small white arrows indicate the main cracks running from the long side tip ends

TMAFM was used to image the nano-Knoop indents for higher maximum indentation depth (10mN). The amplitude image shows a distinct residual indent with some small pile-up in regions around the indent (see figure 3.7.2 (b)). No microcracking was observed. In contrast, images for the micro-Knoop indents on the (001) plane (see figure 3.7.2 (c)) consistently had microcracks emanating from one or both of the end tips of the indenter. This highlights the mechanism change between the micro- and nano-scales and may give some insight into the use of small dimensions in biomaterials and organisms.

3.8 Nanoindentation on *c*-plane of aragonite vs. nanoindentation on *c*-plane of nacre tablets

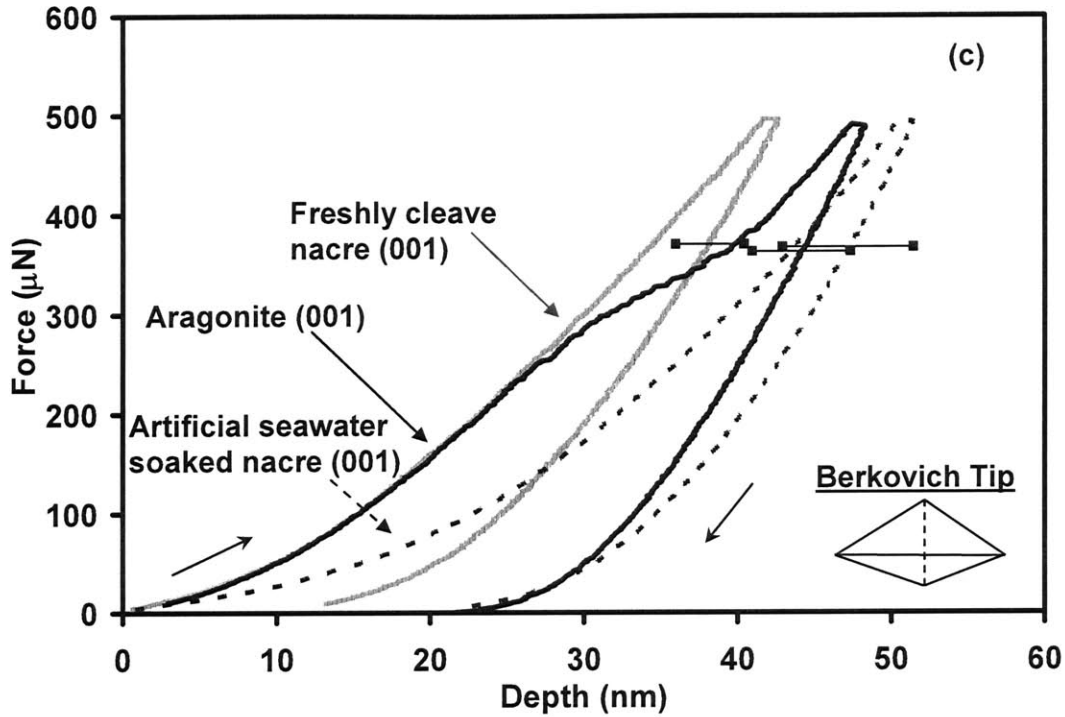


Figure 3.8.1 Comparison of nanoindentation data for single crystal aragonite: dry nacre [Bruet et al, 2005] and wet nacre [Bruet et al, 2005] (maximum load 500 μ N). Indents are all coaxial to the crystal *c*-axis.

In Fig. 3.8.1 the dataset graphed in figure 3.6.6 for nanoindentation using a Berkovich tip on the (001) plane of aragonite is overlaid with published data [Bruet et al, 2005] for individual freshly cleaved and artificial seawater soaked nacre tablets from *T. niloticus* loaded in on the *c*-plane of nacre tablets (see section 3.3). The averaged single crystal data is coincident with the freshly cleaved nacre data up until the onset of dislocation nucleation (i.e. where the load plateaus occur) and then follows a slope that lies between that of the artificial seawater soaked and freshly cleaved nacre. This suggests that the elastic response for the freshly cleaved nacre and aragonite are quite similar and that the elastic moduli should be in reasonable agreement. This is confirmed by the O-P analysis which, at 500 μ N maximum load, gives an elastic modulus of 118.3 ± 9 GPa for the freshly cleaved nacre [Bruet et al, 2005] and 102.8 ± 3.4 GPa for aragonite. The loading

curve for the artificial seawater soaked nacre does not track either of the other curves. It should be noted that the O-P analysis, as previously mentioned, assumes isotropic material behavior, whereas the crystallographic aragonite is inherently anisotropic and hence some degree of error is introduced in these calculations.

The single crystal aragonite curves showed no distinct slope change in the low load regions (refer to figure 3.6.2) as was seen with the nacre data (refer to figure 3.3.2). This gives support to the hypothesis that the slope change resulted from the nanoasperities on the surface of the tablets (see section 3.3) as reported by Bruet et al [2005].

Comparison of the residual depths suggests a higher yield strength for the nacre tablets than for the single crystal calcite. This is confirmed by the Oliver-Pharr analysis (for 500 μ N maximum load), which gives 6.5 ± 0.2 GPa for the single crystal aragonite curves and 10.6 ± 0.9 GPa for the freshly cleaved nacre curves. The nanoscale features of the nacre tablets, i.e. tablet sectors, intra-tablet organic matrix, assemblies of single crystals within sectors (see section 1.4.1), may inhibit dislocation nucleation increasing the yield strength in nacre tablets.

Figure 3.8.2 shows TMAFM imaging of higher load indents (5000 μ N and 10000 μ N) on the *c*-plane of both freshly cleaved nacre and single crystal aragonite. All indents have a distinct residual impression. The distance from the center of the indent to the edge of the pile-up region is similar for both materials (\sim 700-800nm for the 5 mN indents and \sim 1100-1200nm for the 10mN indents). The difference in the plastic behavior between both materials is that the single crystal aragonite has pileup on just two sides of the indenter, whereas the nacre has pile-up on all three sides of the indenter, albeit one side appears to be noticeably less than the other two sides. This is confirmed by line profiles of the residual pileup (data not shown here) [Bruet et al, 2005].

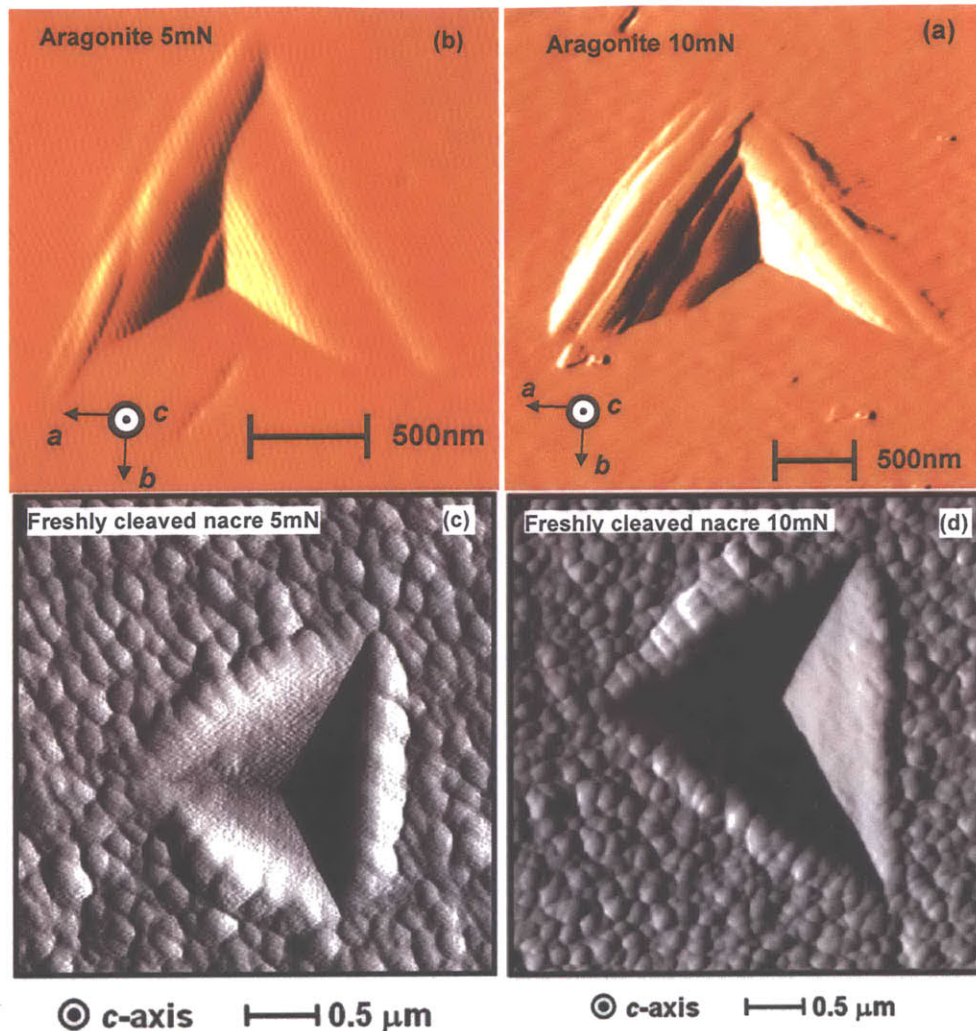


Figure 3.8.2 TMAFM images of Berkovich indents on *c*-plane of (a) aragonite, maximum load 5 mN (b) aragonite, maximum load 10 mN (c) nacre, maximum load 5 mN [Bruet et al, 2005] and (d) nacre 10mN [Bruet et al, 2005].

3.9 Summary

The technique of nanoindentation combined with in-situ atomic force microscopy was used to investigate, for the first time, the nanoscale plastic behavior of single crystal aragonite.

At the lengthscales found in biocomposite materials, aragonite deforms plastically and averts brittle failure. This was confirmed by a comparative study between a micro-Knoop

and nano-Knoop indenter. The nano-Knoop indents showed no evidence of microcracking. Conversely, micro-Knoop indents had microcracks emanating from the end tips of the indenter, illustrating a change in material behavior between the scales. The micro- and nano- Knoop indents gave reasonably consistent hardness values.

Plastic deformation in aragonite results from slip on specific systems within the crystal. Results for the Berkovich, cono-spherical and nano-Knoop indenters all consistently showed displacement continuities that were attributed to the onset of plasticity. Numerous authors have observed displacement discontinuities in crystalline materials during load controlled nanoindentation and attributed this phenomenon to dislocation activity and incipient plasticity through various constitutive models [Gerberich et al, 1996; van Vliet et al, 2003] and TEM imaging [Page et al, 1992]. Pile-up surrounding the Berkovich indenter appeared banded in form, which further suggested slip on specific systems within the single crystals.

An anisotropic plastic response between three mutually orthogonal planes: (001), ($\bar{1}10$) and ($\bar{1}\bar{3}0$) was observed. The anisotropy in the hardness was most pronounced, with the (001) plane having the highest hardness. The top plane of the nacre tablets is the (001) plane, the hardest plane of the three investigated by ~ 30%, and the normal to this plane is coincident with the surface normal of the seashell. In plane plastic anisotropy was also recorded in the TMAFM images, which showed four pile-up lobes around the residual cono-spherical indents and pile-up only occurred on two, and sometimes only one, side of the residual Berkovich indent. Further, the pile up pattern for the Berkovich indents, appeared as banded striations and 3-D representation of these indents suggests [001] slip. No microcracking was evidenced around the residual impressions for any of the indenters.

Berkovich indents on the *c*-plane of single crystal aragonite are compared with results previously published for indents on the top face (*c*-plane) of aragonite tablets in nacre. The elastic moduli, based on examination of the curves and O-P analysis, were found to be similar for the freshly cleaved nacre and the single crystal aragonite. Comparison of

the force versus penetration depth curves reveals a higher yield stress for the freshly cleaved nacre than for the single crystal aragonite. The increase in yield stress for the nacre tablets is believed to result from the nanoscale features of the nacre tablets, which inhibit dislocation nucleation. There was no evidence of the distinct load plateaus that occurred in the curves for aragonite in the nacre curves. TMAFM micrographs of the indents in nacre showed bias in the pileup (pileup occurred on all three sides of the residual indent, with one indenter side noticeably less than the other two sides); the single crystal aragonite showed pileup on just two indenter sides.

Chapter 4 *Finite element simulation of the elastic and the elastic-plastic indentation of single crystal aragonite*

Introduction

Chapter 3 reported the experimental data for nanoindentation of single crystal aragonite. Anisotropic behavior amongst three mutually orthogonal planes in both the Young's modulus and the hardness was found. The pileup observed for nanoindentation on the (001) plane with both the cono-spherical and Berkovich tip was observed to be anisotropic in nature and bands in the Berkovich pile up were suggestive of slip on discrete planes. Further, distinct load plateaus were found in the force-indentation curves, which are indicative of the nucleation of dislocations or an initial mechanism of plastic flow.

In this chapter, the experimental data is modeled using finite element (FE) simulations of nanoindentation. The response in the elastic regime is investigated and compared with experimental data. The observed pile-up in the AFM images for the experimental data is assumed to result from crystal plasticity, by slip on distinct systems. Since there exists very limited data on the slip systems of single crystal aragonite, the classical rate dependent crystal plasticity model was chosen to model the behavior and to interrogate the slip systems activated.

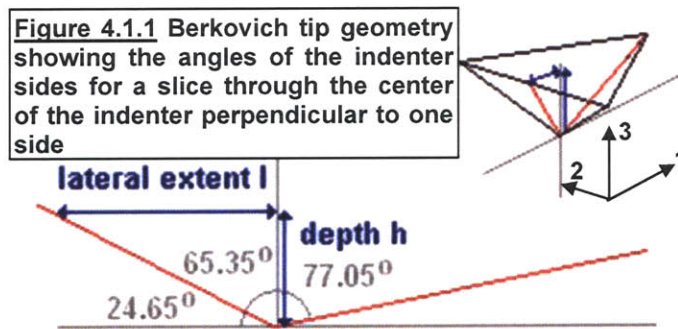
4.1 Details of model

The commercially available *ABAQUS* finite element analysis software was used to model the response of single crystal aragonite in both the elastic and plastic regimes. A different mesh and geometry were used for the elastic models and the elastic-plastic models to explore different aspects of the observed behavior. The elastic model is used to capture the low load regime and it is necessary to model the tip of the indenter in detail, requiring a dense mesh of the aragonite in that region. The elastic-plastic model was used to investigate and interrogate the slip systems of single crystal aragonite that led to the observed pileup patterns in the experimental data reported in chapter 3.

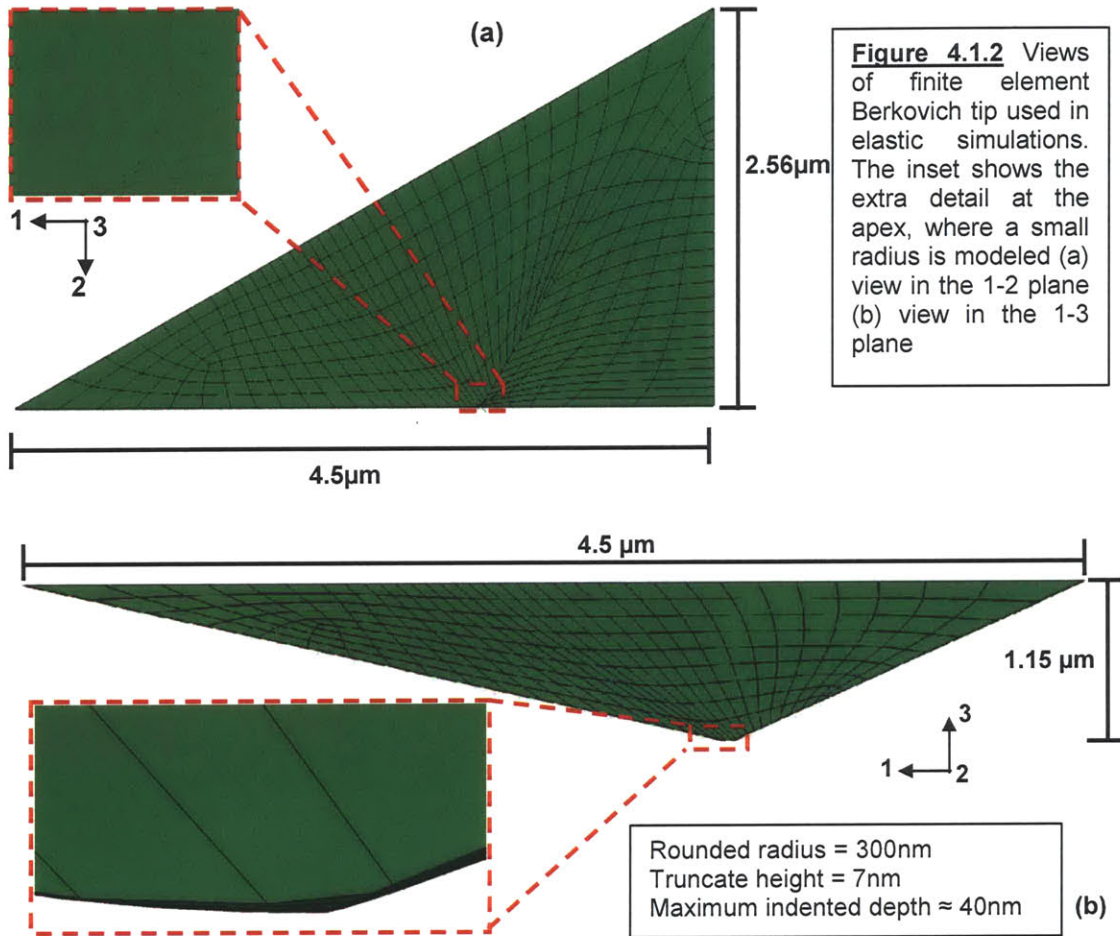
4.1.1 Geometric description of finite element model and nanoindentation tips

Berkovich tip: The Berkovich tip is a three sided pyramidal indenter, with each side having equal geometry. The angles are as shown in figure 4.1.1.

For the elastic model, it is essential to model the geometry of the tip in detail, since the elastic response occurs at low loads/penetration depths. Thus, wear or fabrication errors for the tip have to be taken into account. Instead of an ideally sharp tip, the tip used in the simulations is given a rounded radius and a truncate height (which is defined as the distance between the apex of the rounded tip and the apex of the ideally sharp tip). These values were obtained by performing low load nanoindentation experiments on a standard fused Quartz sample and matching the experimental curves with the *ABAQUS* results by varying the truncate height and radius. The final values used in the simulation were those reported by Bruet et al [2005] (for the same tip): a radius of 300nm and a truncate height of 7nm. For the



elastic simulations half symmetry was employed to model the indent. The indenter was modeled as a rigid body using 413 elements of type R3D4 elements (see figure 4.1.2).



For the elastic-plastic model, the tip is also modeled as a rigid body. However, no tip radius was included and the tip was modeled as ideally sharp using 78 elements of type R3D3. No symmetry was used for the elastic-plastic model and a full indenter tip was modeled (see figure 4.1.3).

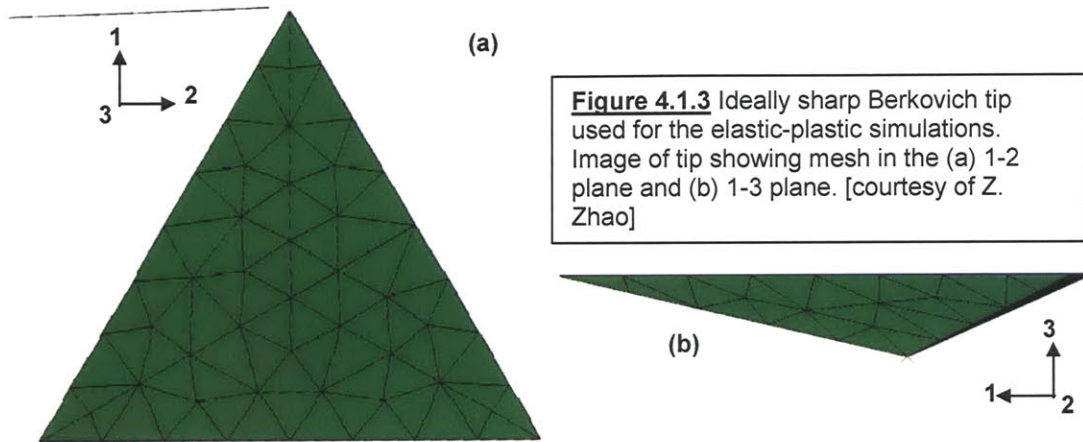


Figure 4.1.3 Ideally sharp Berkovich tip used for the elastic-plastic simulations. Image of tip showing mesh in the (a) 1-2 plane and (b) 1-3 plane. [courtesy of Z. Zhao]

Cono-spherical tip: The cono-spherical tip used for the experiments is a 60° cone with a spherical tip end of radius 1 μm. The tip was modeled for the elastic-plastic simulations using an analytical rigid surface.

Sample used for elastic model:

The sample was modeled with half symmetry for the elastic models (see figure 4.1.4). 23034 elements of type C3D8H were used to model the sample. The mesh was refined in the region where the indenter tip makes contact to avoid numerical issues and to model the interaction between the indenter tip radius and the sample.

The base of the sample is constrained from movement vertically (in the 3-direction) and also in plane (in the 1- and 2-direction). Since the sample is for half symmetry, the side of the sample where the half symmetry cut is taken is constrained in the 2-direction.

The surface interaction for the Berkovich tip and sample surface had no friction and the overclosure is set to *hard*.

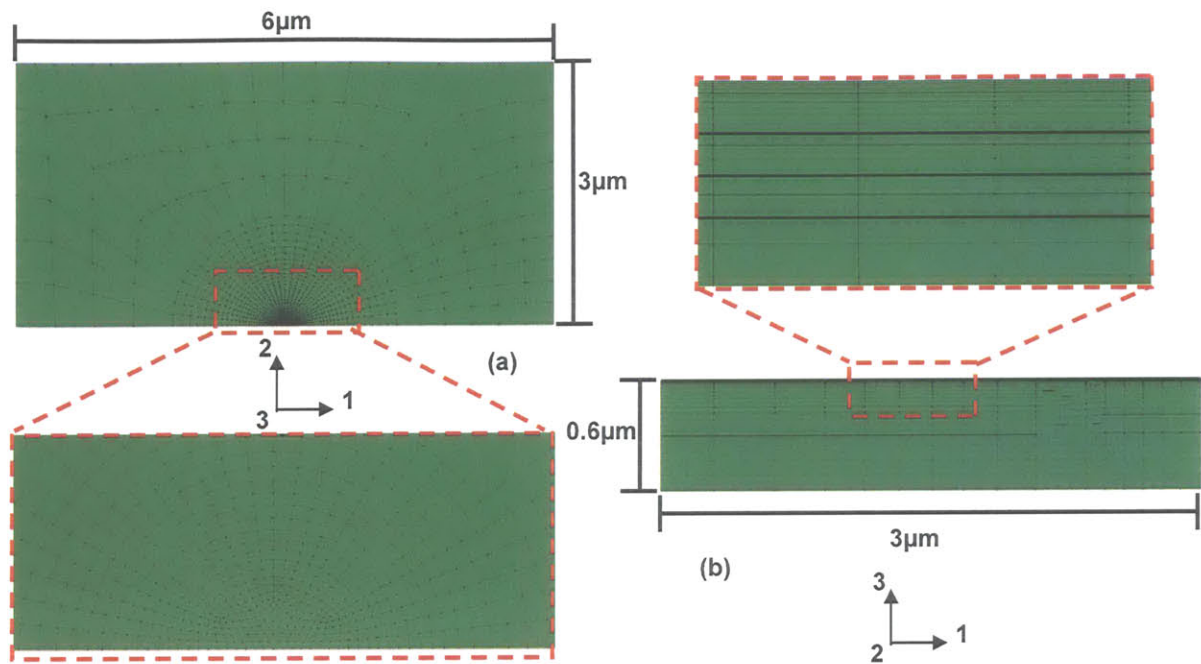
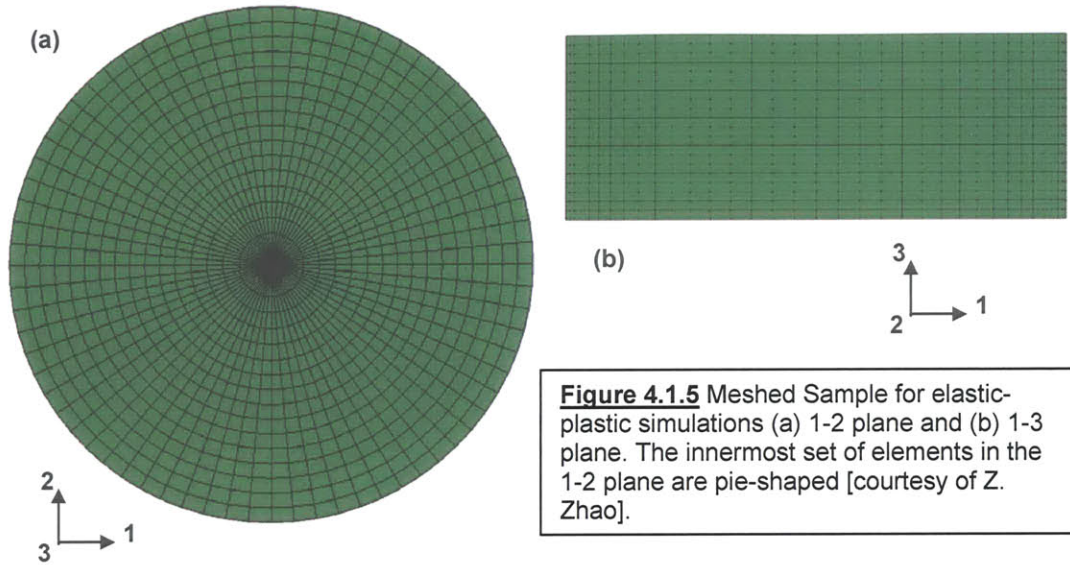


Figure 4.1.4 Sample used for elastic simulations with zoom-in showing details of the more dense mesh where the Berkovich tip first makes contact (a) image of the 1-2 plane (b) image of the 1-3 plane

Sample used for elastic-plastic model: A full model of the sample was used for the elastic-plastic simulations (i.e. no symmetries were used) as a-priori, it was unclear what slip systems would be included and what orientations would be investigated. The sample consisted of 21960 elements: the innermost part of the sample consisted of C3D6 elements, the rest of the sample had C3D8 elements (see figure 4.1.5).

The base of the sample is constrained from movement vertically (in the 3-direction) and also in plane (in the 1- and 2-direction).

The surface interaction for both the Berkovich tip & cono-spherical tip and the sample surface had overclosure set to *hard*. Since the Berkovich tip was ideally sharp, there were contact problems between the surfaces and a friction value of 0.3 between the surfaces was introduced to overcome this problem.



4.1.2 Material models

Several material models were used to model the behavior of the single crystal aragonite: isotropic elastic, anisotropic elastic and elastic (isotropic)-plastic (anisotropic).

Isotropic Elastic

The isotropic elastic model values were chosen based on the fact that experimental data for the *c*-plane single crystal aragonite data closely matched the *c*-plane nacre data (see section 3.8). Isotropic finite element simulations were used to successfully model the *c*-plane data for nacre, as previously reported by Bruet et al [2005], using a Young's modulus of 92 GPa and a Poisson's ratio of 0.17. These values were employed in the isotropic finite element simulation for single crystal aragonite.

Anisotropic Elastic

The anisotropic elastic constants used in the simulation were the most recently reported experimental values, found using Brillouin spectroscopy, by Liu [Liu et al, 2005]. For

orthorhombic crystals, we have 9 elastic constants. These values, as reported by Liu et al [2005], are tabulated below;

| C_{11} | C_{22} | C_{33} | C_{44} | C_{55} | C_{66} | C_{12} | C_{13} | C_{23} |
|----------|----------|----------|----------|----------|----------|----------|----------|----------|
| 171.1 | 110.1 | 98.4 | 39.3 | 24.2 | 40.2 | 60.3 | 27.8 | 41.9 |

Table 4.1.1 Elastic constants of aragonite used in anisotropic elastic finite element simulations. The a -axis is aligned with the 1-direction, the b -axis is aligned with the 2-direction and the c -axis is aligned with the 3-direction.

To simulate the indents on the (001) plane the a -axis was aligned perpendicular to one of the indenter sides (when looking top-down on the indenter), with the b -axis parallel to one of the indenter sides (see figure 4.1.6). For the $(\bar{1}10)$ and $(\bar{1}\bar{3}0)$ planes the c -axis was perpendicular to one of the indenter sides and the sample oriented within the a - b plane around the c -axis to align the indenter perpendicular to the planes (see schematic in figure 4.1.7).

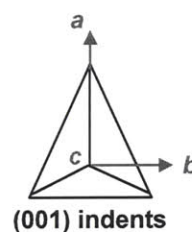


Figure 4.1.6 Orientation for (001) indents

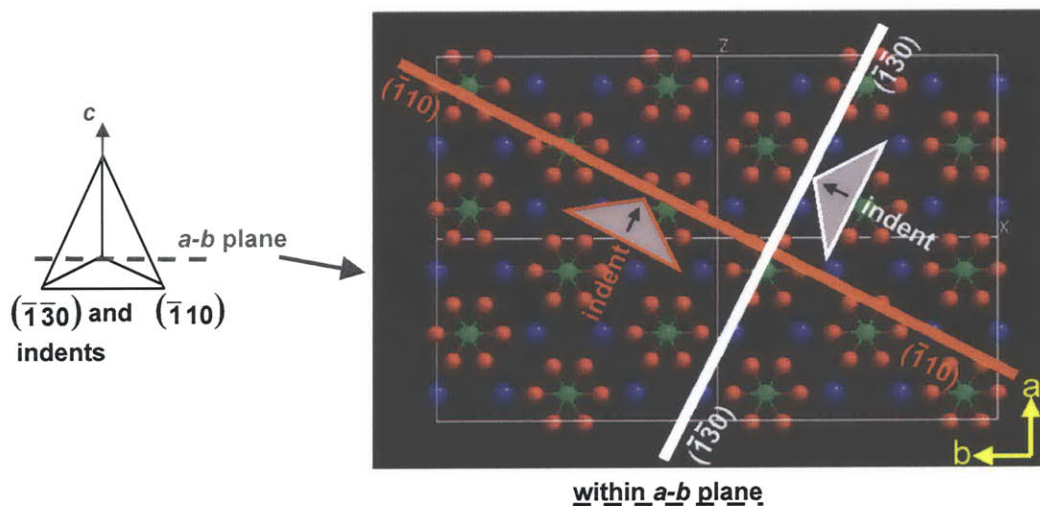


Figure 4.1.7 Schematic of orientations of indents for the $(\bar{1}10)$ and $(\bar{1}\bar{3}0)$ planes. The c -axis is aligned perpendicular to one indenter side and the sample rotated around the c -axis to the correct orientation. The orientations are overlaid on the crystal structure

If the stiffness matrix is transformed so that the 1 direction is perpendicular to the $(\bar{1}10)$ plane, the 2 direction is perpendicular to the $(\bar{1}\bar{3}0)$ direction and the 3 direction is perpendicular to the (001) (or *c*-plane), the resultant stiffness matrix is:

| C_{11} | C_{22} | C_{33} | C_{44} | C_{55} | C_{66} | C_{12} | C_{13} | C_{23} |
|----------|----------|----------|----------|----------|----------|----------|----------|----------|
| 158.1 | 122.7 | 98.4 | 36.2 | 27.3 | 40.16 | 60.26 | 30.7 | 39.0 |

Table 4.1.2 Transformed elastic constants of aragonite to line up perpendicular to indented planes

Elastic-plastic single crystal model

The single crystal elasto-viscoplasticity model developed here follows closely the development of Kalidindi et al [Kalidindi et al, 1992]. The algorithm outlined in that paper is also employed. Numerous authors have contributed to the development of the model including, Taylor [Taylor, 1938], Mandel [Mandel, 1965], Rice [Rice, 1971], with one of the major contributions coming from Pierce, Asaro and Needleman who developed the rate-dependent form of the model [Pierce et al, 1983]. The single crystal model has previously been employed to capture pile-up patterns under nanoindentation [Wang et al, 2004]. The polycrystalline model has been used to successfully capture numerous applications, including earing in cup drawing [Balasubramanian et al, 1996], texture evolution of polycrystalline metals [Anand, 2004] and surface roughening in fcc metals [Zhao et al, 2004]. The implementation of the model for this Thesis concerned single crystal plasticity and hence the number of grains (equivalent to the number of crystals for this model) is set to 1 and no stress averaging is necessary.

The constitutive equation for the second Piola-Kirchoff stress, \mathbf{T}^e , in the crystal is given in terms of the fourth order elasticity tensor, \mathcal{C} and the Cauchy-Green elastic strain tensor, \mathbf{E}^e , as:

$$\mathbf{T}^e = \mathcal{C}[\mathbf{E}^e]$$

where the elastic strain measure work conjugate to \mathbf{T}^e is the Cauchy-Green elastic strain tensor, which is defined by:

$$\mathbf{E}^e = \frac{1}{2} \{ \mathbf{F}^{eT} \mathbf{F}^e - \mathbf{1} \}$$

These are used to evaluate the symmetric Cauchy stress tensor, \mathbf{T} , which is found using:

$$\mathbf{T}^e = \mathbf{F}^{e-1} \{ (\det \mathbf{F}^e) \mathbf{T} \} \mathbf{F}^{e-T}$$

Here, \mathbf{F}^e , is the elastic

deformation gradient (see figure 4.1.8). The Kroner-Lee decomposition is used to relate the deformation gradient, \mathbf{F} , and the plastic deformation gradient, \mathbf{F}^p (the deformation gradient of the elastically relaxed space):

$$\mathbf{F} = \mathbf{F}^e \mathbf{F}^p, \det \mathbf{F}^e > 0$$

with $\det \mathbf{F}^p = 1$ from incompressibility. The plastic deformation gradient is obtained from the flow rule,

$$\dot{\mathbf{F}}^p = \mathbf{L}^p \mathbf{F}^p$$

where,

$$\mathbf{L}^p = \sum_{\alpha} \dot{\gamma}^{\alpha} \mathbf{S}_0^{\alpha}, \quad \mathbf{S}_0^{\alpha} = \mathbf{m}_0^{\alpha} \otimes \mathbf{n}_0^{\alpha}$$

\mathbf{m}_0^{α} and \mathbf{n}_0^{α} are the orthonormal unit vectors that define the slip direction and slip plane normal, respectively, of the slip system α in a fixed reference configuration. These combine to give the Schmid matrix, \mathbf{S}_0^{α} . $\dot{\gamma}^{\alpha}$ is the plastic shearing rate on the slip system α . Here, $\dot{\gamma}^{\alpha}$ is assumed to be a function of both the resolved shear stress, τ^{α} , and the slip system deformation resistance, s^{α} :

$$\dot{\gamma}^{\alpha} = \hat{\gamma}^{\alpha}(\tau^{\alpha}, s^{\alpha})$$

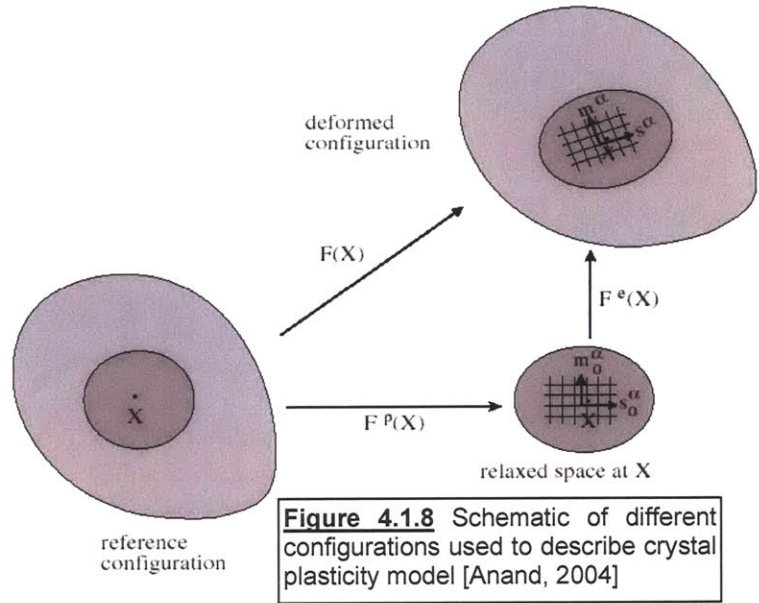


Figure 4.1.8 Schematic of different configurations used to describe crystal plasticity model [Anand, 2004]

To evaluate the resolved shear stress, τ^α , for the slip system α it is assumed that the local configuration for a crystal defined by \mathbf{F}^P is an isoclinic relaxed configuration, and the plastic stress power per unit volume in this isoclinic configuration is defined by;

$$\dot{w}^P \equiv (\mathbf{C}^e \mathbf{T}^e) \cdot \mathbf{L}^P, \text{ and } \mathbf{C}^e \equiv \mathbf{F}^{eT} \mathbf{F}^e$$

Hence, the resolved shear stress is defined as:

$$\dot{w}^P = \sum_{\alpha} \tau^{\alpha} \dot{\gamma}^{\alpha}$$

and using the expression for \mathbf{L}^P ,

$$\tau^{\alpha} \equiv (\mathbf{C}^e \mathbf{T}^e) \cdot \mathbf{S}_0^{\alpha}$$

The approximation that the elastic stretch is very small (thus, $\mathbf{C}^e \approx \mathbf{1}$) is applied to give:

$$\tau^{\alpha} \approx \mathbf{T}^e \cdot \mathbf{S}_0^{\alpha}$$

The slip resistances, s^α , evolve according to:

$$\dot{s}^{\alpha} = \sum_{\beta} h^{\alpha\beta} |\dot{\gamma}^{\beta}|,$$

here, $h^{\alpha\beta}$ is the rate of strain hardening on slip system α due to shearing on slip system β .

The specific constitutive functions used in our modeling are developed below and again follow closely the work of Kalidindi et al [Kalidindi et al, 1992]. For the elastic-plastic model, the anisotropic elastic behavior of aragonite is neglected. The isotropic fourth order elasticity tensor given by:

$$\mathcal{E} = 2\mu \mathcal{L} + [\kappa - (2/3)\mu] \mathbf{1} \otimes \mathbf{1}$$

with μ and κ the elastic shear and bulk moduli respectively. The evolution of the plastic shearing rate is given as:

$$\dot{\gamma}^{\alpha} = \dot{\gamma}_0 \left| \frac{\tau^{\alpha}}{s^{\alpha}} \right|^{1/m} \text{sign}(\tau^{\alpha})$$

with $\dot{\gamma}_0$ and m are material parameters. $\dot{\gamma}_0$ is a reference shearing rate and m defines the rate sensitivity of slip. $h^{\alpha\beta}$ is defined as:

$$\mathbf{h}^{\alpha\beta} = \mathbf{q}^{\alpha\beta} \mathbf{h}^{(\beta)}, \text{ (no summation on } \beta \text{)}$$

where $h^{(\beta)}$ is the single slip hardening rate on slip system β and $q^{\alpha\beta}$ is the matrix describing the latent hardening behavior of a crystallite (the hardening on slip system α due to slip on slip system β). Here, $q^{\alpha\beta}$ is given by:

$$q^{\alpha\beta} = \begin{pmatrix} \mathbf{A} & q\mathbf{A} & q\mathbf{A} & q\mathbf{A} \\ q\mathbf{A} & \mathbf{A} & q\mathbf{A} & q\mathbf{A} \\ q\mathbf{A} & q\mathbf{A} & \mathbf{A} & q\mathbf{A} \\ q\mathbf{A} & q\mathbf{A} & q\mathbf{A} & \mathbf{A} \end{pmatrix}$$

where q is the ratio of the self hardening rate to the latent hardening rate and \mathbf{A} is a 3x3 matrix fully populated by ones. The specific form for the single slip hardening rate is;

$$h^{(\beta)} = h_0 \left[1 - \frac{s^\beta}{s_s} \right]^a$$

where h_0 , a , s_s are the hardening parameters. Here they are assumed equivalent for all the systems.

Details of the slip systems chosen for the model are included in section 4.2.2 below, where the application of the model is discussed. The elastic properties were defined using $E = 123$ GPa and $\nu = 0.34$. Since very limited data exists on the plastic behavior of aragonite, the model is used to interrogate the kinematically plausible slip systems. Hence, the evolution of slip resistance is taken to be equivalent for each system and since the hardening parameters/load-unload data were not being investigate for these simulations the hardening parameters were taken to be equivalent to those used by Kalidindi et al [1992]: $q = 1.4$, $h_0 = 180$ MPa, $a = 2.25$, $s_s = 148$ MPa and $s_0 = 16$ MPa. These parameters are for copper and it is acknowledged that they are not suitable for modeling the hardening behavior of aragonite; new simulations are being run with more appropriate hardening parameters: $q = 1.4$, $h_0 = 180$ GPa, $a = 2.25$, $s_s = 148$ GPa and $s_0 = 10$ GPa.

4.2 Results

4.2.1 Results for elastic finite element model

Isotropic elastic model:

The results for the isotropic elastic finite element model are plotted with the experimental results for nanoindentation reported in section 3.6.2 in figure 4.2.1.

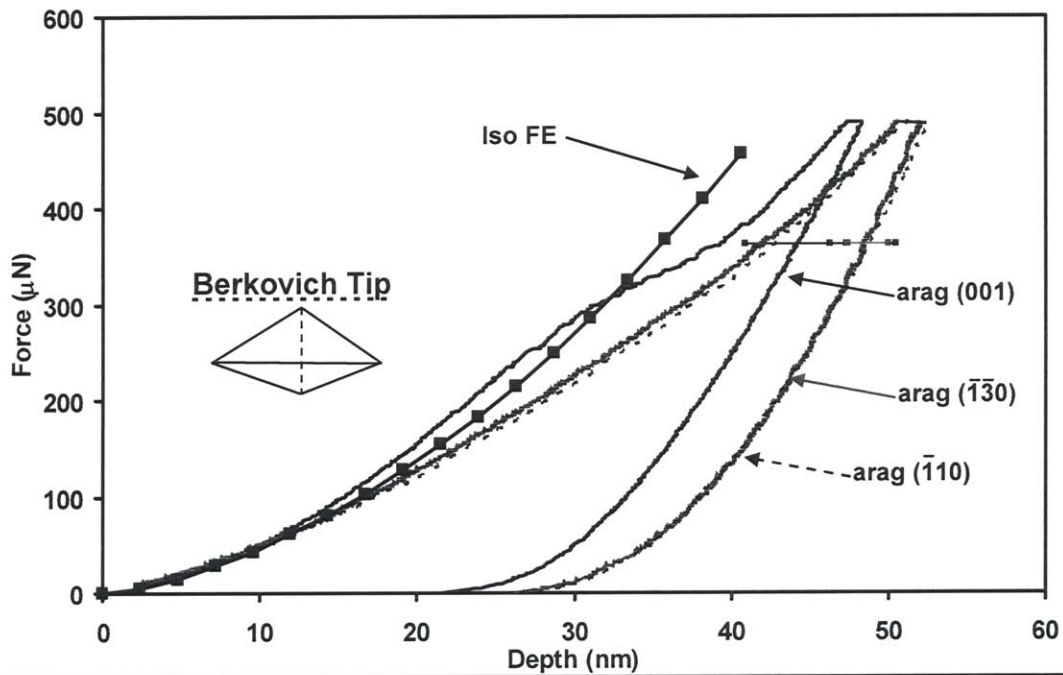


Figure 4.2.1 Overlay of isotropic finite element simulation result with the averaged experimental load-unload curves for single crystal aragonite on the (001), ($\bar{1}10$) and ($\bar{1}\bar{3}0$) planes.

The isotropic model matches the data for the (001) reasonably well up until the onset of plasticity (which we take here to be where the slope change occurs in the averaged data). As previously discussed the nanoindentation data for the ($\bar{1}10$) and ($\bar{1}\bar{3}0$) planes show some amount of

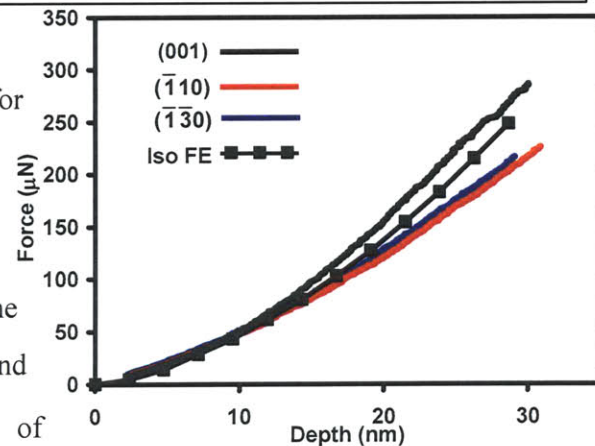
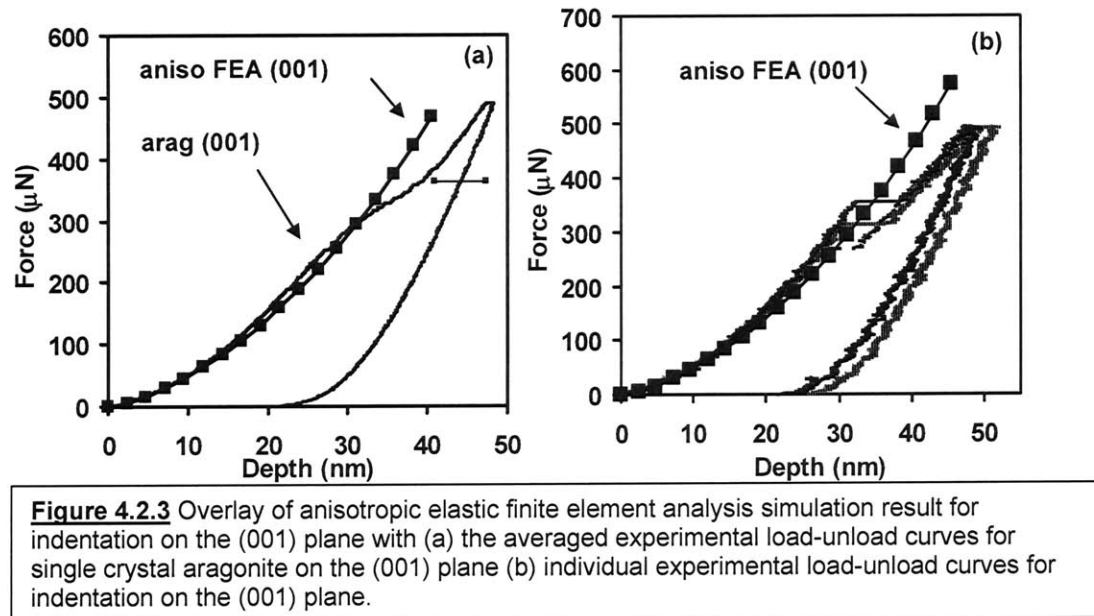


Figure 4.2.2 Low load/depth portion of curve shown in figure 4.2.1

anisotropy in their O-P reduced elastic moduli: the values for the (001), $(\bar{1}10)$ and $(\bar{1}\bar{3}0)$ planes were 102.8 ± 2.4 GPa, 100.1 ± 3.4 GPa and 108.1 ± 2.3 GPa respectively (for the Berkovich data, maximum load $1000\mu\text{N}$). However, this anisotropy is $<7\%$ and thus we expect the elastic response to be similar for each of the curves. If we investigate the very low load region (see figure 4.2.2), the isotropic finite element simulation does match all three planes with reasonable accuracy.

Anisotropic elastic model:

The results for the anisotropic elastic model, using the experimentally determined constants reported by Lui et al [2005], are plotted with the averaged experimental load-unload data for nanoindentation on the (001) plane in figure 4.2.3(a). The anisotropic elastic simulation is quite consistent with the experimental data for single crystal aragonite for the initial portion of the curve (the elastic regime). The low load/depth portion of the curve is shown in figure 4.2.4 showing excellent agreement.



It is clear that the experimental data deviates from the elastic curve when the dramatic slope change occurs for the experimental data (see comparison of data in figure 4.2.3). It was discussed in chapter 3 that this slope change occurs due to load plateaus in the

individual curves and figure 4.2.3(b) plots the simulation data with three sample individual curves.

This result is consistent with our hypothesis that the load plateaus represent the onset of plasticity in the aragonite. The elastic curve matches the experimental data up until the load plateaus occur, which is further evidence that we are in the elastic regime until this point and that the load plateaus represent the initiation of plasticity as discussed in Chapter 3.

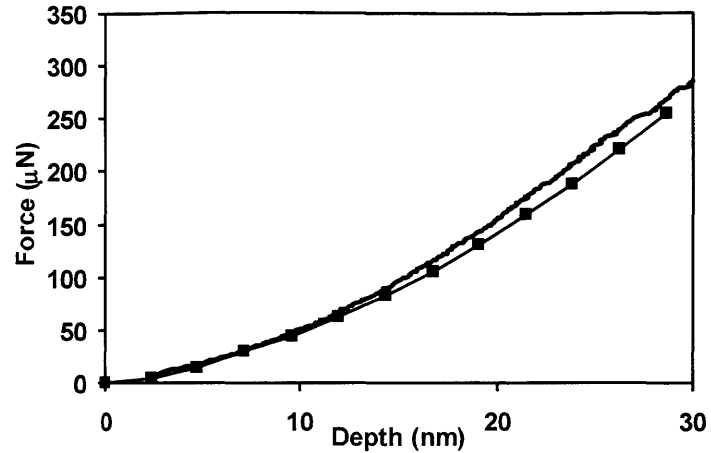
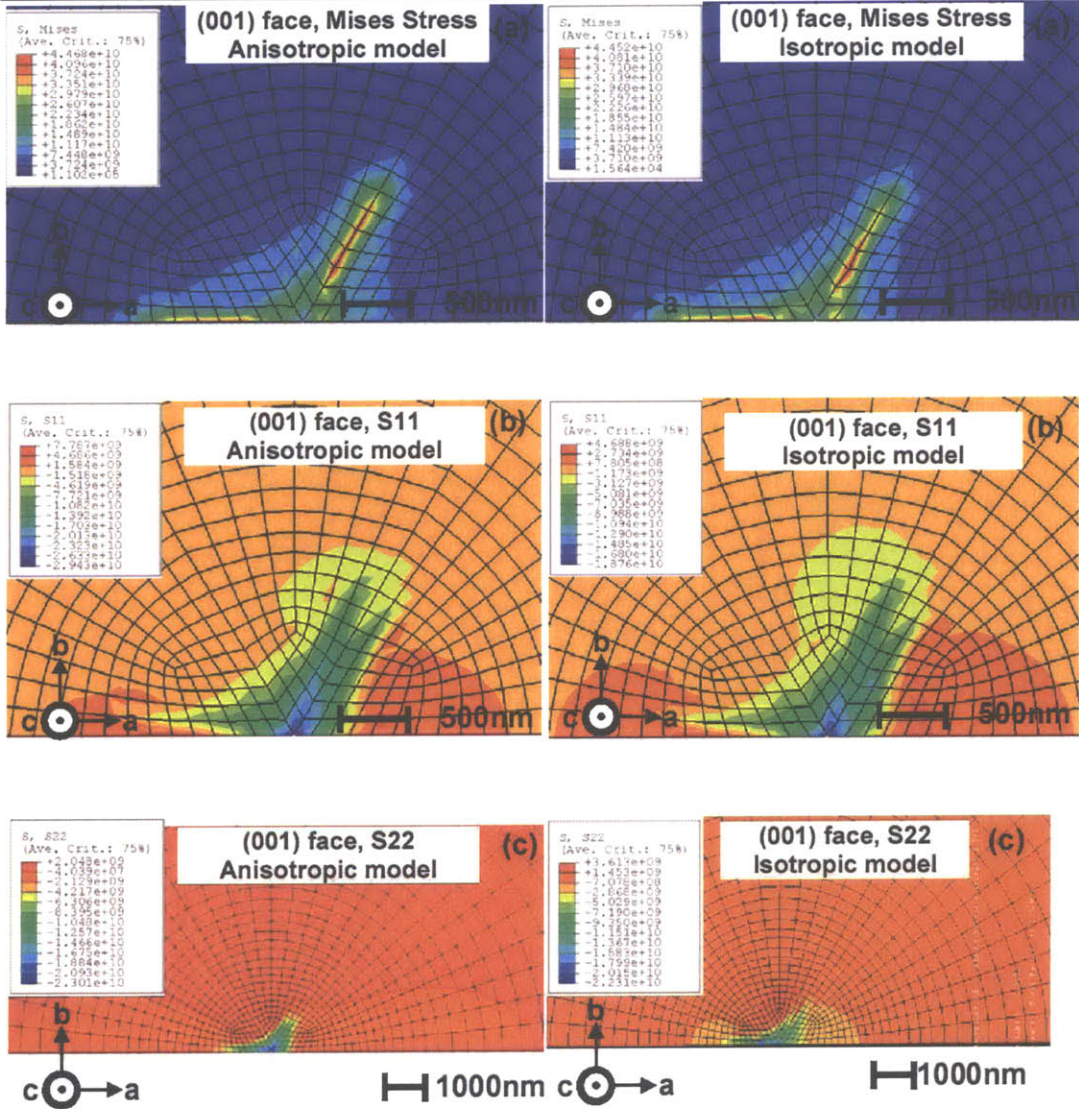
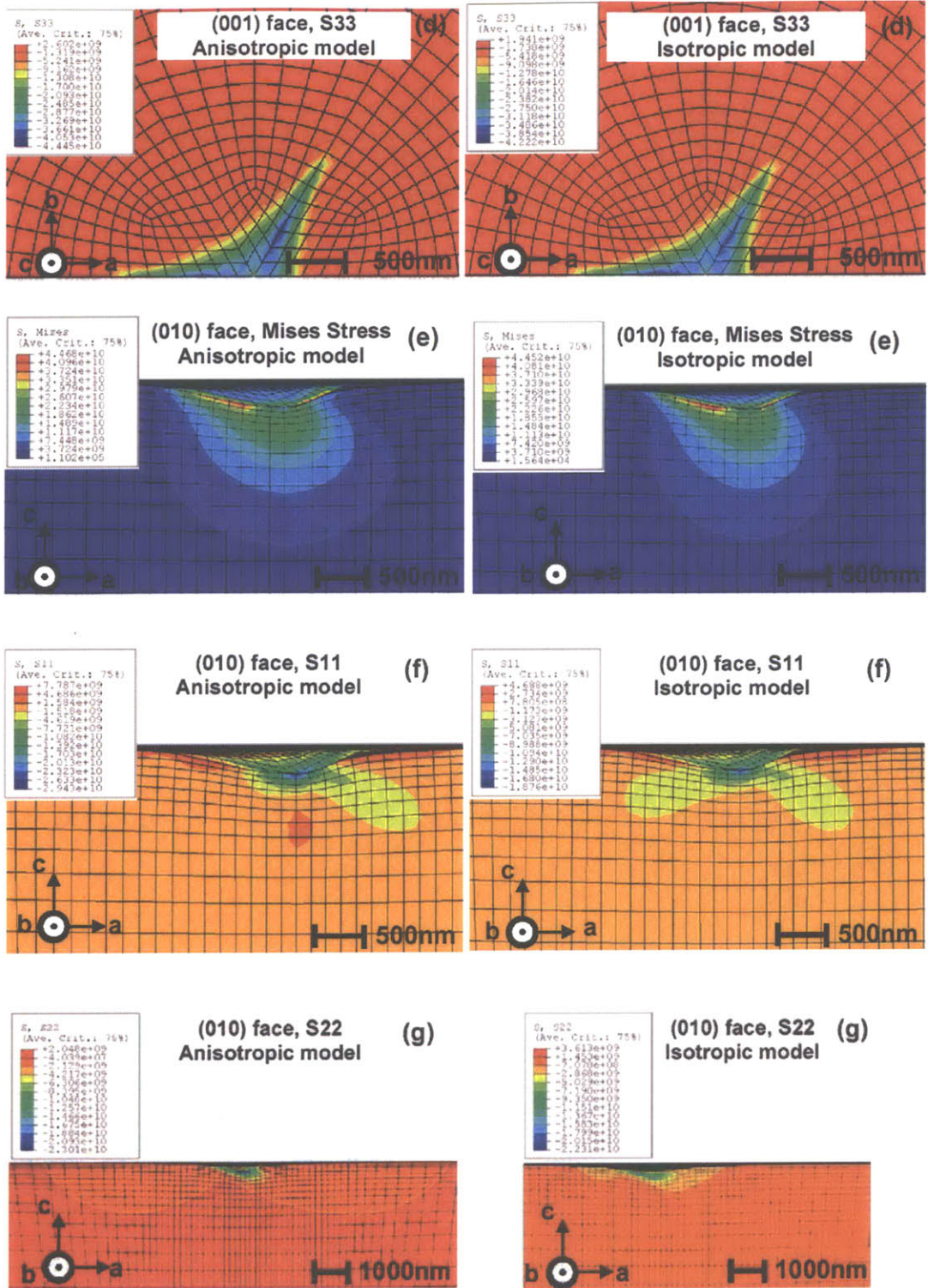


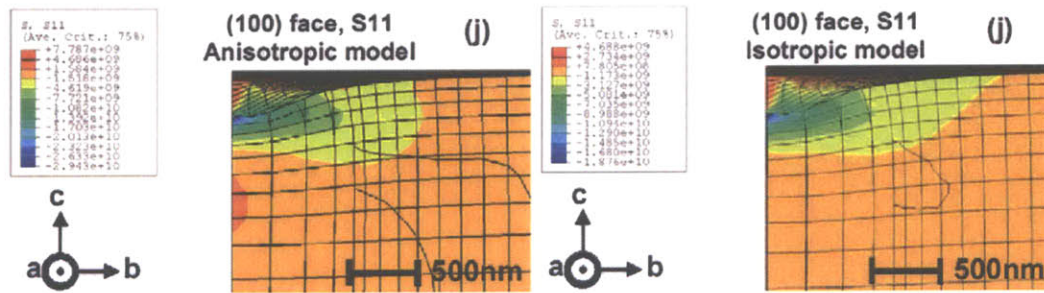
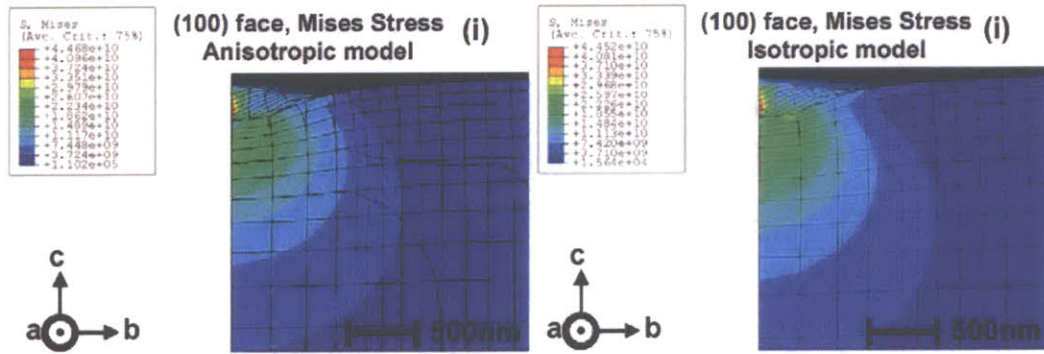
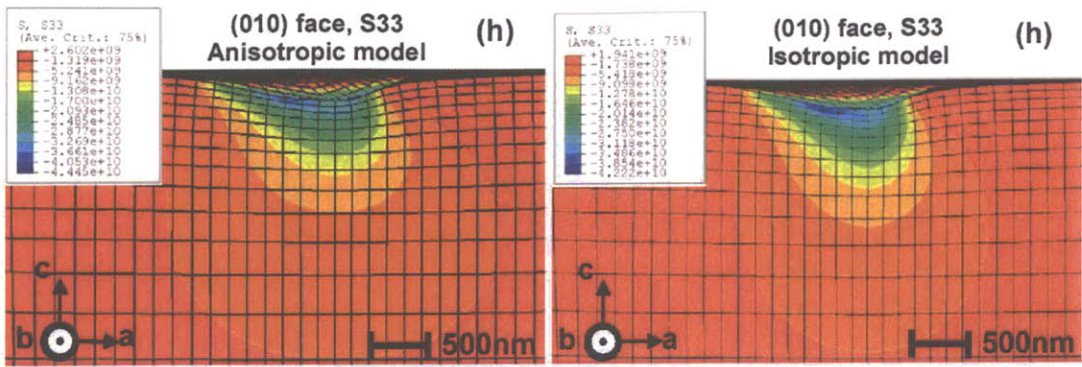
Figure 4.2.4 Low load/depth portion of curve shown in figure 4.2.3 (a).

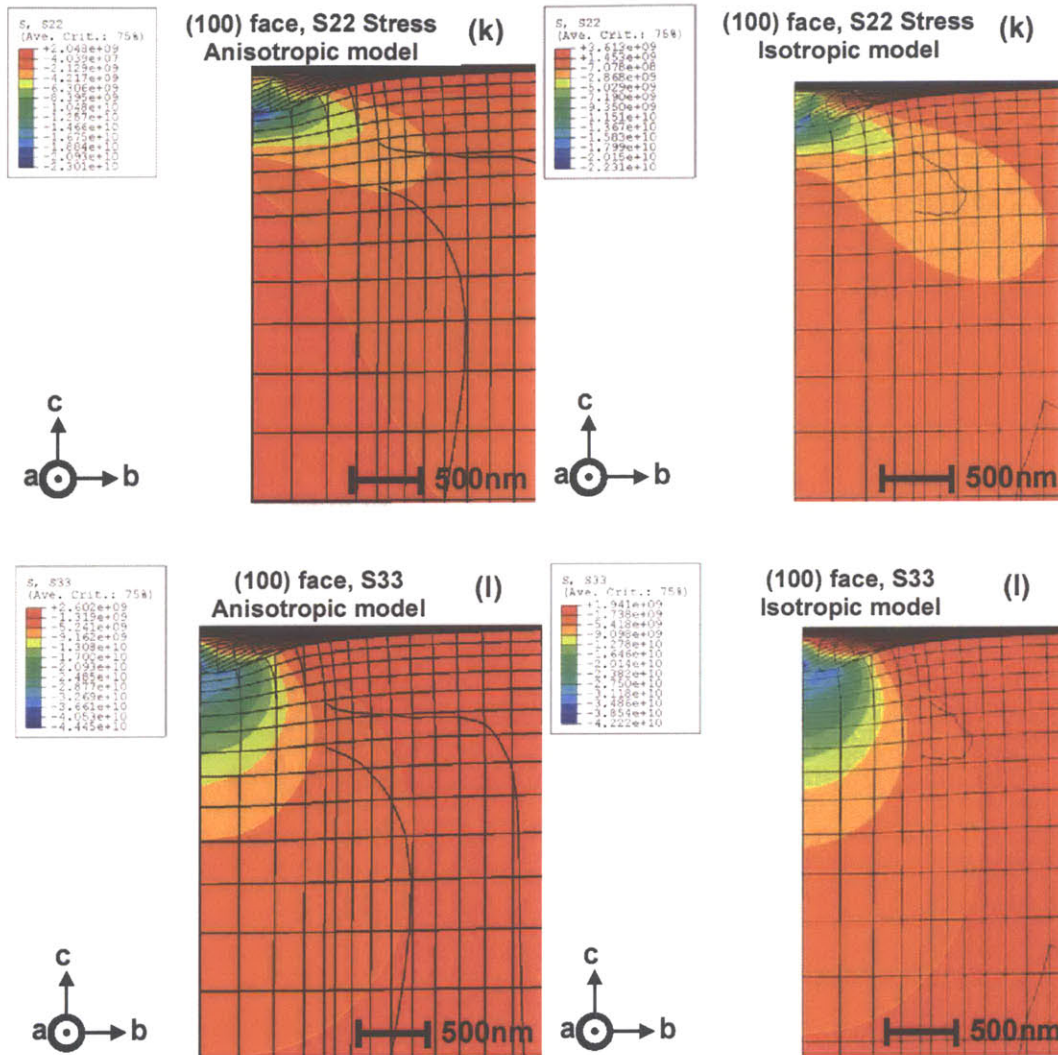
In figure 4.2.5, the stress contours for the anisotropic and isotropic finite element models are compared. The contours are shown for the models loaded to the average force at which the first load plateau occurs in the Berkovich experimental data ($285\mu\text{N}$, which was the closest incremental value below the experimentally observed average value of load plateau, $309\mu\text{N}$). This enables a rough approximation of the yield strength of single crystal aragonite for indentation on the (001) plane, by examining the Mises stress. Both the anisotropic and isotropic model give values of ~ 20 GPa. This value is reasonably consistent with the yield strength reported previously for simulations of nanoindentation in freshly cleaved (dry) nacre tablets, by Bruet et al [2005], of 11GPa. The experimental data, as reported in section 3.8, suggests a higher yield strength for the nacre tablets than for the single crystal aragonite. The ~ 20 GPa reported here is for the Mises stress and thus only a first approximation of the yield strength of the single crystal aragonite; the actual value of yield strength is directionally dependent and a function of the critical resolved shear stress on specific slip systems. Future work on the critical resolved shear stresses of various slip systems and the hardening parameters will enable a more accurate comparison.

Figure 4.2.5 Stress contours from ABAQUS finite element simulations of Berkovich indentation. The contours are plotted at the average load plateau force level $\sim \mu\text{N}$. The anisotropic results are in the left column and the isotropic results are in the right column. The (010) face is sectioned through the centre point of the indenter. Stress contours shown are for (a) (001) face, Mises stress (b) (001) face, S11 (c) (001) face, S22, (d) (001) face, S33 (e) (010) face, Mises stress (f) (010) face, S11 (g) (010) face, S22 (h) (010) face, S33 (i) (100) face, Mises stress (j) (100) face, S11 (k) (100) face, S22 (l) (100) face, S33. Note that the *a*-axis is aligned with the 1-axis; the *b*-axis is aligned with the 2-axis; the *c*-axis is aligned with the 3-axis









The stress values distributions are approximately similar for both the isotropic and anisotropic models, although the stress for the anisotropic material is typically marginally higher. The simulations were displacement controlled and given the elastic constants in the 1-, 2- and 3- directions ($C_{11} = 171.1, C_{22} = 110.1, C_{33} = 98.4$) for the anisotropic model are higher than the Young's modulus for the isotropic model ($E = 92$ GPa) and the shear constants for the anisotropic model ($C_{44} = 39.3, C_{55} = 24.2, C_{66} = 40.2$) are on average higher than the shear modulus for the isotropic model (~ 39 GPa: calculated from $E = 92$ GPa and $\nu = 0.17$), this result is expected. The stress contours for the anisotropic model are more directionally dependent than the isotropic model.

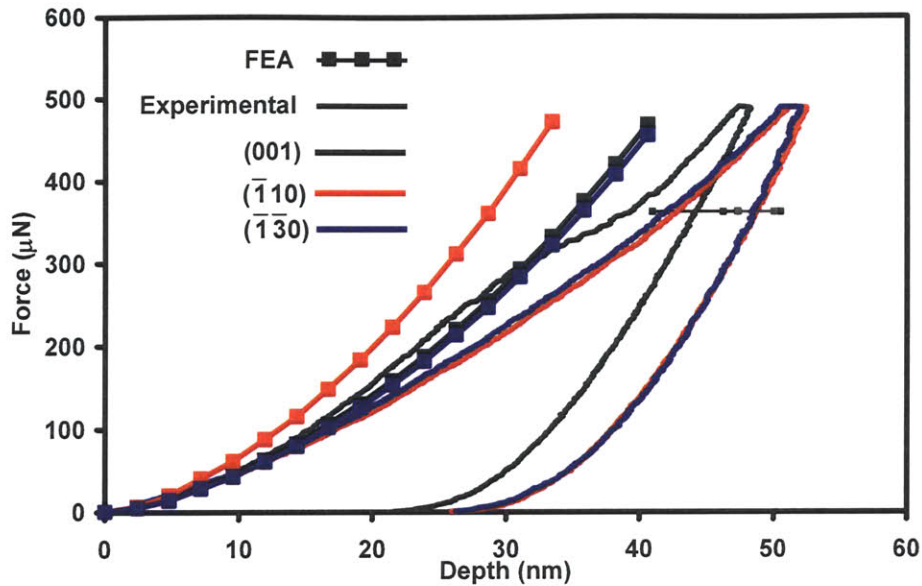


Figure 4.2.6 Comparison of anisotropic elastic finite element analysis simulations for the (001), $(\bar{1}10)$ and $(\bar{1}\bar{3}0)$ planes with the experimental data.

The simulations were also performed for the $(\bar{1}10)$ and $(\bar{1}\bar{3}0)$ planes and the results are plotted in figure 4.2.6. The $(\bar{1}\bar{3}0)$ matched the experimental data in the early portion of the curve, whereas the modeled $(\bar{1}10)$ data appears to be a lot stiffer than the experimental data. As a first approximation, the stiffness for the 1, 2, 3 directions from the transformed matrix ($C_{11} = 158.1, C_{22} = 122.7, C_{33} = 98.4$), can be used to interpret the behavior since the loading compresses in these three directions. The 1- direction stiffness is the highest of the three values, which is the $(\bar{1}10)$ plane and this plane has the stiffest response. The Oliver Pharr reduced values for the (001), $(\bar{1}10)$ and $(\bar{1}\bar{3}0)$ planes were 102.8 ± 2.4 GPa, 100.1 ± 3.4 GPa and 108.1 ± 2.3 GPa respectively, which does not show the $(\bar{1}10)$ as the stiffest plane. However, the difference in elastic moduli among the three planes is <7% and the O-P analysis is an approximation since it assumes an isotropic material. From the O-P reduction we would expect the stiffness response for the (001) and $(\bar{1}\bar{3}0)$ to be quite similar and the response of the (001) plane is only marginally stiffer than the $(\bar{1}\bar{3}0)$ plane. If the C_{11} and C_{22} values are compared (from the transformed matrix), it is expected that the $(\bar{1}\bar{3}0)$ would be significantly stiffer,

however, this is not the case for the experimental or FEA data. This is likely due to the fact that the stress state is multiaxial, with normal and shear stresses and, thus, a comparison based on C_{11} and C_{22} alone is not appropriate given the anisotropic nature of the material combined with the inhomogeneous multiaxial stress field. The low load/penetration depth region is shown in figure 4.2.7.

As previously discussed in section 3.6.2 the elastic region of the $(\bar{1}10)$ and $(\bar{1}\bar{3}0)$ planes being much smaller relative to the (001) plane may be attributable to plasticity

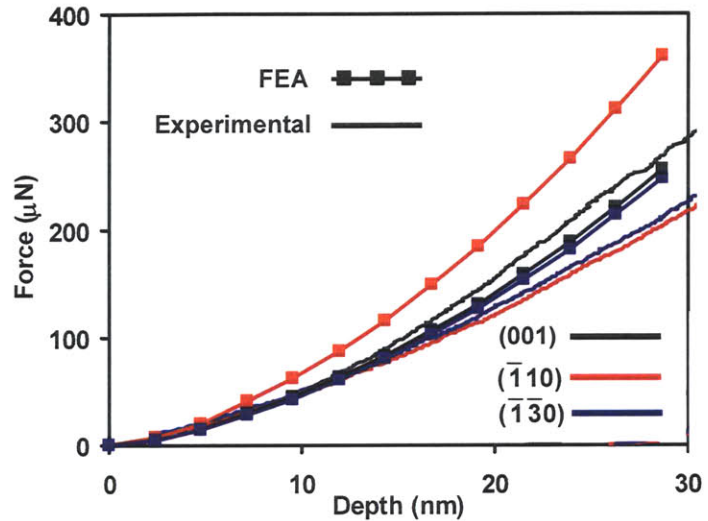


Figure 4.2.7 Low load/depth portion of curve shown in figure 4.2.6.

occurring at a much lower load due to preferential orientation of the slip systems and thus the elastic region of these curves is not as pronounced as that for the (001) plane. This is supported by the O-P reduction of the hardness values for the $(\bar{1}10)$ and $(\bar{1}\bar{3}0)$ planes (4.6 ± 0.3 GPa and 4.36 ± 0.4 GPa respectively) that are $\sim 2/3$ that of the (001) plane (6.2 ± 0.3 GPa) indicating plasticity would initiate at smaller indent loads. This is also dependent on which slip systems are activated in the different indent directions. There was little evidence of load plateaus in the experimental data for the $(\bar{1}10)$ and $(\bar{1}\bar{3}0)$ planes, and thus it is possible that first yield occurs at a lower load than the (001) plane and is a more diffuse set of events in these directions.

4.2.2 Results for elastic-plastic finite element model

As discussed in Chapter 3 very limited data exists on the mechanical properties of aragonite. Given the modeling success of the crystal plasticity model as outlined in

section 4.1.2 above, it was used as an investigative tool for our material to find the activated slip systems in the observed anisotropic plastic pile-up in the experimental data.

Based on the results of high temperature and pressure experiments in aragonite, the systems $(010)[100]$ [Veit, 1922; Renner et al, 1996] and $(001)[010]$ [Renner et al, 1996] have been proposed. Rybacki [Rybacki et al, 2003] also noted (001) to be the predominant glide plane. Our data showed pile-up on the c -plane which is only kinematically admissible if slip occurs in the (001) direction or at some angle point out of the c -plane. With these observations in mind, the slip systems postulated for the simulations were the cubic family, $\{100\}\langle 001\rangle$. These systems are shown in figure 4.2.8.

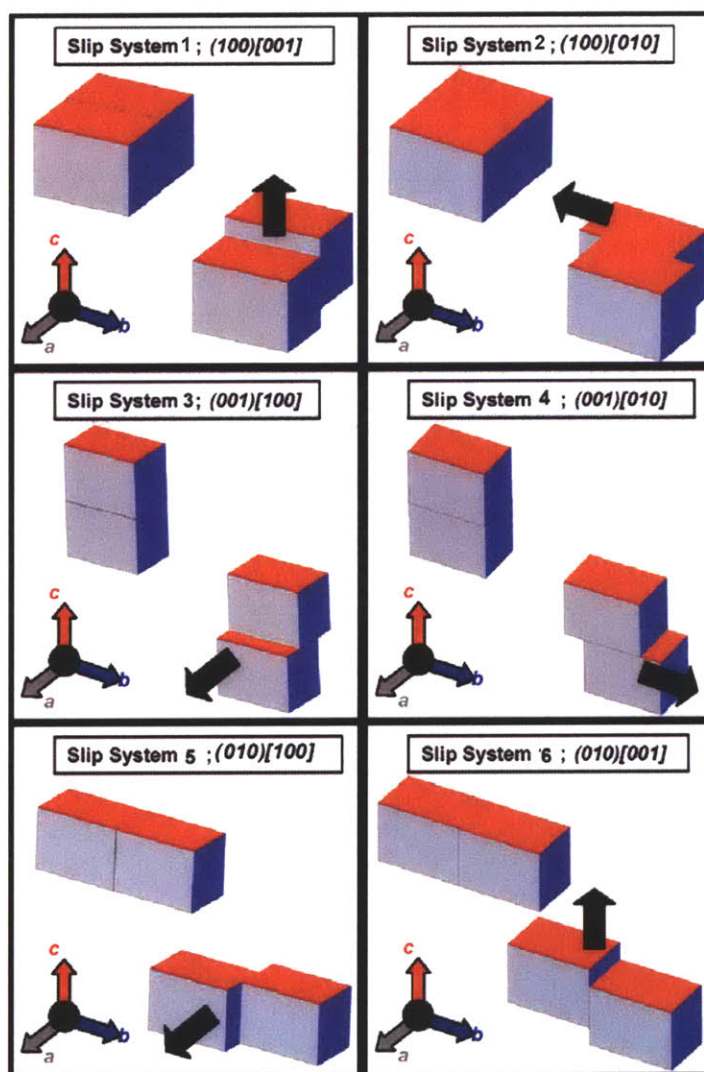


Figure 4.2.8 Initially postulated slip systems based on investigations by previous authors [Veit, 1922; Renner et al, 1996; Rybacki et al, 2003]

The postulated systems were then applied to the model of cono-spherical indentation. Since the cono-spherical tip is geometrically symmetric, this tip removes geometric anisotropy and isolates any observed anisotropic behavior to be due to the crystal plasticity alone. The result of the cono-spherical indentation using the cubic slip systems is illustrated in figure 4.2.9.

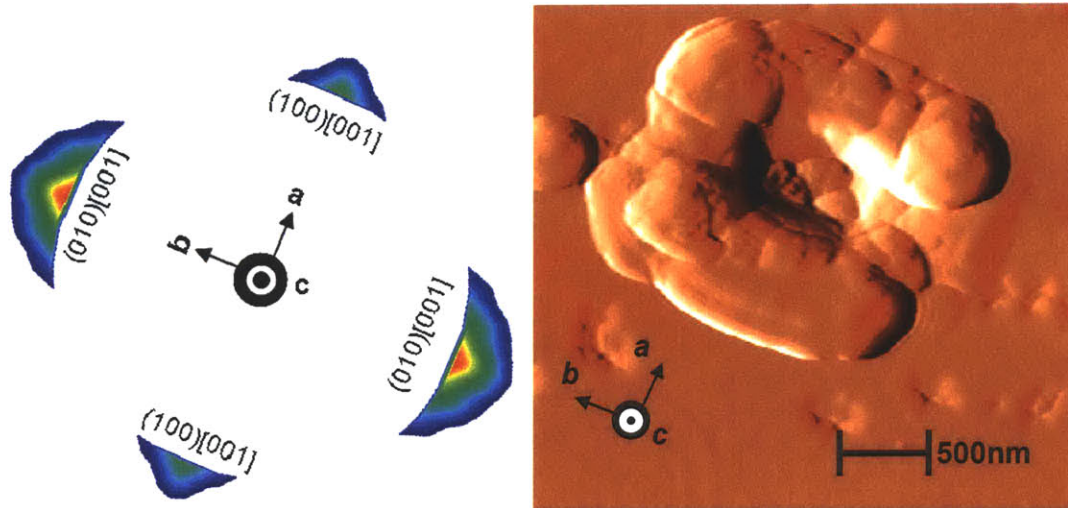


Figure 4.2.9 Results of the Abaqus single crystal plasticity model using the cubic family of slip systems $\{100\}\langle 001\rangle$, with the predominant slip system in each pile up zone labeled [courtesy of Z. Zhao].

It is clear that the simulations and initially postulated slip systems do not match the cono-spherical experimental data. If the geometry of the pile-up is examined, however, the relative angles of the four pile-up lobes are equivalent to the ratio of the sides of the lattice unit cell a/b (see figure 4.2.10).

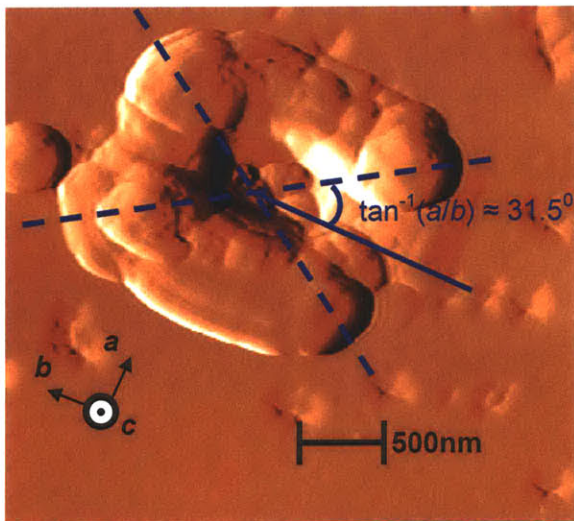


Figure 4.2.10 Schematic showing the ratio of the pile-up angles is closely related to the length of the unit crystal sides. The measured angle is 32.5° and the calculation from the crystal unit cell axis lengths is shown ($\approx 31.5^\circ$).

This observation led to the proposition of an additional set of active slip systems for aragonite. It was postulated based on our observation that the $(110)[001]$ and $(\bar{1}10)[001]$ systems would capture the experimental data, thus the $\{110\}\langle 001\rangle$ family of slip systems was added to the simulation. Schematics of these slip systems are indicated in figure 4.2.11.

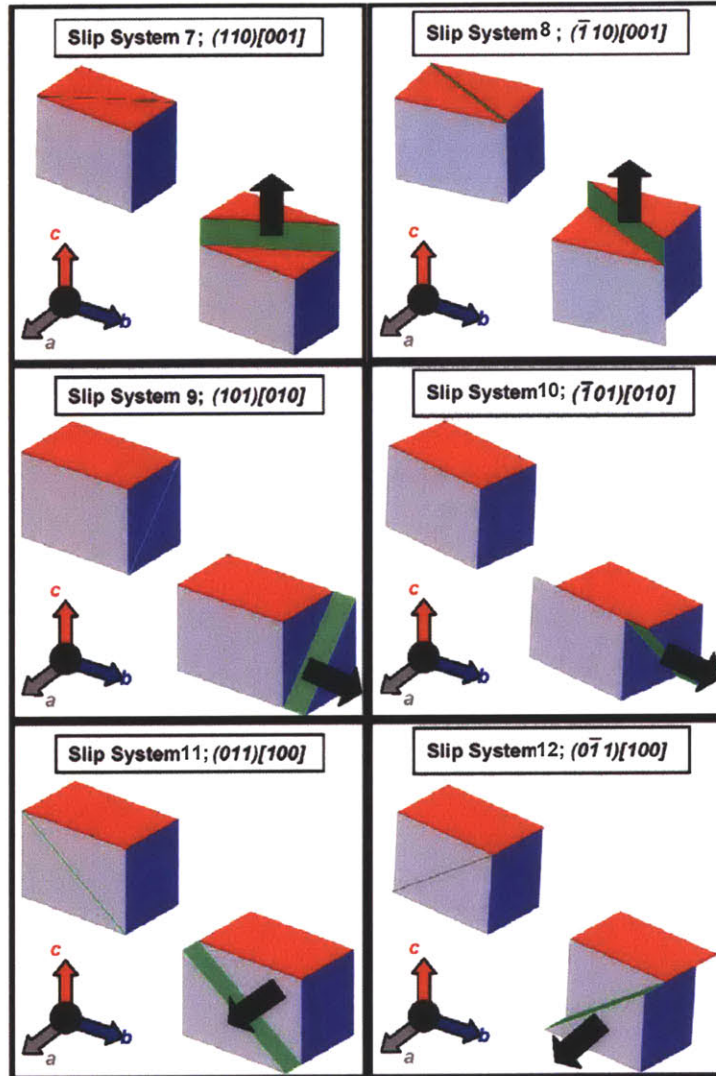


Figure 4.2.11 Schematic of additional postulated slip systems, which are slip on the diagonal planes in the normal directions.

With the new slip systems added to the original cubic family of slip systems, the cono-spherical simulation was repeated. This set of slip systems matched the data quite accurately and the results are plotted below in figure 4.2.12. Given that all systems were given the same resistance and evolution of hardening, each system had an equal opportunity to be activated. The governing roles of the $(110)[001]$ and $(\bar{1}\bar{1}0)[001]$ were evident from the simulation and thus are taken to be active systems in aragonite.

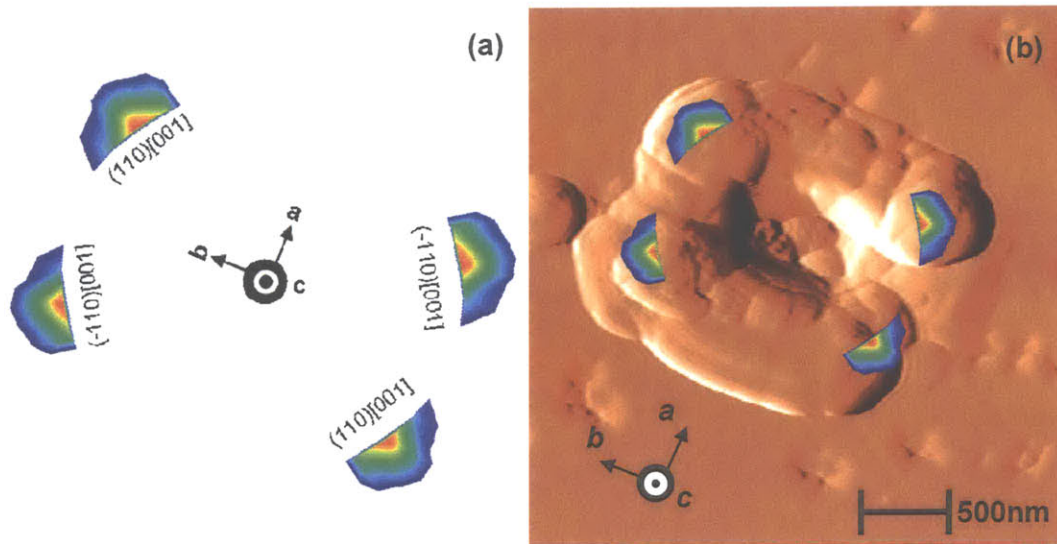


Figure 4.2.12 Results of cono-spherical simulations (a) showing the governing roles of the $(110)[001]$ and $(\bar{1}\bar{1}0)[001]$ slip systems (b) showing the close correlation with experimental data [courtesy of Z. Zhao].

Cross-sectional slices were taken through the modeled sample to examine the kinematic mechanisms leading to the experimentally observed slip. These cross-sections along with a schematic explaining the kinematic mechanisms are plotted in figure 4.2.13. It should be noted that the scale of slip in these cross-sections (represented by the color gradient) is not equivalent for each system, with the $(110)[001]$ and $(\bar{1}\bar{1}0)[001]$ exhibiting the most slip. The material flows downwards away from the indenter in the $[001]$ direction and then laterally in the $[100]$ and $[010]$ directions. The observed pile-up then results by the upwards slip on the $(110)[001]$ and $(\bar{1}\bar{1}0)[001]$ systems.

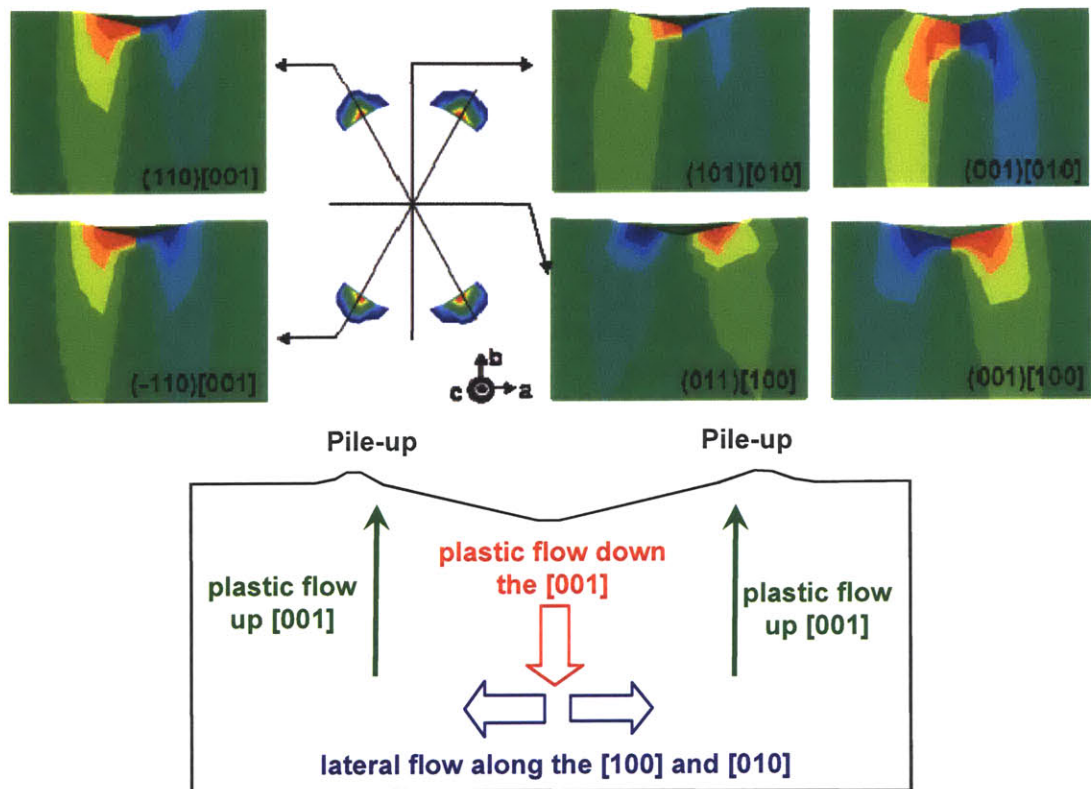


Figure 4.2.13 Pile-up mechanism of single crystal aragonite under nanoindentation with cono-spherical indenter. (a) shows through thickness cross sections showing contours of amount of slip activity in indicated individual slip systems (red color indicates maximum positive slip and blue color indicates maximum negative slip and green color is unslipped region). (b) schematic representation of the proposed pile-up mechanism [courtesy of Z. Zhao].

With the cono-spherical data successfully modeled using the 12 slip systems, the model was then employed to simulate the Berkovich data. The Berkovich simulation is, thus, used to verify the postulated slip systems based on the cono-spherical data.

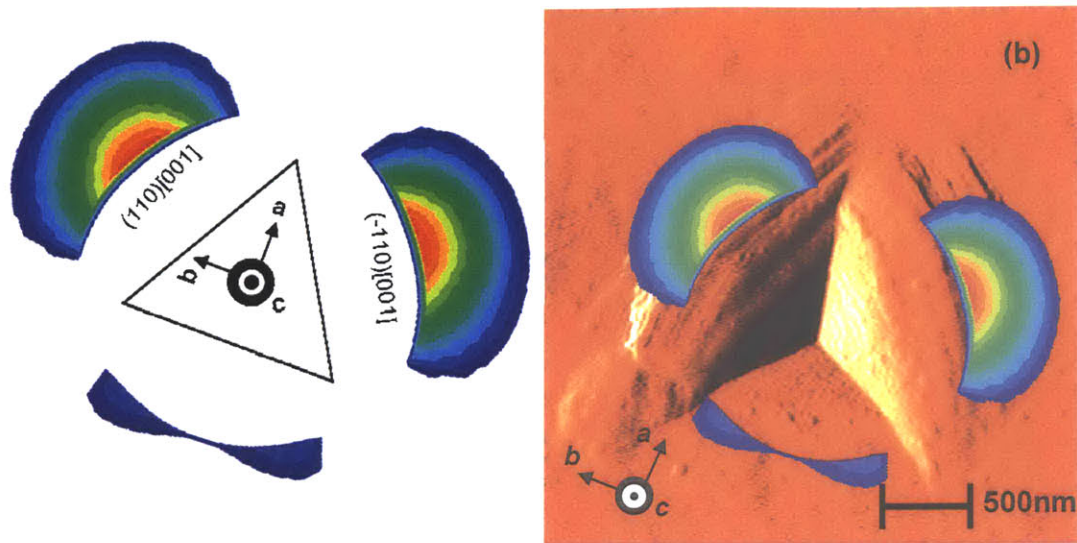


Figure 4.2.14 Pile-up mechanism of single crystal aragonite under nanoindentation with Berkovich indenter. (a) shows through thickness cross sections showing contours of amount of slip activity in indicated individual slip systems (red color indicates maximum positive slip and blue color indicates maximum negative slip and green color is unslipped region). (b) schematic representation of the proposed pile-up mechanism [courtesy of Z. Zhao].

The model data captured the Berkovich simulations quite well and once again the predominant slip is on the $(110)[001]$ and $(\bar{1}10)[001]$ slip systems. Hence, this strongly suggests that the previously unreported $(110)[001]$ and $(\bar{1}10)[001]$ slip systems have a governing role in the plastic behavior of aragonite. Although no precise conclusions can be drawn, if the crystal structure is examined (see figure 4.2.15), the $(110)[001]$ and $(\bar{1}10)[001]$ systems are plausible.

It is believed that the four pileup lobes seen in the cono-spherical indents, due to slip on $(110)[001]$ and $(\bar{1}10)[001]$ systems result in pileup on two indenter sides for the Berkovich indenter; two pileup lobes are exaggerated due to favorable orientation with the indenter and two are suppressed due to nonfavorable orientation. This is, as shown in figure 4.2.14, true for indentation with the a -axis perpendicular to one indenter side and the b -axis parallel to one indenter side. It is hoped that future modeling work will investigate the different orientations of the sample relative to the Berkovich indenter to examine the various pileup patterns in section 3.6.3.

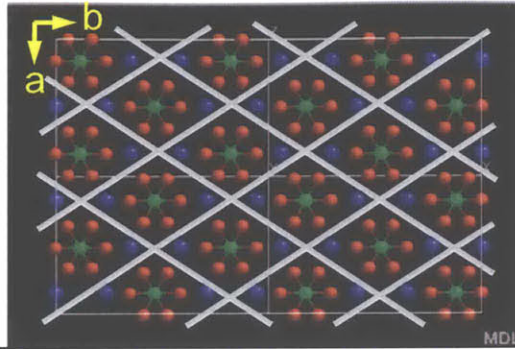


Figure 4.2.15 Image of the a - b plane of CaCO_3 aragonite structure highlighting the plausibility of the $(110)[001]$ and $(\bar{1}10)[001]$ systems.

The slip systems modeled here were for slip on the diagonal planes in the orthogonal directions, i.e. the family $\{110\}\langle 001\rangle$, based on the olivine reported systems and the experimental observation of the banded pileup (see figure 3.6.6) surrounding the Berkovich indenter, which was suggestive of vertical slip. Another possible set of systems would be slip on the diagonal planes in the diagonal directions, i.e. $\{110\}\langle \bar{1}10\rangle$ and future studies will investigate the plausibility of these systems.

4.4 Summary

ABAQUS Finite Element simulations were used to capture both the elastic and plastic behavior of single crystal aragonite. The elastic simulations accurately captured the load displacement data for the low load (elastic) regime of the (001) and $(\bar{1}\bar{3}0)$ experiments but did not match the $(\bar{1}10)$ as well. It is believed that the $(\bar{1}10)$ system enters the plastic regime at lower depths than the other planes due to preferential orientation of the slip systems. The Mises stress contours for the anisotropic and isotropic simulations were examined at the average first load plateau depth to give an approximate value for Yield strength of single crystal aragonite of 20GPa. This value is higher than that reported for nacre tablets [Bruet et al, 2005], although experimental data suggests nacre tablets have a higher yield stress. Future work evaluating the critical resolved shear stress on specific slip systems and accurate hardening parameters will enable a more accurate comparison to be made.

Limited data exists on the plastic behavior of aragonite and thus a single crystal plasticity model that has been previously successfully employed for numerous applications was used to interrogate the slip systems activated. The cono-spherical indenter was used to find the correct slip-systems initially as it is symmetric and the observed anisotropic pile up can be attributed solely to the crystal anisotropy.

The investigation began by postulating the cubic family of slip planes based on previous experiments at high temperatures and pressures on porous and polycrystalline aragonite. This set of slip systems failed to capture the cono-spherical pile-up. It is observed that the four lobes of the cono-spherical pile-up are oriented at angles equal to the lattice ratio, a/b and this suggested including the $\{110\}\langle 001\rangle$ family of planes in the model. With these planes added to our cubic set of planes, the model successfully captured the data and the pile-up was predominantly governed by slip on the $(110)[001]$ and $(\bar{1}10)[001]$ systems. The 12 systems that successfully captured the cono-spherical data were then employed to capture the berkovich data and successfully reproduced the observed experimental pile-up. It is hoped that future studies will be used to investigate other possible slip systems, specifically the $\{110\}\langle \bar{1}10\rangle$ family.

Chapter 5 *Conclusions and Future Work*

The primary experimental and modeling efforts reported in this Thesis investigate the inorganic component of seashell nacre, aragonite. This component, as with most inorganic minerals in biocomposites, is crystallographic in nature. The tablets have a strong preferential orientation where a tablet plane is orthogonal to the *c*-axis of aragonite. It is strongly believed that the crystallographic orientation plays an important role in the material behavior of the biocomposite, although the link between crystallographic orientation and function is still not fully understood [see, for example, Lowenstam et al, 1989; Weiner et al, 2005].

The microscale design features of seashell nacre were investigated using high resolution microscopy (SEM, AFM). The cross-sectional ‘brick and mortar’ view was examined for tablet overlap between neighboring planes ($22.2 \pm 9\%$) and tablet length $7.8 \pm 2.7\mu\text{m}$. Top view images of nacre revealed the nucleation zones and tablet sector boundaries and a new protocol was used to obtain SEM images of nacre where the top-plane of tablets is transparent revealing the layer below. A *SolidWorks* 3-D model was then created based on an SEM image in which the top layer is transparent and this was used for geometrical analysis of the seashell nacre. The tablet area was found to be $57.4 \pm 19 \mu\text{m}^2$ and cross-sectional cuts (revealing the brick and mortar structure) of the *SolidWorks* model gave tablet lengths of $\sim 6.7 \mu\text{m}$ and overlap of $\sim 22\%$. A Voronoi tessellation layer, using the nucleation zones as the scatter points, was used to create a layer assuming homogenous growth. This layer matched the layers from the *Solidworks* model, suggesting that there is no growth bias in plane.

Aragonite is ubiquitous in biological and geological systems, yet a fundamental mechanistic understanding is still lacking. This Thesis presents the first investigation into the anisotropic nanoscale plasticity of single crystal aragonite. This study was performed using three indenter tips: Berkovich, cono-spherical and Knoop. For the Berkovich and cono-spherical indenters, loads of $500\mu\text{N}$ and $1000\mu\text{N}$ were used to investigate the small

scale behavior of aragonite on three mutually orthogonal planes, the (001), ($\bar{1}10$) and ($\bar{1}\bar{3}0$). Anisotropic behavior between the three planes was apparent from the load-unload data. This was confirmed by O-P analysis which gave (modulus, hardness) pairs of (102.8 ± 2.4 GPa, 6.2 ± 0.3 GPa), (100.1 ± 3.4 GPa, 4.6 ± 0.3 GPa) and (108.1 ± 2.3 GPa, 4.36 ± 0.4 GPa) for the (001), ($\bar{1}10$) and ($\bar{1}\bar{3}0$) planes respectively (reduction of the curves for maximum load of $1000\mu\text{N}$ for the Berkovich tip). The (001) plane is the hardest of the three planes by $\sim 30\%$, with the anisotropy in the elastic modulus a lot less pronounced ($<7\%$).

For the (001) plane, distinct load plateaus occurred at loads of $309 \pm 27.6 \mu\text{N}$ for the Berkovich indenter and $424.4 \pm 61.0 \mu\text{N}$ for the cono-spherical indenter. As with other authors who have found similar response for indentation in crystalline materials [Page et al, 1992; Gerberich et al, 1996; Van Vliet et al, 2003], these loads are attributed to the onset of plasticity. These load plateaus were not seen in the nanoindentation data for the ($\bar{1}10$) and ($\bar{1}\bar{3}0$) planes. It is believed that this is due to preferential slip occurring on these systems at lower loads, which is supported by the recorded lower hardness of these planes.

Higher load indents ($5000\mu\text{N}$ and $10000\mu\text{N}$) were used to facilitate imaging using TMAFM. The Berkovich indents had pileup that typically occurred on just two indenter sides. A rotation stage was integrated into the nanoindentation rig to allow the single crystals to be rotated relative to the Berkovich nanoindentation tip. The imaged residual indents had pileup (typically on two indenter sides) that was orientation dependent, suggestive of slip on specific active systems. The cono-spherical indenter had pileup concentrated in four lobes surrounding the indenter. Since the cono-spherical indenter is geometrically symmetric, this bias in the pileup is solely attributable to the anisotropic crystal behavior.

Finite element simulations were performed to simulate the nanoindentation data. Isotropic elastic simulation data matched the (001) quite well up until the onset of

plasticity but was a poorer match for the $(\bar{1}10)$ and $(\bar{1}\bar{3}0)$ planes. Anisotropic elastic simulations of the three planes matched the data better in the low load regime. For the (001) plane, it matched the experimental curves up until the first load plateau.

An isotropic elastic, anisotropic plastic model was used to investigate and interrogate the active slip systems leading to the observed pileup. 12 systems $\{100\}\langle 001\rangle$ and $\{110\}\langle 001\rangle$ were postulated based on previous investigation at high temperatures and pressures on polycrystalline [Rybacki et al, 2003] and porous [Renner et al, 1996] aragonite and on olivine [Raleigh et al, 1968]. The pileup patterns accurately captured the experimentally observed pileup patterns and the governing roles of the (110)[001] and $(\bar{1}10)$ were observed.

There is still a dearth of data concerning the plastic behavior of single crystal aragonite. This Thesis has begun to explore the operative slip systems in single crystal aragonite and a new set of active slip systems has been proposed. The next step would be to investigate the slip systems on the other planes tested experimentally, namely the $(\bar{1}10)$ and $(\bar{1}\bar{3}0)$ planes. This will be possible through application of the single crystal plasticity model simulations presented in this Thesis, with the crystal structure reoriented to model the other planes.

It is hoped that the model can be used to investigate the hardening parameters of the active slip systems of single crystal aragonite. The investigation presented in this Thesis applied the single crystal plasticity model to investigate and interrogate the activate slip systems for the single crystal aragonite. However, as the aim was to find the active slip systems, each system included in the model was given the same hardening parameters equivalent to values previously presented for copper [Kalidindi et al, 1992]. Curve fitting can now be employed between simulated nanoindentation data and experimental data to interrogate the hardening parameters for the slip systems reported.

A component of mollusc shells, that relative to nacre has received comparatively little attention, is the hard outer prismatic layer, which is the first line of defense against attack

from predators. A comparative nanoindentation study between the calcitic prismatic layer and single crystal calcite, similar to the comparative study between the *c*-plane of the nacre tablets and the *c*-plane of single crystal aragonite will help us understand the role of the calcite within the prismatic layer. Appendix A presents early results for nanoindentation on the three cleavage planes.

Isolating the individual constituents of biocomposite materials and investigating their mechanical behavior at the nanoscale can yield a lot of information, which will help us understand the ultrastructural mechanisms used by nature. With this knowledge of the individual components, more sophisticated models of biocomposite materials can be developed, which will eventually lead to a better understanding of nature's secrets.

Appendix A *Nanoindentation study on the three cleavage planes of calcite*

A component of mollusc shells that relative to nacre has received little attention is the hard outer prismatic layer, which is the first line of defense against attack from predators. This material consists of mutually parallel, adjacent structural units of crystallographic calcite (the hexagonal form of CaCO_3) and an organic component between the prisms [Chateigner et al, 2000; Tong et al, 2002]. A comparative nanoindentation study between the calcitic prismatic layer and single crystal calcite, similar to the comparative study between the *c*-plane of the nacre tablets and the *c*-plane of single crystal aragonite has been initiated to help us understand the role of the calcite crystals within the prismatic layer.

A.1 Nanoindentation investigation of single crystal calcite using cono-spherical indenter

The three planes of the cleavage rhombohedron of calcite were indented using a cono-spherical indenter. Figure 3.5.1 (chapter 3) shows the cleavage rhombohedron within the hexagonal unit cell. With reference to the hexagonal unit cell co-ordinates, the planes of the cleavage rhombohedron are the set $\{10\bar{1}4\}$. The planes are labeled A, B, C here and future work with Laue X-ray diffraction will be used to identify and label which of the three planes are A, B and C respectively. The experimental techniques are identical to those presented for aragonite in section 3.6.1. The only exception was that the samples were gently cleaved with a hammer, which gave a sufficiently flat surface for nanoindentation and no polishing was required.

A.1.1 Nanoindentation Results for Cono-spherical indenter: Force vs. penetration depth curves

Averaged nanoindentation data (force vs. penetration depth for $n = 20$ experiments per set) for the three planes is graphed in figure A.1.1. The curves shown are for maximum loads of $500\mu\text{N}$ and $1000\mu\text{N}$ performed at a loading rate of $50\mu\text{N/s}$.

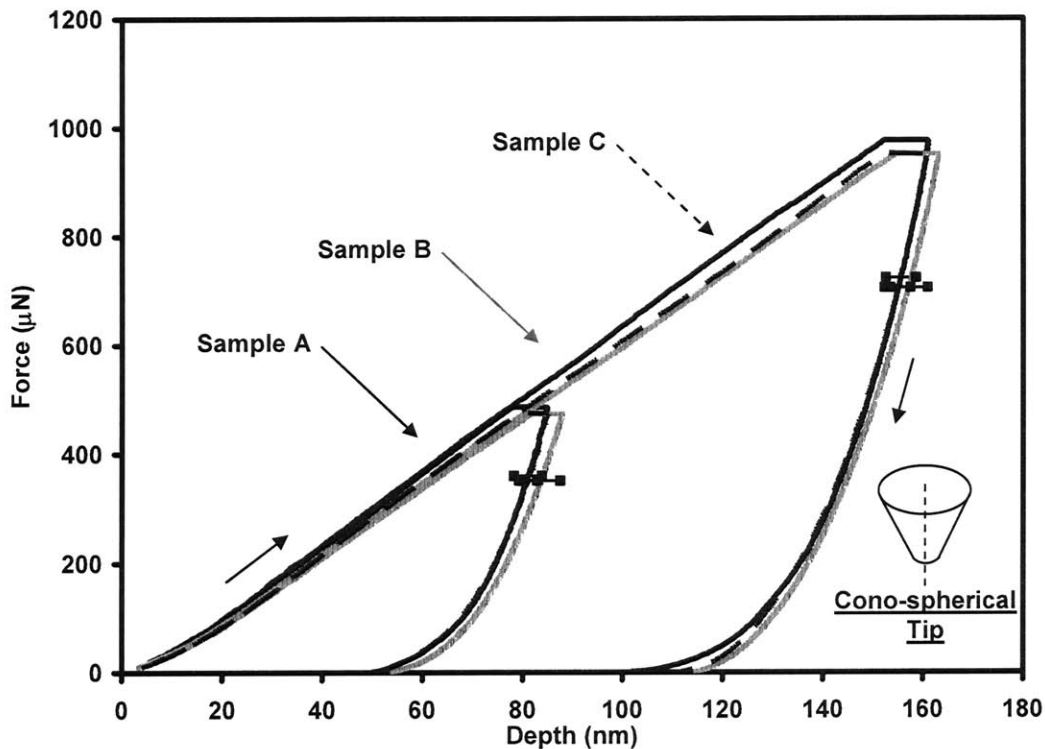


Figure A.1.1 Nanoindentation data for single crystal calcite using an (ideally) $1\mu\text{m}$ radius, 60° conical tip. Averaged curves on loading and unloading at maximum loads of $500\mu\text{N}$ (number of experiments, $n = 20$, $5\mu\text{m}$ spacing in both the X- and Y- direction between each indent) and $1000\mu\text{N}$ ($n = 20$) at a loading rate of $50\mu\text{N/s}$. The horizontal error bars indicate the maximum standard deviation of the curves for that particular dataset. Data with loading direction perpendicular to the three cleavage planes labeled A, B and C here are shown. Arrows indicate the direction of loading and unloading.

As is evident from the three loading-unloading curves for the cleavage planes, there is little anisotropy between the planes. All three curves follow a similar load-unload path and the residual impression depth, as measured from the unloading curves in figure A.1.1, was approximately equivalent for each curve. An O-P reduction was performed on

this data to give (modulus, hardness) pairs of (77.4 ± 3.7 GPa, 3.5 ± 0.1 GPa), (69.7 ± 3.2 GPa, 3.4 ± 0.1 GPa) and (74.3 ± 2.2 GPa, 3.4 ± 0.4 GPa) for the A, B and C plane at for indentations at maximum loads of $1000\mu\text{N}$. This verifies the approximately equivalent nanoscale mechanical behavior, in terms of elasticity and hardness, between the planes.

Figure A.1.2 shows a sample individual curve for each of the three planes at loads of $1000\mu\text{N}$. No distinctive load plateaus were seen in the individual load-unload curves as was seen in the individual curves for the (001) plane of single crystal aragonite.

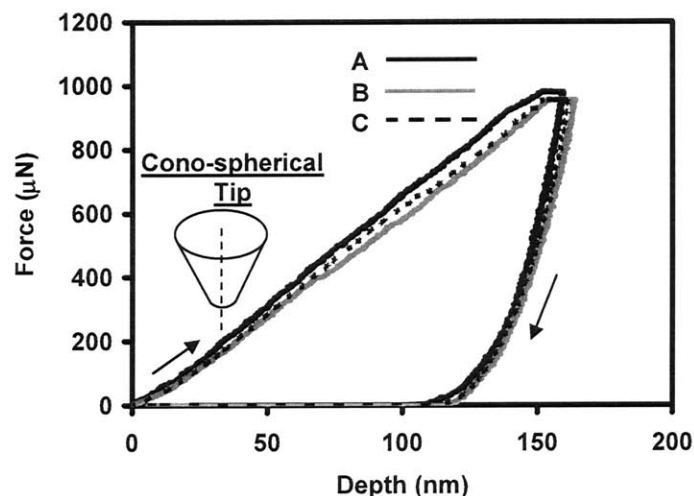


Figure A.1.2 Sample individual loading-unloading curves from the dataset shown in Fig. A.1.1. One curve is shown from each sample A, B and C as indicated. (maximum load = $1000\mu\text{N}$)

In figure A.1.3, the averaged load-unload data

for the three cleavage planes of calcite is plotted with the data for the three mutually orthogonal planes investigated for single crystal calcite. It is clear from the curves that the stiffness of the single crystal calcite and single crystal aragonite are similar (as measured from unloading curves) but the hardness of the calcite is less than the aragonite for the orientations investigated. The residual impression depths, as measured from the unloading curves, are significantly higher for the calcite curves. This results in the lower hardness for calcite.

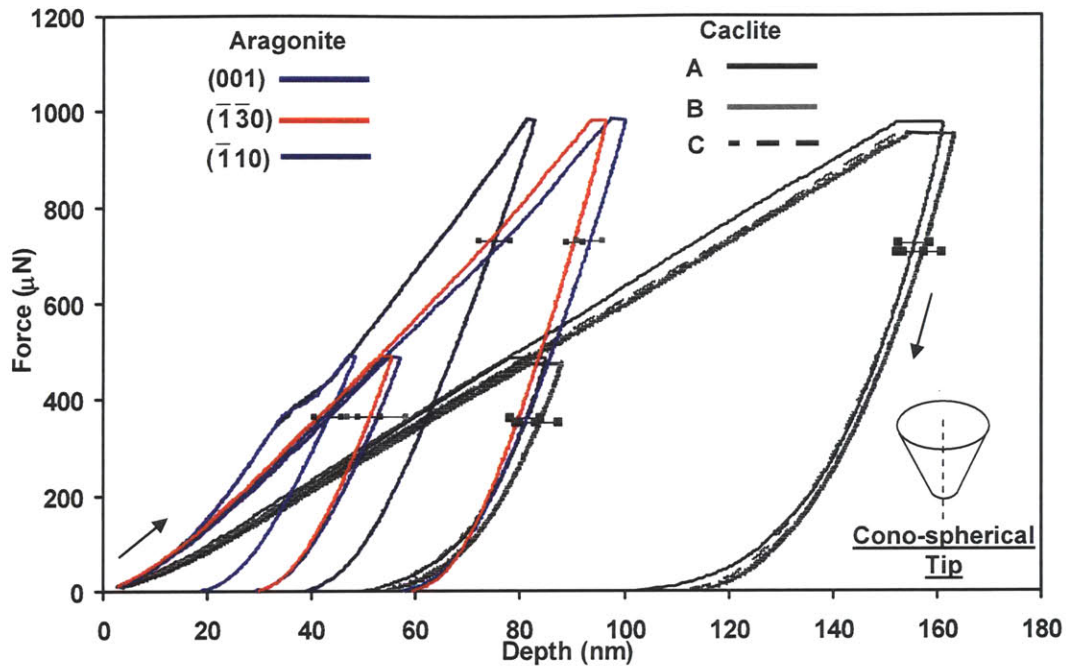


Figure A.1.3 Comparison of averaged force vs. penetration depth for the single crystal aragonite and single crystal calcite for the three orthogonal planes of aragonite and the three cleavage planes of calcite, as indicated.

A.1.2 Nanoindentation Results for Cono-spherical indenter: Force vs. penetration depth curves

Higher load indents (maximum load 10mN) were performed on the three planes of calcite to facilitate TMAFM. All planes showed distinct residual impressions and bias in the pileup direction surrounding the residual indent. This is suggestive of slip occurring on distinct systems as was investigated for the aragonite data.

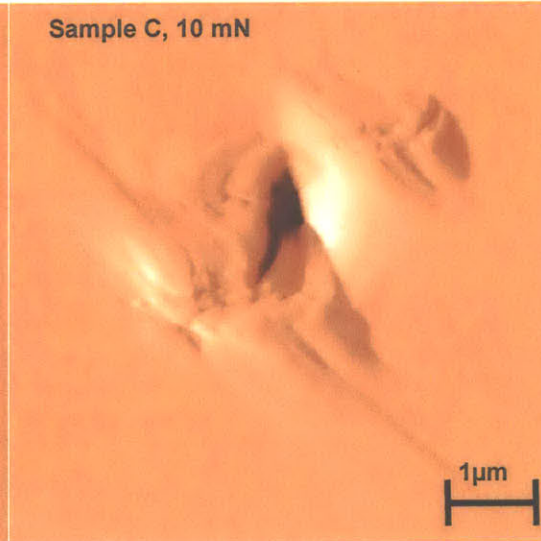
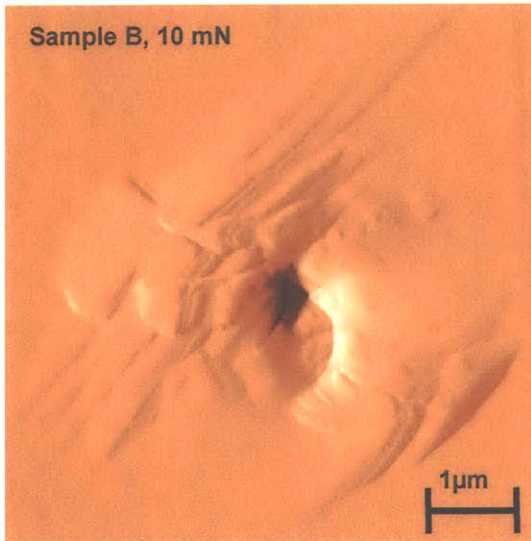
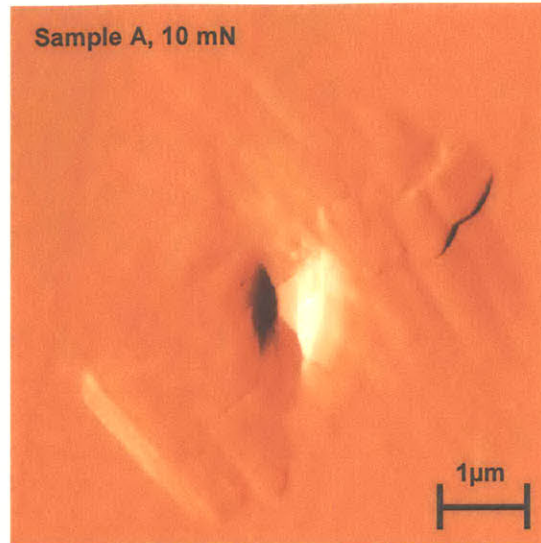
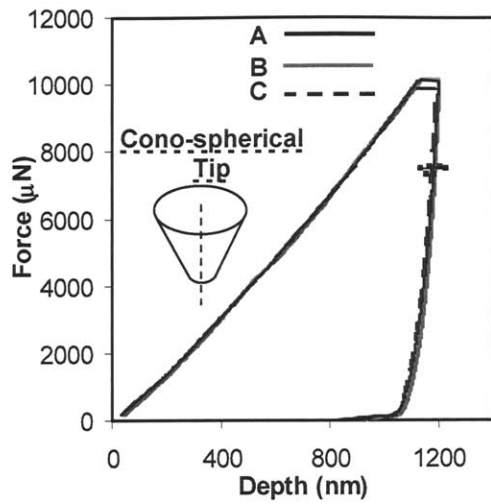


Figure A.1.4 Higher load nanoindentation using a cono-spherical tip on single crystal calcite (maximum load 10 mN, load-unload rate = 1000 μ N/s). (a) Averaged load vs. unload curves ($n = 20$) for the three cleavage rhombohedron planes of single crystal calcite. The three curves overlay each other. Residual impressions after nanoindentation to maximum loads of 10 mN (b) sample A, (C) sample B and (D) sample C.

For the aragonite (001) plane, the pileup was concentrated in four pileup lobes surrounding the residual indents. For calcite, the pile up is typically in two areas around the indenter, with one of the areas having striations that extend further away from the residual impression.

Appendix B *Individual load-unload curves from nanoindentation study*

The raw data for the averaged curves reported in the nanoindentation studies in this Thesis are included below.

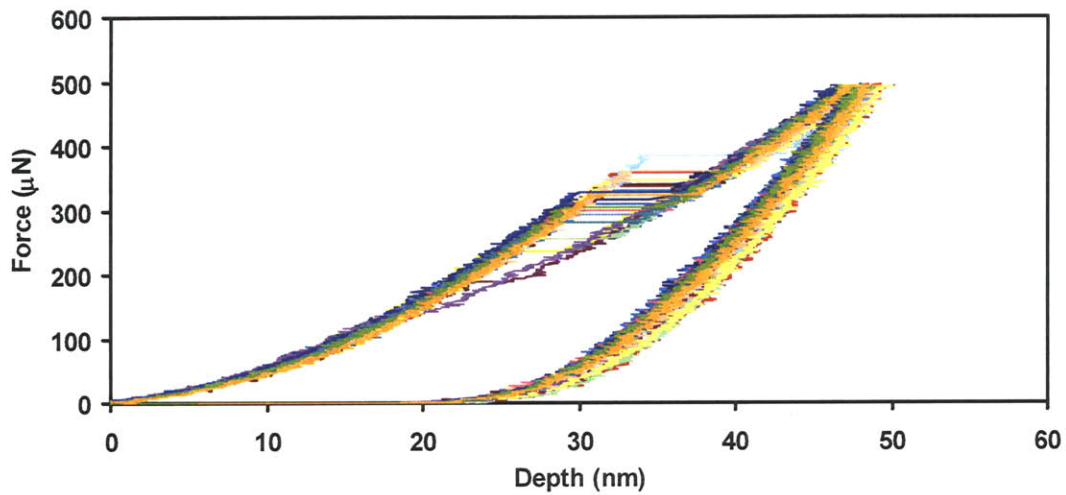


Figure B.1.1 Load-unload curves for nanoindentation in single crystal aragonite using Berkovich probe tip on the (001) plane (maximum loaded depth = 500 μN , $n = 20$, 5 μm spacing in the X- and Y- direction, load-unload rate 50 $\mu\text{N/s}$)

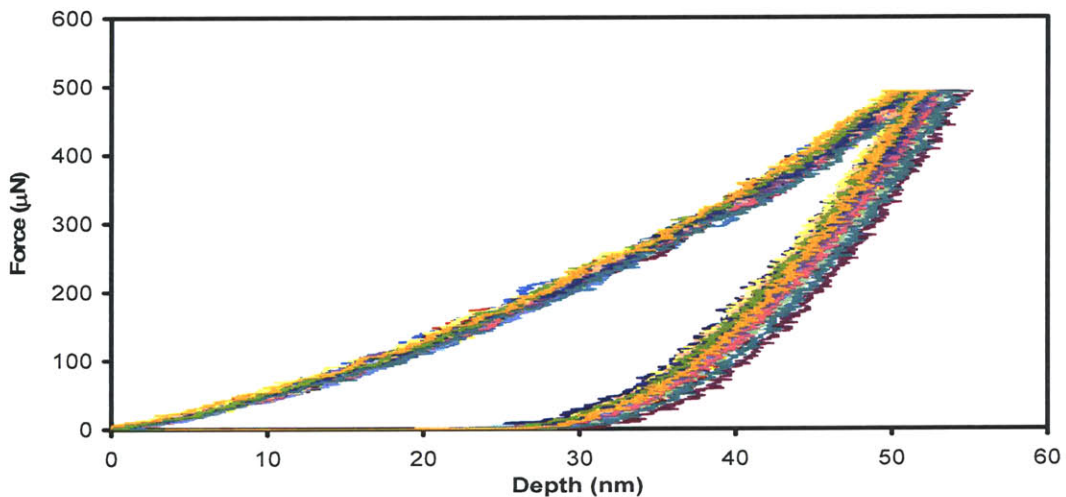


Figure B.1.2 Load-unload curves for nanoindentation in single crystal aragonite using Berkovich probe tip on the $(\bar{1}10)$ plane (maximum loaded depth = 500 μN , $n = 20$, 5 μm spacing in the X- and Y- direction, load-unload rate 50 $\mu\text{N/s}$)

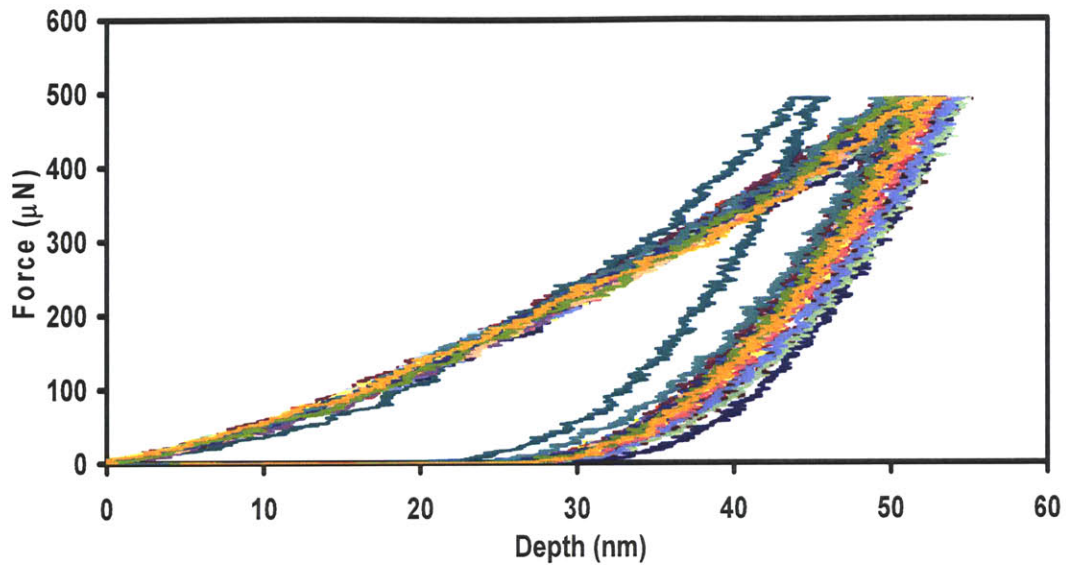


Figure B.1.3 Load-unload curves for nanoindentation in single crystal aragonite using Berkovich probe tip on the $(\bar{1}\bar{3}0)$ plane (maximum loaded depth = 500 μN , $n = 20$, 5 μm spacing in the X- and Y- direction, load-unload rate 50 $\mu\text{N/s}$)

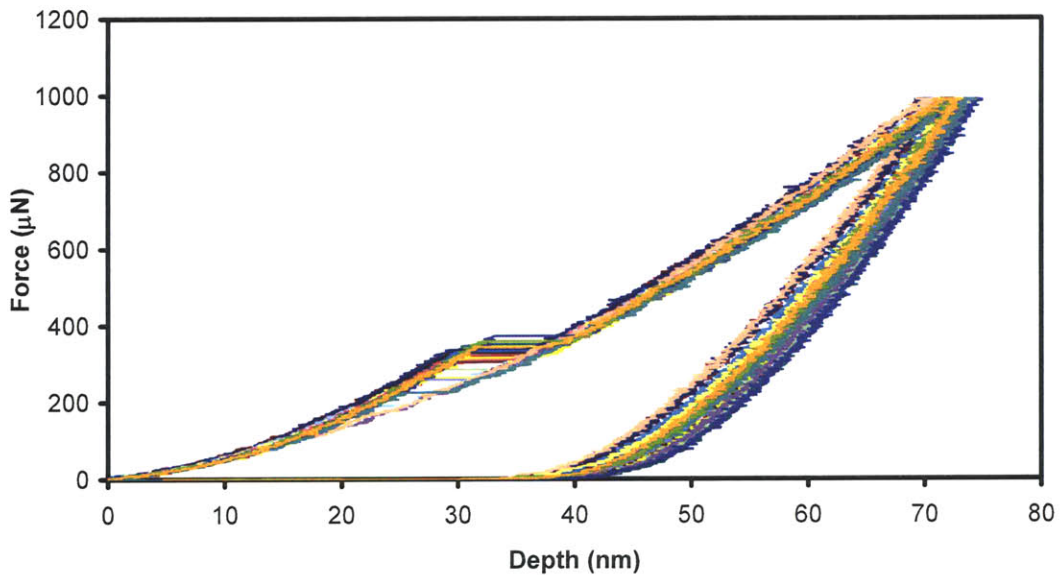


Figure B.1.4 Load-unload curves for nanoindentation in single crystal aragonite using Berkovich probe tip on the (001) plane (maximum loaded depth = 1000 μN , $n = 20$, 5 μm spacing in the X- and Y- direction, load-unload rate 50 $\mu\text{N/s}$)

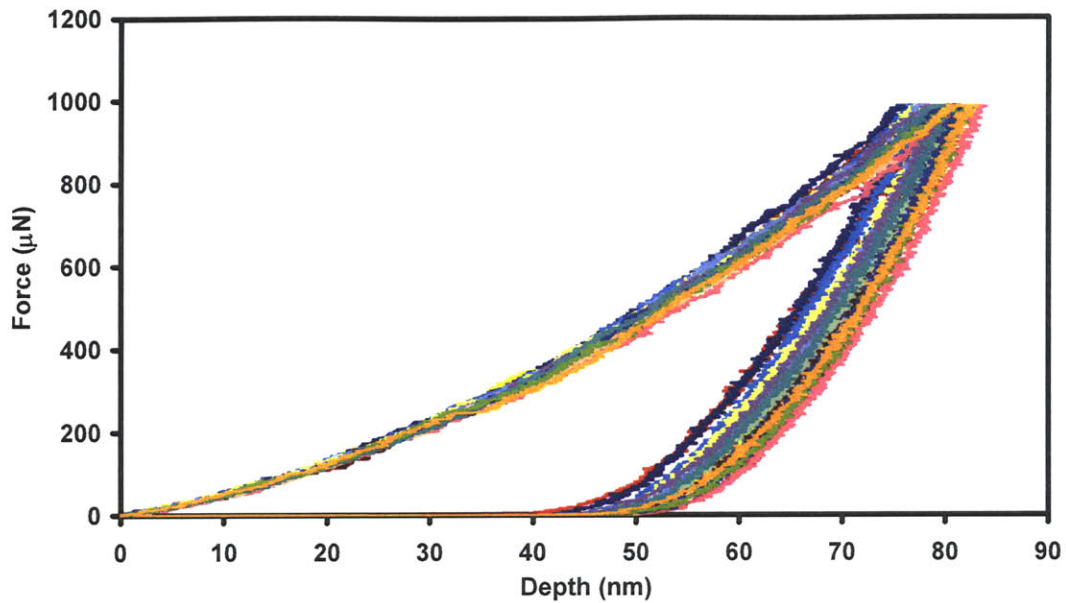


Figure B.1.5 Load-unload curves for nanoindentation in single crystal aragonite using Berkovich probe tip on the $(\bar{1}10)$ plane (maximum loaded depth = 1000 μN , $n = 20$, 5 μm spacing in the X- and Y- direction, load-unload rate 50 $\mu\text{N/s}$)

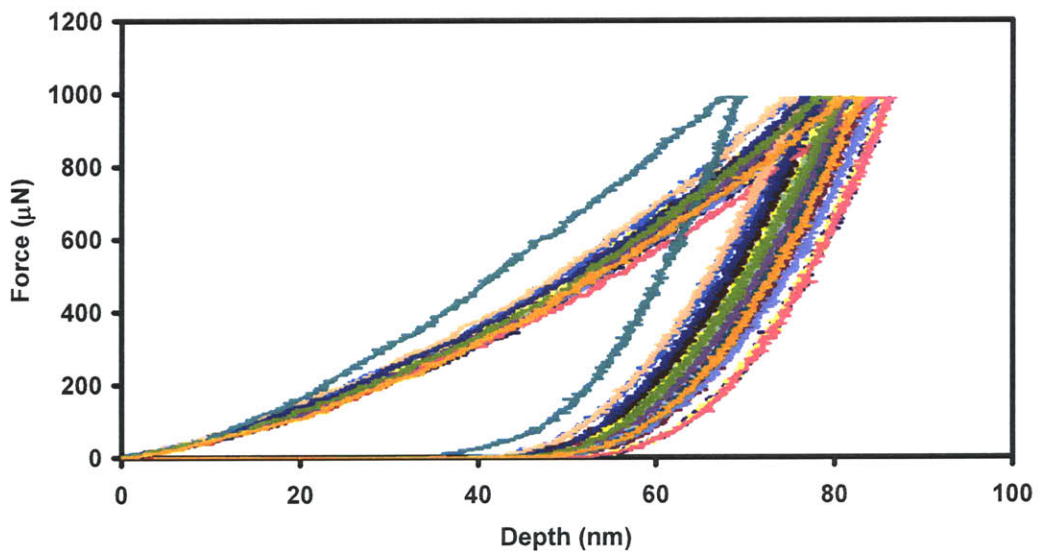


Figure B.1.6 Load-unload curves for nanoindentation in single crystal aragonite using Berkovich probe tip on the $(\bar{1}\bar{3}0)$ plane (maximum loaded depth = 1000 μN , $n = 20$, 5 μm spacing in the X- and Y- direction, load-unload rate 50 $\mu\text{N/s}$)

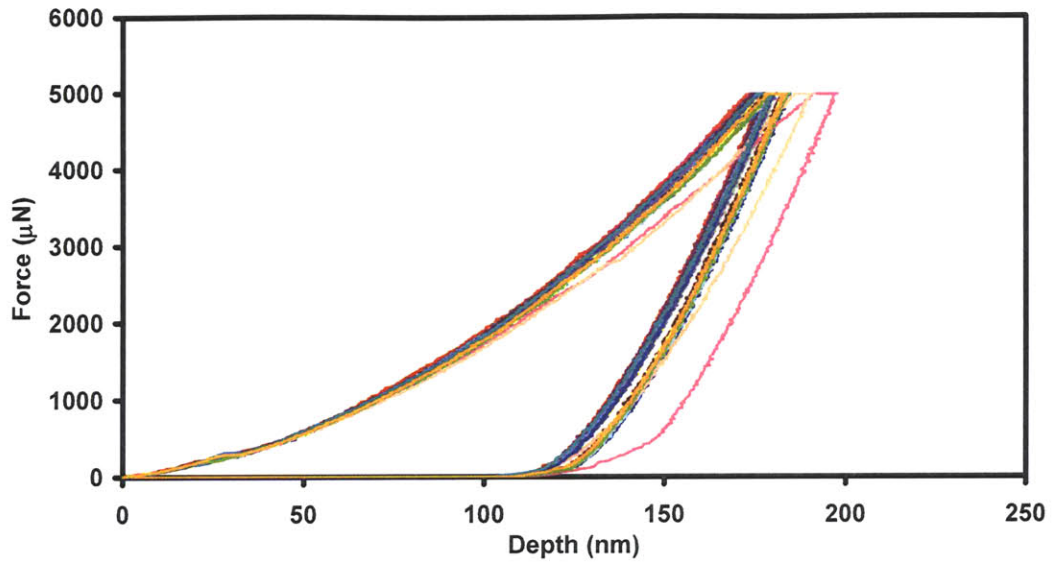


Figure B.1.7 Load-unload curves for nanoindentation in single crystal aragonite using Berkovich probe tip on the (001) plane (maximum loaded depth = 5000 μN , $n = 20$, 15 μm spacing in the X- and Y- direction, load-unload rate 1000 $\mu\text{N/s}$)

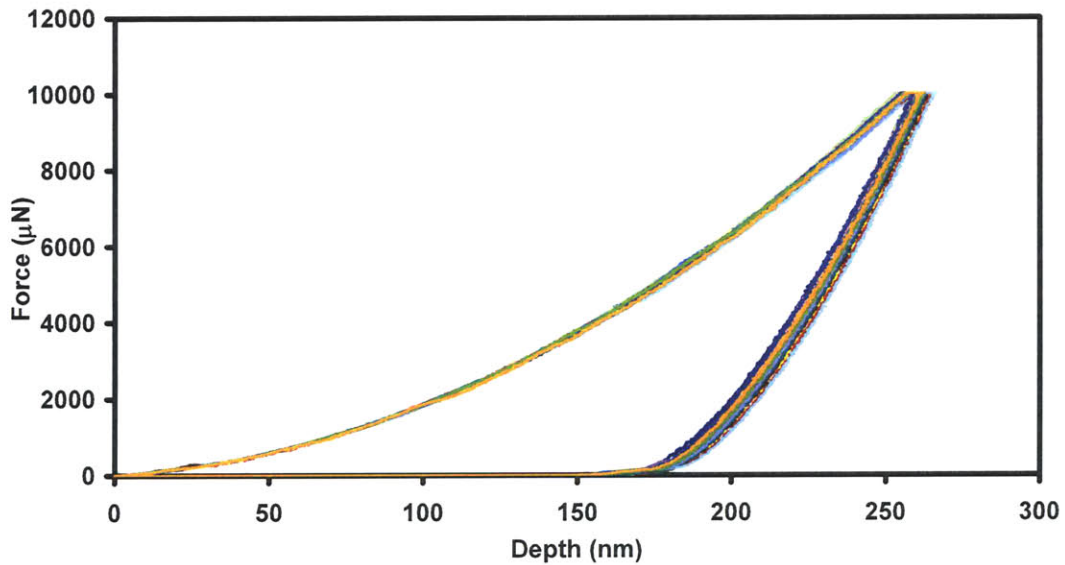


Figure B.1.8 Load-unload curves for nanoindentation in single crystal aragonite using Berkovich probe tip on the (001) plane (maximum loaded depth = 10000 μN , $n = 20$, 15 μm spacing in the X- and Y- direction, load-unload rate 1000 $\mu\text{N/s}$)

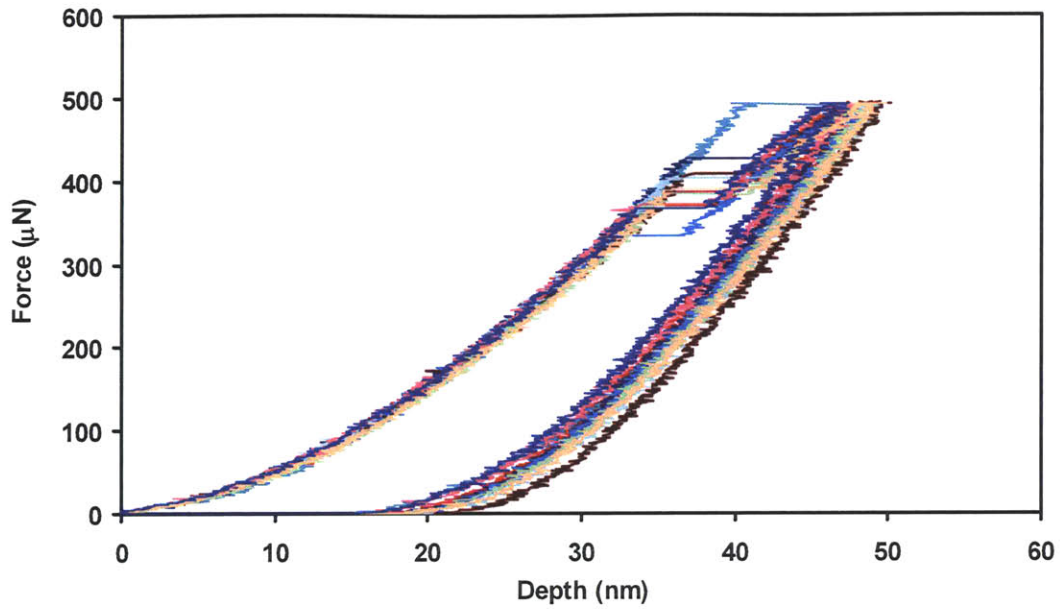


Figure B.1.9 Load-unload curves for nanoindentation in single crystal aragonite using an (ideally) $1\mu\text{m}$ radius, 60° conical tip on the (001) plane (maximum loaded depth = $500\mu\text{N}$, $n = 20$, $5\mu\text{m}$ spacing in the X- and Y- direction, load-unload rate $50\mu\text{N/s}$)

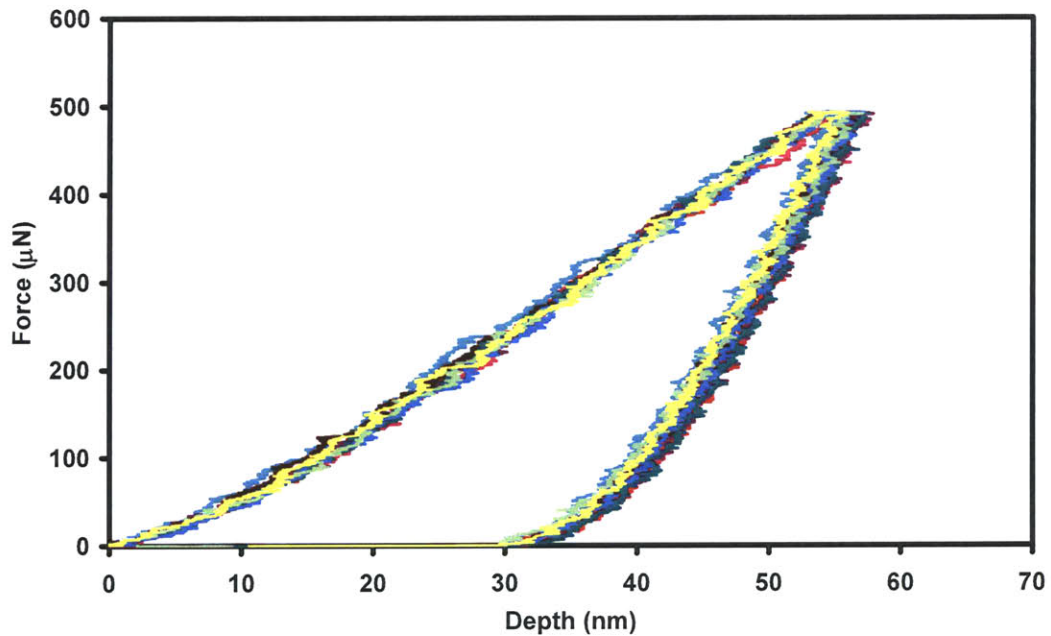


Figure B.1.10 Load-unload curves for nanoindentation in single crystal aragonite using an (ideally) $1\mu\text{m}$ radius, 60° conical tip on the $(\bar{1}10)$ plane (maximum loaded depth = $500\mu\text{N}$, $n = 20$, $5\mu\text{m}$ spacing in the X- and Y- direction, load-unload rate $50\mu\text{N/s}$)

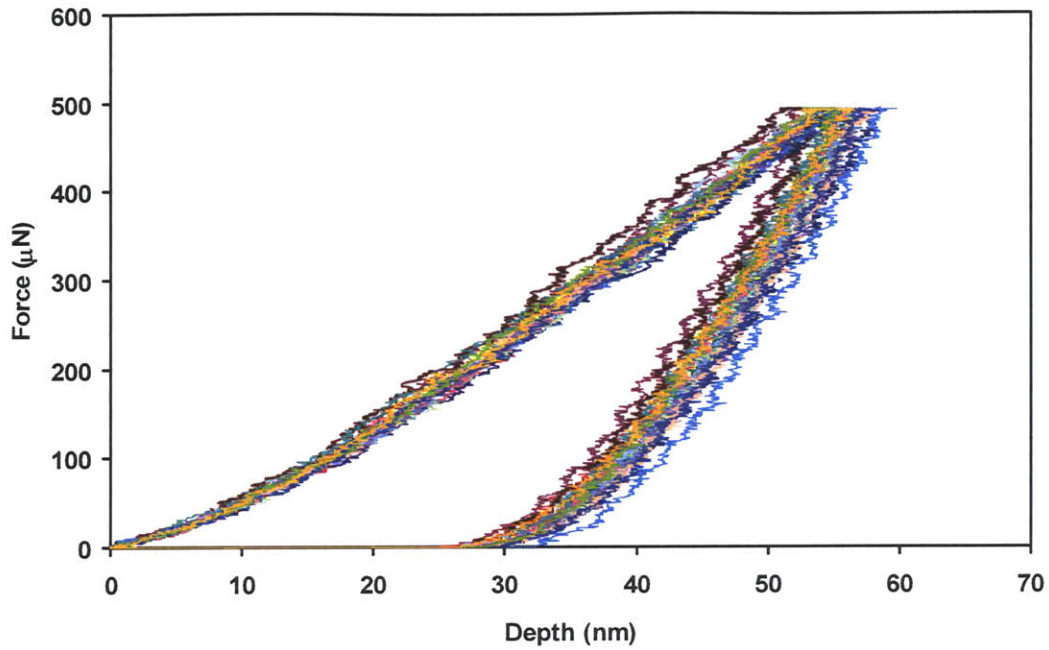


Figure B.1.11 Load-unload curves for nanoindentation in single crystal aragonite using an (ideally) $1\mu\text{m}$ radius, 60° conical tip on the $(\bar{1}\bar{3}0)$ plane (maximum loaded depth = $500\mu\text{N}$, $n = 20$, $5\mu\text{m}$ spacing in the X- and Y- direction, load-unload rate $50\mu\text{N/s}$)

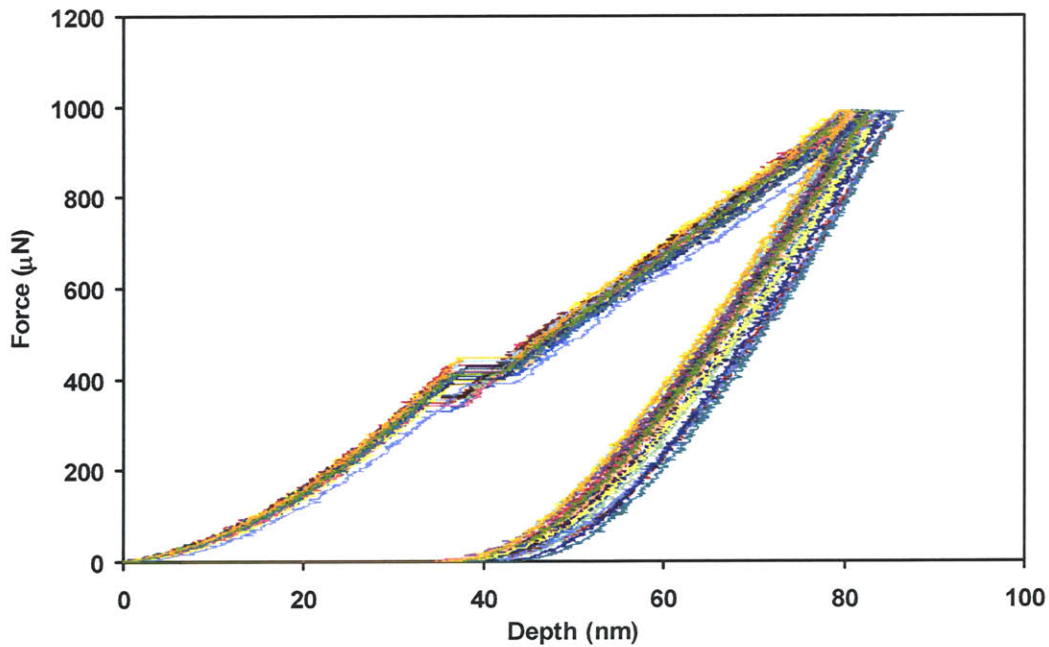


Figure B.1.12 Load-unload curves for nanoindentation in single crystal aragonite using an (ideally) $1\mu\text{m}$ radius, 60° conical tip on the (001) plane (maximum loaded depth = $1000\mu\text{N}$, $n = 20$, $5\mu\text{m}$ spacing in the X- and Y- direction, load-unload rate $50\mu\text{N/s}$)

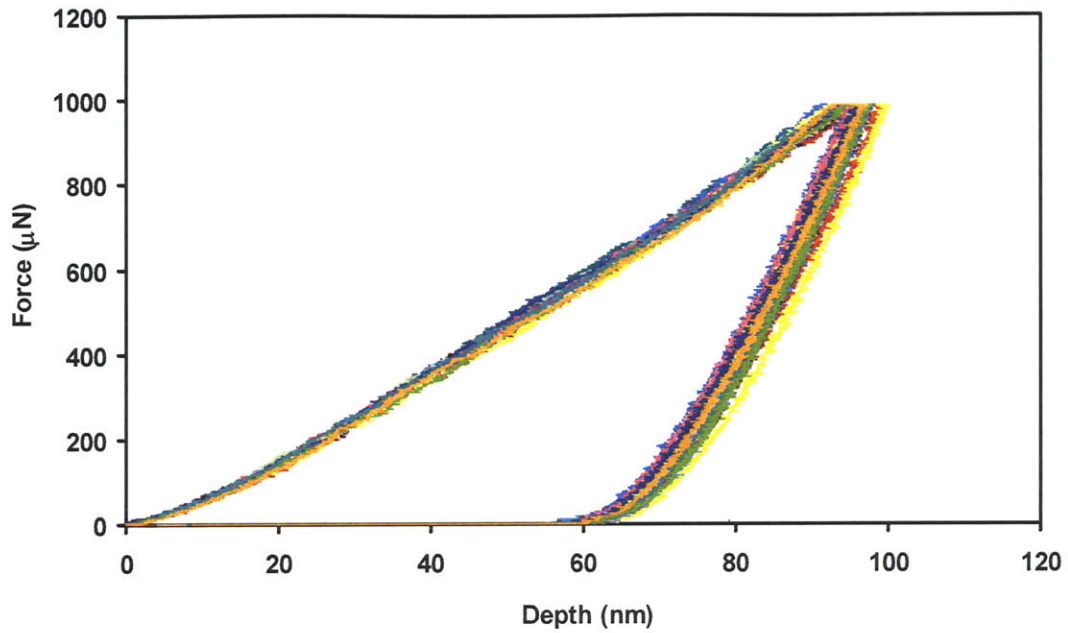


Figure B.1.13 Load-unload curves for nanoindentation in single crystal aragonite using an (ideally) $1\mu\text{m}$ radius, 60° conical tip on the $(\bar{1}10)$ plane (maximum loaded depth = $1000\mu\text{N}$, $n = 20$, $5\mu\text{m}$ spacing in the X- and Y- direction, load-unload rate $50\mu\text{N/s}$)

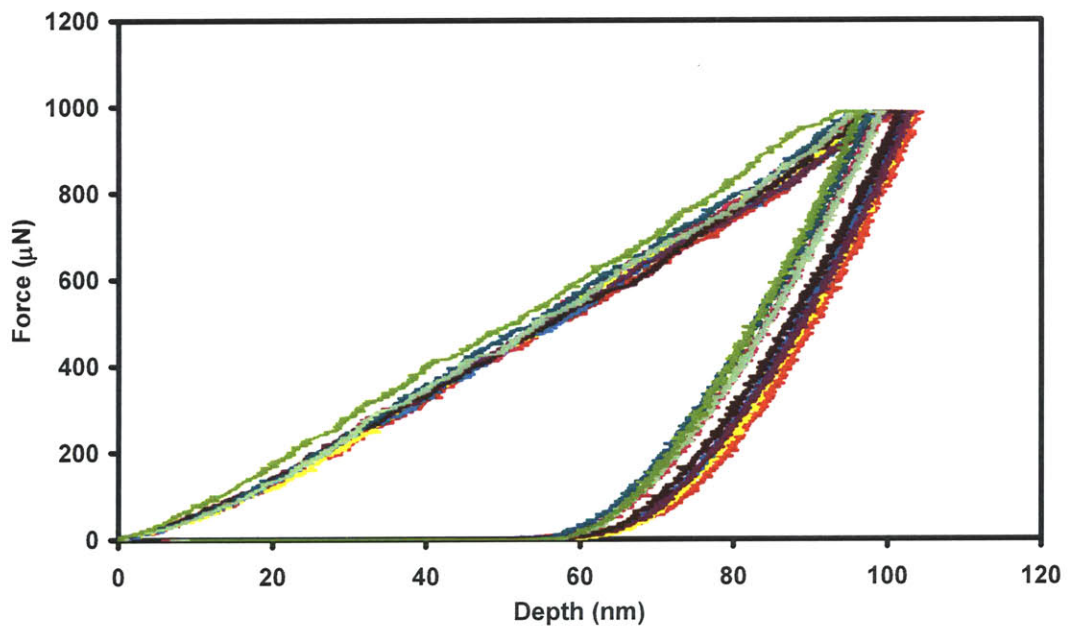


Figure B.1.14 Load-unload curves for nanoindentation in single crystal aragonite using an (ideally) $1\mu\text{m}$ radius, 60° conical tip on the $(\bar{1}\bar{3}0)$ plane (maximum loaded depth = $1000\mu\text{N}$, $n = 20$, $5\mu\text{m}$ spacing in the X- and Y- direction, load-unload rate $50\mu\text{N/s}$)

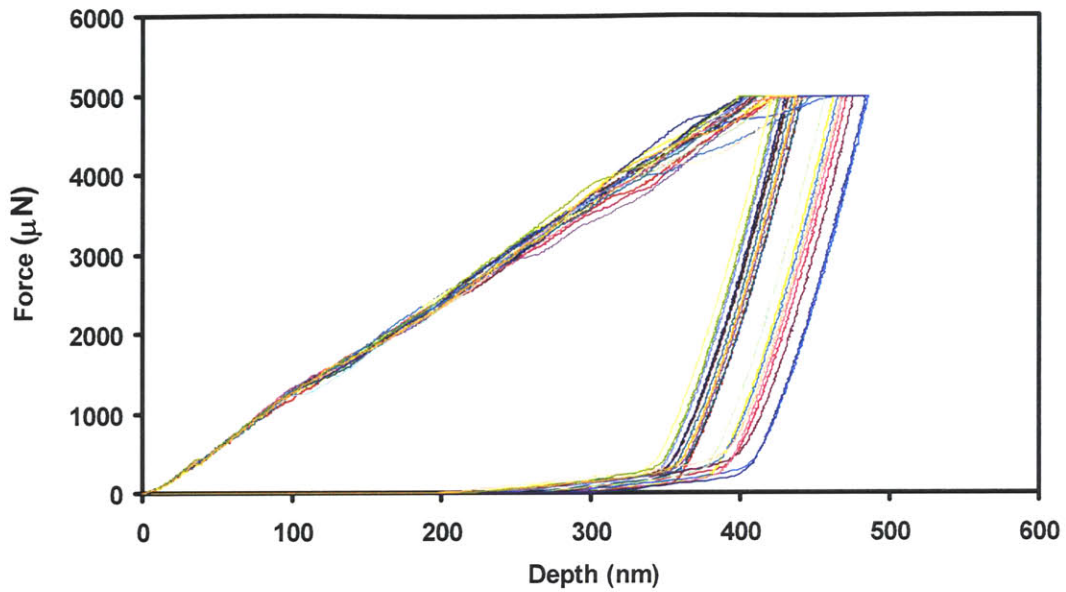


Figure B.1.15 Load-unload curves for nanoindentation in single crystal aragonite using an (ideally) $1\mu\text{m}$ radius, 60° conical tip on the (001) plane (maximum loaded depth = $5000\mu\text{N}$, $n = 20$, $15\mu\text{m}$ spacing in the X- and Y- direction, load-unload rate $1000\mu\text{N/s}$)

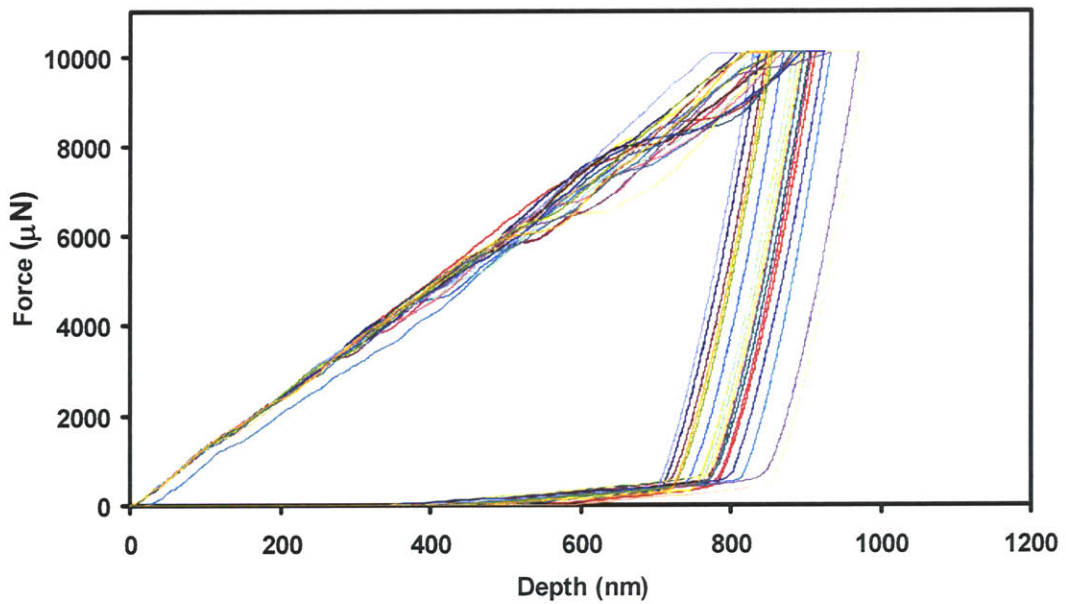


Figure B.1.16 Load-unload curves for nanoindentation in single crystal aragonite using an (ideally) $1\mu\text{m}$ radius, 60° conical tip on the (001) plane (maximum loaded depth = $10000\mu\text{N}$, $n = 20$, $15\mu\text{m}$ spacing in the X- and Y- direction, load-unload rate $1000\mu\text{N/s}$)

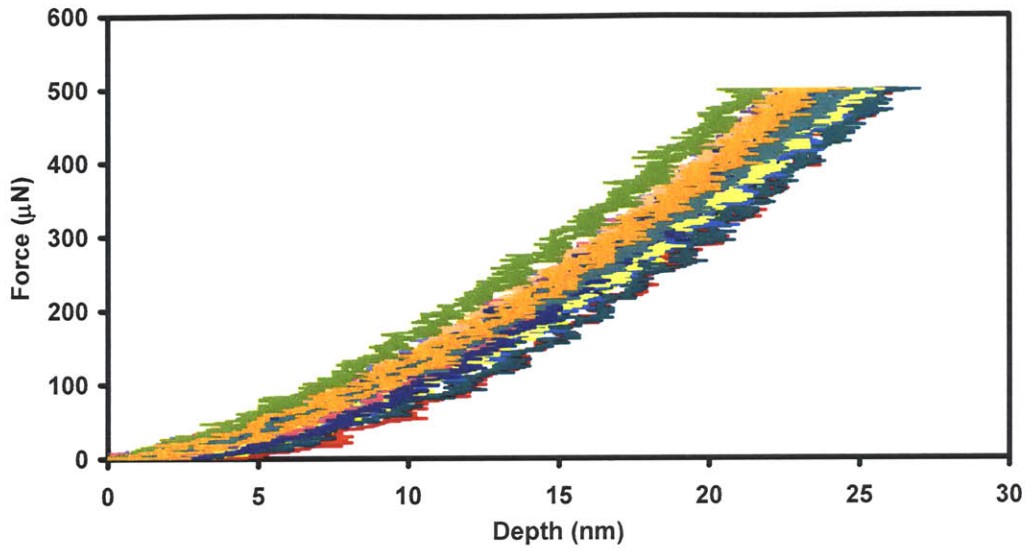


Figure B.1.17 Load-unload curves for nanoindentation in single crystal aragonite using a nano-Knoop tip on the (001) plane (maximum loaded depth = 500 μN , $n = 20$, 5 μm spacing in the X- and Y- direction, load-unload rate 50 $\mu\text{N/s}$)

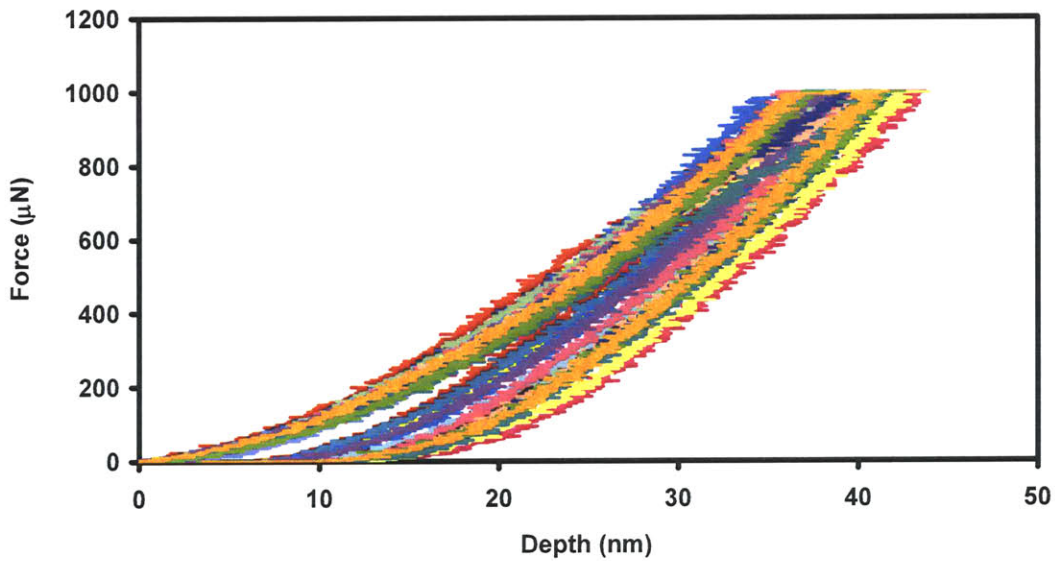


Figure B.1.18 Load-unload curves for nanoindentation in single crystal aragonite using a nano-Knoop tip on the (001) plane (maximum loaded depth = 1000 μN , $n = 20$, 5 μm spacing in the X- and Y- direction, load-unload rate 50 $\mu\text{N/s}$)

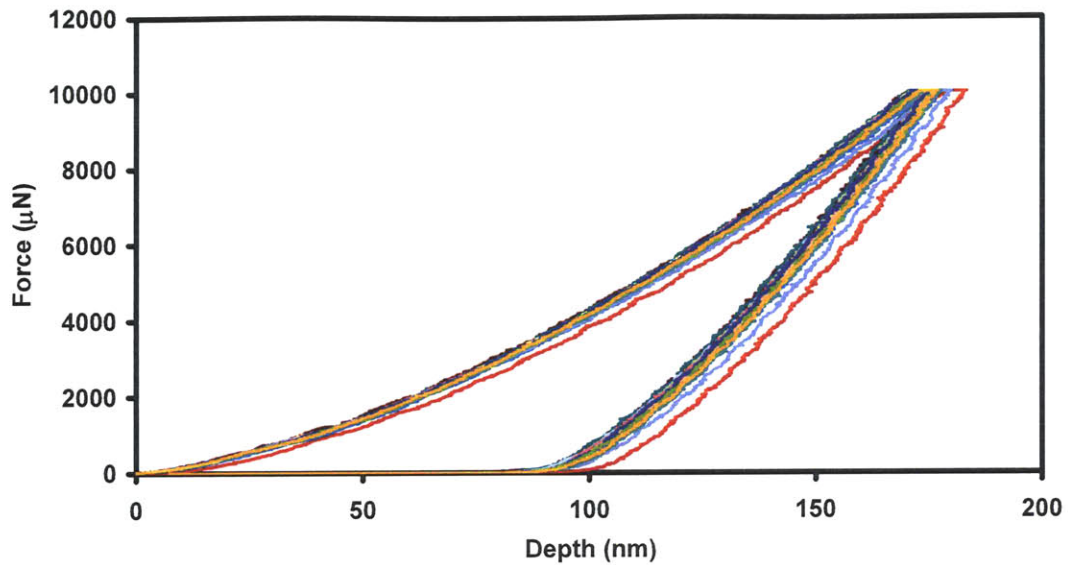


Figure B.1.19 Load-unload curves for nanoindentation in single crystal aragonite using a nano-Knoop tip on the (001) plane (maximum loaded depth = 10000 μN , $n = 20$, 15 μm spacing in the X- and Y- direction, load-unload rate 1000 $\mu\text{N/s}$)

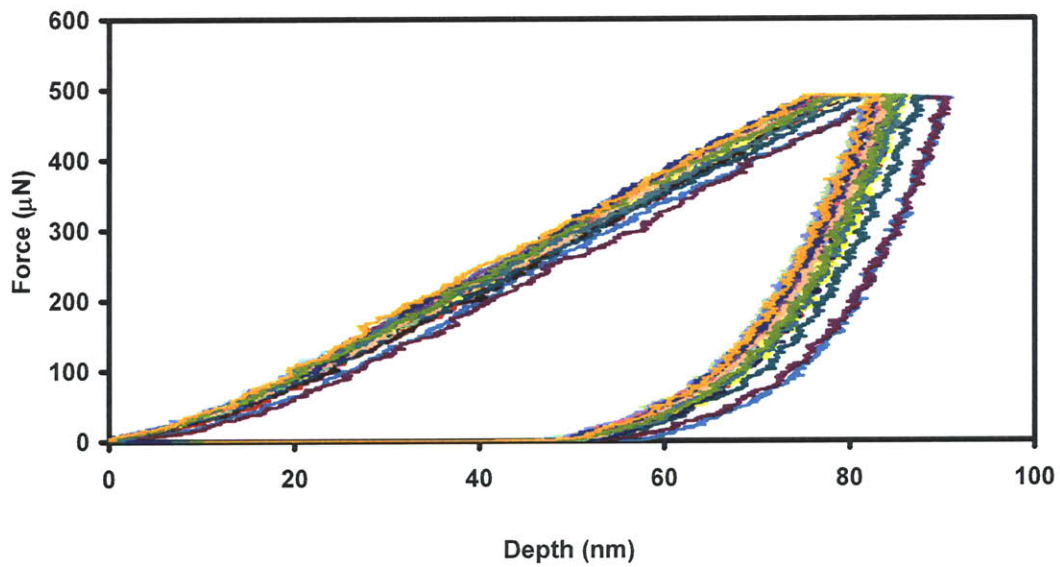


Figure B.1.20 Load-unload curves for nanoindentation in single crystal calcite using an (ideally) 1 μm radius, 60° conical tip for sample A (maximum loaded depth = 500 μN , $n = 20$, 5 μm spacing in the X- and Y- direction, load-unload rate 50 $\mu\text{N/s}$)

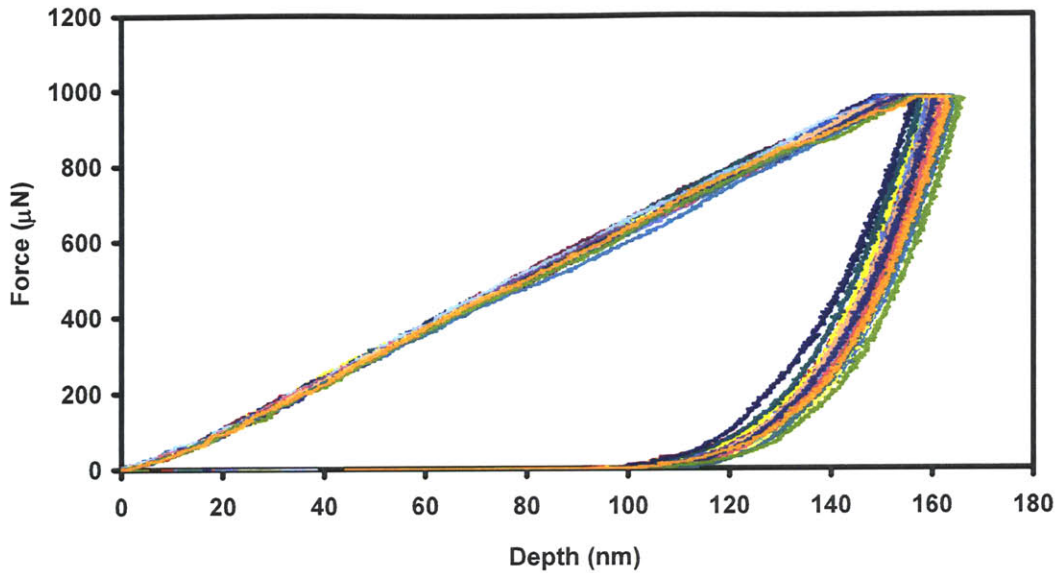


Figure B.1.21 Load-unload curves for nanoindentation in single crystal calcite using an (ideally) 1 μm radius, 60° conical tip for sample A (maximum loaded depth = 1000 μN, $n = 20$, 5 μm spacing in the X- and Y- direction, load-unload rate 50 μN/s)

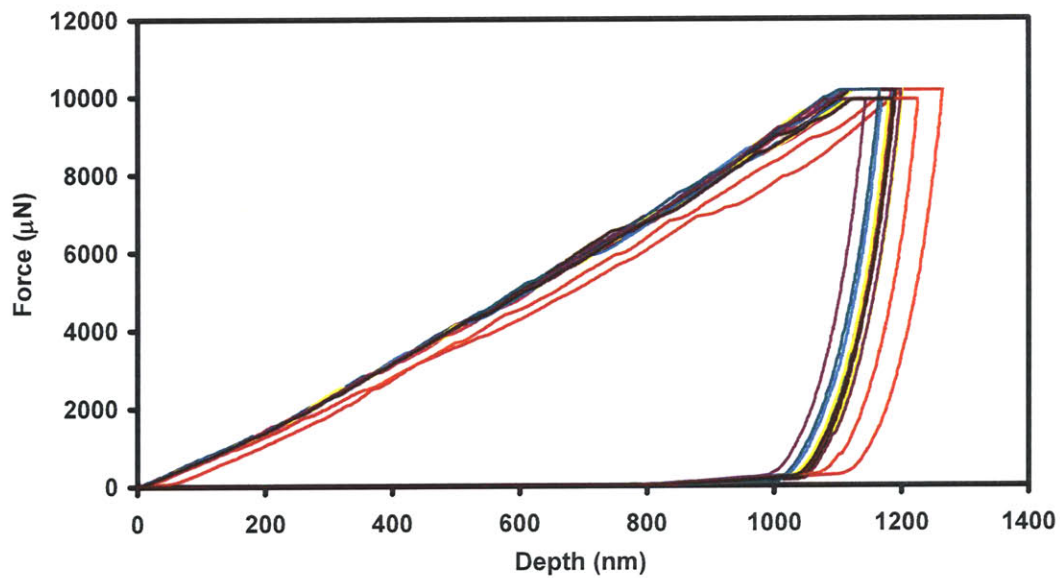


Figure B.1.22 Load-unload curves for nanoindentation in single crystal calcite using an (ideally) 1 μm radius, 60° conical tip for sample A (maximum loaded depth = 10000 μN, $n = 20$, 15 μm spacing in the X- and Y- direction, load-unload rate 1000 μN/s)

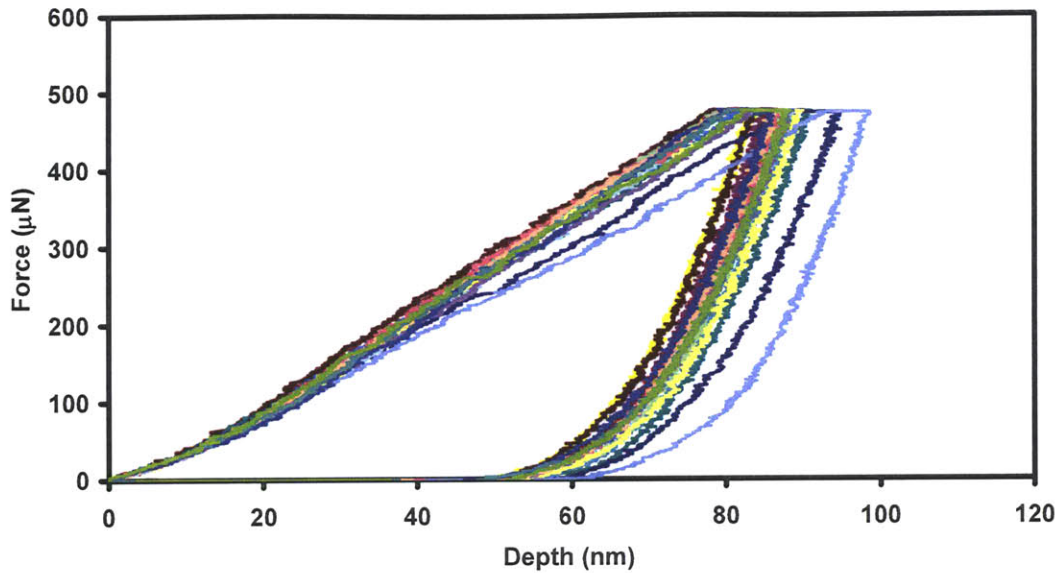


Figure B.1.23 Load-unload curves for nanoindentation in single crystal calcite using an (ideally) $1\mu\text{m}$ radius, 60° conical tip for sample B (maximum loaded depth = $500\mu\text{N}$, $n = 20$, $5\mu\text{m}$ spacing in the X- and Y- direction, load-unload rate $50\mu\text{N/s}$)

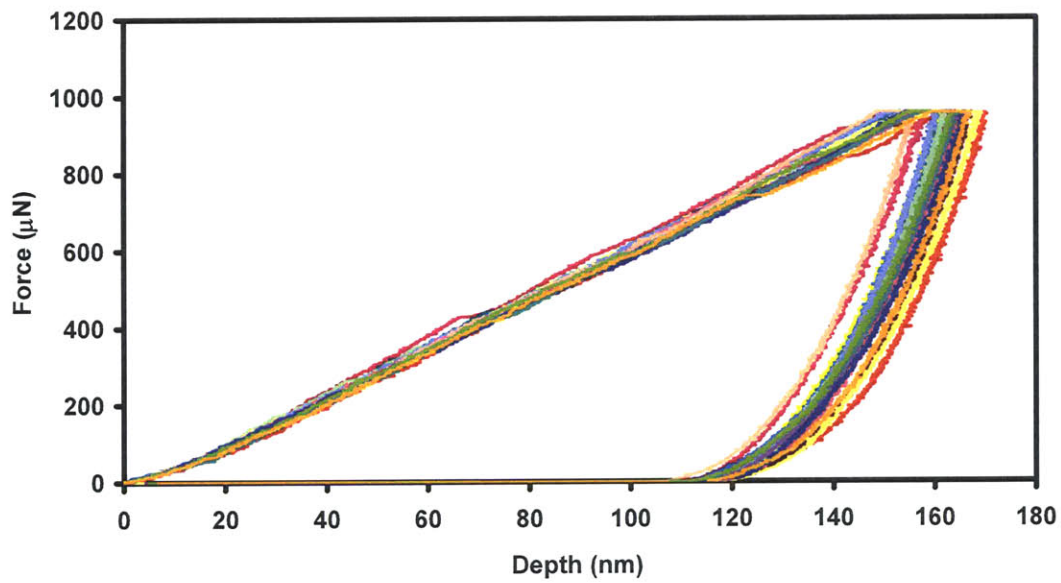


Figure B.1.24 Load-unload curves for nanoindentation in single crystal calcite using an (ideally) $1\mu\text{m}$ radius, 60° conical tip for sample B (maximum loaded depth = $1000\mu\text{N}$, $n = 20$, $5\mu\text{m}$ spacing in the X- and Y- direction, load-unload rate $50\mu\text{N/s}$)

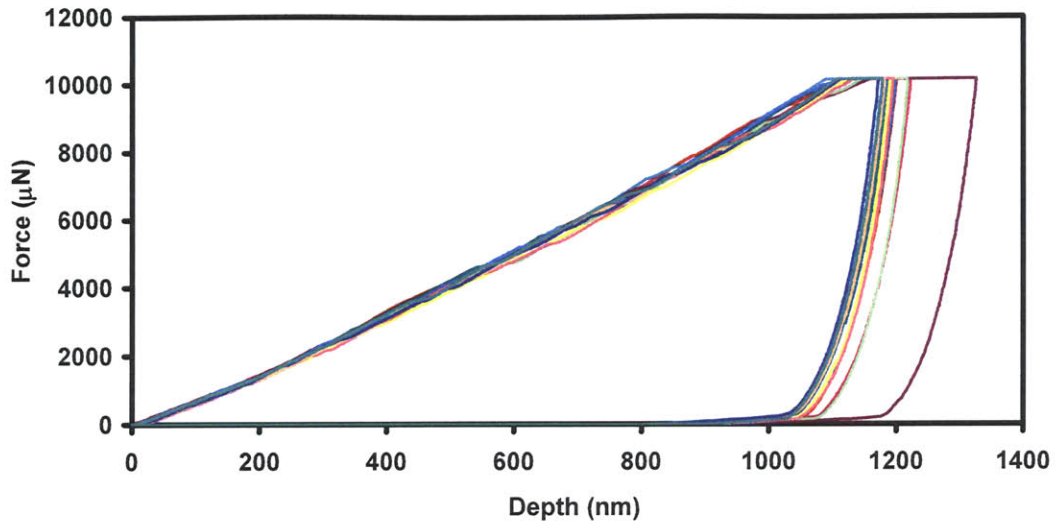


Figure B.1.25 Load-unload curves for nanoindentation in single crystal calcite using an (ideally) $1\mu\text{m}$ radius, 60° conical tip for sample B (maximum loaded depth = $10000\mu\text{N}$, $n = 20$, $15\mu\text{m}$ spacing in the X- and Y- direction, load-unload rate $1000\mu\text{N/s}$)

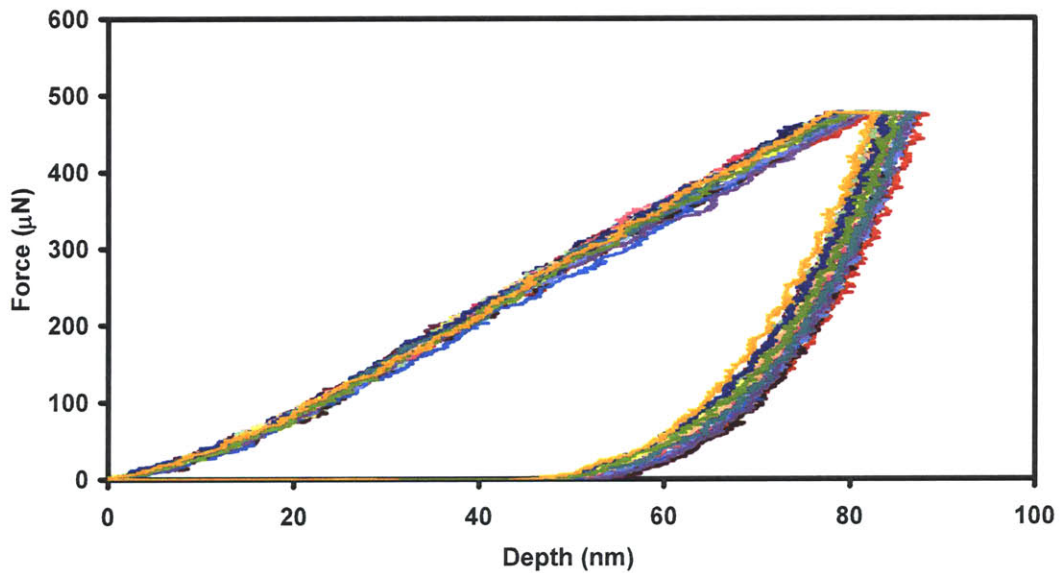


Figure B.1.26 Load-unload curves for nanoindentation in single crystal calcite using an (ideally) $1\mu\text{m}$ radius, 60° conical tip for sample C (maximum loaded depth = $500\mu\text{N}$, $n = 20$, $5\mu\text{m}$ spacing in the X- and Y- direction, load-unload rate $50\mu\text{N/s}$)

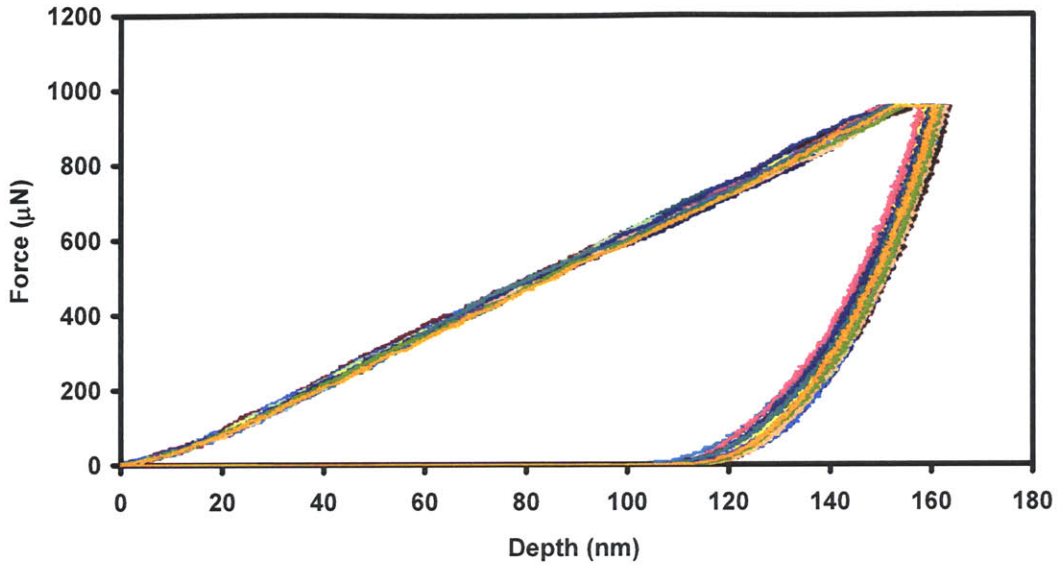


Figure B.1.27 Load-unload curves for nanoindentation in single crystal calcite using an (ideally) $1\mu\text{m}$ radius, 60° conical tip for sample C (maximum loaded depth = $1000\ \mu\text{N}$, $n = 20$, $5\ \mu\text{m}$ spacing in the X- and Y- direction, load-unload rate $50\mu\text{N/s}$)

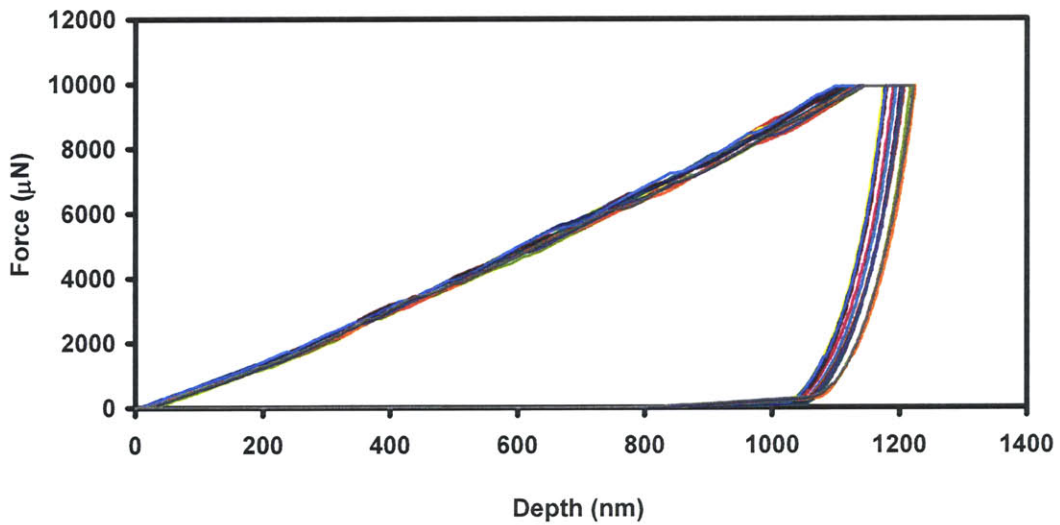


Figure B.1.28 Load-unload curves for nanoindentation in single crystal calcite using an (ideally) $1\mu\text{m}$ radius, 60° conical tip for sample C (maximum loaded depth = $10000\ \mu\text{N}$, $n = 20$, $15\ \mu\text{m}$ spacing in the X- and Y- direction, load-unload rate $1000\mu\text{N/s}$)

Appendix C *Oliver-Pharr Analysis Method*

The Oliver-Pharr analysis method was used to reduce the Young's Modulus E_R and Hardness H of the material from the individual nanoindentation curves. The method is based on a fit of the unloading curve between 95 and 20 % of the maximum load to the power law relation:

$$P = B(h-h_{max})^m$$

The variables are:

P = Maximum indent load

B = constant

h = indentation depth

h_{max} = maximum indentation depth

m = constant

The variables B and m are determined from the fitting of the individual nanoindentation curves. The derivative of the power law relation with respect to h is evaluated at the maximum load to calculate the contact stiffness S ,

$$S = \left(\frac{dP}{dh} \right)_{h_{max}}$$

The contact depth, h_c , is calculated with the following equation:

$$h_c = h_{max} - \frac{3P_{max}}{4S}$$

where the second term accounts for sink in around the indenter. The hardness, H , is calculated using:

$$H = \frac{P_{max}}{A(h_c)}$$

where $A(h_c)$ is the projected contact area of the tip at the height h_c . The area function is obtained experimentally and this procedure is explained below. The reduced modulus, E_r , is calculated using:

$$E_r = \frac{\sqrt{\pi}}{2\sqrt{A(h_c)}} S$$

The reduced modulus, E_r , is related to the specimen and indenter moduli and Poisson's ratios by:

$$\frac{1}{E_r} = \left(\frac{1-\nu^2}{E} \right)_{\text{specimen}} + \left(\frac{1-\nu^2}{E} \right)_{\text{indenter}}$$

where E and ν are the specimen/indenter Young's modulus and Poisson's ratio respectively. A tip-shape calibration is performed to determine the area function of the tip before each set of experiments. This method is based on the assumption that the Young's modulus is constant and independent of the indentation depth. A standard fused quartz sample is used for the calibration with $E_r = 69.6$ GPa. The area function relating the projected contact area (A) to the contact depth is obtained from these experiments using:

$$A(h_c) = \frac{\pi}{4} \left(\frac{S}{E_r} \right)^2$$

and for an ideal Berkovich geometry:

$$A(h_c) = 24.5h_c^2$$

The experimental calibration of the tip area function is done by performing a series of indents at various normal loads (contact depths) on the standard fused quartz sample, with $A(h_c)$ calculated from the above expressions. The computed area, A , versus contact depth, h_c , is plotted and a fitting procedure employed to fit $A(h_c)$ to a sixth order polynomial of the form:

$$A(h_c) = C_0h_c^2 + C_1h_c + C_2h_c^{1/2} + C_3h_c^{1/4} + C_4h_c^{1/8} + C_5h_c^{1/16}$$

Adapted from TriboScope® Users Manual, © 2003 Hysitron

References

Anand, L. (2004) Single-crystal elasto-viscoplasticity: application to texture evolution in polycrystalline metals at large strains. *Computer Methods in Applied Mechanics and Engineering*, 193, 5359-5383.

Ashby, M. F. (2005). *Materials Selection in Mechanical Design*, 3rd Edition. Oxford: Butterworth Heinemann.

Ashby, M. F. & Jones, D. R. H. (1996). *Engineering Materials 1*, 2nd Edition. Oxford: Butterworth Heinemann.

Ashby, M. F., Gibson, L. J., Wegst, U. & Olive, R. (1995). The mechanical properties of natural materials. I. Material property charts. *Proceedings of the Royal Society of London A*, 450, 123-140.

Balasubramanian, S., Anand, L. (1996). Single crystal and polycrystal elasto-viscoplasticity: Application to earing in cup drawing of FCC metals. *Computational Mechanics*, 17, 209-225.

Bar-Cohen, Y. (Ed.). (2006). *Biomimetics: Biologically inspired technologies*. Florida: Taylor & Francis Group.

Beniash, E., Simmer, J. P. & Margolis, H. (2005). The effect of recombinant mouse amelogenins on the formation and organization of hydroxyapatite crystals in vitro. *Journal of Structural Biology*, 149, 182-190.

Bevelander, G. & Nakahara, H. (1969). An electron microscope study of the formation of the nacreous layer in the shell of certain bivalve molluscs. *Calcified Tissue Research*, 3, 84-92.

Bilezikian, J. P., Raisz, L. G. & Rodan, G. A. (2002). Principles of Bone Biology, 2nd Ed. California: Academic Press.

Bragg, W. L. (1924). The structure of Aragonite. *Proceedings of the Royal Society of London, A*, 105, 16-39.

Bridgman, P. W. (1939). The high pressure behavior of miscellaneous minerals. *American Journal of Science*, 239, 7-18.

Bruet, B. J. F., Qi, H., Panas, R., Tai, K., Frick, L., Boyce, M. C. & Ortiz, C. (2005). Nanoscale morphology and indentation of individual nacre tablets from the gastropod mollusc *Trochus Niloticus*. *Journal Materials Research*, 20, 2400-2419.

Bryan, W. H. & Hill, D. (1941). Hexacoral growth as spherulitic crystallization. *Proceedings of the Royal Society, Queensland*, 52, 78-91.

Buerger, J. M. (1945). The genesis of twin crystals. *American Mineralogist*, 30, 469-482.

Carter, N. L. Steady state flow of rocks. *Reviews of Geophysics and Space Physics*, 14, 301-360.

Chateigner D., Hedegaard, C. & Wenk, H.-R. (2000). Mollusc shell microstructures and crystallographic textures. *Journal of Structural Geology*, 22, 1723-1235.

Checa, A. (2000). A new model for periostracum and shell formation in Unionidae (Bivalvia, Mollusca). *Tissue & Cell*, 32, 405-416

Chen, B., Peng, X., Wang, W., Zhang, J. & Zhang, R. (2002). Research on the microstructure of insect cuticle and the strength of a biomimetic preformed hole composite. *Micron*, 33, 571-574.

- Chen, C.-C., Lin, C.-C., Liu, L.-G., Sinogeikin, S. V. & Bass, J. D. (2001). Elasticity of single-crystal calcite and rhodochrosite by Brillouin spectroscopy. *American Mineralogist*, 86, 1525-1529.
- Cuitiño, A.M. & Ortiz, M. (1992). Computational modelling of single crystals. (1992). *Modelling and Simulation in Materials Science and Engineering*, 1, 255-263.
- Currey, J. D. (1977). Mechanical properties of mother of pearl in tension. *Proceedings of the Royal Society of London B: Biological Sciences*, 196, 443-463.
- Currey, J. D. & Taylor, J. D. 1974). The mechanical behavior of some molluscan hard tissues. *Journal of Zoology, London*, 173, 395-406.
- Erban, H. K. (1972) On the structure and growth of the nacreous tablets in gastropods. *Biomineralisation*, 4, 14.
- Evans, A. G., Suo, Z., Wang, R. Z., Aksay, I. A., He, M. Y. & Hutchinson, J. W. Model for the robust mechanical behavior of nacre. *Journal of Materials Research*, 16, 2475-2484.
- Feng, Q. L. Li, B. H., Pu, G., Zhang, D. M., Cui, F. Z. & Li, H. D. (2000). Crystallographic alignment of calcite prisms in the oblique prismatic layer of *Mytilus edulis* shell. *Journal of Materials Science*, 35, 3337-3340.
- Gao, H., Ji, B., Jager, I. L., Arzt, E. & Fratzl, P. (2003). Materials become insensitive to flaws at the nanoscale: Lessons from nature. *Proceedings of the National Academy of Sciences of the United States of America*, 100, 5597-5600.
- Gerberich, W. W., Nelson, J. C. Lilleodden, E. T., Anderson, P. & Wyrobek, J. T. (1996). Indentation induced dislocation nucleation: The initial yield point. *Acta Materiala*, 44, 3585-3598.

Guillemin, G., Patat, J.-L., Fournie, J. & Chetail, M. (1987). The use of coral as a bone graft substitute. *Journal of Biomedical Materials Research*, 21, 557-567.

Han, Y. H., Li, H., Wong, T. Y. & Bradt, R. C. (1991). Knoop microhardness anisotropy of single-crystal aragonite. *Journal of American Ceramic Society*, 74, 3129-3132.

Hartman, W. D. & Goreau, T. F. (1970). Jamaican coralline sponges: Their morphology, ecology and fossil relatives. *Symposium of Zoological Society of London*, 25, (205-243)

Habelitz, S., Marshall, G. W., Balooch, M. & Marshall, S. J. (2002). Nanoindentation and storage of teeth. *Journal of Biomechanics*, 35, 995-998.

Hunt, S. & Oates, K. (1978). Fine Structure and Molecular Organization of the Periostracum in a Gastropod Mollusc *Buccinum undatum* L. and Its Relation to Similar Structural Protein Systems in Other Invertebrates. *Philosophical Transactions of the Royal Society of London, Series B, Biological Sciences*, 283, 417-459.

Ivanov, B. A. & Deutsch, A. (2002). The phase diagram of CaCO_3 in relation to compression and decomposition. *Physics of Earth and Planetary Interactions*, 129, 131-143.

Jackson, A. P., Vincent, J. F. V. & Turner, R. M. (1988). The mechanical design of nacre. *Proceedings of the Royal Society of London, B*, 234, 415-440.

Kalidindi, S. R., Bronkhorst, C. A. & Anand, L. (1992). Crystallographic texture evolution in bulk deformation processing of FCC metals. *Journal of Mechanics of Physics and Solids*, 40, 537-569.

Kelley, D. S., Karson, J. A., Blackman, D. K., Fruh-Green, G. L., Butterfield, D. A., Lilley, M. D., Olson, E. J., Schrenk, M. O., Roe, K. K., Lebon, G. T., Rivizzigno, P. &

the AT3-60 Shipboard Party. (2001). An off-axis hydrothermal vent field near the Mid-Atlantic Ridge at 30°N. *Nature*, 412, 145-149.

Kotov, N. A. (Ed.). (2006). Nanoparticle assemblies and superstructures. Florida: Taylor & Francis Group.

Lakes, R. (1993). Materials with structural hierarchy. *Nature*, 361, 511-515

Li, X., Chang, W.-C., Chao, Y. J., Wang, R. & Chang, M. (2004). Nanoscale structural and mechanical characterization of a natural nanocomposite material: the shell of red abalone. *Nanoletters*, 4, 613-617.

Li, X. & Nardi, P. (2004). Micro/nanomechanical characterization of natural nanocomposite material-the shell of Pectinadae. *Nanotechnology*, 15, 211-217.

Liu, L. G., Chen, C. G., Lin, C. C. & Yang, Y. J. (2005). Elasticity of single-crystal aragonite by Brillouin spectroscopy. *Physics and Chemistry of Minerals*, 32, 97-102.

Lowenstam, H. A., Weiner, S. (1989). On Biomineralization. New York: Oxford University Press.

Lucas, A., Gaude, J., Carel, C., Michel, J.-F. & Cathelineau, G. (2001). A synthetic aragonite based ceramic as a bone graft substitute and substrate for antibiotics. *International Journal of Inorganic Materials*, 3, 87-94.

Mandel, J. (1965). Generalization de la theorie de la plasticite de W. T. Koiter. *International Journal of Solids and Structures*, 1, 273-295.

Mann, S., Webb, J. & Williams, R. J. P. (Ed's). (1989). Biomineralization: Chemical and biochemical perspectives. New York: VCH Publishers.

Mann, S. (2001). *Biom mineralization: principles and concepts in bioinorganic materials chemistry*. Oxford: Oxford University Press.

Manne, S., Zaremba, C. M., Giles, R., Huggins, L., Walters, D. A., Belcher, D. A., Morse, D. E., Stucky, G. D., Didymus, J. . Mann, S. & Hansma, P. K. Atomic force microscopy of the nacreous layer in mollusk shells. *Proceedings of the Royal Society of London: Biological Sciences*, 256, 17-23.

Menig, R., Meyers, M. H., Meyers, M. A. & Vecchio, K. S. (2000). Quasistatic and dynamic mechanical response of *Haliotis rufescens* (abalone) shells. *Acta Materiala*, 48, 2383-2398.

Mutvei, H. (1982). Ultrastructural studies on cephalopod shell part 1 : The septa and siphonal tube in Nautilus. *Bulletin of the Geological Institutions of the University of Uppsala New Series*, 3, 237-261.

Mutvei, H. (1978). Ultrastructural characteristics of the nacre in some gastropods. *Zoologica Scripta*, 7, 287-296.

Oliver, W. C., Pharr, G. M. (2004). Measurement of hardness and elastic modulus by instrumented indentation: Advances in understanding and refinement in methodology. *Journal of Materials Research*, 19, 3-20.

Ono, S., Kikegawa, T., Ohishi, Y. & Tsuchiya, J. (2005). Post-aragonite phase transformations in CaCO₃ at 40GPa. *American Mineralogist*, 90, 667-671.

Ota, Y., Iwatisha, T., Kasuga, T., Abe, Y. & Seki, A. (2002). Bone formation following implantation of fibrous calcium compounds (β -Ca(PO₃)₂, CaCO₃ (aragonite)) into bone marrow. *Journal of Materials Science: Materials in Medicine*, 13, 895-900.

Page, T. F., Oliver, W. C. & McHargue, C. J. (1992). The deformation behavior of ceramic crystals subjected to very low load (nano)indentations. *Journal of Materials Research*, 7, 450-473.

Peirce, D., Asaro, R. J. & Needleman, A. (1983) Material rate dependence and localized deformation in crystalline solids. *Acta Metallurgica*, 31, 1951-1976.

Pokroy, B. & Zolotoyabko, E. (2003). Microstructure of natural plywood-like ceramics: a study by high-resolution microscopy and energy-variable X-ray diffraction. *Journal of Materials Chemistry*, 13, 682-688.

Politi Y., Arad, T., Klein, E., Weiner, S. & Addadi, L. (2004). Sea urchin spine calcite forms via a transient amorphous calcium carbonate phase. *Science*, 306, 1161-1164.

Qi, H. J. Ortiz, C. & Boyce, M. C. (2006). Mechanics of biomacromolecular networks containing folded domains. *Journal of Engineering Materials and Technology*, in press.

Raleigh, C. B. (1968). Mechanisms of plastic deformation of olivine. *Journal of Geophysical Research*, 73, 5391-5406.

Reeder, R. J. (1983). Carbonates: Mineralogy and chemistry – Reviews in Mineralogy, V 11. Washington: Mineralogical Society of America.

Renner, J. & Rummel, F. The effect of experimental and microstructural parameters on the transition from brittle failure to cataclastic flow of carbonate rocks. *Tectonophysics*, 258, 151-169.

Rice, J. R. (1971). Inelastic constitutive relations for solids: an internal variable theory and its applications to metal plasticity. *Journal Mechanics and Physics of Solids*, 19, 433-455.

Rybacki, E. Experimental deformation of synthetic aragonite marble. (2003). *Journal of Geophysical Research*, 180, 1-15.

Sarikaya, M. (1994). An introduction to biomimetics: a structural viewpoint. *Microscopy Research and Technique*, 27, 360-375.

Sarikaya, M. & Aksay, I. A. (1995). Biomimetics: Design and processing of materials. New York: American Institute of Physics Press.

Schmid, S. M., Panozzo, R. & Bauer, S. (1987). Simple shear experiments on calcite rocks: rheology and microfabric. *Journal of Structural Geology*, 9, 747-778.

Smith, B. L., Schaffer, T. E., Viani, M., Thompson, J. B., Frederick, N. A., Kindt, J., Belcher, A., Stucky, G. D., Morse, D. E. & Hansma, P. K. (1999). *Nature*, 399, 761-763.

Song, F. & Bai, Y. L. (2003). Effects of nanostructures on the fracture strength of the interfaces in nacre". *Journal of Materials Research*, 18, 1741-1744.

Suito, K., Namba, J., Horikawa, T., Taniguchi, Y., Sakurai, N., Kobayashi, M., Onodera, A., Shimomura & Kikegawa, T. (2001). Phase relations of CaCO₃ at high pressure and high temperature. *American Mineralogist*, 86, 997-1002.

Voigt, W. (1910-reprint 1928). Lehrbuch der Kristallphysik. Berlin: Teubner,

Swainston, http://www.reef.crc.org.au/research/fishing_fisheries/statusfisheries/harvest_trochus.htm

Taylor, G. I. (1938). Plastic strain in metals. *Journal of the Institute of Metals*, 62, 307-324.

Taylor, J. D., Kennedy, W. J. & Hall, A. (1969). Shell structure and mineralogy of the bivalvia: Introduction Nuculacea-Rrigonacea. *Bulletin of the British Museum of Natural History Zoology Supplement*, 3, 1.

Tong, H., Hu, J., Ma, W., Zhong, G., Yao, S. & Cao, N. (2002). In situ analysis of the organic framework in the prismatic layer of mollusc shell. *Biomaterials*, 23, 2593-2598.

Van Vliet, K. J., Li, J., Zhu, T., Yip, S. & Suresh, S. (2003). Quantifying the early stages of plasticity through nanoscale experiments and simulations. *Physical Review B*, 67, 104105.

Wainwright, S. A., Biggs, W. D., Currey, J. D., Gosline, J. M. (1976). *Mechanical Design in Organisms*. New York: John Wiley & Sons.

Wang, R. Z., Suo, Z., Evans, A. G., Yao, N. & Aksay, I. A. (2001) Deformation mechanisms in nacre. *Journal Materials Research*, 16, 2485-2493.

Wang, R. Z., Wen, H. B., Cui, F. Z., Zhang, H. B. & Li, H. D. (1995). Observations of damage morphologies in nacre during deformation and fracture. *Journal of Materials Science*, 30, 2299-2304.

Wang, R. Z., Addadi, L. & Weiner, S. (1997). Design strategies of sea urchin teeth: structure, composition and micromechanical realtions to function. *Philisophical Transactions of the Royal Society of London B*, 35, 469-480.

Wang, Y., Raabe, D., Kluber, C. & Roters, F. (2004). Orientation dependence of nanoindentation pile-up patterns and microtextures in copper single crystals. *Acta Materialia*, 52, 2229-2238.

Weiner, S., Sagi, I. & Addadi, L. (2005). Choosing the crystallization path less travelled. *Science*, 309, 1027-1028.

Wenk, H. R., Takeshita, T., Van Houtte, P. & Wagner, F. (1986). Plastic anisotropy and texture development in calcite polycrystals. *Journal of Geophysical Research*, 91, 3861-3869.

Yoshio, O., Iwashita, T., Kasuga, T., Abe, Y. & Seki, A. (2002). Bone formation following implantation of fibrous calcium compounds (β -Ca(PO₃)₂, CaCO₃ (aragonite)) into bone marrow. *Journal of materials science: Materials in medicine*, 13, 895-900.

Yuen, P. S., Lister, M. W. & Nyburg, S.C. (1978). The four-center charge distribution of the carbonate ion and the lattice energies of calcite and aragonite. *The Journal of Chemical Physics*, 68, 1936-1941.

Zaremba, C. M., Belcher, A. M., Fritz, M., Li, Y., Mann, S., Hansma, P. K., Morse, D. E., Speck, J. S. & Stucky, G. D. (1996). *Chemistry of Materials*, 8, 679-690.

Zhao, Z., Radovitzky, R. & Cuitiño, A. (2004). A study of surface roughening in fcc metals using direct numerical simulation, *Acta. Materialia*, 52, 5791-5804.

Zhu, T. Li, J., Van Vliet, K. J., Ogata, S., Yip, S. & Suresh, S. (2004). Predictive modelling of nanoindentation-induced homogeneous dislocation nucleation in copper. *Journal of Mechanics of Physics and Solids*, 52, 691-724.